

**SYNTHESIS OF HYDROXYAPATITE
NANOPARTICLES (nano-HAp) FROM OSTRICH
BONE FOR BIOMEDICAL APPLICATIONS**



A THESIS SUBMITTED TO THE
CENTRAL DEPARTMENT OF CHEMISTRY
INSTITUTE OF SCIENCE AND TECHNOLOGY
TRIBHUVAN UNIVERSITY
NEPAL

FOR THE AWARD OF
DOCTOR OF PHILOSOPHY
IN CHEMISTRY

BY
KOMAL PRASAD MALLA
SEPTEMBER 2022



TRIBHUVAN UNIVERSITY
Institute of Science and Technology

DEAN'S OFFICE

Kirtipur, Kathmandu, Nepal



EXTERNAL EXAMINERS

Reference No.:

The Title of Ph.D. Thesis: " Synthesis of Hydroxyapatite nanoparticles (nano-HAp) from Ostrich Bone for Biomedical Applications "

Name of Candidate: Komal Prasad Malla

External Examiners:

- (1) Associate Prof. Dr. Surya Prasad Adhikari
Institute of Engineering, Pulchowk Campus
Tribhuvan University, NEPAL
- (2) Prof. Dr. Ajaya Kumar Singh
Government V.Y.T. PG. Autonomous College Durg
Chhatisgarh, INDIA
- (3) Prof. Dr. Zuriati Zakaria
Universiti Teknologi Malaysia
MALAYSIA

July 27, 2023

(Dr. Surendra Kumar Gautam)
Asst. Dean

DECLARATION

Thesis entitled “**Synthesis of Hydroxyapatite Nanoparticles (nano-HAp) from Ostrich Bone for Biomedical Applications**” which is being submitted to the Central Department of Chemistry, Institute of Science and Technology (IOST), Tribhuvan University, Nepal for the award of the degree of Doctor of Philosophy (Ph.D.), is a research work carried out by me under the supervision of Prof. Dr. Rameshwar Adhikari of Central Department of Chemistry, Tribhuvan University and co-supervised by Asst. Prof. Dr. Ram Jeewan Yadav of Department of Chemistry, Prithvi Narayan Campus, Tribhuvan University.

This research is original and has not been submitted earlier in part or full in this or any other form to any university or institute, here or elsewhere, for the award of any degree.

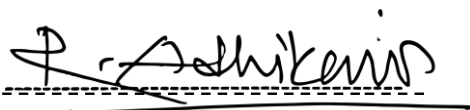


Komal Prasad Malla

RECOMMENDATION

This is to recommend that **Komal Prasad Malla** has carried out research entitled “**Synthesis of Hydroxyapatite Nanoparticles (nano-HAp) from Ostrich Bone for Biomedical Applications**” for the award of Doctor of Philosophy (Ph.D.) in **Chemistry** under our supervision. To our knowledge, this work has not been submitted for any other degree.

He has fulfilled all the requirements laid down by the Institute of Science and Technology (IOST), Tribhuvan University, Kirtipur for the submission of the thesis for the award of Ph.D. degree.



Prof. Dr. Rameshwar Adhikari

Supervisor

Central Department of Chemistry

Tribhuvan University

Kirtipur, Kathmandu, Nepal



Asst. Prof. Dr. Ram Jeewan Yadav

Co-Supervisor

Department of Chemistry

Prithvi Narayan Campus

Tribhuvan University, Pokhara, Nepal



त्रिभुवन विश्वविद्यालय
TRIBHUVAN UNIVERSITY
विज्ञान तथा प्रविधि अध्ययन संस्थान
Institute of Science and Technology
रसायन शास्त्र केन्द्रीय विभाग
CENTRAL DEPARTMENT OF CHEMISTRY
कीर्तिपुर, काठमाडौं, नेपाल
Kirtipur, Kathmandu, NEPAL

पत्र संख्या:
Ref. No.:

LETTER OF APPROVAL

.Date: 25/02/2080

On the recommendation of Prof. Dr. Rameshwar Adhikari and Asst. Prof. Dr. Ram Jeewan Yadav, this Ph.D. thesis submitted by Komal Prasad Malla, entitled "Synthesis of Hydroxyapatite Nanoparticles (nano-HAp) from Ostrich Bone for Biomedical Applications" is forwarded by Central Department Research Committee (CDRC) to the Dean, IOST, T.U.

Dr. Jagadeesh Bhattarai

Professor

Head

Central Department of Chemistry

Tribhuvan University

Kirtipur, Kathmandu

Nepal

ACKNOWLEDGEMENTS

I am grateful to my respected supervisors, Prof. Dr. Rameshwar Adhikari for his generous supervision, meticulous work arrangement and inspiring teaching in the incarnation of this work and Asst. Prof. Dr. Ram Jeewan Yadav, for showing me how to add creativity to my research in a way that helped me learn more.

I am obliged to my respected German supervisors, Dr. Sven Henning, Dr. Ralf Lach, Professor Dr. Mario Beiner, Professor Dr. Julia Beate Langer and Mr. Marcel Auerbach at Fraunhofer Institute for Microstructure of Materials and Synthesis, Halle, Merseburg University of Applied Sciences, Merseburg and Martin Luther University (MLU), Halle-Wittenberg for their generous laboratory support for my research stay in Germany. I would like to express my sincere gratitude to the German Academic Exchange Service (DAAD) for providing binationally supervised research stay grants to continue my research work at MLU, Halle-Wittenberg and Polymer Synthesis and Modification (PSM) GmbH, Merseburg, Germany.

I would like to thank the head of department and former head of department of the Central Department of Chemistry in Kirtipur for their support in my research. I am very grateful to the faculty, staff and friends in the Central Department of Chemistry and Research Centre for Applied Science and Technology (RECAST) Kirtipur for their warm cooperation and valuable suggestions for my work. I would like to acknowledge the Dean's Office of the Institute of Science and Technology (IOST), Tribhuvan University, for my Ph.D. registration and the Office of the Vice Chancellor, Pokhara University, for providing study leave for my research work. I would like to acknowledge with thankfulness the University Grants Commission (UGC) in Sanothimi Bhaktapur, Nepal for providing Ph.D. research support grants (Ph.D.74-75/S&T) for this work. I would like to acknowledge Professor Dr. Shinichi Sakurai, Professor Dr. Hideki Yamane and professor Dr. Sono Sasaki for providing me laboratory excess for electrospinning of polymer composite scaffolds and its characterizations in the Department of Biobased Materials, Kyoto Institute of Technology (KIT), Matsugasaki Hashikamicho, Sakyo Ward, Kyoto, Japan. I gratefully acknowledge Associate Professor Mrs. Bindu Malla, Department of Pharmacology, Gandaki Medical College, Pokhara, for the acute toxicity test of nano-HAp-GEL suspension in Albino Wister rats.

I would like to thank my colleges, Dr. Jyoti Giri, Dr. Rajesh Pandit, Dr. Netra L. Bhandari, Dr. Shanta Pokhrel and Dr. Shankar P. Khatiwada (Tri-Chandra Multiple Campus, Tribhuvan University, Ghantaghar, Kathmandu); Dr. Kedar Nath Dhakal, Mr. Achyut Nepal, Mr. Prakash Gautam and Mr. Ramesh Puri for their cooperation in this research work. I am obligated to my late parents for preparing me for nothing except the struggle for my education. I am thankful to my spouse for all her trouble and endurance during my studies. I am also thankful to my treasured sons and all family members for the moments of tears and laughter during my work and studies.



Komal Prasad Malla

ABSTRACT

The present work aimed at extracting nanosized hydroxyapatite (nano-HAp) from ostrich bone waste powder, characterizing it in terms of its structure and properties, including its oral acute toxicity, and using the nano-HAp and vitamin D3 (VD3) as a filler to prepare biodegradable polymer nanocomposite scaffolds through electrospinning technique for further biomedical investigation. The materials (HAp and electrospun scaffolds) were analysed using advanced analytical tools such as Fourier Transform Infrared (FTIR) and Energy Dispersive X-ray (EDX) spectroscopies, X-ray diffraction (XRD), Electron Microscopy such as scanning electron microscopy (SEM), Transmittance electron microscopy (TEM), Optical microscopy (OM), Thermogravimetric Analysis (TGA) and Zeta Potential measurements. The FTIR spectra showed that the HAp extracted by the thermal decomposition of bone powder at 950 °C for 6 h led to the removal of the organic moieties and the presence of phosphate (PO_4^{3-}), carbonate (CO_3^{2-}) and hydroxyl (OH^-) groups as main constituents. The XRD showed the crystalline texture of the HAp with an average particle diameter of 19.23 nm, while the hexagonal particle morphology was observed by SEM Microscopy. The high thermal stability of the synthesized HAp was attested by the negligible mass loss on heating it up to 1000 °C during the TGA test. The acute toxicity test of nano-HAp revealed a lethal 50% dose (LD50) value of more than 2000 mg/kg body weight in the experimental rats which indicates the nano-HAp safe for biomedical applications. In another stage of investigations, the electrospun nanocomposite scaffold fibres of polymer and nano-HAp revealed morphological variation, particularly in the fibre thickness, phase segregation and surface texture, as a function of the nanoparticles content. During mechanical testing, a brittle-to-ductile transition was observed in the fibres at a filler concentration between 3–12 wt.-%. The change in the micromechanical behavior of scaffold fibres from fibre-cracking to thin layer yielding has been attributed to the observed behavior. The value of the Water Drop Contact Angle (WDCA) on the scaffold surfaces was found to decrease drastically with the nanofiller content (from 79.0° to 44.8° on increasing the filler from 3 wt.-% to 12 wt.-%) in turn providing evidence to the enhanced hydrophilicity of the scaffolds, an essential requirement for biological tissues adherence and growth. The results of an *in vitro* biomedical test of the scaffold in phosphate buffer saline (PBS) solution showed a higher degradation rate of neat scaffolds compared to composite scaffolds owing to crystalline nature of nano-HAp implying some stability of the latter in case of their uses inside the body. Optical laser microscopy showed noticeable signs of

scratch and breakage line formation on the scaffold surfaces after second weeks of *in vitro* degradation in PBS solution for seven weeks of incubation period. The nano-HAp thus synthesized using waste biomass has been found to possess high promise for being used as an excellent biomedical material for various biomedical applications.

Keywords: acute toxicity, deformation behavior, *in vitro* degradation, morphology, nano-HAp

LIST OF ACRONYMS AND ABBREVIATIONS

3D	: Three Dimensional
ALP	: Alkaline Phosphate
AOW	: Absolute Organ Weight
AT	: Acute Toxicity
BCP	: Biphasic Calcium Phosphate
BTE	: Bone Tissue Engineering
BTR	: Bone Tissue Regeneration
CB	: Composite Blend
CHAp	: Carbonated Hydroxyapatite
CNS	: Central Nervous System
CP	: Calcium Phosphate
CTAB	: Cetyltrimethylammonium Bromide
ECM	: Extra Cellular Matrix
ES	: Electrospinning
FDA	: Food and Drug Administration
FTIR	: Fourier Transform Infrared Spectroscopy
FWHM	: Full Width at Half Maxima
GEL	: Gelatin
GHS	: Globally Harmonized System
HAp	: Hydroxyapatite
ICDD	: International Centre for Diffraction Data
ISO	: International Organization for Standardization
MoFE	: Ministry of Forest and Environment

OECD	: Organization for Economic Cooperation and Development
OM	: Optical Microscopy
PBS	: Phosphate Buffer Saline
PCL	: Polycaprolactone
PLLA	: Poly- L- Lactic Acid
ROW	: Relative Organ Weight
SEM	: Scanning Electron Microscopy
TCP	: Tricalcium Phosphate
TEM	: Transmission Electron Microscope
TGA	: Thermogravimetric Analysis
TTAB	: Tetradecyltrimethylammonium Bromide
UTS	: Ultimate Tensile Strength
VD3	: Vitamin D3
W/O	: Water-in-Oil (Microemulsion)
WDCA	: Water Drop Contact Angle
XRD	: X-ray Diffraction
α -TCP	: Alpha Tricalcium Phosphate

LIST OF SYMBOLS

Å	: Angstrom
a.u.	: Arbitrary Unit
cm ⁻¹	: Per Centimetre
D	: Crystallite Size
Da	: Dalton
°C	: Degree Celsius
g	: Gram
GPa	: Giga Pascal
h	: Hours
LD50	: 50% Lethal Dose
kDa	: Kilo Dalton
kV	: Kilo Volt
λ	: Wavelength of X-ray
μg	: Microgram
mg	: Milligram
mM	: Milli Mole
mm	: Millimeter
MPa	: Mega Pascal
MPa	: Mega Pascal
nm	: Nanometer
%	: Percentage
rpm	: Revolutions Per Minute
θ	: Theta (Bragg angle)
wt.-%	: Weight Percentage

LIST OF TABLES

	Page No.
Table 1: Hierarchical level of bone and their scales	11
Table 2: The elements and their wt.-% found in bone minerals	12
Table 3: Mechanical properties of human cortical bone	13
Table 4: List of common members of CP family, with their names, abbreviations, formula, Ca/P molar ratio, crystal structure and solubility	19
Table 5: List of the method used for the synthesis of HAp	21
Table 6: An overall summary of methods of extraction, heating temperature, holding time and physicochemical properties of HAp extracted from various animal bones	28
Table 7: A summary of the source's extraction method, heating temperature, holding time and physicochemical parameters of HAp extracted from fish bones and scales	34
Table 8: A summary of the source, extraction method, heating temperature, holding time and physicochemical parameters of HAp extracted from shell sources	41
Table 9: List of chemicals and polymers used in the study	53
Table 10: Mixing by volume ratios of water, oil, surfactants and co-surfactants for preparation of W/O microemulsion	57
Table 11: Mixing volumes of water, oil surfactants and co-surfactants for the preparation of W/O microemulsion	58
Table 12: List of samples used in the study	58
Table 13: The volume of nano-HAp and VD3 blended in PCL, PLLA and GEL composite blends	59

Table 14:	Grouping of rats and their numbers for acute toxicity test of nano-HAp-GEL suspension	67
Table 15:	Summary of tools and techniques used for the sample preparation for various purposes	68
Table 16:	Summary of analytical tools/techniques used for the characterization of HAp and scaffolds	69
Table 17:	Major and trace elements found in ostrich bone HAp	76
Table 18:	Comparison of phase analysis of segregated ostrich bon HAp with ICDD file no. 00-09-0432	78
Table 19:	Observation variables of group III rats administered nano-HAp-GEL suspension at a dosage of 2000 mg/kg body mass (n=5)	84
Table 20:	The total organ weight of rats which received nano-HAp-GEL suspension at a dose of 300 mg/kg of gr. II (n=3), 2000 mg/kg of gr. III (n=5), & and gr. I, vehicle (n=3)	88
Table 21:	The relative organ weight of rats which received plain gelatin, gr. I, (n=3), nano-HAp-GEL suspension at a dose of 300 mg/kg, gr. II (n=3) and 2000 mg/kg, gr. III (n=5)	89
Table 22:	Average fiber diameter of scaffolds with respect to volume fraction percentage of filler	93
Table 23:	WDCA values of each scaffold with drop shapes	101
Table 24:	Hydrolytic degradation of scaffolds in PBS solution for 7 weeks	105

LIST OF FIGURES

	Page No.
Figure 1: Structure of common polymer unit used in preparing biomedical scaffolds; (a) monomer unit of polycaprolactone (PCL), (b) monomer unit of poly-L-lactic acid (PLLA), & (c) monomer unit of gelatin (GEL)	3
Figure 2: Structure of Vitamin D3	5
Figure 3: The hierarchical organization of bone from a macrostructural to sub-nano structural level	10
Figure 4: Chemical composition of human bone	11
Figure 5: Composition of bone tissue	14
Figure 6: Different stages of secondary fracture healing	17
Figure 7: Schematic drawing showing the crystalline texture of the HAp in its hexagonal lattice framework, showing the "C" and "P" sites	20
Figure 8: TEM micrographs of the HAp prepared from $\text{Ca}(\text{H}_2\text{PO}_4)_2 \cdot \text{H}_2\text{O}$ and $\text{Ca}(\text{OH})_2$ showing the effect of time of milling with P_2O_5	22
Figure 9: SEM images of calcinated samples of HAp: (a) Bovine, (b) Porcine, (c) Human and (d) Reference sample of HAp (Sigma-Aldrich)	25
Figure 10: XRD patterns of A-type and B-type substituted HAp before and after calcination at 600 °C, 800 °C and 1000 °C	26
Figure 11: SEM micrographs of HAp obtained from cuttlefish bone	31

Figure 12:	SEM micrograph of the FHAp powder (a & b), sintered FHAp powder (c), SHAp powder (d & e) and sintered SHAp powder (f)	33
Figure 13:	FESEM images of the abalone shell cross-section (a) and the samples exposed to different hydrothermal times: (b) 6 h, (c) 18 h and (d) 72 h; The inset (e) is a magnified view of the selected red area. (f) HAp hexagonal crystallites schematic diagram	35
Figure 14:	Powder XRD spectra of hydroxyapatite (HAp) prepared by using (a) crab shells, (b) eggshells and (c) wet chemical process	36
Figure 15:	The flow sheet diagram of the synthetic route of HAp powder from waste mussel shells	37
Figure 16:	The SEM images of nano-HAp powders: (a) raw mussel shell; (b) dried mussel shell; (c), heated mussel shell; and (d) commercial mussel shell	38
Figure 17:	SEM images of HAp calcined at 800 °C, 900 °C & 1000 °C. (a) HA 800, (b) HA 900 and (c) HA 1000.	40
Figure 18:	Major biomedical applications of biosource-based nano-HAp	42
Figure 19:	Fluorescent images of NIH3T3 fibroblast cell spreading and proliferation a day after seeding into: (a) Amminolysed PLLA cylinder, (b) Amminolysed PLL cylinder + HAp, (c) Amminolysed PLLA cylinder Simvastatin and (d) Amminolysed PLL cylinder+HAp+Simvastatin	44
Figure 20:	Pictorial representation of different drug conjugation processes over the surface of HAp. A: Coating of HAp surface with nanoparticles, B:	46

Physical interactions of antibiotics, C: Physical interaction of anticancer drugs, D: Core-shell magnetic HAp, E: Noncovalent attachment, F: Covalent attachment of Drugs

Figure 21:	The figure shows the 3D printed design of anatomical femoral and vertebral plate-fused scaffolds. (A) 3D printed model of the rabbit femoral scaffold. (B) The CT-scan data-based femoral scaffolds of rabbit.	48
Figure 22:	The figure shows the implant and tendon graft within the bone tunnel in ACL reconstruction. (A) The 3D perspective of the bone tunnel in ACL reconstruction. (B) A cross-sectional view of the bone tunnel. (G: Graft; S: Screw-like scaffold; BT: Bone tunnel; and M: Macropore)	49
Figure 23:	Ostrich farmhouse visit in Gangolya-1, Rupendehi District, Nepal	52
Figure 24:	Photograph of Albino Wistar rat used in an acute toxicity test	52
Figure 25:	Schematic diagram fo the research plan	54
Figure 26:	Photographs of (a) raw bones, (b) its pieces and (c) bone powder after grinding	54
Figure 27:	Photograph of alkaline hydrothermal hydrolysis to remove impurities from bone powder	55
Figure 28:	Photographs showing steps in the extraction of HAp from ostrich bone powder	55
Figure 29:	Photograph of the preparation of W/O microemulsion for segregation of nano-HAp from recalcined bone ash powder	56
Figure 30:	Flow chart of W/O microemulsion technique used to segregate the nano-HAp form aggregate bulk of the	57

	HAp particles	
Figure 31:	Blending of nano-HAp in VD3 and polymer composite solutions for fabrication of scaffold	59
Figure 32:	Instrumental setup for electrospinning of fibrous scaffold: (a) Rotating drum, (b) polymers solution in a syringe, (c) Pumping set, (d) DC power supply	60
Figure 33:	Photograph of the tensile test sample of the electrospun scaffold mounted on the rectangular frame of graph paper	63
Figure 34:	Photograph of incubation of the scaffolds at 37 °C for simulation in a biological environment for 7 weeks	64
Figure 35:	Crosslinking between gelatin and nano-HAp	65
Figure 36:	Diagrammatic representation of the summary of the experimental works	67
Figure 37:	FTIR spectra of raw ostrich bone powder	73
Figure 38:	FTIR spectra of HAp calcined at 950 °C for 6 h	74
Figure 39:	EDX spectra of HAp obtained from the ostrich bone ash calcined at 950 °C for 6 h	77
Figure 40:	XRD patterns of (a) the segregated HAp using W/O microemulsion technique, (b) HAp recalcination at 950 °C for 6 h, (c) HAp calcined at 650 °C for 6 h and (d) the bone powder	77
Figure 41:	SEM micrographs of (a) the bone powder calcined at 650 °C for 6 h, (b) the bone powder after recalcination at 950 °C for another 6 h and (c) the nano-HAp extracted after segregation	79
Figure 42:	TGA analysis curve of the HAp (obtained from the bone powder calcined at 650 °C for 6 h) heated from 100 °C to 1000 °C under N₂ atmosphere	81

Figure 43:	The effect of nano-HAp-GEL suspension on percentage body weight gain. The data are expressed as an average (Vehicle n=3, 300 mg/kg n=3, 2000 mg/kg n=5, $p > 0.05$)	86
Figure 44:	FTIR spectra of VD3, PCL, PLLA, GEL, CB-1 and CB-6	91
Figure 45:	Photographs of SEM images of scaffolds: (a) CB-1, (b) CB-2, (c) CB-3, (d) CB-4, (e) CB-5 and (f) CB-6	94
Figure 46:	TEM micrograph of single scaffold fiber (CB-3) stained with RuO₄ (a) Low magnification, (b) High magnification	95
Figure 47:	Stress-strain curves of fibrous scaffolds: (a) CB-1, (b) CB-3, (c) CB-4, (d) CB-5 & (e) CB-6	97
Figure 48:	Tensile properties of the nanofibrous scaffolds as a function of the filler (nano-HAp) fraction percentage (a) elastic modulus, (b) tensile strength and (c) strain at break; the lines are visualizing the trend only	99
Figure 49:	Photographs of representative SEM images of CB-4 after tensile test: modulated crazing in fibers; a) overview image, b) detail	100
Figure 50:	Representative SEM images of sample CB-6 after tensile test: thin layer yielding behaviour; a) overview image, b) detail	100
Figure 51:	The graphs of <i>in vitro</i> degradation test of representative scaffolds of CB-1, CB-4, CB-5 and CB-6	104
Figure 52:	Representative laser microscopy images of degrading electrospun CB-1 scaffolds (a) before degradation and (b) after 7 weeks days incubation in PBS solution	106

TABLE OF CONTENTS

	Page No.
Declaration	ii
Recommendation	iii
Letter of Approval	iv
Acknowledgements	v
Abstract	vii
List of Acronyms and Abbreviations	ix
List of Symbols	xi
List of Tables	xii
List of Figures	xiv
Table of contents	xix
CHAPTER 1	1
1. INTRODUCTION	1
1.1 Introduction	1
1.1.1 Biomaterials for Bone Tissue Engineering	1
1.1.2 Need of Developing Biomaterials Based on Local Resources	2
1.2 Rationale of the Study	6
1.3 Objectives	7

1.3.1 General Objective	7
1.3.2 Specific Objectives	7
1.4 Scope and Organization of Thesis	7
1.5 Limitations and Delimitations	8
1.5.1 Limitations	8
1.5.2 Delimitations	9
CHAPTER 2	10
2. LITERATURE REVIEW	10
2.1 Human Bone	10
2.1.1 Hierarchical Organization of the Bone	10
2.1.2 Chemical Composition	11
2.1.3 Type of Bone	12
2.1.4 Composition of Bone	12
2.1.5 Mechanical Properties	13
2.1.6 Structural Properties of Bone Cells	14
2.1.7 Healing Mechanism of Fracture Bone	15
2.2 Hydroxyapatite (HAp) and its Source	17
2.2.1 Synthesis of HAp from Biowastes	19
2.2.2 Biogenic Sources of HAp	24
2.2.3 HAp form Animal and Bird Bones	24
2.2.4 HAp from Fish Biowastes	30
2.2.5 HAp from Shells	35
2.3 Biomedical Applications of HAp	42

2.3.1 Tissue Engineering Scaffold	42
2.3.2 Drug Delivery Transporter	45
2.3.3 3D Printing of Composite	47
2.3.4 Implant Coating	49
2.3.5 Research Gap	51
CHAPTER 3	52
3. MATERIALS AND METHODS	52
3.1 Materials	52
3.1.1 Ostrich Bone	52
3.1.2 Albino Wistar Rats	52
3.1.3 Chemicals, Solvents and Polymers	53
3.2 Methods Used	54
3.2.1 HAp Preparation	54
3.2.2 Microemulsion Technique	55
3.2.3 Preparation of Biomedical Scaffolds	57
a. Solution Preparation	57
b. Electrospinning Setup	58
3.3 Characterization Techniques	59
3.3.1 Fourier Transform Infrared (FTIR) Spectroscopy	59
3.3.2 X-ray Diffraction (XRD)	60
3.3.3 Scanning Electron Microscopy (SEM)	60
3.3.4 Transmission Electron Microscopy (TEM)	60

3.3.5 Energy Dispersive X-ray (EDX) Spectroscopy	61
3.3.6 Zeta Potential Measurement	61
3.3.7 Optical Microscopy (MO)	61
3.3.8 Thermogravimetric Analysis (TGA)	61
3.3.9 Tensile Testing	61
3.3.10 Wettability/Hydrophilicity Test	62
3.3.11 <i>in vitro</i> Degradation Test	63
3.4 Acute Toxicity Test	64
3.4.1 Preparation of Oral Gavage Solutions	64
3.4.2 Experimental Animals	65
3.4.3 Toxicity Test	65
CHAPTER 4	70
4. RESULTS AND DISCUSSION	70
4.1 Nano-HAp Preparation and Characterization	70
4.1.1 Physicochemical Parameters of HAp	70
4.1.2 Structural Characterization	71
4.1.3 Morphological Characterization	75
4.1.4 Structural Stability	79
4.2 Acute Toxicity Analysis of nano-HAp	83

4.2.1 Observation of Physical Signs, Behavioural Effects and Sensory Parameters	83
4.2.2 Observation of Body Weight Loss	86
4.2.3 Analysis of Absolute and Relative Mass of Body Organs	87
4.3 Characterization of Electrospun Biomedical Scaffolds	91
4.3.1 Structural Characterization of the Scaffold	91
4.3.2 Microscopic Analysis of Scaffold Fibers	93
4.3.3 Microscopic Analysis of Single Fibers	95
4.3.4 Deformation Behavior of Scaffolds	96
4.3.5 Microscopic Analysis of Fracture Surface after Tensile Test	99
4.3.6. Wettability Analysis of the Scaffolds	100
4.4 <i>In vitro</i> Biomedical Test of the Scaffolds	103
CHAPTER 5	108
5. CONCLUSION AND RECOMMENDATIONS	109
5.1. Conclusions	108
5.2 Recommendations for Future Works	109
CHAPTER 6	111
6. SUMMARY	111
REFERENCES	115
APPENDIX	
List of Publications	
List of Presentations	

CHAPTER 1

1. INTRODUCTION

1.1 Introduction

1.1.1 Biomaterials for Bone Tissue Engineering

In recent years, for bone tissue engineering (BTE), many synthetic bone substitutes and scaffolds have been made to fix the issues of using autografts and allografts due to the limited supply of bone materials, complications at the donor site, the risk of disease transmission and immune rejection. Polymer-based biomaterials can be made into different structures with mechanical properties, topography, geometry and architecture for biomedical uses. Studies shows that these materials do not have bioactivity and osteoconductive properties which are the fundamental requirements for the proliferation and differentiation of bone tissues. Some fillers are needed to add to these polymer composite scaffolds for improving bioactivation (Hannink & Arts, 2011; Raucci *et al.*, 2012). Some calcium phosphate (CP)-related biomaterials, such as hydroxyapatite (HAp), tricalcium phosphate (TCP) and biphasic calcium phosphate (BCP), are the common fillers used generally in polymer composite scaffolds for biomedical applications (Kareem, 2018). Various studies have shown that adding a certain percentage of HAp as a filler to a polymer composite scaffold improves its bioactivity and mechanical properties of scaffolds. Such scaffolds are highly demanded for *in vitro* and *in vivo* biomedical applications in comparison to scaffolds fabricated from polymers only (Tanner, 2010; Tanner *et al.*, 1994).

For decades, various techniques, such as solvent casting, freeze drying, gas foaming, rapid prototyping, 3D printing and electrospinning (ES), have been used to fabricate scaffolds for biomedical applications (Rajzer *et al.*, 2018; Sattary *et al.*, 2018). Among them, ES is the most commonly used low-cost, versatile and bottom-up technique for fabrication of fibrous scaffolds. Many researchers used this technique to make scaffolds using synthetic and natural polymers applied for drug delivery and BTE (Barhate & Ramakrishna, 2007; J.-P. Chen & Chang, 2011; Fahmy *et al.*, 2016; Linh & Lee, 2012; Mi, Jing, *et al.*, 2014; Puppi *et al.*, 2011). Studies show that the fiber diameter of the polymer composite scaffold fabricated by ES method has a range of nano to microscale, which is suitable to imitate the problems of cell proliferation and

differentiation in the natural environment of the extracellular matrix (ECM) and applied part of host tissue (Thorvaldsson *et al.*, 2008). Barhate & Ramakrishna (2007) reported that such scaffolds have a well-defined architecture, morphology and controllable pore size that could closely mimic the structure of ECM. On the other hand, due to the unavailability of autografts and limited availability of bone substitutes, problems with the donor site, risk of disease transmission and immune rejection encountered while using allografts, various biodegradable scaffolds have been used for bone tissue engineering. Such scaffolds have been constructed into a variety of structures with suitable mechanical characteristics, topography, geometry and architecture for a biomedical of applications

In order to promote the bioactivation of the polymer composite scaffolds, the incorporation of bioactive substances is necessary (Raucci *et al.*, 2012). For this purpose, some of calcium phosphate related bioceramics such as hydroxyapatite (HAp), tricalcium phosphate (TCP), biphasic calcium phosphate (BCP), etc., are commonly used to fabricate such scaffolds (Londoño-Restrepo *et al.*, 2016; Panda *et al.*, 2014).

Hence by using a hybrid composite approach, combining the beneficial roles of biodegradable polymers, vitamins and bioactive ceramic for adjusting the structural, mechanical and biological properties would be greatly advantageous for biomedical application (Nithya & Sundaram, 2015; Su *et al.*, 2013). Furthermore, fabrication of such scaffolds demands the principles of biology, clinical science and engineering as well (Zhang *et al.*, 2019). The scaffold fabricated using all these principles supports to develop as a prototype for networking with adjoining cells and creating an extracellular matrix (ECM), which provides physical support to the newly produced tissues (Pati *et al.*, 2015). When such scaffold is implemented in bone tissue regeneration studies it helps to revitalized the bone tissue from that fracture area should be combined with the nearby tissue and show its bioactivity.

1.1.2 Need of Developing Biomaterials Based on Local Resources

Studies shows that several natural and synthetic polymers and biomaterials have been used to prepare scaffolds for biomedical applications. Among the various synthetic polymers, polycaprolactone (PCL) and poly-L-lactic acid (PLLA) are commonly used polymers to fabricate scaffolds. These polymers are US Food and Drug

Administration (FDA)-approved biodegradable polymers for clinical use (Nithya & Sundaram, 2015; Shuai *et al.*, 2020). Due to its non-toxic nature, PCL is widely used to fabricate fibrous scaffolds for BTE (M. I. Hassan *et al.*, 2014). This polymer has better biocompatibility with host tissue and low acidic by-products (Bhattarai *et al.*, 2018; Mota *et al.*, 2013; Shuai *et al.*, 2020). The scaffold of this polymer has better elasticity in comparison to the other polymers such as; polyamide (PA), polyurethane (PU) and polyvinyl alcohol (PVC) (Narayanan *et al.*, 2015). Despite this, due to its hydrophobic nature, it has some disadvantages, such as a slow biodegradation rate in comparison to natural polymers like silk, collagen, gelatin, chitosan, etc. Studies have shown that due to the presence of a hydrocarbon chain in the monomer unit of the PCL (**Figure 1a**), the scaffold of this polymer has poor cell adhesion, motility and integration with the host tissue response (Yoon & Kim, 2011). Owing to these reasons this polymer is one of the best alternatives for the fabrication of scaffold.

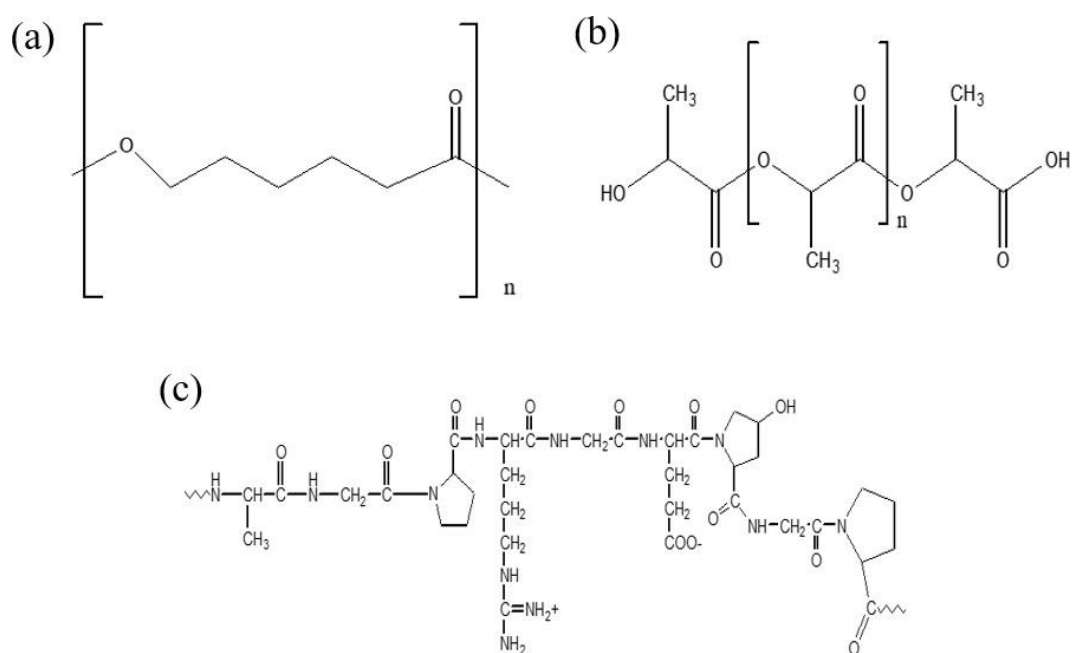


Figure 1: Structure of common polymer unit used in preparing biomedical scaffolds; (a) monomer unit of polycaprolactone (PCL), (b) monomer unit of poly-L-lactic acid (PLLA) and (c) monomer unit of gelatin (GEL)

On the other hand, poly-L-lactic acid (PLLA) also has a slow degradation rate as like PCL due to the presence of a hydrophobic methyl group (CH_3) in its monomer backbone (**Figure 1b**). This group acts as a physical barrier and hinders contact with biofiller on the scaffolds (Goulart *et al.*, 2016). Despite these the scaffold of this

polymer has a high mechanical strength and elastic modulus; owing to this, it is commonly used in various biomedical applications. In addition, the non-enzymatic hydrolysis of the ester linkages of PLLA into lactic acid breaks apart the electrospun fiber *in vivo* which is a natural pathway in the carbohydrate metabolism of all vertebrates and microbes that can be broken down into CO₂ and H₂O (Ba Linh *et al.*, 2013; Sattary *et al.*, 2018; Shuai *et al.*, 2020). Studies shows that PLLA is degraded by hydrolysis in two physiological conditions. Firstly, the ester groups are broken apart by hydrolysis without the support of enzymes. Secondly, it breaks down inside the cell as like a biopolymer (Ba Linh *et al.*, 2013; Meng *et al.*, 2010). However, the scaffold fabricated by this polymer has a high mechanical strength and elastic modulus which is beneficial for bone tissue engineering. Despite these, due to its higher crystallinity, its fragments can cause inflammation in the applied part *in vivo*, which could limit its application to fabricate scaffolds for bone tissue engineering (Anjaneyulu *et al.*, 2017).

Gelatin (GEL) is a hydrophilic another biopolymer (**Figure 1c**) that is predicted to have both hydrophilicity and good biodegradability, similar to the collagen matrix as found in human bone (Sattary *et al.*, 2018). The individual scaffold of either PCL or PLLA or a composite blend of both fabricated by blending with GEL could be expected to have a better degradation rate than PCL and PLLA alone. Owing to the hydrophilic nature of GEL, it supports to enhances the biodegradation rate of the scaffold blended with PCL and PLLA *in vivo/in vitro* (Kim *et al.*, 2006). So, the GEL is mainly used to blend with many polymers to fabricate a biodegradable scaffold for biomedical applications.

The studies of Meng *et al.* (2010) and Venugopal *et al.* (2008) have shown that scaffolds made of PCL/GEL, PCL/PLLA and GEL/PLLA have better biocompatibility, physiochemical properties and mechanical properties than the scaffolds fabricated by using individual polymers (Meng *et al.*, 2010; Venugopal *et al.*, 2008). Zhou and Lee reported that such scaffolds have better results in the proliferation and differentiation of osteoblast cells compared to those fabricated from polymers only to use for a bone tissue regeneration study (Zhou and Lee, 2011).

Vitamin D3 (VD3) (**Figure 2**) has long been recognized for its critical function in the control and maintenance of calcium, phosphorus balance and bone metabolism (Huang *et al.*, 2010; Satter *et al.*, 2014). It serves to control the activities of osteoblast

and osteoclast cells in bone metabolism. These cells are responsible for bone formation, resorption and regeneration (Anderson, 2017). According to Lei *et al.* (2019) and Sattary *et al.* (2018) bone cell development is a dynamic process that involves both osteoblast and osteoclast cells. It has a vital role for the control of calcium and phosphorus in the bone metabolism as well as the activities of osteoblast and osteoclast cells. It plays an important role for keeping bones in good shape and posture (Kato *et al.*, 2015; Katsogiannis *et al.*, 2015; Linh *et al.*, 2013; Posa *et al.*, 2016). Studies show limited application of this vitamin for biomedical applications mainly for BTR studies. Literature show that this vitamin also contributes to the scaffold's bioactivity and enhancement of its osteoconductive properties. Therefore, application of this vitamin along with nano-HAp prepared from ostrich bone and polymers (PCL, PLLA and GEL) could be a rationale work to fabricate scaffolds for biomedical applications.

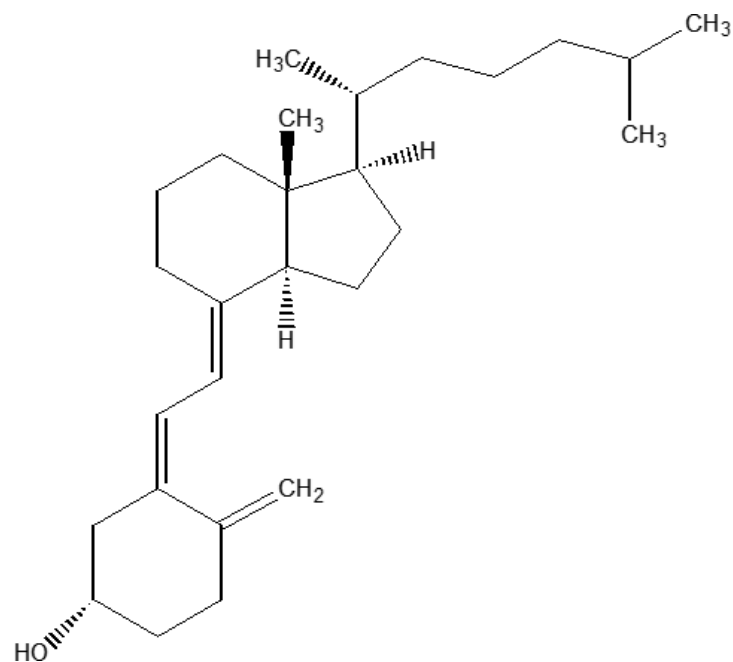


Figure 2: Structure of Vitamin D3

Among the various CP related bioceramics, HAp is an extensively studied bioceramic for biomedical application due to its nontoxic, bioactive, biocompatible and osteoconductive nature (Arsad *et al.*, 2011). Study show that this ceramic is widely used in many non-load-bearing orthopaedic applications, such as filler in a polymer composite, as a coating for implants, drug delivery, dentistry and many more (Alshemary *et al.*, 2015; Fahmy *et al.*, 2016). The bioactive and biodegradable nature

of HAp makes it a material of choice for various biomedical applications because of its similar composition to the mineral phase of human bone. However, one of the drawbacks of using this ceramic as a filler to blend in polymer composites is due to its crystalline nature, it causes a significant reduction in the mechanical and degradation properties of the scaffold upon increasing its content in the composite blends.

Different studies have shown that scaffolds fabricated only from polymers are not suitable for biomedical application as discussed above in section 1.1.1. Certain materials, such as growth factors, minerals, vitamins and drugs, are necessary to incorporate to improve the bioactivity of the scaffolds (Wang *et al.*, 2019; Zhang *et al.*, 2019). Recently, hybrid models of different minerals, vitamins, growth factors and drugs incorporated into polymers have been used for better performance of scaffolds for biomedical applications (Ba Linh *et al.*, 2013; Sattary *et al.*, 2019; Zhang *et al.*, 2019). These hybrid models of composite scaffolds should be expected to improve the bioactivity, mechanical strength, biocompatibility and degradation rate as well. In terms of bone cell adhesion, migration, phenotype preservation and cellular matrix transmission, these scaffolds are better than scaffolds fabricated by using polymer blends only (Beachley & Wen, 2010; Mota *et al.*, 2013; Puppi *et al.*, 2010).

Studies show that only small number of fillers (5–10 wt.-%) maintain the bioactivity and mechanical integrity of the scaffolds. Zhang *et al.* (2019) reported that blending of the controllable amount of nano-HAp as a filler in polymer composite blends improve the structural, mechanical and biological properties of the scaffold.

Chiu and Waldman (2016) reported that the natural ECM is a 3D scaffold that can provide physical support as well as regulate a variety of cellular functions. When this scaffold is immersed in the bodily fluid environment, either *in vitro* or *in vivo*, it helps to expose the HAp from the scaffold surface, allowing the bioactivity and osteoconductive nature of HAp to be fully demonstrated in the target area of applied part (Roseti *et al.*, 2017; Satter *et al.*, 2014; Zhang *et al.*, 2005). Hence from the background of above discussion a research gap was found to prepare a scaffold using biodegradable polymers; PLC, PLLA, GEL and VD3 and some volume fraction % of nano-HAp by electrospinning process for biomedical application.

1.2 Rationale of the Study

According to Dorozhkin (2010), the chemically synthesized HAp might have a toxic effect for *in vivo* biomedical applications. Another matter is its route of synthesis is comparatively expensive than biogenic sources which demands for a higher degree of purity of calcium and phosphorus precursors (Varadarajan *et al.*, 2014). Therefore, the utilization of locally available biowastes such as ostrich bone is a rationale of choice for the HAp synthesis. This is locally available in the ostrich slaughterhouse only as a biowaste which is not further used for value added purposes. Moreover, studies show that the cortical bones of ostrich contain a high amount of minerals due to its habitat and food habits in comparison to the similar counterparts from other animals i.e. bovine, goat, buffalo etc. Ostrich bones contain a higher Ca/P molar ratio (>1.67) which is a great advantage of using ostrich bone to prepare nonstoichiometric HAp for biomedical applications. Hence, this study has emphasized the utilization of waste ostrich bones as an economical and eco-friendly source to prepare high value HAp with the potential of biomedical applications. In this regard, the present work focuses on the preparation of HAp using waste ostrich bones. Furthermore, nano-HAp is segregated from the bulk of the particles using the water-in-oil (W/O) microemulsion technique which is carried out its acute oral toxicity test on Wistar Albino rats. Finally, fabrication of nano-HAp and VD3 blended polymer composite scaffolds *via* electrospinning to investigate their biomedical applications is a novelty of this work.

1.3 Objectives

1.3.1 General Objective

This study aims to prepare nano-HAp from ostrich bone, conduct acute toxicity test of the prepared nano-HAp and fabricate its polymer composite scaffolds using the electrospinning method and hence carry out *in vitro* biomedical test using the scaffolds.

1.3.2 Specific Objectives

The specific objectives of the project are:

- To extract nano-HAp from ostrich bone and characterize it using various spectroscopic, microscopic, optical and thermal techniques;

- To test the acute toxicity of the nano-HAp in Albino Wistar rats following the OECD-420 guideline;
- To prepare polymer nanocomposites scaffolds using the nano-HAp as filler and hence study their morphological, micromechanical, wettability properties; and
- To carry out study the *in vitro* biomedical test of the scaffolds in PBS solution.

1.4 Scope and Organization of Thesis

This study targets the conversion of ostrich bone waste to nano-HAp, which is a highly demanded calcium phosphate-related bioceramic. This ceramic has a highly osteoconductive and bioactive nature compared to chemically synthesized ones and can be used in various orthopaedic applications. For this, the research work first targets to check acute toxicity in Albino Wister rates and then used as a filler to prepare polymer composite scaffolds by using electrospinning techniques.

The thesis is organized as follows: A brief introduction of the basic viewpoint of the proposed work, including the objectives, hypotheses and limitations of the study, will be the content of **Chapter 1**. A detailed review of the preparation methodologies of HAp using animal-based biowaste and their biomedical applications will be illustrated in **Chapter 2**. The explanation of how the HAp is extracted from ostrich bone will be presented in **Chapter 3**. It also describes how the nano-HAp is segregated from the bulk of the particles using W/O microemulsion techniques, how nano-HAp is tested for acute toxicity in Albino Wister rats and how nano-HAp and VD3-incorporated polymer composite scaffolds are prepared by electrospinning. **Chapter 4** presents and discusses the results of experimental work. First, it gives insights into the extraction and segregation of nano-HAp from ostrich bone. Different properties of HAp will be studied using various characterization tools and techniques, including spectroscopy, electron microscopy, thermal and electrical. The acute toxicity test will be discussed on the basis of OECD Guidelines-420. The fabrication, characterization and *in vitro* degradation of scaffolds will be discussed thoroughly. Finally, **Chapters 5 and 6** present the conclusion and summary of the work, respectively.

1.5 Limitations and Delimitations

1.5.1 Limitations

1. In the past, various CP-based biomaterials have been used for quick healing of the fractured bones. However, the bioactive and bioresorbable phases of nano-HAp are the materials of choice because of their similarity to the mineral composition of human bone. Various methods have been used for the synthesis of HAp. Nevertheless, this study is limited to the synthesis of HAp from ostrich bone, an unexplored biosource.
2. The acute toxicity test of nano-HAp in Albino Wistar rats focuses only on physical observation, body weight loss, comparative studies of the toxic effect on internal organs of the test and the vehicle groups.
3. Different methods have been used for the fabrication of nano-HAp incorporated polymer composite scaffolds for biomedical applications. This study focuses only on the electrospinning (ES) method due to its simplicity, cost-effectiveness and ease of handling.
4. Although the fabricated scaffolds may be applicable for various *in vitro* and *in vivo* biomedical fields, this study is limited to the *in vitro* degradation test of scaffolds in PBS solution.

1.5.2 Delimitations

The general delimitations of this study are as follows.

1. Owing to the probability of dehydroxylation of HAp, the bone powder cannot be heated above 950 °C for 6 h during extraction according to the procedure followed in this study.
2. The abundance of trace amounts of calcium phosphates and related compounds beyond HAp cannot be ignore in the bone powder.
3. For the segregation of nano-HAp from the bulk of the particles, the W/O microemulsion technique is only suitable, so other types of emulsion-based segregation methods are beyond the scope of this study.
4. The exact status of the cytotoxic effect of nano-HAp in the internal organs of rats through histopathological investigation cannot be defined.

5. The probability of microscale to nanoscale diameter in nonwoven scaffold fibers under fixed processing parameter of electrospinning cannot be controlled.

CHAPTER 2

2. LITERATURE REVIEW

2.1 Human Bone

The bone tissue is organized hierarchically, which adds to its mechanical role in body support and mobility, as well as in other functions. To make a scaffold for treating bone injuries, fractures and many more bone tissue engineering (BTR) it is essential to understand detailed information about the physical, chemical and mechanical properties of bone is necessary to understand (Kareem, 2018). For this reason, it is important to study the structural, chemical composition and mechanical properties of bone minerals.

2.1.1 Hierarchical Organization of the Bone

According to Rho *et al.* (1998) before fabricating the polymer and bioactive composite scaffold, it is important to understand how the different levels of hierarchical structural organization of bone relate to each other. The hierarchical organization of bone from a macrostructural to a sub-nanostructure level is presented in **Figure 3**.

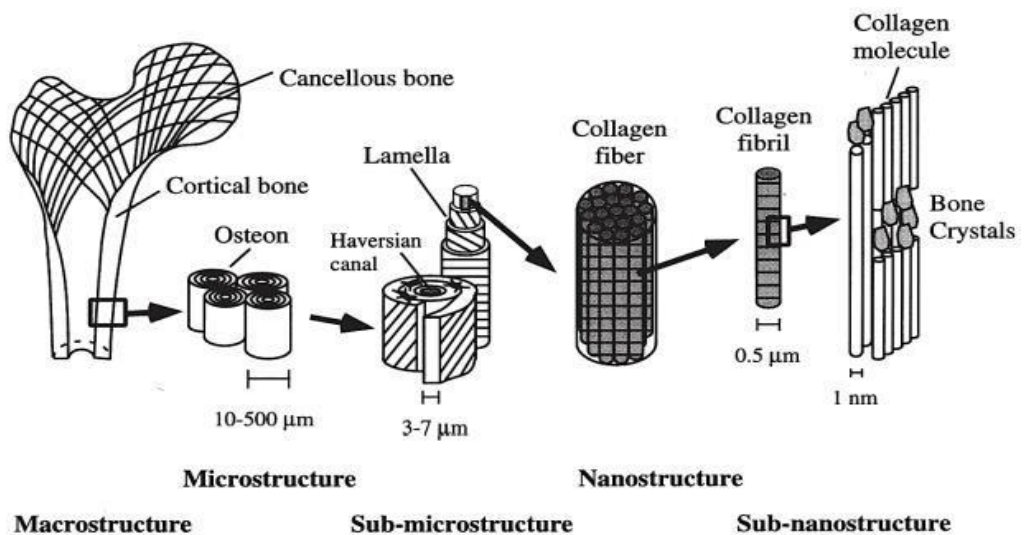


Figure 3: The hierarchical organization of bone from a macrostructural to sub-nano structural level (Source: Rho *et al.*, 1998)

On the base of the scale (**Table 1**), the structural organization of bone can be classified into five tiers.

Table 1: Hierarchical level of bone and their scales (**Source:** Kareem, 2018)

Hierarchical level	Parts of bone	Scales
Macroscopic	Cancellous and cortical	> 0.5 mm
Microscopic	Osteons or Haversian systems and trabeculae	10-500 μm
Submicroscopic	lamellae and mineralized collagen fibers	1-10 μm
Nanostructure	mineralized collagen fibrils	100 nm -1 μm
Sub nanostructure	molecular and atomic structure of major components	< 100 nm

2.1.2 Chemical Composition

Malla *et al.* (2020) reported that at the material level, animal bone is a complex composite matrix composed of 25% total organic materials, 65% total inorganic materials and 10% absorbed water components on a wet weight basis. The composition of animal bone is presented in **Figure 4**. The mineral-component of bone is primarily composed of submicroscopic crystals of HAp which are used for various metabolic activities, whereas the organic component is responsible for the flexibility of bone due to the presence of collagen matrix (95%) and proteins (Dorozhkin, 2010; Sagadevan & Dakshnamoorthy, 2013). Besides these, there are other organic substances existing in small amounts, such as chondroitin sulphate and keratin sulphate, along with different lipids such as phospholipids, cholesterol, fatty acids and triglycerides (Bano *et al.*, 2019).

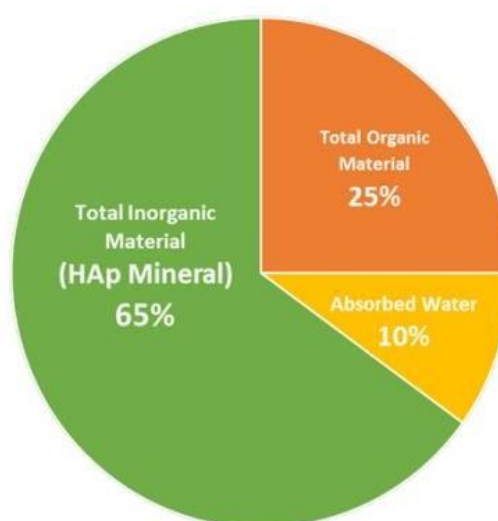


Figure 4: Chemical composition of human bone (**Source:** Malla *et al.*, 2020)

2.1.3 Type of Bone

In the human bone, the adult skeleton has basically two unique types of bone: cortical bone and cancellous bone. Cortical bone is a compact, low-porosity tissue that predominately exists in the shafts of long bones and is responsible for the mechanical qualities of bone (Buckwalter *et al.*, 1996) whereas cancellous bone is a spongy type of bone which is associated to various soft tissues. A typical cortical bone consists of 25% organic phase (i.e., bone matrix), 65% mineral phase (i.e., carbonated HAp) and 10% water (**Figure 4**). About 99% of the total body calcium which is the highest mineral contained in human bone is stored in cortical and cancellous bones while the remaining 1% only circulates in the body fluid (Kareem, 2018).

2.1.4 Composition of Bone

Calcium and phosphorus are the major mineral constituents of animal bone. It typically contains 36.7 wt.% calcium, 16.0 wt.% phosphorous and a trace amount of other minerals (Kehoe, 2008), but it also contains a significant amount of carbonate (7.4 wt.%). The presence of carbonate in the biological apatite is of vital importance because it is the main source of lattice distortion of HAp, which creates micro-stresses and crystalline defects in its surrounding area of the crystal lattice, which, in turn, plays an important role in its solubility (Zhou *et al.*, 2007). For this reason, the HAp is better than the chemically synthesized one for biomedical applications. The elements and their wt.% found in bone minerals are presented in **Table 2**.

Table 2: The elements and their wt.-% found in bone minerals (**Source:** Kehoe, 2008)

Mineral constituents	Symbols	Wt.%
Calcium	Ca	24.50
Phosphorous	P	11.50
Carbonate	CO ₃ ²⁻	7.40
Sodium	Na	0.70
Magnesium	Mg	0.55
Potassium	K	0.03
Chloride	Cl ⁻	0.01
Fluoride	F ⁻	0.02
Water absorbed	H ₂ O	25.00
Trace elements	Sr ²⁺ , Pb ²⁺ , Zn ²⁺ , Cu ²⁺ , Fe ²⁺	9.70

2.1.5 Mechanical Properties

The fracture-resistance of bone is influenced by a number of factors, including bone quantity (i.e., mass), bone location, the spatial distribution of the bone mass (i.e., shape, a ratio of cortical to cancellous bone and micro architecture) and the material properties of the bone matrix (i.e., mineral/collagen ratio, collagen fiber orientation and water content). In spite of this, the mechanical property of bone also depends on test conditions such as the kind of load (compressive or tensile), rate of loading and the direction of the applied stress relative to the orientation of bone microstructure.

These properties of bone serve as the fundamental factors to design scaffolds with the necessary material qualities and adequate mechanical strength to withstand the various loads acting on the bone. From a mechanical standpoint, human bone is mineralized collagen and HAp composite. Collagen imparts elasticity and resilience to the bone, whereas HAp imparts rigidity and tenacity (Wang & Gupta, 2011; Weiner & Wagner, 1998). It has a mechanically high loading and bending capacity and its excellent fracture and wear resistance allows it to withstand excessive stresses. Bone substitutes that are mechanically, chemically and physically compatible with bone would be the best option for developing composites that resemble natural bone. The representative mechanical property of human bone is listed in **Table 3**.

Table 3: Mechanical properties of human cortical bone (**Source:** Orlovskii *et al.*, 2002)

Mechanical properties	Test direction applied to a bone axis (Parallel)	Test direction applied to a bone axis (Normal)
Mechanical properties (MPa)	124-174	49
Compressive strength (MPa)	170-193	133
Young's modulus (GPa)	17-18.9	11.5
Microhardness (VPN)	30-60	-
Fracture toughness (MPa/m ^{1/2})	2-12	8
Bending strength (MPa)	160	-
Ultimate tensile strength (UTS)	0.014-0.031	0.007
Ultimate compressive strength	0.0185-0.026	0.028
Yield tensile strength	0.007	0.004
Yield compressive strength	0.010	0.011
Shear strength (MPa)	54	-

2.1.6 Structural Properties of Bone Cells

The bone is a living tissue that maintains its balance and strength through frequent production and resorption (Nakamura, 2007). The osteocytes (>90%), osteoclasts (<10%) and osteoblasts (<10%) are the three main types of bone cells responsible for bone homeostasis. These bone cells originate from two stem cell lineages one is from mesenchymal stem cells (MCSs) and another hematopoietic stem cells (HPSs) (Fazzalari, 2011). The composition of bone tissue is shown in **Figure 5**.

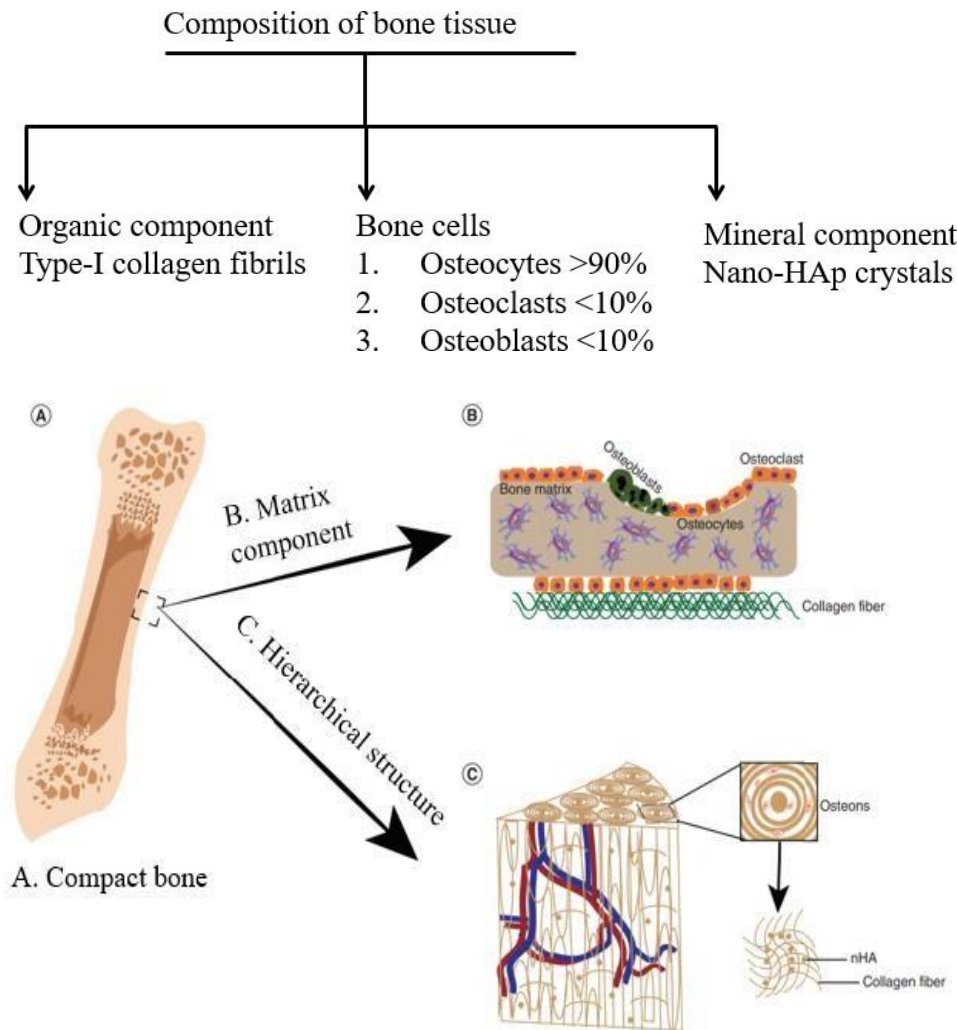


Figure 5: Composition of bone tissue (Source: Zhang *et al.*, 2020)

Zhang *et al.*, (2020) reported that osteocytes make up more than 90% of mature bone cells which are the most abundant cells in bone tissue. This tissue is distinguished by a cytoplasmic process that connects them to the processes of neighboring osteocytes. Furthermore, osteocytes are former mature osteoblasts that become encased in a calcified chamber of the bone matrix during bone development (lacuna). In comparison to osteoblasts and osteoclasts, osteocytes have a lifespan of roughly 25

years. It plays an important role in the bone remodeling process by guiding osteoclasts to the area that requires remodeling and managing the mineralization of the bone matrix produced by osteoblasts. In instances where more calcium is required, such as lactation, osteocytes also maintain mineral haemostasis. The studies of Mellon and Tanner (Mellon & Tanner, 2012) have shown that osteocytes can influence osteoclast production by producing cytokines like RANKL, which cause to form Osteoclasts. Finally, osteoclasts are massive, multinucleated cells located in contact with a calcified bone surface and within pits known as Howship's lacunae, which arise because of their own resorptive activity. They belong to the hematopoietic cell lineage and are derived from mononuclear-macrophage cells. Unlike osteocytes, osteoclasts have a relatively short lifespan of roughly two weeks. They play an important role in bone modeling throughout growth and bone remodeling, which helps to maintain the mature skeleton's integrity (Albanese & Faletti, 2016; Oranger *et al.*, 2014).

On the other hand, osteoblast cells are responsible for the creation of the protein matrix in bone, which contains mainly type I collagen and type V collagen as well as non-collagenous proteins. Type-I collagen makes up 90-95% of the organic matter so it is the most vital part of the protein. They also contribute to bone resorption by secreting factors that recruit and promote the differentiation of monocyte/macrophage lineage cells into mature osteoclasts, as well as produce proteases that degrade the osteoid and prepare the bone surface for osteoclast-mediated remodeling (Kular *et al.*, 2012). Osteoblasts are formed from mesenchymal stem cells (MCSs) and are distinguished by their position on the bone surface as well as physical characteristics such as round forms and single big nuclei near to the cell membrane with enlarged Golgi apparatus on their apical surfaces (Burr & Allen, 2019). Following bone production, osteoblasts can undergo apoptosis (i.e., programmed cell death) and become flattened dormant cells that cover the bone surface (bone lining cells), or become incorporated in the bone matrix as osteocytes.

2.1.7 Healing Mechanism of Fracture Bone

Generally, the loss of continuity and mechanical stability of a bone is called a bone fracture (Kareem, 2018). It can be caused by trauma like sports injuries, falls and road accidents, or by medical conditions like osteoporosis and bone cancer (Burr & Allen, 2019). There are two types of fractures found in road accidents: open and closed.

Open fractures cause skin wounds and damage to soft tissue, which makes them more likely to get infected. Closed fractures, on the other hand, leave the skin intact and have a lower risk of infection (Iyer, 2019). Most fractures heal in about 6–8 weeks when the broken bone's function and structure are fully restored. There are two ways to fix a broken bone: directly or naturally and two kinds of healing mechanisms primary and secondary.

Primary healing necessitates the suppression of callus growth as well as the stiff stability of the broken bone. As the conventional treatment options, such as cast immobilization or external fixation, usually include some degree of movement. This type of healing is less common than secondary healing. Gap and touch healing are examples of primary healing. The first phase of gap healing includes gap filling by woven bone layer creation, followed by supporting lamellar bone formation in a transverse orientation to the original bone.

Nevertheless, in the secondary healing also known as the remodeling phase of healing, osteons are created parallel to the original orientation of the bone and fracture ends are rebuilt. Osteons grow in the same original bone orientation at the fracture site during contact healing, which occurs when the fractured ends are in direct touch. After the capillaries have broken through the fracture line, the osteoclasts produce cutting cones around the fracture line, resulting in the creation of new Haversian networks across the fracture site (Lieberman & Friedlaender, 2005). Basically, it occurs in three overlapping stages (**Figure 6**).

a) Inflammation stage: This is the first stage of healing and remains around 7 days and is caused by bone matrix, soft tissue and vascular damage, which results in hematomas formation. This reaction immobilizes fracture motion through swelling of the injury site (Sfeir *et al.*, 2005). The inflammatory cells then recruit cells to start bone repairing through cytokines released such as: transforming growth factor-beta (TGF- β), platelet-derived growth factor, fibroblast growth factor (PDGF) and interleukin-1 and-6 (IL-1 and IL-6), which cause local mesenchymal cells to differentiate into osteoblasts (McKinley, 2003).

b) Reparative stage: This stage can be divided into two parts;

- i. soft callus/cartilage formation stage: In this stage, the stimulated cells produce vascularized reparative callus to improve the stability of bone ends. The peak of this phase occurs 7-10 days after fracture and
- ii. hard callus formation stage: This stage involves the calcification of the soft callus tissue into the woven bone by endochondral ossification and vessel invasion. This is usually accompanied by intramembranous ossification in the periphery of the fracture site (Burr & Allen, 2019).

c) Remodeling stage: This is the final stage of secondary healing. At this stage, the callus begins to mature and remodel itself. Both osteoblast cells, which build bone and osteoclast cells, which break down bone, work together to turn woven bone into stronger lamellar bone (Dimitriou *et al.*, 2011; Lieberman & Friedlaender, 2005). It begins 3-4 weeks after injury and may take years to restore the original bone shape (Doostmohammadi *et al.*, 2012; Wraighte & Scammell, 2006).

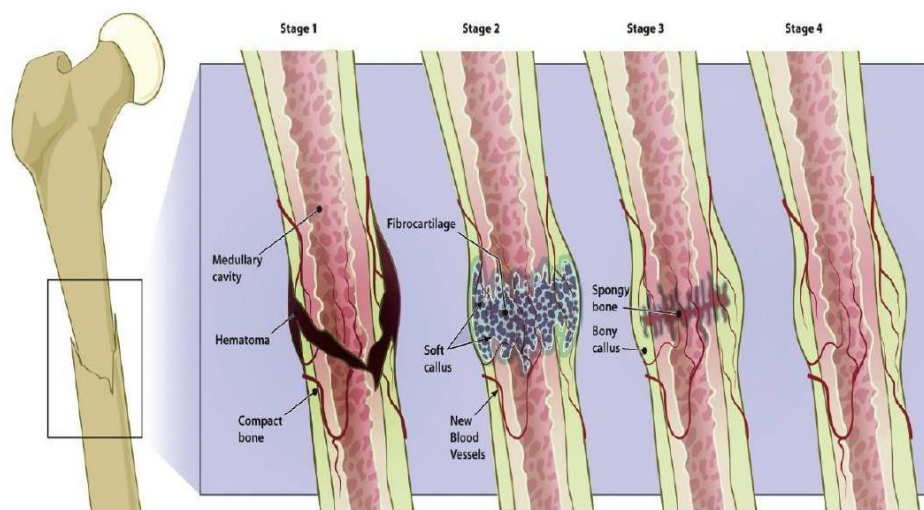


Figure 6: Different stages of secondary fracture healing (Source: Burr & Allen, 2019)

2.2 Hydroxyapatite (HAp) and its Source

The molecular formula of HAp is represented by $\text{Ca}_{10}(\text{PO}_4)_6(\text{OH})_2$ instead of $\text{Ca}_5(\text{PO}_4)_3(\text{OH})$. It is because the crystal structure is made up of two units. However, the HAp of the complex apatite group can have its OH group undergone replaced with carbonate, chloride, or fluoride to make the corresponding carbonated or chlorapatite or fluorapatite based on which ions are being used (Agbeboh *et al.*, 2020). Various methods for the synthesis have been documented during the last

couple of decades. The complexity of producing the desired characteristics in HAp, such as phase purity, crystallinity, stoichiometry, size and morphology, motivates further research to improve the synthesis method. The synthesis of HAp with its various sizes, morphologies and textures, can be achieved by means of different methods using chemical precursors as well as biogenic sources. Some calcium and phosphorous precursors used for synthesis are not eco-friendly and might be toxic for biomedical applications (Bahrololoom *et al.*, 2009). However, some of the commonly applied chemical methods used for the synthesis are sol-gel (Sari *et al.*, 2014), precipitation (Gergely *et al.*, 2010), co-precipitation (Arsad *et al.*, 2011b), sonochemical (Yorug & Ipek, 2012), hydrothermal (Neira *et al.*, 2009), mechanochemical (Dinda *et al.*, 2020) and microemulsion (Hossain *et al.*, 2012). Nevertheless, excessive time for preparation and requirement of highly pure grade calcium and phosphorus precursors as starting materials are some drawbacks of these methods (Akram *et al.*, 2014).

On the other hand, biogenic sources are economical and safer sources in comparison to chemical sources for synthesis (Barakat *et al.*, 2009; Rana *et al.*, 2017). Studies show that the animal wastes such as the bones, exoskeletons, shells and scales of vertebrates and fishes are alternative economic and eco-friendly sources for synthesis of HAp. In addition, the HAp synthesized from these sources are safer to use for *in vivo* applications because no foreign chemicals are utilized during its synthesis (Panda *et al.*, 2014). Studies show that HAp extracted from biogenic sources exhibits better biological activity in comparison to chemically synthesized once due to the presence of naturally doped cations (e.g., Na⁺, K⁺, Mg⁺², Sr⁺², Zn⁺², etc.) and/or anions (e.g., F⁻, Cl⁻, SO₄⁻², CO₃⁻², etc.) (O'Hare *et al.*, 2010; Palmer *et al.*, 2008; Paz *et al.*, 2012; Raucci *et al.*, 2012). For sustainable development, biogenic resources should be recycled, reused and channelled toward the production of value-added products. (Oduote *et al.*, 2019). Different researchers have used these sources for synthesis. Barakat *et al.* (2009) and Sofronia *et al.* (2014) used bovine bones, Lu, Fan *et al.* (2007) used pig bone and teeth; Abdulrahman *et al.* (2014), Wu *et al.* (2016) and Agbebiaka *et al.* (2020) used eggshell waste. Similarly, Ferreira *et al.* (2014) used ostrich eggshells, Kongsri *et al.* (2013), Panda *et al.* (2014) used fish scales, Venkatesan and Kim (2010) used fish bones for the synthesis. Similarly, Zainon *et al.* (2012) and Kim *et al.* (2014) used cuttlefish bones. Chattanathan *et al.* (2013) used

catfish bone and Piccirillo *et al.* (2013) and Wan *et al.* (2006) used plant sources for the synthesis of HAp. Despite the above biogenic sources, there are still numerous unexplored sources for synthesis; ostrich bone is one of them. Therefore, in this study, this source was used for the synthesis because, based on the review of biogenic sources of synthesis, no literature was available to synthesize HAp from this source.

2.2.1 Synthesis of HAp from Biowastes

Numerous studies show that most of the members of the CaP family consist of three vital elements namely calcium, oxygen and phosphorus in their molecular structure. Some of the common members of CaP family, including HAp, with their molecular formula and important properties, are presented in **Table 4**.

Table 4: List of common members of CP family, with their names, abbreviations, formula, Ca/P molar ratio, crystal structure and solubility (**Source:** Akram *et al.*, 2014)

Names of CPs	Abbreviation	Formula	Ca/P molar ratio	Crystal structure	Solubility at 37 °C (-log K _{sp})
Amorphous calcium phosphate	ACP	Ca _x H _y (PO ₄) ₂ . nH ₂ O	1.20 -2.20		--
α-Tricalcium phosphate	α-TCP	α-Ca ₃ (PO ₄) ₂	1.50	Monoclinic	28.5
β-Tricalcium phosphate	β-TCP	β-Ca ₃ (PO ₄) ₂	1.50	Rhombo-Hedral	29.6
Dicalcium phosphate dihydrate (Brushite)	DCPD	CaHPO ₄ . 2H ₂ O	1.00	Monoclinic	6.73
Dicalcium phosphate anhydrous (Monetite)	DCPA	CaHPO ₄	1.00	Ortho-Rhombic	6.04
Monocalcium phosphate monohydrate	MCPM	Ca(H ₂ PO ₄) ₂ . H ₂ O	0.50	Triclinic	1.14
Monocalcium phosphate anhydrous	MCPA	Ca(H ₂ PO ₄) ₂	0.50	Triclinic	1.14
Tetracalcium phosphate	TCP	Ca ₄ (PO ₄) ₂ O	2.00	Monoclinic	--
Octa calcium phosphate	OCP	Ca ₈ H ₂ (PO ₄) ₆ .5H ₂ O	1.33		6.04
Calcium-deficient hydroxyapatite	CHAp	Ca _{10-x} (HPO ₄) _x (PO ₄) _{6-x} (OH) _{2-x}	1.50 -1.60	Hexagonal	--

Names of CPs	Abbreviation	Formula	Ca/P molar ratio	Crystal structure	Solubility at 37 °C (-log K _{sp})
Fluorapatite	Fap	Ca ₁₀ (PO ₄) ₆ F ₂	1.67	Hexagonal	--

The nonstoichiometric hydroxyapatite is one of the most widely studied bioceramics whose properties are similar to the bone minerals present in the vertebrate bone. As mentioned earlier in section 2.1.2, the bones contain 65% nano HAp in addition to 10% water and 25% organic materials in a wet weight basis (Ghiasi *et al.*, 2019). Studies show that living organisms can crystallize and deposit a wide variety of CPs based mineral compounds during biomineralization processes in the body (Dorozhkin, 2010; Nudelman & Sommerdijk, 2012; Szcześ *et al.*, 2017). Among the various CaP-based biominerals, HAp is found in pathological calcifications of tissues such as urinary calculus, stones and atherosclerotic lesions despite bones and teeth (Dorozhkin, 2016; Szcześ *et al.*, 2017). Among the listed calcium phosphates, HAp is the most intensely studied one, which has a calcium to phosphorus (Ca/P) ratio 10:6 commonly expressed as 1.67, while that of nonstoichiometric hydroxyapatite ranges within 1.5 to 1.9 (Singh *et al.*, 2018). In addition, HAp has a specific orientation of Ca²⁺ and PO₄³⁻ ions in two binding sites: the "C" site (Ca²⁺) and the "P" site (PO₄³⁻) in their molecular structure. Generally, the "C" sites are organised in a rectangular configuration within a crystal lattice, whereas the "P" sites are positioned in a hexagonal arrangement (**Figure 7**) with a P63/m space group in the c-axis faces (Haider *et al.*, 2017). This structure has a cell dimension a = b = 9.42Å and c = 6.88Å, where this space group has a six-fold symmetry axis and a three-fold helix structure. This crystal structure appears as 400Å long and 150Å wide in bone and 400Å wide and 1000Å long in dental enamel (Elliott *et al.*, 2002).

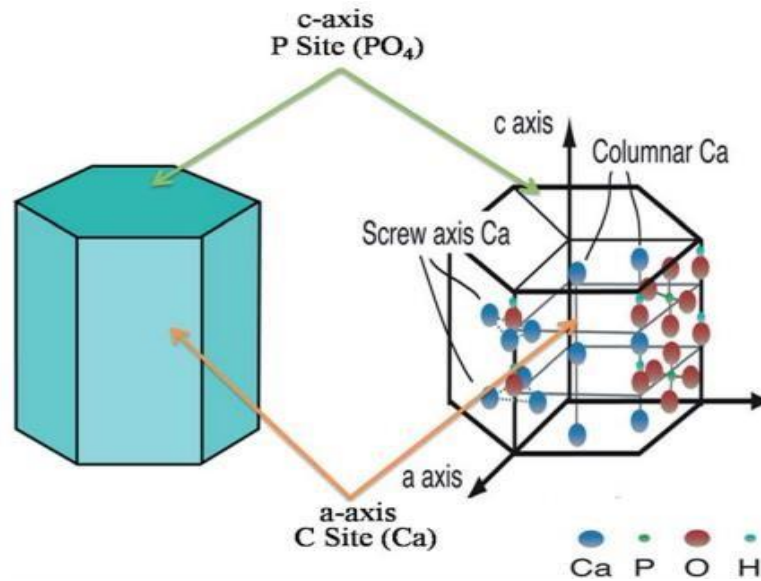


Figure 7: Schematic drawing showing the crystalline texture of the HAp in its hexagonal lattice framework, showing the "C" and "P" sites (Source: Haider *et al.*, 2017)

However, the biosource-based HAp has been found to have either a deficiency or excess of Ca^{2+} , OH^- or PO_4^{3-} ions in its crystal lattice. In such HAp, cations like Na^+ , Mg^{2+} and Zn^{2+} replace the Ca^{2+} ion position in the crystal lattice, whereas carbonate (CO_3^{2-}) ions may replace either PO_4^{3-} ions (commonly called "A-type substitution") or OH^- ions (commonly called "B-type substitution"), while F^- ions also substitute for OH^- ions in some cases (called "B-type substitution") (Bano *et al.*, 2019). However, the appearance of foreign elements other than calcium, phosphorous and oxygen mimics it in the biosource-based HAp and carbonate ion is very common in biosource-based HAp (Kulanthaivel *et al.*, 2015).

Over the decades, numerous methods have been used to synthesize HAp from chemicals precursors and using natural resources (Akhavan, 2012; Sadat-Shojai *et al.*, 2013). Nevertheless, the rigorous review of Sadat-Shojai *et al.* reported the primary 3 groups and 12 subgroups for the synthesis of HAp as presented in **Table 5**.

Table 5: List of the method used for the synthesis of HAp (**Source:** Sadat-Shojai *et al.*, 2013)

S. No.	Methods used	Sub-methods used
1.	Dry method	I. Solid state II. Mechanochemical
2.	Wet method	I. Chemical precipitation II. Hydrolysis III. Sol-gel IV. Hydrothermal V. Emulsion VI. Sonochemical
3.	High temperature method	I. Combustion II. Pyrolysis III. Synthesis from biogenic source combination procedures

In the dry method, high-energy milling of calcium and phosphate precursors were carried out and the formation of HAp would occur within 2-8 h. The particle size depends on the milling type, time and rotational speed of the mill, as well as on the calcination temperature. According to Ruksudjarit *et al.* (2008) the contamination from milling and the long thermal treatment are the prominent weaknesses of this method. However, for bulk production, these methods are generally used due to their simplicity in controlling the steps of preparation and processing conditions for the final products. This method has been found to produce HAp with Ca/P ratio close to that of stoichiometric HAp and for better crystallinity. Dinda *et al.* (2020) used $\text{Ca}(\text{H}_2\text{PO}_4)_2\text{H}_2\text{O}$, monocalcium phosphate, as well as oxide and hydroxides of calcium, $\text{Ca}(\text{OH})_2$ and phosphorous pentoxide (P_2O_5) for synthesis.

The results show that with increasing the milling time, the particle size also increased from $17.3\pm 6.2\text{nm}$ to $22.3\pm 6.8\text{nm}$ at 30 min to 2 h milling time. **Figure 8** depicts TEM micrographs of HAp prepared by ball-milling of $\text{Ca}(\text{H}_2\text{PO}_4)_2\text{H}_2\text{O}$ and $\text{Ca}(\text{OH})_2$ after 15 min, 30 min, 1 h and 2 h respectively. The average particle size observed at different stages of milling was found to be 17.3 ± 6.2 for 30 min, 19.4 ± 6.5 and 22.3 ± 6.8 for 1 h and 2 h respectively. It has been found that as the milling time goes on, HAp crystal gets rougher and the lattice strain goes down. The gradual increase in crystallite size and decrease in lattice strain are caused by dynamic recovery and recrystallization. This happens because the powder particles stuck between the balls and the reactor wall get hotter as the balls hit each other with a lot of energy.

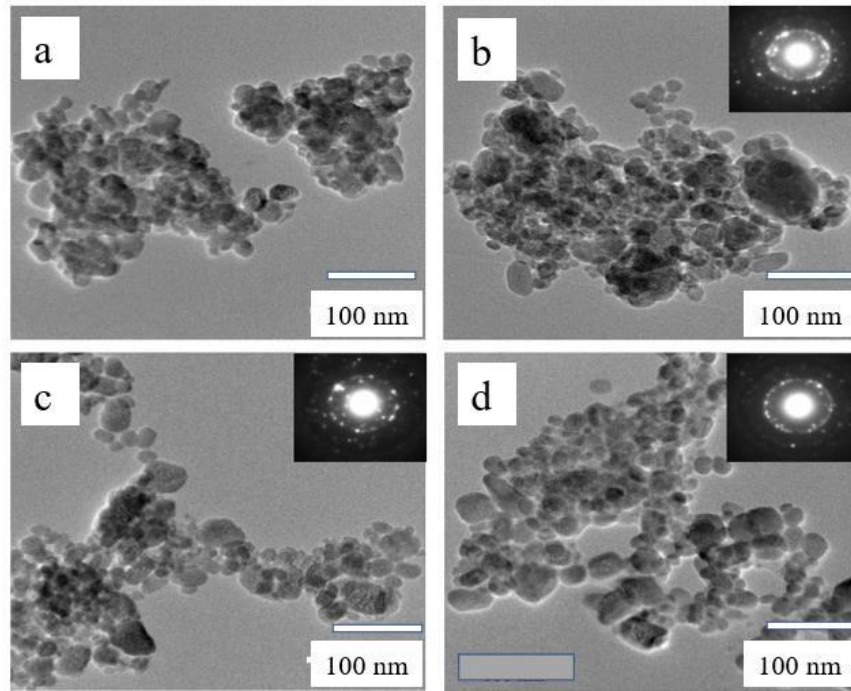


Figure 8: TEM micrographs of the HAp prepared from $\text{Ca}(\text{H}_2\text{PO}_4)_2$, H_2O and $\text{Ca}(\text{OH})_2$ showing the effect of time of milling with P_2O_5 (Source: Dinda *et al.* 2020)

Yeong *et al.* (2001) used, in similar manner, calcium oxide and hydrogen phosphate as starting materials for the preparation of HAp via a high-energy mechanical activation method. Using this approach, a highly crystalline phase of HAp (having the particles diameter in the range of 25 nm) was obtained after 20 h of mechanical activation.

In contrast to dry methods, various calcium and phosphorous precursors, acids, alkalis, polar and non-polar solvents are used in wet chemical methods. Several attempts have been made to prepare HAp using these methods. Therefore, this method might be a superior one compared to the dry method (Ghiasi *et al.*, 2019). Several wet methods have been proposed by various researchers, including sol-gel precipitation (Guo *et al.*, 2020), layer hydrolysis of calcium phosphate, microemulsion (Irfan *et al.*, 2020; Ma *et al.*, 2016), microwave-assisted irradiation (Irfan *et al.*, 2021; G. S. Kumar *et al.*, 2018; Mubarak Ali, 2019; Sözügeçer & Bayramgil, 2021), ultrasonic-assisted irradiation (Gopi *et al.*, 2012; Indira & Malathi, 2021; Klinkaewnarong & Utara, 2018; Wan *et al.*, 2006) and chemical precipitation (Bang *et al.*, 2015; Ganachari *et al.*, 2016; Yuan *et al.*, 2013). The degree of crystallinity and phases depend on the solvent and purity of the precursors used. However, precipitation is still the most commonly studied method for synthesis

among all wet chemical methods. And, according to Paz *et al.* (2012) and Yelten-Yilmaz (2018) the quality of HAp obtained by this method is more or less equivalent to that obtained through the biomineralization pathway.

Hydrothermal is another common method of HAp synthesis, in which, the reaction mixtures are placed inside an autoclave that provides a suitable environment of elevated temperature and pressure for the ageing of the HAp. Such a method was used by Neira *et al.* (2009) to synthesize highly crystalline HAp with diverse morphologies using hydrated calcium nitrate and diammonium hydrogen phosphate as calcium and phosphorous precursors assisted by urea. Over the past few decades, the researchers have reviewed the various aspects and chemical methods of synthesis of the HAp for various application. For instance, various wet chemical methods of synthesis, processing as well as their influences on the crystalline texture were discussed by Orlovskii *et al.* (2002), Ben-Nissan & Pezzotti Ben-Nissan & Pezzotti (2004). Their studies basically concentrated on structural characterization and the physical properties of the HAp including the crystals nucleation and growth and dissolution of different stages of calcium phosphates and surface modification.

The studies of Oladele *et al.* (2018) have shown that bioresource-based HAp has a negative zeta-potential implying their better osteoconductive as well as osteoinductive properties compared to chemically synthesised analogue. So, biosource based HAp is highly advantageous for bone tissue regeneration studies due to the better proliferation and differentiation of the osteoblast cells in the scaffold surface. Moreover, owing to naturally doped ions such as Na^+ , Ba^{2+} , Sr^{2+} , Zn^{2+} , Fe^{2+} , Mg^{2+} , K^+ , Si^{2+} , F^- and CO_3^{2-} in the crystal lattice it shows better antimicrobial activities than chemically synthesised one (Akram *et al.*, 2014). Studies have shown that the release of Ca^{2+} ions (*in vivo*) from this HAp are closer to human bone HAp and slightly faster than the release of chemically synthesized crystalline HAp (Fathi *et al.*, 2008; Le Ray *et al.*, 2005).

2.2.2 Biogenic Sources of HAp

The prominent biogenic resources of HAp are the bones of various animals (e.g., bovine, buffalo, sheep, goat, pig, camel, horse, etc.), bones and scales of marine and freshwater animals, bird bones (e.g., chicken, turkey, duck, emu, ostrich, etc.) and shell sources (e.g., eggshell, seashell, mussel shell, cockleshell etc.). Besides these

both aquatic and freshwater plants might be minor alternative sources for synthesis however their detail studies are excluded in this study.

2.2.3 HAp form Animal and Bird Bones

According to Hart *et al.* (2022), with an increasing global population, the consumption of animal and bird meat has recently increased. This means a large amount of animal-related biowaste is produced annually. Among the various biogenic resources, animal bones are one of the most important biowastes that are commonly available in animal slaughterhouses, meat shops, meat processing factories, etc. A study shows that cortical bone is comparatively more suitable than trabecular bone for the extraction of HAp because this bone contains higher mineral (calcium and phosphorous) deposition than trabecular bone in the form of an insoluble salt (Obada *et al.*, 2022).

Ruksudjarit *et al.* (2008) jointly used calcination at 800 °C and a vibro-milling technique to extract HAp from bovine bone. They determined that ball milling and vibro-milling of bone powder is sufficient for the extraction of HAp. However, prolonged ball milling (> 8 h) damages the crystalline shape which is one of the prominent demerits of this method. Barakat *et al.* (2009) extracted HAp with calcium to phosphorous (Ca/P) ratio of 1.86 and 1.56 from the bovine cortical bone using a combination of alkaline hydrothermal hydrolysis and subcritical water process.

Londono-Restrepo *et al.* (2019) investigated the effect of crystal size change on the shape and width of X-ray diffraction patterns of HAp extracted from human, porcine and bovine bones by calcination method at 720 °C. The results of SEM images (**Figure 9**) show a crystalline, elongated morphologies. A group of crystals can be seen in porcine due to an agglomeration and combination of HAp (**Figure 9b**). However, in human bone HAp, there are irregular shapes, with some spherical crystals and hexagonal structures having well-defined faces. In addition, bovine and porcine bone HAp shows a highly spongy morphology in comparison to human bone HAp. Results show that the average particle dimension is $117\pm 19\text{ nm}\times 42\pm 9\text{ nm}$ for bovine bone HAp, $62\pm 9\text{ nm}\times 28\pm 4\text{ nm}$ for porcine bone HAp and $330\pm 60\text{ nm}\times 200\pm 40$ for human bone HAp respectively. **Figure 9(d)** depicts Sigma Aldrich HAp (reference sample) with a spherical, tightly agglomerated morphology and a particle size of 484 nm, indicating that bone source-derived HAp has larger particles than chemically synthesised one.

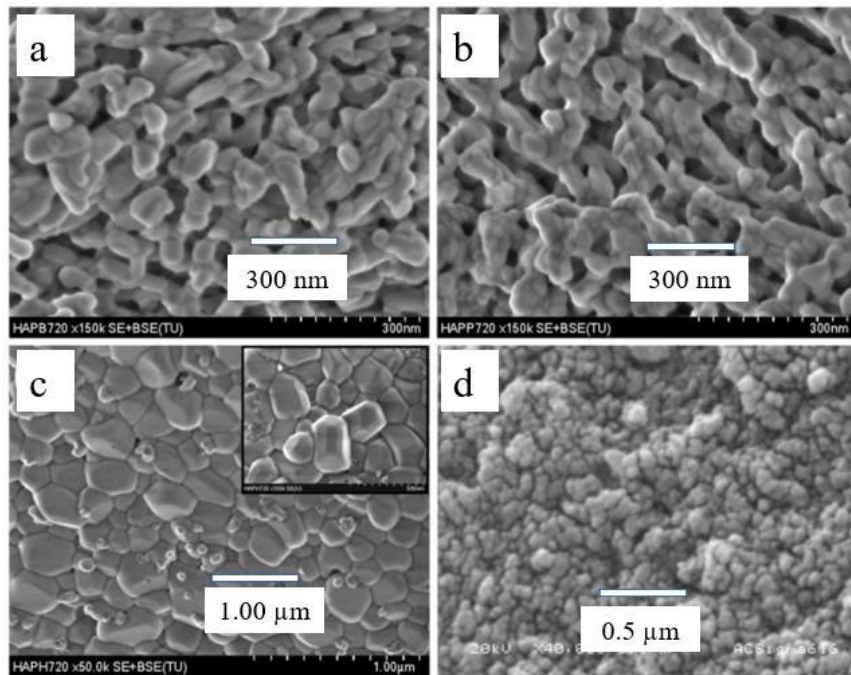


Figure 9: SEM images of calcinated samples of HAp: (a) Bovine, (b) Porcine, (c) Human and (d) Reference sample of HAp (Sigma-Aldrich). (Source: Londoño-Restrepo *et al.*, 2019)

Odusote *et al.* (2019) also used bovine bone for the extraction of HAp. For this, the defatted and clean bone powder was heated at 650 °C for 3 h and at 750 °C for another 6 h in an electric furnace. Results showed pure crystalline HAp with a rod-like morphology having a dimension of 250 nm × 150 nm. Likewise, Sun *et al.* (2017) used the calcination method for the extraction of HAp from same source by 2 h of heating at 750 °C. The results showed that irregular-shaped HAp with a particle size of 20-100 μm and calcium to phosphorous (Ca/P) molar ratio was found greater than 1.67. The reason for the higher value of Ca/P ratio might be due to the carbonate ion (CO_3^{2-}) substitution in place of phosphate ions (PO_4^{3-}) in the HAp crystal lattice. However, the results of the XRD pattern showed the existence of β -TCP together with HAp. But the study by Zainon *et al.* (2012) reported that HAp decomposes to β -TCP at a temperature greater than 1000 °C. The findings of Hassan *et al.* (2015) and Sun *et al.* (2017) revealed that this process might be started at 850 °C (Hassan *et al.*) and 750 °C (Sun *et al.*) during calcination process.

Nirmala *et al.* (2011) used the calcination method to extract HAp from cow bone. Before calcination, the bones were washed and dried at 160 °C for 48 h and then subjected to grinding to a particle size of less than 500 μm. After that, it was calcined at 850 °C for 1 h and reground to reduce the particle size to less than 450 μm. The results showed that crystalline HAp was produced with spherical morphology and a

Ca/P molar ratio equivalent to 1.61 which is nearly equivalent to stoichiometric value (1.67) of chemically synthesized HAp. Bano *et al.* (2019) extracted carbonated hydroxyapatite (CHAp) from the same cow bones. For this, the bones were cleaned, dried, autoclaved and ground to a particle size of less than 500 μm and then calcined at 600 $^{\circ}\text{C}$ to 1000 $^{\circ}\text{C}$ for 3 h. The XRD results revealed that all main peaks of HAp belong to crystalline regions. The crystallite size of the particles ranges from 3.9 nm to 83.12 nm (raw HAp and HAp1000) as shown in the **Figure 10**.

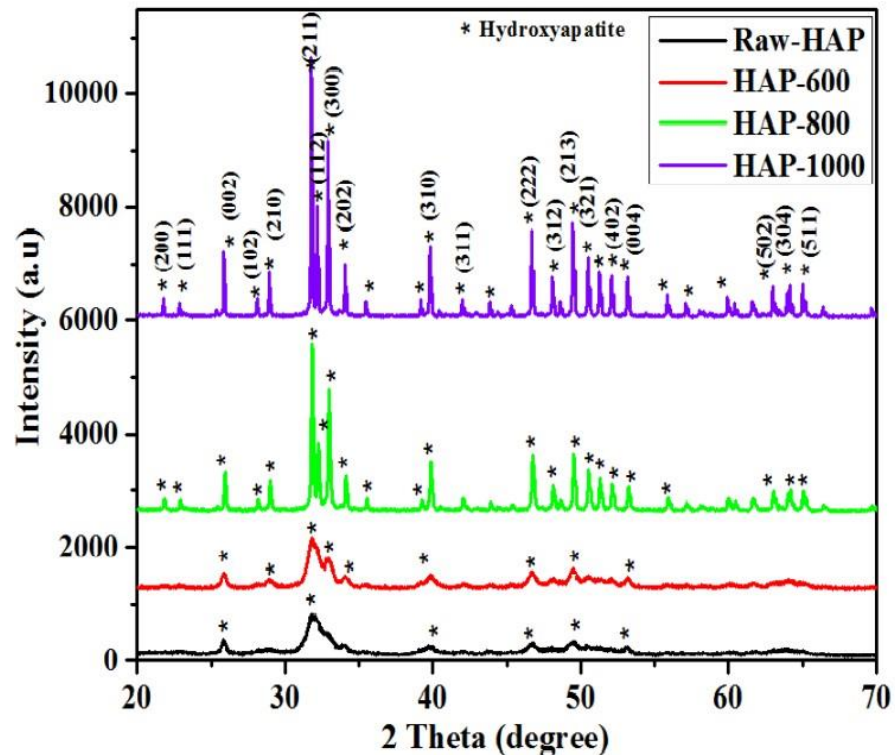


Figure 10: XRD patterns of A-type and B-type substituted HAp before and after calcination at 600 $^{\circ}\text{C}$, 800 $^{\circ}\text{C}$ and 1000 $^{\circ}\text{C}$. (Source: Bano *et al.*, 2019)

Similarly, Pawarangan and Yusuf (2018) also extracted HAp from buffalo femur bone jointly by precipitation and sintering methods. For this, the clean bone powder was treated with strong alkali and then acetone for 24 h separately, followed by being sintered at 1000 $^{\circ}\text{C}$ for 4 h. The XRD and EDX results show a crystalline HAp with a Ca/P molar ratio equal to 1.67. In another study, Ismail & Abdullah (2020) used same method of extraction using goat bones and joints. The Ca/P molar ratio of the bone sample before calcination was found to be 1.75, while after calcination it changes to 1.83, 1.86 and 2.43 at temperatures of 900 $^{\circ}\text{C}$, 1000 $^{\circ}\text{C}$ and 1100 $^{\circ}\text{C}$, respectively. But, for common sample, the ratio is 1.48 before calcination and 3.97 at the calcination temperature of 900 $^{\circ}\text{C}$. Finding shows that in each case, the Ca/P molar

ratio increases as the calcination temperature increases. However, the higher Ca/P ratio indicates HAp has been changed to α -TCP, which has a Ca/P molar ratio (1.67) greater than stoichiometric HAp.

Similarly, Jaber *et al.* (2018) prepared an irregular-shaped HAp by calcination of camel bone at 1000 °C for 3 h of heating and 1 h of ball milling. The XRD results showed a crystalline HAp and the EDX results showed the existence of Mg and Na, in addition to Ca, P and O with Ca/P molar ratio equivalent to 1.66. Rahavi *et al.* (2017) extracted HAp separately by 2 h of calcination of camel and horse bone at 700 °C. The results showed that the irregular size of HAp ranged from 97 nm for camels and 28 nm for horse bone, respectively. The Ca/P molar ratios were found to be 2.04 for camel and 2.13 for horse bone. The EDX results showed that, in addition to calcium and phosphorus, traces of Na⁺, Mg²⁺, Sr²⁺, Fe²⁺, Al³⁺ and Zn²⁺ ions were found in both sources which make it non-stoichiometric HAp.

Using pig bone source, Ofudje *et al.* (2018) extracted bone-based HAp. For this, the clean and the dry bone sample is heated in an electric furnace at 600 °C, 800 °C and 1000 °C respectively. The results show that HAp has a rod-like morphology with a length of 38-52 nm and a width of 7-13 nm. The Ca/P molar ratio of this (calcined at 1000 °C) was found to be 1.88, which was slightly higher than the Ca/P ratio of HAp extracted from human bone. Esmaeilkhanian *et al.* (2019) extracted HAp from turkey bone waste by heating it at 850 °C and using a milling process. The SEM and EDX results showed that the average particle size of ball-milled HAp was found to be 85 nm with a Ca/P molar ratio of 1.63.

Janus *et al.* (2008) and Haberko *et al.* (2006) jointly used calcination in addition to alkaline heat treatment methods to extract HAp from pig bones. To remove the collagen and other fatty tissues, the clean bone sample was treated with concentrated NaOH (4M) solution at 100 °C for 24 h. After that, the pH was neutralized before calcination at 800 °C and 1200 °C, respectively. Results showed that a pure HAp phase was produced at 800 °C, whereas a mixture of HAp and calcium oxide (CaO) was found at 1200 °C. Furthermore, both researchers independently extracted various shapes of HAp from this source in a 70-80 nm range. In addition to the small amount of CaO, the Ca/P molar ratios in both works were found to be 1.70 and 1.72, respectively. The higher Ca/P ratios might be attributed to the presence of CaO. The

overall summary of the methods used for the extraction of HAp from different bones is listed in **Table 6**.

Table 6: An overall summary of methods of extraction, heating temperature, holding time and physicochemical properties of HAp extracted from various animal bones

Source	Extraction method	Heating temperature (°C) & holding time	State, particle shape & size	Ca/P molar ratios	Trace element	Reference
Bovine Bone	Calcination & Vibro-milling	800, 3h	Nano crystalline <100nm	1.66	-	Ruksudjarit <i>et al.</i> , 2008
Bovine bone	Thermal decomposition, subcritical water process & Alkaline hydrothermal process	750, 6h 275, 1h 250, 5h	300nm, nano rod Nano flakes -	1.65 1.56 1.86	- - -	Barakat <i>et al.</i> , 2009
Bovine, porcine & human bones	Calcinations	720	Crystalline, elongated, dimension 117±19 nm x42±9 nm (bovine) 62±9 nm x28±4 nm (porcine) 330±60 nm x200±40 nm (human)	-	-	Londoño-Restrepo <i>et al.</i> , 2019
Bovine bone	Calcinations	750, 2h -1000	Irregular at 750 °C 20 - 100 µm Semi spherical at 800 °C	>1.67	Na ⁺ , Mg ²⁺ , Sr ²⁺ , Ba ²⁺ , Zn ²⁺	Sun <i>et al.</i> , 2017
Cow bone	Calcination	850, 1h	Spherical < 450 µm	1.61	-	Zainon <i>et al.</i> , 2012
Cow	Autoclaved &	600 - 1000, 3h	Crystalline	-	-	M. N. Hassan

Source	Extraction method	Heating temperature (°C) & holding time	State, particle shape & size	Ca/P molar ratios	Trace element	Reference
bone	Calcination		hexagonal 3.9 - 83.12 nm Crystalline			<i>et al.</i> , 2015
Buffalo bone	Wet precipitation & sintering	650, 850 & 1050, 7h	Irregular crystalline	1.67 at 850°C	Na ⁺ , Mg ²⁺	Nirmala <i>et al.</i> , 2011
Goat/ Caprine bone & joint	Calcination	900–1000 & 1100, 7h	Crystalline irregular	1.73 at 900 °C 1.86 at 1000 °C & 2.43 at 1100 °C	Na ⁺ , Mg ²⁺	Ismail & Abdullah, 2020
Camel bone	Calcination & planetary ball milling	1000, 3h & 1 h ball milling	Crystalline, irregular 79-97 nm,	1.66	Na ⁺ , Mg ²⁺	Jaber <i>et al.</i> , 2018
Camel & horse bones	Calcination	700, 2h	Irregular 97nm (Camel) 28 nm (Horse)	2.04 Camel 2.13 Horse	Na ⁺ , Mg ²⁺ , Sr ²⁺ Fe ²⁺ , Zn ²⁺ , & Al ³⁺	Rahavi <i>et al.</i> , 2017
Pig bones	Calcination	600, 800 & 1000	Crystalline rod like 38-58 nm length & 7- 13 nm width	1.88 at 1000 °C	Na ⁺ , Mg ²⁺ , Sr ²⁺ Fe ²⁺ , & Zn ²⁺	Janus <i>et al.</i> , 2008
Turkey bones	Calcination & ball milling	850, 2h	Spherical, 85 nm	1.63	Na ⁺ , K ⁺ Mg ²⁺ Si ⁴⁺	Esmailkhanian <i>et al.</i> , 2019
Pig bones	Alkaline Hydrothermal, calcination	800-1200	Irregular, plate-like, 70-180 nm	1.7 – 1.72	-	Haberko <i>et al.</i> , 2006

2.2.4 HAp from Fish Biowastes

A massive amount of fish-related biowaste (chiefly bones and scales) is produced every year around the globe due to the globally increasing consumption of fish by world population. Since fish bones and scales are rich source of calcium, phosphate and carbonate this waste is an alternative source for extraction of HAp (Mustafa *et al.*, 2015; OBADA *et al.*, 2022). This waste is generally available in local fish markets, seashores and fish processing factories and it has a low risk of disease transmission and religious sentiment. Around 91 million tonnes of fishes are caught globally every year from natural and freshwater resources (Surya *et al.*, 2021). But only 50–60 % of these might be used as a source of meat for human consumption and the remaining parts, such as scales, internal organs, bones, etc., are discarded as biowastes (Hoyer *et al.*, 2012). Therefore, an effective utilisation of the biowaste, especially scales and bone can be used for the production of HAp and on the other hand this utilization of biowaste help to reduce the environmental liabilities and biohazard risks to humans. Furthermore, it helps to mitigate the problems of waste disposal too. Studies show that among the different body parts of fish, the bone and scale contain mainly collagen and calcium phosphate, which is a rich source of HAp. Ivankovic *et al.* (2010) synthesised HAp by alkaline hydrothermal treatment of cuttlefish bone. The SEM micrographs of this HAp (**Figure 11**) show a highly porous and rod-like morphology with an average diameter range of 200-300 nm.

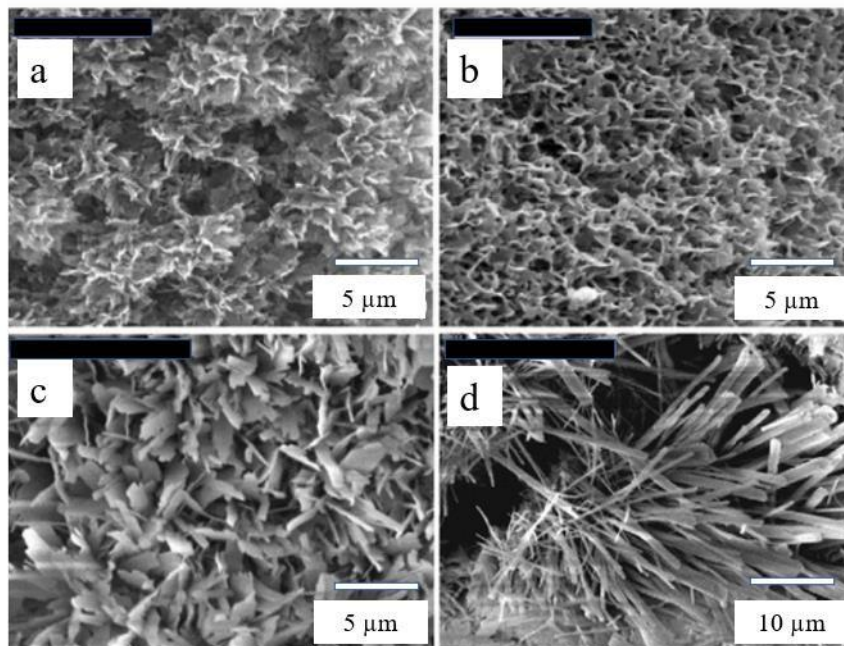


Figure 11: SEM micrographs of HAp obtained from cuttlefish bone (Source: Ivankovic *et al.*, 2010)

Boutinguiza *et al.* (2012) separately used swordfish and tuna fish bones to extract HAp. For this, the defatted and deproteinized bone samples were subjected to calcination for 12 h at 600 °C and 950 °C. Their results show the formation of B-type substituted HAp when calcinated at 600 °C, while the results of the same characterization at 950 °C confirmed the HAp along with β -TCP. Similarly, a comparative study of calcination and alkaline hydrolysis for the extraction of HAp from tuna fishbone (*Tunnus obesus*) was performed by Venkatesan *et al.* group (Venkatesan *et al.*, 2011). In one of the applied procedures, the fishbone was subjected to heat treatment directly at 900 °C for 5 h of holding time. In another procedure, the fishbone was soaked with 2 M NaOH for alkaline heat treatment and subjected to calcination at 250 °C for 5 h holding time. Results showed that both methods could produce HAp of good quality. However, the HAp produced through the calcination method was more crystalline with larger particle size and a smaller Ca/P ratio (1.65) in comparison to the HAp of alkaline heat-treatment process. Balu *et al.* (2020) subjected cuttlefish bone to the novel oil-bath medicated precipitation method for the extraction of HAp with particle size of 20.86 nm.

Like bone, fish scale is also an alternative source for extraction of HAp because it also contains a large amount of calcium, phosphate and carbonate in the collagen matrix, which makes the scale surface smooth and more flexible in comparison to bone (Pati *et al.*, 2010). Many researchers used this biowaste for extraction of HAp. Paul *et al.* (2017) extracted HAp from *Catla catla* fish scales by calcination at 200-1200 °C. The crystallite size of this HAp is found to be 30 nm, whereas the size of HAp synthesised by the chemical route is found to be 60 nm. Furthermore, the results of inductively coupled plasma atomic emission spectroscopy showed that the HAp derived from fish scales calcined at 1200 °C contained valuable cations (Mg^{2+} , Sr^{2+} , Na^+ , K^+ , etc.) as well. Similarly, in another study, Mondal *et al.* (2016) extracted HAp from *Labio, rohita and Catla catla* fish scales by the calcination method. They heated the scales at 1000° C and then pulverised them for 16 h for extraction. The results showed that the Ca/P ratio of this HAp was found to be 1.71, which is slightly higher than the stoichiometric ratio of 1.67. The TEM micrographs showed that small rice grain-shaped particles were visible together with some spherical large ones, with an average particle size of 76.62 nm.

In another study, Panda *et al.* (2014) extracted pure and crystalline HAp from freshwater fish scales (*Labeo rohita* and *Catla catla*) by using a combination of alkaline heat treatment and a calcination method. For this, the samples were treated with 1N NaOH before being subjected to a solution of calcium chloride dihydrate ($\text{CaCl}_2 \cdot 2\text{H}_2\text{O}$) at 75 °C to compensate for the scale's calcium deficiency, followed by 1 h of calcination at 800 °C. The EDX results showed that the HAp has a Ca/P molar ratio of 1.62, which is nearly equal to the stoichiometric ratio of chemically synthesized HAp.

Similarly, Pon-On *et al.* (2016) also prepared HAp from a freshwater fish scale (*Probarbus Jullieni/Sauvage*). For this, the cleaned and dried fish scales were soaked for 15 min and stirred in 4% HCl for the deproteinization process. Subsequently, the solution was neutralised by NaOH to obtain a HAp-rich slurry and then filtered. The residue was boiled at 100 °C for 30 min to deactivate the enzyme before being stored at 20 °C for further investigation. The results showed a flat plate-like structure with a width of 15-20 nm and a length of 100 nm. The presence of phosphate ion (PO_4^{3-}) substitution (B-type) by carbonate ions (CO_3^{2-}) results a higher Ca/P molar ratio (2.01) confirmed by FTIR analysis.

Huang *et al.* (2011) extracted semicrystalline HAp from Tilapia fish scales by an enzymatic hydrolysis. For this, two types of enzymes, namely, protease and flavoenzyme was used to hydrolyse collagen from the scales. The first phase of hydrolysis was done by a 1% protease solution for 2.5 h and the second phase was done by a 0.5% flavoenzyme solution for another 30 min. The HAp (FHAp) obtained by this method has a Ca/P molar ratio greater than 1.76 with an irregular shape and an average particle size of 720 nm. The SEM micrograph (**Figure 12 a & b**) has an elongated morphology in comparison to the reference sample (Sigma SHAp) having an irregular spherical morphology (**Figures 12 d & e**) after 4 h sintering at 800 °C. In comparison to sintered SHAp (**Figure 12 f**), the particles of FHAp have an irregular surface morphology. In addition, the results of EDX analysis showed the existence of a trace number of foreign elements (e.g., Na^+ , K^+ , Mg^{2+} and Sr^{2+}) as well in this type of HAp.

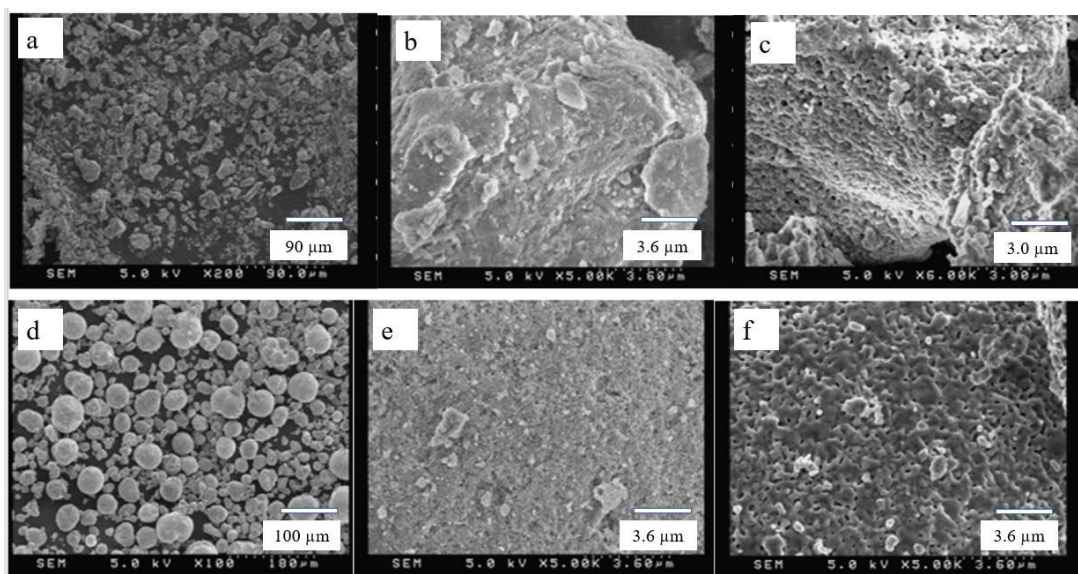


Figure 12: SEM micrograph of the FHAp powder (a & b), sintered FHAp powder (c), SHAp powder (d & e) and sintered SHAp powder (f) (Source: Huang *et al.*, 2011)

Fish based biowaste, especially bone and scales, might be alternative source for the extraction of HAp. Calcination is a common cost effective and efficient method for the conversion of fish bones and scales into the HAp. Alkaline heat treatment and enzymatic hydrolysis is the alternative methods for the conversion of fish bone and scales into HAp. Many researchers reported that this method could yield semicrystalline HAp, whereas the calcination method produces crystalline HAp in general. The overall summary of the methods used to prepare HAp from fish-based biowastes, their state, particle shape and size, Ca/P molar ratios and trace element content are listed in **Table 7**.

Table 7: A summary of the source's extraction method, heating temperature, holding time and physicochemical parameters of HAp extracted from fish bones and scales

Species and parts of fish source	Extraction method	Calcination temperature (°C) & time	State, Particle shape & size	Ca/P molar Ratio	Elements found	References
Cuttlefish bones	Alkaline hydrolysis & calcination	900, 5h	Crystalline rod shape, 200-300 nm	1.65 >1.65	-	Ivankovic <i>et al.</i> , 2010
Sword and Tuna, bones	Calcination	600 -950, 12 h	Crystalline, rod like	-	-	Boutinguiz <i>et al.</i> , 2012
Tunnu -sobesus fish bones	Calcination & alkaline Hydrolysis	900, 5h &250, 5h	Crystalline	1.65 > 1.65	-	Venkatesan <i>et al.</i> , 2011

Cuttlefish & catfish bone	Calcination & alkaline hydrolysis	900, 5h	Crystalline rod shape	1.65	-	Rahavi <i>et al.</i> , 2017
Cuttlefish bones	Oil-bath Medicated precipitation	-	Crystalline rod, 20.86 nm	1.6	-	Balu <i>et al.</i> , 2020
Catla catla fish scales	Calcination	200 & 1200,1h	Crystalline, 30 nm	-	Na ⁺ , K ⁺ , Mg ²⁺ , Sr ²⁺	Paul <i>et al.</i> , 2017
Labiorohita & Catla catla fish scales	Calcination and milling 16 h	1000 16h	Crystalline, Spherical 76.62 nm	1.71	-	Mondal <i>et al.</i> , 2016
Labeorohita & Catla fish scales	Alkaline heat treatment & calcination	800, 1h	Crystalline, 76.62 Nm	1.62	-	Panda <i>et al.</i> , 2014
Fresh water probarbus Jullieni fish scale	Acid treatment & heating	-	Crystalline flat plate width 15-20 nm & length 100 nm	1.76	Na ⁺ , K ⁺ , Mg ²⁺ , Sr ²⁺	(Pon-On <i>et al.</i> , 2016)
Tilapiafish scales	Enzymatic hydrolysis Protease & Lavoenzyme	-	Porous, irregular, 720 nm	1.76	Na ⁺ , K ⁺ , Mg ²⁺ , Sr ²⁺	Huang <i>et al.</i> , 2011

2.2.5 HAp from Shells

The exoskeletons of both marine and freshwater animals contain a higher amount of minerals like calcium and phosphate. A huge amount of these skeleton is available in seaside and sea food processing factories as discarded biowastes (Meski *et al.*, 2019). This biowaste contains sufficient amount of calcium carbonate as aragonite or calcite, which is a good source of calcium precursor for synthesis of HAp (Meski *et al.*, 2019). For the synthesis of HAp, the shells are cleaned with diluted mineral acids to remove the adhering impurities. After that, it is subjected to crush into powder and calcined for 2 h at 800 °C. The high temperature treatment decomposes the carbonate form of calcium precursor into its oxide or hydroxide form and further treatment of phosphate precursors in an alkaline medium is done to prepare HAp.

Different researchers used these sources for the preparation of HAp. Rujitanapanich *et al.* (2014) used oyster shell as a calcium precursor to synthesise HAp by applying the precipitation method. For this, the shells were first subjected to calcination to convert calcium carbonate to CaO and then treated with phosphate precursors in an alkaline medium (pH >10).

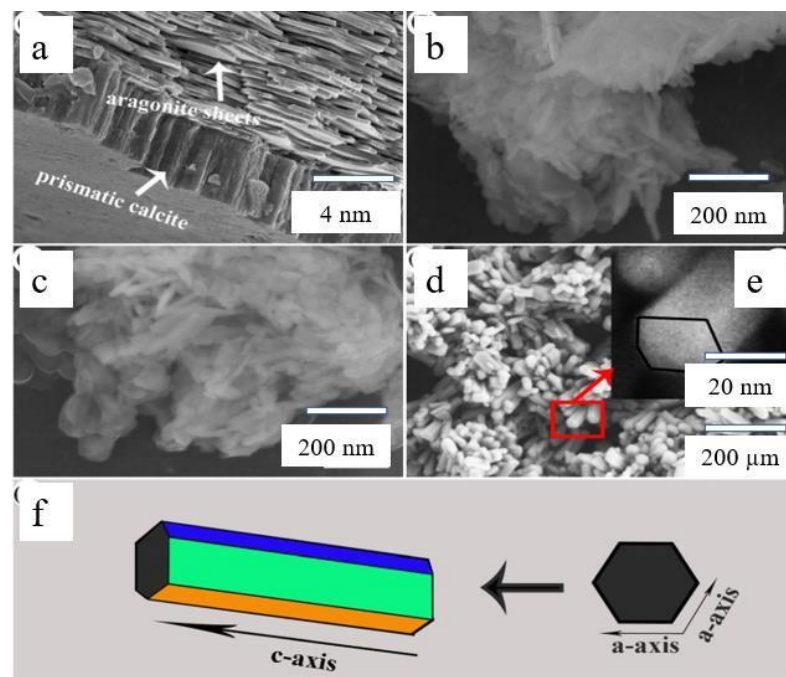
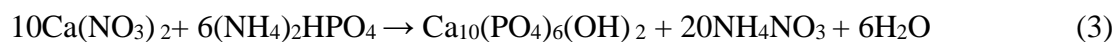


Figure 13: FESEM images of the abalone shell cross-section (a) and the samples exposed to different hydrothermal times: (b) 6 h, (c) 18 h and (d) 72 h; The inset (e) is a magnified view of the selected red area. (f) HAp hexagonal crystallites schematic diagram (**Source:** Chen *et al.*, 2015)

The reaction involved in this process is shown in **equations 1 to 3**. It is then subjected to ageing for 24 h and then recalcined at 900 °C for another 2 h. The XRD pattern showed a highly crystalline nature with a particle size of 89.5 nm.



In another study, Chen *et al.* (2015) used the abalone shell as a source of calcium precursors for synthesis. For this, the shell was immersed in 10% acetic acid to remove adhering impurities, then left for some days for natural drying, after which it was powdered. For the synthesis, the calculated amount of shell powder and diammonium hydrogen phosphate $(\text{NH}_4)_2\text{HPO}_4$ were mixed in an alkaline medium ($\text{pH} > 8$). After that, the mixture was autoclaved at 150 °C for 6 h, 18 h and 72 h, respectively. The results showed the regular rod-like and flake-like morphology at 18 h of hydrothermal time. However, when the hydrothermal time was increased to 72 h, they noticeably found a clear, uniform, rod-like hexagonal morphology of the HAp. The FESEM micrograph of this is shown in **Figure 13**.

Irfan *et al.* (2020) used crab shells (*Scylla serrata*) and eggshells separately as calcium sources for HAp synthesis.

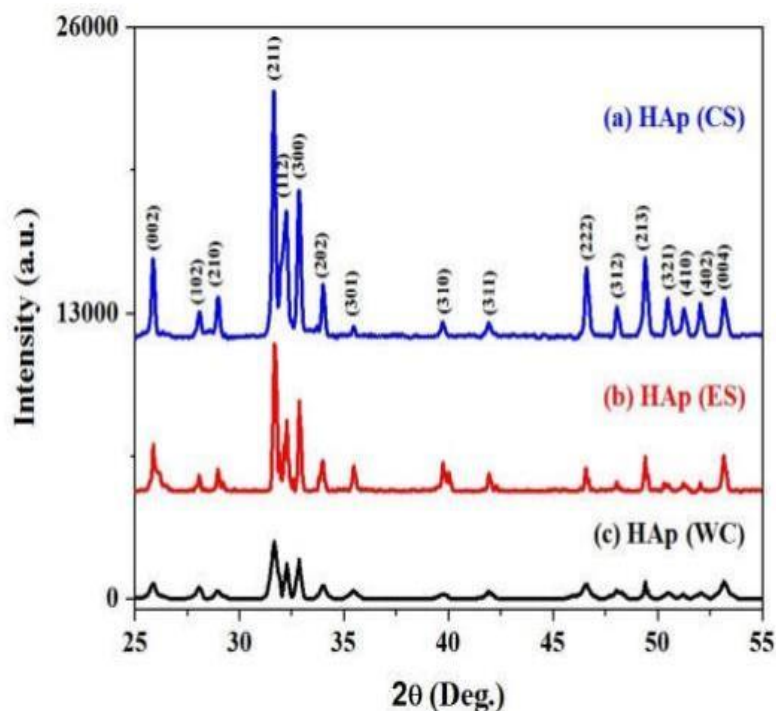


Figure 14: Powder XRD spectra of hydroxyapatite (HAp) prepared by using (a) crab shells, (b) eggshells and (c) wet chemical process (**Source:** Irfan *et al.*, 2020)

For the conversion of the carbonate of calcium into CaO, they calcined the samples for 3 h at 800 °C and 1000 °C separately. Likewise, for the conversion of CaO to HAp, they chose phosphoric acid (H₃PO₄) as a source of phosphorous and used the co-precipitation method. The results of the XRD diffraction peak (**Figure 14**) indicate a fine crystalline structure. Furthermore, the results of the SEM-EDX pattern showed the existence of basic elements with a 1.64 Ca/P molar ratio for crab shells and 1.63 for eggshells, respectively.

Gergely *et al.* (2010) used two different mechanochemical techniques (attrition milling and ball milling) to prepare HAp from eggshell waste using H₃PO₄ as a phosphorous precursor. Similarly, in another study, Santhosh and Prabhu (2013) synthesised HAp from seashells by applying calcination and wet chemical precipitation methods jointly. Their results showed that pure crystalline rod-shaped HAp has a particle size of 101 nm and a Ca/P ratio of 1.8.

Muski *et al.* (2019) synthesised nano-HAp from sea mussel shells as a calcium precursor using a combination of calculation and a wet chemical precipitation method. For this, the mussel shell was cleaned and dried at 80 °C for 24 h.

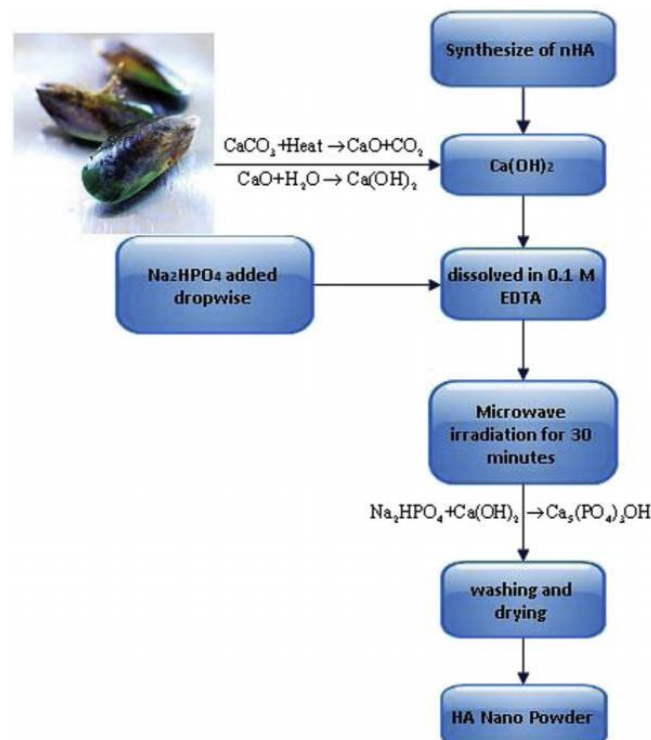


Figure 15: The flow sheet diagram of the synthetic route of HAp powder from waste mussel shells (Source: Shavandi *et al.*, 2015)

The dried shells were ground and the resulting powder was first calcined at 900 °C for 30 min to convert CaO and it was then dissolved in a 1:1 v/v ethanol solution with continuous stirring for 1-2 h. Then after, 200 ml of 0.06 M, ammonium dihydrogen phosphate ($\text{NH}_4\text{H}_2\text{PO}_4$) was added dropwise with continuous stirring for 24 h to obtain HAp. In another study, using the fast microwave irradiation method, Shavandi *et al.* (2015) synthesised HAp from waste mussel shells as a source of calcium. By using less energy and at a faster rate, this method produced high amounts of HAp. The flow sheet diagram of the preparation is shown in **Figure 15**.

Their results showed that applying this method produced pure crystalline HAp with a particle size of 30-70 nm and a Ca/P ratio of 1.65. The SEM micrographs of the raw mussel shell (a), dried (b), heated (c) and commercial HAp (d) samples are shown in **Figure 16**, which reveals that the dried HAp has an agglomerated form with rod-shaped crystals and has a porous morphology similar to commercial samples.

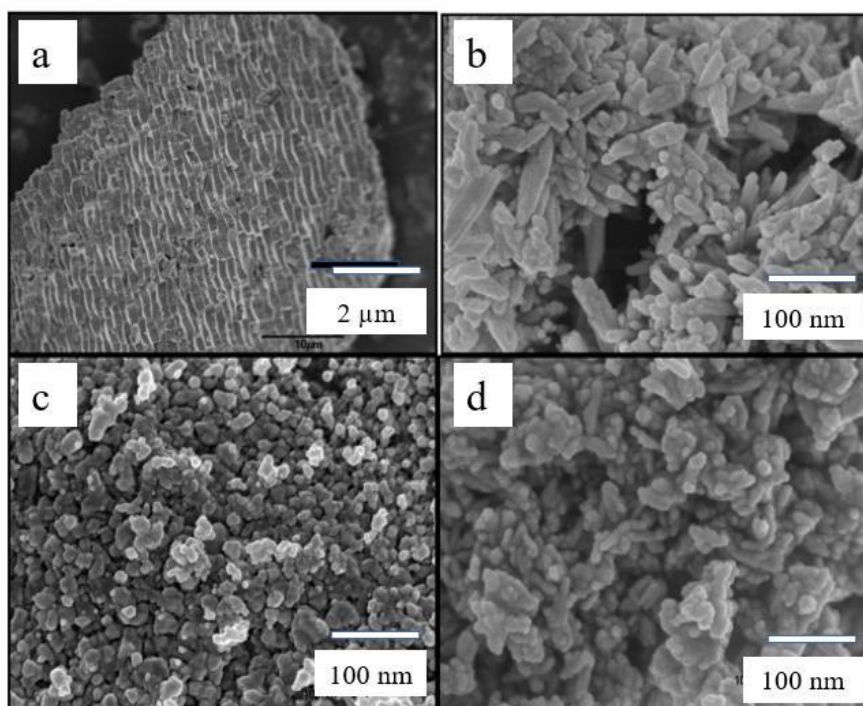


Figure 16: The SEM images of nano-HAp powders: (a) raw mussel shell; (b) dried mussel shell; (c), heated mussel shell; and (d) commercial mussel shell (**Source:** Shavandi *et al.*, 2015)

Khiri *et al.* (2016) used ark clam shell (*Anadara granosa*) as a calcium precursor to produce HAp jointly by using calcination and a precipitation method. For this, the shells were thoroughly cleaned and calcined at 900 °C to convert the CaCO_3 into

CaO. They were then subjected to 24 h ball milling to get a particle size of 45 μm . This powder was used to prepare a molar solution of $\text{Ca}(\text{OH})_2$. Then, using the titration method with adding 0.6 M of H_3PO_4 to prepare HAp in an alkaline medium. The results of the XRD pattern sintered at 200-1000 $^\circ\text{C}$ showed the single phase of HAp. The Ca/P ratio was found to be in the range of 1.69-2.0. The particle size of 35-69 nm was recorded when heated at 200 $^\circ\text{C}$. However, when the sintering temperature was increased above 200 $^\circ\text{C}$, the particle size also changed in the range of 0.13-0.24 and 0.33-0.79 μm , respectively. Ferreira *et al.* (2016) reported the wet chemical precipitation method for the preparation of HAp from ostrich eggshells. Under stirring conditions, the cleaned and dried eggshell powder was dispersed in deionized water along with 1 M of lactic acid to produce 0.5 M CaCO_3 . Then a 0.3M H_3PO_4 solution was slowly dropped into it and a pH of around 3 was maintained while the solution was kept for 24 h with continuous stirring. After that, a 1 M KOH solution was added to raise the pH up to 12 and the solution was left for 46 h with continuous stirring to obtain the precipitation of HAp. It was then pressed into pellets at 100 MPa and heated at 700 $^\circ\text{C}$, 900 $^\circ\text{C}$ and 1100 $^\circ\text{C}$ for 2 h at a heating rate of 5 $^\circ\text{C}/\text{min}$. The characterised results revealed that at 700 $^\circ\text{C}$, a single phase nanocrystalline HAp was produced, but the particle size increased during sintering at 900 $^\circ\text{C}$ and 1100 $^\circ\text{C}$.

Pal *et al.* (2017) prepared HAp by using clamshells through a combination of calcination and mechanochemical techniques. In this technique, the cleaned and dried crushed shell samples were calcinated for 3 h at 1000 $^\circ\text{C}$ to convert the CaCO_3 to CaO. Then the CaO and H_3PO_4 were milled at 300 rpm for 20 h. The results showed that pure crystalline HAp was obtained at a weight ratio of CaO and H_3PO_4 of 1:1.5 with a crystal size of 53 nm. Agbabiaka *et al.* (2020) used calcination and hydrothermal methods to synthesise HAp from chicken (*Gallus domesticus*) eggshells. In this method, the cleaned and dried shells were divided into three parts to carry out three-stage calcination at 800 $^\circ\text{C}$, 900 $^\circ\text{C}$ and 1000 $^\circ\text{C}$, respectively. The calcined samples were separately dispersed in beakers containing 100 mL of distilled water and 20 mL of orthophosphoric acid and were subjected to vigorous stirring under a mechanical stirrer on a hot plate at 90 $^\circ\text{C}$. Ageing treatment of the samples gave lumped white solids for each sample after one week and was subsequently pulverised into powder. The results showed that HAp synthesised at 1000 $^\circ\text{C}$ has a Ca/P molar

ratio of 1.65, which is nearly equal to the stoichiometric ratio of chemically synthesized HAp. The SEM images (**Figure 17**) calcinated at 800 °C showed a crystalline flake-like morphology, whereas those calcinated at 900 °C and 1000 °C showed spherical and irregular shapes.

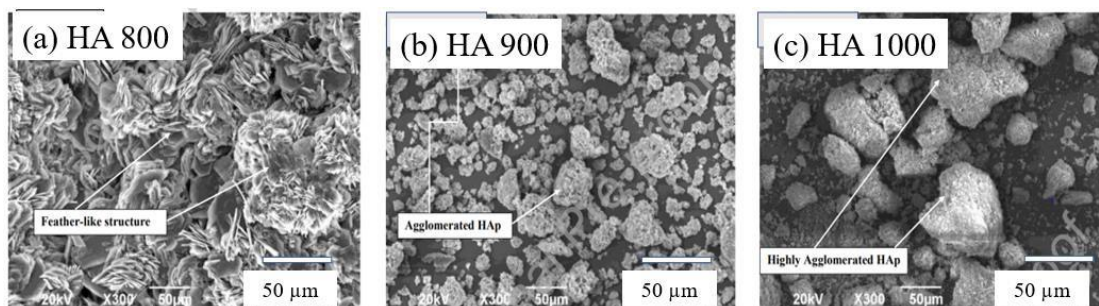


Figure 17: SEM images of HAp calcinated at 800 °C, 900 °C & 1000 °C. (a) HA 800, (b) HA 900 and (c) HA 1000. (**Source:** Agbabiaka *et al.*, 2020)

Thus, it is obvious that the shells are an economical source of calcium precursors and can be used for HAp synthesis, although it demands a few additional steps. Most of the methods which are discussed above and listed in **Table 8** show that calcination is the consistent method of conversion of the CaCO_3 of the shells to CaO . The CaO or its hydroxyl form is treated with different phosphorous precursors for the synthesis. On the other hand, HAp can also be prepared by direct contact of shell powder with phosphorous precursors. Chen *et al.* (2014) prepared nanocrystalline HAp by the direct treatment of abalone shell powder with diammonium phosphate solution. However, the most frequently applied methods for synthesis are wet chemicals (wet chemical precipitation, sol-gel precipitation, alkaline hydrothermal), mechanochemical (ball milling, attrition milling) and microwave irradiation (rapid microwave irradiation) and thermal treatment. One of the noteworthy points is that an alkaline medium (i.e., pH value >10) is highly appreciated for synthesising from these sources, mainly in the wet chemical method. Another factor to consider is that proper CaO or Ca(OH)_2 proportions of phosphorous precursors are required to maintain HAp quality. However, Ferreira *et al.* (2003) Ben-Nissan *et al.* (2015) & Macha *et al.* (2015) showed the direct treatment of CaCO_3 of ostrich eggshell powder with orthophosphoric acid by the wet chemical method without maintaining an alkaline pH. The results in **Table 8** show that the extraction of HAp from shell sources produces particles of different shapes and sizes. However, most of the methods were able to synthesise rods and needle-like shapes in addition to spherical ones. This,

however, cannot be a foregone conclusion. In addition, most of the extracted HAp has a particle size range below 500 nm, except for the cockle shell (4.03–10.40 μm).

In terms of crystallinity, most of the HAp extracted by using calcination in addition to the precipitation method has a high degree of crystallinity. However, Ferreira *et al.* (2016) & Macha *et al.* (2015) successfully synthesised low crystalline HAp from ostrich eggshell using the precipitation method.

Table 8: A summary of the source, extraction method, heating temperature, holding time and physicochemical parameters of HAp extracted from shell sources

Sources	Phosphorous source	Method used	pH	Properties of HAp (Phase, Shape, size & Ca/P)	Reference
Sea mussel shell	H ₃ PO ₄	Calcination & wet chemical precipitation	-	-	Meski <i>et al.</i> , 2019
Abalone shell	H ₃ PO ₄	Alkaline hydrothermal	8-10	Crystalline, hexagonal rod shape 89.5nm, 1.67	Chen <i>et al.</i> , 2015
Oyster shell	H ₃ PO ₄	Calcination & wet chemical precipitation			Rujitanapanich <i>et al.</i> , 2014
Crab shell & eggshell	H ₃ PO ₄	Calcination, Co-precipitation.	-	Crystalline, 293nm (CS), 182 nm (ES), 1.64 (CS), 1.65(ES)	Irfan <i>et al.</i> , 2020
Seashell	H ₃ PO ₄	Calcination, Wet chemical precipitation,	10	Crystalline, rod shape, 101 nm, 1.8	Santhosh & Prabu, 2013
Mussel shell	H ₃ PO ₄	Calcination plus rapid microwave irradiation	13	Crystalline, rod-like, 30-70nm, 1.65	Shavandi <i>et al.</i> , 2015
Ark clam shell	H ₃ PO ₄	Calcination, Wet chemical precipitation and ball milling	8	Single crystalline (at 200-1000 °C), 35-69nm (at 200 °C), 1.69-2.00	Khiri <i>et al.</i> , 2016
Clam shell	H ₃ PO ₄	Calcination	-	Crystalline, 53nm	Pal <i>et al.</i> , 2017

Furthermore, the HAp synthesised from the shell source also has a non-stoichiometric nature. It has a variable Ca/P molar ratio, with most HAp extracted using combined methods having a Ca/P ratio greater than stoichiometric HAp (>1.67) and precipitation HAp having a Ca/P ratio less than 1.67. In conclusion, this value should depend on the processing techniques, habitat and food habits of shell-bearing animals as well. The overall summary of the methods used to prepare HAp from shell-based biowastes, source of phosphorous precursors, pH and properties are listed in **Table 8**.

2.3 Biomedical Applications of HAp

An extensive survey of literature shows that HAp is one of the most broadly studied bioceramic compounds found in human bones and teeth. Both chemically synthesized and biosource-based HAp can be utilized in several interdisciplinary areas of applications, including chemistry, biology, geology, odontology and biomedical (Kumar *et al.*, 2012; Lett *et al.*, 2016; Son *et al.*, 2011). However, it is preferably employed for various biomedical applications rather than chemically synthesized one because of the better bioactivity, biocompatibility, appropriate chemistry for cell growth and the presence of various naturally doped ions such as Na^+ , K^+ , Zn^{2+} , Cu^{2+} , Sr^{2+} , Mg^{2+} , etc. in this source of HAp, it is preferably employed for various biomedical applications rather than chemically synthesized (Kodali *et al.*, 2022; Lu *et al.*, 2019; Mondal and Pal, 2019). This study is focused on the major biomedical applications of HAp as illustrated in the **Figure 18**.

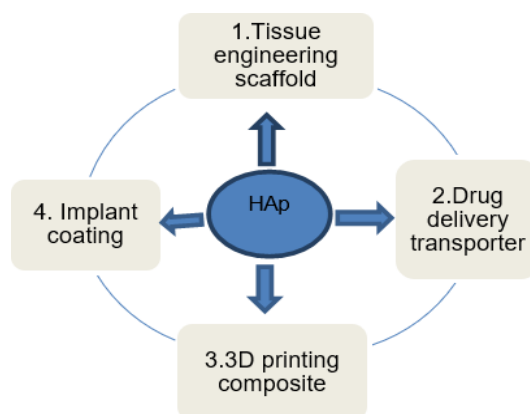


Figure 18: Major biomedical applications of biosource-based nano-HAp

2.3.1 Tissue Engineering Scaffold

Hard tissue, especially bone and teeth, is an organic and mineral composite natural biomaterial found in animal body. Moreover, the collagen fibrils are an organic part

of hard tissue whereas nano-HAp is a mineral part of the human bone which is embedded in the collagen matrix that shows its mineral activities in the body. Recently, the demand for such HAp has increased per day in biomedical field because of many clinical disorders in human bones, such as bone infection, bone malignancies and bone loss caused by trauma, etc. and road accident (Lu *et al.*, 2019; Ramírez-Agudelo *et al.*, 2018). Due to the excellent osteoconductive property of biosource-based HAp, it has been used for the treatment of bone disorders and in BTE, including bone fracture healing. Furthermore, BTE involves the reconstruction of new bones and cartilage in the injured parts of the body. For this, a BTR scaffold can be used, which serves as a template for the interaction between surrounding cells and the ECM. A potential BTE scaffold should be biocompatible, promoting cell interaction, differentiation and proliferation and improved mechanical properties to withstand external forces as well (Fang *et al.*, 2010; Vaz *et al.*, 2005).

Scaffolds fabricated from synthetic and natural polymers such as polycaprolactone (PCL), polylactic acid (PLA), polybutylene adipate co-terephthalate (PBAT), polyurethane (PU), gelatine (GEL), etc. are generally used for these purposes. Moreover, scaffolds fabricated from such polymers act as a prototype for networking with adjoining cells and creating ECM for better cell attachment (Pati *et al.*, 2015). However, extensive studies show that only a polymer scaffold is not sufficient for proliferation and differentiation of osteoblast and osteoclast cells. As a result, including fillers like growth factors, minerals, vitamins, stimulants, bone morphogenic proteins and other substances is strongly recommended for improved differentiation and proliferation of osteoblast and osteoclast cells (Bakan, 2018; Ghosh *et al.*, 2020; Harun *et al.*, 2018; Ishack *et al.*, 2017; Kulanthaivel *et al.*, 2015). Chitosan, bio glass, hydrogels, nanocrystalline cellulose and HAp are commonly used as fillers (Fathi *et al.*, 2008; Janković *et al.*, 2015; Madhumathi *et al.*, 2009; Marins *et al.*, 2019; Shin *et al.*, 2003). Among them, HAp is the most frequently used filler to prepare hybrid scaffolds because of its biocompatible and osteoconductive nature for biomedical applications (Bhandari *et al.*, 2021; Rattan *et al.*, 2012; Su *et al.*, 2013). Various studies show that it aids in osteoblast cell adhesion, proliferation, phenotypic conservation and cellular matrix transmission (Abdulrahman *et al.*, 2014; Mota *et al.*, 2013; Prabhakaran *et al.*, 2009). As a result, HAp-incorporated polymeric scaffolds are being studied for their ability to regenerate bone tissue quickly, even in cases of

acute fracture (Beachley & Wen, 2010; Mota *et al.*, 2013; Zhang *et al.*, 2019). To create such scaffolds, various methods such as solution casting, rapid prototyping, 3D printing and electrospinning, have been used (Beachley & Wen, 2010; Harun *et al.*, 2018; Yoon and Kim, 2011; Zhang *et al.*, 2019).

Using the electrospinning method, Fang *et al.* (2010) prepared the nanofibrous scaffold of PCL/PLA and a blend of PCL/PLA blended with nano-HAp for BTE. Results showed that the scaffold loaded with nano-HAp had better osteoblast-like MC3T3-E1 cell adhesion and proliferation more significantly than the scaffold fabricated simply using PCL or PLA. Thus, this hybrid model of a composite scaffold will have better scope in BTR and BET. Similar kinds of studies were carried out by Shuai *et al.* (Shuai *et al.*, 2020). They have shown the importance of HAp for osteoblast cell growth and proliferation on a HAp-PLLA scaffold incorporated with poly glycolic acid (PGA) fabricated by the laser 3D printing method. They used PGA to enhance the hydrolytic degradation rate of PLLA and to expose embedded HAp in PLLA matrix.

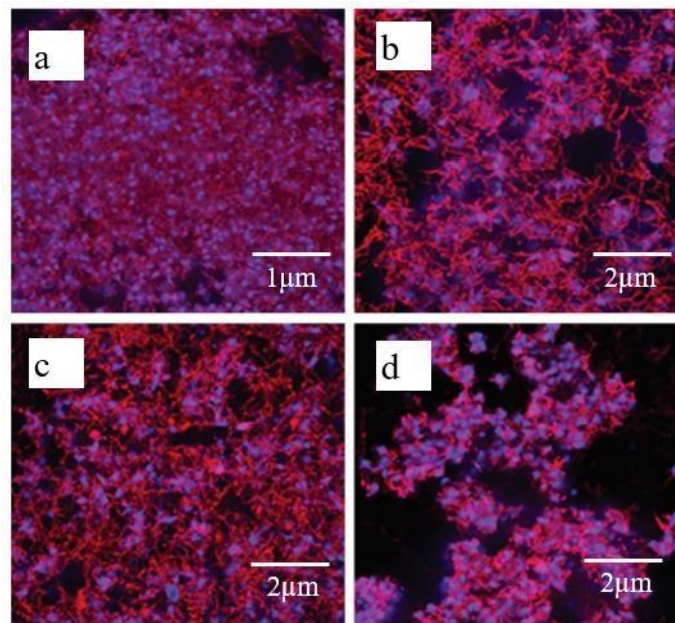


Figure 19: Fluorescent images of NIH3T3 fibroblast cell spreading and proliferation a day after seeding into: (a) Amminolysed PLLA cylinder, (b) Amminolysed PLLA cylinder + HAp, (c) Amminolysed PLLA cylinder + Simvastatin and (d) Amminolysed PLLA cylinder+HAp+Simvastatin (Source: Lee *et al.*, 2013)

Marins *et al.* (2019) shows that a PCL/GEL scaffold incorporated with nano-HAp and niobium pentoxide (Nb_2O_5) nano particles exhibited better osteogenic cell

differentiation and proliferation than a scaffold without fillers due to the synergistic effect of polymer and mineral compound. Similarly, Lee *et al.* (2013) also fabricated aminolyzed PLLA microcylindrical fibres loaded with HAp and simvastatin (a stimulant used for bone morphogenic protein 2) by the electrospinning method for the improvement of NIH3T3 fibroblast cell differentiation *in vitro*. The result showed that the composite fibres had better adhesion, osteogenic differentiation and improvement in proliferation of NIH3T3 fibroblast cells compared to PLLA, PLLA/HAp and PLLA/Simvastatin microcylindrical fibres a day after seeding, as shown in **Figure 19**. In this figure, the aminolysed PLLA fibres are stained in red and the nucleus of fibroblast cells is in blue, fluorescent.

Petricca *et al.* (2006) also confirmed that the composite mixture of poly D, L-lactico-glycolic acid (PLGA) and HAp has better mechanical properties and a higher osteogenic response than the PLGA membrane, which makes it a good choice for bone substitute scaffolds for BET. In another study, Ramfrez-Agudelo *et al.* (2018) evaluated the effect of antibacterial activity (Gram+ve, *Staphylococcus aureus* and Gram-ve, *Porphyromonas gingivalis*) on HAp and Doxycycline (Dox) loaded hybrid nanofibrous PCL/GEL scaffolds. The study showed that in comparison to individual polymer scaffolds, the HAp and Dox-loaded scaffolds have a better inhibitory effect due to the synergistic effect of HAp and drugs. Further studies have shown that such scaffolds effectively control the A-431 cancer cells as well. Hence, in the future, the HAp and anticancer drug-loaded scaffold might have potential scope in oncology.

2.3.2 Drug Delivery Transporter

Another area of application of HAp is in drug delivery systems (DDS). Because of its high crystalline surface bioactive and biocompatible nature, HAp is one of the most researched drug delivery carriers among calcium phosphate bioceramics (Okada & Matsumoto, 2015; Yang *et al.*, 2013; Yi *et al.*, 2016). It supports the controlled release of drugs to improve the delivery efficiency in target regions (Lu *et al.*, 2019). Furthermore, due to the presence of OH group on its surface and polar charge in the crystal lattice, it is a good drug transporter. Palazzo *et al.* (2007) reported its ability to attract and to preserve DNA molecules and peptide chains.

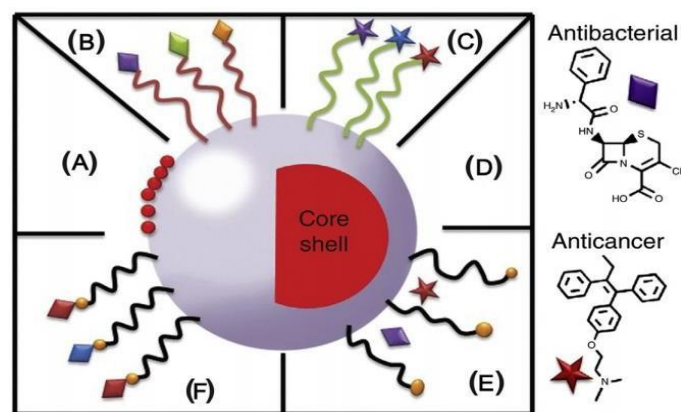


Figure 20: Pictorial representation of different drug conjugation processes over the surface of HAp. A: Coating of HAp surface with nanoparticles, B: Physical interactions of antibiotics, C: Physical interaction of anticancer drugs, D: Core-shell magnetic HAp, E: Noncovalent attachment, F: Covalent attachment of Drugs (**Source:** Mondal *et al.*, 2018)

The studies of Haider *et al.* (2014), Kwak *et al.* (2016) and Rimola *et al.* (2008) have revealed that it is a drug delivery carrier for genes, proteins and growth factors as well. Due to its rough surface along with the "P" and "C" sites, it is also suitable for protein binding during the mineralization process (Haider *et al.*, 2017). For decades, various approaches have been developed for the pairing of drugs on the HAp surface. One of the models proposed by Mondal *et al.* (2018) is shown in **Figure 20**. In this model, they classified two major groups of conjugations of drugs over the surface of HAp; one is by means of cleavable covalent linkages and the other is attachment through physical interactions. Some therapeutic drugs such as Doxorubicin (DOX), Raloxifene and Ofloxacin are conjugated with nano-HAp by cleavable covalent linkage, while Ibuprofen, sodium ampicillin and vancomycin are found to show linkage with HAp by the mode of physical interaction. Nevertheless, the mode of linkage depends on the polar functional groups of drugs and their interactions with HAp. Recent studies have shown that the efficacy of HAp as a novel carrier for anticancer drugs explores its potential application for drug delivery in cancer therapy (Ghosh *et al.*, 2020).

In another study, Haider *et al.* (2014) incorporated nano HAp into the PLGA substrate for the preparation of the HAp/PLGA composites. Then, insulin and bone morphogenic proteins (BMP) were coated and fixed on its surface so that it could be used to speed up the growth of osteoblastic cells. The results showed that after the protein was stuck to the surface of the HAp and mixed with poly lactide-co-glycoside

(PLGA), the composite sped up the growth of osteoblastic cells and bone formation compared to the PLGA substrate. Likewise, Hong *et al.* (2004) modified the surface HAp with a spacer by using glutamic acid (GA). They immobilised the protein drug on the free terminal groups (either-COOH or-NH₂) of the spacer. The drug-loaded HAp is mixed with a polymer solution to transport it to the target site for the efficacy of targeted drugs. Study shows that the oriented proteins on the surface of nano-HAp have better drug delivery ability compared to the non-oriented (absorbed) proteins. In another study, Palazzo *et al.* (2007) investigated the adsorption and desorption of cis-diamminedichloroplatinum (II) (cisplatin) and the new platinum (II) complex di(ethylenediamineplatinum) medronate (DPM), as well as the clinically relevant bisphosphonate alendronate, onto the HAp surface. The results showed that HAp's properties could be changed for therapeutic use of anticancer drugs.

In a study, Madhumathi *et al.* (2009) deposited HAp on the surface of chitosan hydrogel membranes and investigated the differentiation and proliferation of MG-63 osteosarcoma cells over it. They reported better proliferation and differentiation of investigated cell-lines on the surface of the membranes and that such types of membranes could be used for bone or cartilage tissue engineering. Above and beyond these studies, numerous studies have been dedicated to the justifiable use of HAp as a drug delivery as well as the carrier on the surface of implanting materials. So, HAp might be a hopeful bioceramic for a target drug delivery system in the future.

2.3.3 3D Printing of Composite

For decades, 3D printing has emerged as a promising technology for creating various bone-like scaffolds (Kim *et al.*, 2018). Recently, using 3D printing techniques, scaffolds with diverse and complex structures have been fabricated by Kim *et al.* for orthopaedic applications. Various biodegradable and non-biodegradable polymers such as PCL, PLLA, PBAT, PU, GEL, etc. and HAp incorporated 3D printing hybrid composite scaffolds are suggested for bone tissue regeneration study because such a scaffold has better bioactivity along with mechanical strength in comparison to a polymer scaffold. As a result, researchers have long been working on this type of scaffold for orthopaedic applications (Do *et al.*, 2015; Haleem *et al.*, 2020; Liu *et al.*, 2016; Mondal and Pal, 2019; Oladapo *et al.*, 2021; Wang *et al.*, 2020).

In a study by Yao *et al.* (2015), nano-HAp incorporated into composite blends of polycaprolactone (PCL/nano-HAp) and polypropylene fumarate (PPF/nano-HAp) demonstrated great success in fracture bone support for healing in a rabbit bone model. The computed tomography scan (CT-scan) data-based design of rabbit femoral scaffold models is shown in **Figure 21**.

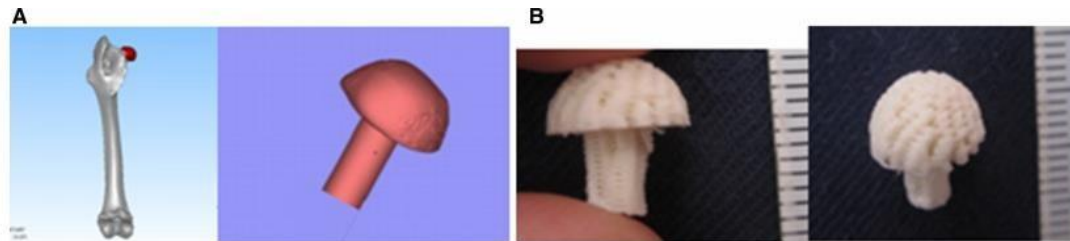


Figure 21: The figure shows the 3D printed design of anatomical femoral and vertebral plate-fused scaffolds. (A) 3D printed model of the rabbit femoral scaffold. (B) The CT-scan data-based femoral scaffolds of rabbit. (Source: Yao *et al.*, 2015)

This model has proven that 3-D printing is a very effective technique to develop some body parts of the skeleton by using polymers and ceramics for *in vivo* applications. On the other hand, Kim *et al.* (2018) used a mechanical extrusion-based 3D bioprinter to make a nano-HAp-PCL composite scaffold that has better mechanical strength and a higher rate of cell growth than the PCL scaffold.

Liu *et al.* (2016) prepared an osteogenic PLA/HAp screw-like scaffold loaded with mesenchymal stem cells (MSCs) by a 3D printing method for tissue engineering. The tests (*in vitro* and *in vivo*) results of these scaffolds showed MSCs suspended in the Pluronic F-127 hydrogel, which promotes the bone growth and formation of the interface inside the bone tunnel as shown in **Figure 22**. Moreover, this figure depicts schematic diagrams of the implant and tendon graft within the bone tunnel in anterior cruciate ligament (ACL) reconstruction. This study shows that the technology for printing 3D biomaterials has a big positive effect on orthopaedic applications.

Similarly, Martnez-Vázquez *et al.* (2015) used rapid prototyping to create gelatine and silicon-doped HAp-blended composite scaffolds containing vancomycin. This scaffold has better-augmented differentiation and gene expression of the MC3T3-E1 osteoblastic cells in comparison to the scaffold without filler. *In vitro*, studies showed that the short-term release of antibacterial drugs effectively stopped the growth of bacteria. Because silicon-doped HAp and vancomycin work together, this scaffold is better at killing bacteria than the GEL scaffold.

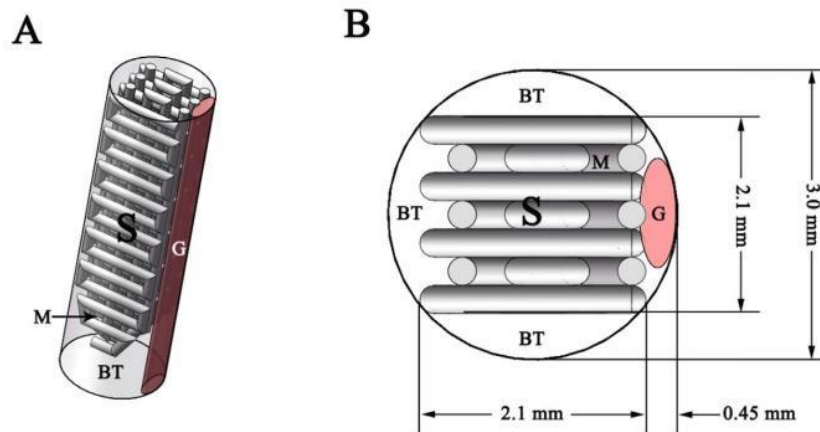


Figure 22: The figure shows the implant and tendon graft within the bone tunnel in ACL reconstruction. (A) The 3D perspective of the bone tunnel in ACL reconstruction. (B) A cross-sectional view of the bone tunnel. (G: Graft; S: Screw-like scaffold; BT: Bone tunnel; and M: Macropore) (Source: Liu *et al.*, 2016)

In another study, Lopez-Noriega *et al.* (2015) fabricated collagen-HAp incorporating poly-lactic-co-glycolic acid (PLGA) microparticles on the encapsulated pro-osteogenic peptide PTHrP 107–111 by the 3D printing method. This scaffold has great potential for BTE because of the peptide release, which shows pro-osteogenic effects on bone cells. Similarly, Ishak *et al.* (2017) prepared HAp/ β -TCP scaffolds coated with dipyrindamole agents and bone morphogenetic protein-2 (BMP-2) using the 3D printing method. The application of this scaffold has shown better stimulation of A2A receptors and has promoted critical bone defect regeneration. In addition to these studies, various researchers have used HAp in 3-D printed materials. These materials could be used to improve the bioactivity of implanting materials by putting drug delivery carriers on their surface.

2.3.4 Implant Coating

Despite the numerous advantages of nano-HAp in implant coating, it has certain limitations for orthopaedic applications due to its high young's modulus, low fracture toughness and poor resorption properties (Rattan *et al.*, 2012). Many researchers have introduced different tools and techniques for coating nano-HAp on the implant surface. Plasma spraying, electrostatic spraying, electrophoretic deposition, pulsed laser deposition, hot pressing, sol-gel deposition, spin-coating, sputtering coating, ion

beam assisted deposition and layer-by-layer sputtering are some of the commonly used techniques (Haider *et al.*, 2014).

Using electrophoretic deposition (EPD), Shi *et al.* (2016) coated ternary blends of graphene oxide-chitosan-HAp (GO-CS-HAp) composite blends on the titanium substrate, which showed effective attachment of osteoblastic (MG-63) cells and better antimicrobial activity. On the other hand, Guimond-Lisher and his co-workers (2016) coated nano-HAp and silver nanoparticles (n-HAp-Ag) on the same substrates using vacuum plasma spray techniques. Their findings showed that such coatings exhibited no cytotoxicity to the primary human bone cells and promoted better antibacterial activity against Gram +ve and Gram -ve bacteria (*E. coli* and *S. aureus*) as compared to the previous ones. Due to its osteogenic properties, Nano-HAp has been used as an implant coating material for a long time. When compared to an uncoated material, this material has a higher affinity for the host bone tissues.

A study of Bose *et al.* (2015) revealed that nanocrystalline HAp had better bioactivity and biocompatibility than microcrystalline. It is used to create biocompatible implant coatings that outperform microcrystalline HAp. Furthermore, this type of coating is applied to metallic prostheses, particularly stainless steel or titanium or its alloys, to improve the surface properties of implant materials for cell adhesion, differentiation, mineralization and osteointegration (Arcos & Vallet-Regí, 2020). The study of Blazutti Marcal *et al.* (2017) & Rattan *et al.* (2012) reported that a thin coat of nano-HAp had better bond strength and sufficient contact area at the bone-implant interface compared to an uncoated substrate. Zinc-doped fluoridated HAp (ZnFHA) is a common coating material used in implant coating. Huang *et al.* (2016) coated this material on the titanium substrate using an electrolytic deposition method. Results showed that this coating was totally crack-free and dense, which better supported the proliferation and spread of osteoblast cells in the implanted substrate compared to the uncoated one. This coating promotes alkaline phosphatase (ALP) expression, which is a probable effect of a combination of nanostructured surface effects and the release of Zn^{2+} and F^{-} ions from the doped surface. This coating is highly recommended for most bioimplant materials.

In a study, Mihailescu *et al.* (2016) deposited 2 wt.% MgF_2 and 5 wt.% MgO into the bovine source HAp using a pulsed laser technique and this composite of coating material is used for coating on a titanium substrate. It helps to improve the

biocompatibility and antimicrobial activity of the substrate. The results showed that this implant had a better (72h) anti-biofilm effect against *Micrococcus sp.* and *Enterobacter sp.* in comparison to the uncoated ones. So, depositing a certain amount of MgF₂ and MgO makes HAp more bioactive, which could make it a good material for making reliable coatings for orthopedic implant applications. Likewise, Mihilescu *et al.* (2016) & Guimod-Lischer *et al.* (2016) formulated a silver-doped hydroxyapatite (Ag-HAp) coating using a vacuum plasma spray technique. These coatings also showed good antibacterial activity against *E. coli* and *S. aureus*, as well as having no cytotoxicity to primary human bone cells. A high Ag⁺ ion release rate from this coating reduces bacterial activity on the implant surface. Studies showed that implanted zinc and magnesium-doped HAp exhibited excellent antibacterial activity compared to normal HAp (Bakhsheshi-Rad *et al.*, 2018; Díaz *et al.*, 2014; Y. Huang *et al.*, 2016). In this regard, natural HAp has better performance than a chemically synthesized one. Further investigation of such HAp coatings on implanted materials should focus on improving the precise coating and deposition techniques. The development of a cost-effective way to cover all the basic requirements of the implant coating seems like a dire need.

2.3.5 Research Gap

After the critical literature review regarding the synthesis and biomedical applications of biogenic sources-based nano-HAp, it is concluded that exploration of high-density HAp from animal biowastes is needed for investigation. In this regard, no comprehensive research on ostrich bone-based nano-HAp as a potential biomaterial has been carried out in terms of structural characteristics, acute toxicity tests and its application as a filler in a polymer composite scaffold for the purpose of biomedical applications.

CHAPTER 3

3. MATERIALS AND METHODS

3.1 Materials

3.1.1 Ostrich Bone

The hydroxyapatite used in this study was extracted from ostrich waste bone. 10 kg of bone sample was collected from the ostrich farmhouse at Gangolya-1, Rupendehi, Nepal (**Figure 23**).



Figure 23: Ostrich farmhouse visit in Gangolya-1, Rupendehi District, Nepal

3.1.2 Albino Wistar Rats

For the acute toxicity test, 11 healthy Albino Wistar rats (*Ratus norvegicus*), each approximately 10 weeks old and weighing 100 – 133 g (**Figure 24**), were brought from the animal breeding center, Department of Plant Resources (DPR), Ministry of Forest and Environment (MoFE), Thapathali, Kathmandu, Nepal on 2077/05/10.



Figure 24: Photograph of Albino Wistar rat used in an acute toxicity test

3.1.3 Chemicals, Solvents and Polymers

Different chemicals and polymers used for the extraction, segregation and fabrication of scaffolds incorporated with nano-HAp and VD3 are listed in **Table 9**. These materials were purchased from different suppliers as indicated in the table. All of them were analytical grade and used without further purification.

Table 9: List of chemicals and polymers used in the study

Chemicals and Polymers	Formula	Specifications/Information
Sodium hydroxide	NaOH	Merck, GmbH, Germany M _w = 40 g/mol, Purity = 99.9 %
Dimethyl ketone (Acetone)	(CH ₃) ₂ O	Merck, GmbH, Germany M _w = 58.08 g/mol, Purity ≥ 99 %
Triton X-100 (Octoxinol Octoxynol-10)	C ₁₆ H ₂₆ O ₂	Packard Co. Inc, USA M _w = 625 g/mol, Purity ≥ 99 %
Cyclohexane	C ₆ H ₁₂	Merck, GmbH, Germany M _w = 84.16 g/mol, Purity = 99.9 %
Cetyltrimethylammonium bromide (CTAB)	C ₁₉ H ₄₂ BrN	Merck, GmbH, Germany M _w = 364.45 g/mol, Purity ≥ 99 %
Tetradecyltrimethylammonium bromide (TTAB)	C ₁₇ H ₃₈ BrN	Merck, GmbH, Germany M _w = 336.39 g/mol, Purity ≥ 99 %
1-butanol	C ₄ H ₉ OH	Merck, GmbH, Germany M _w = 74.12 g/mol, Purity ≥ 99 %
Ethanol	C ₂ H ₅ OH	Merck, GmbH, Germany M _w = 46.07 g/mol, Purity = 99 %
2,2,2-trifluoro ethanol (TFE)	C ₂ H ₂ F ₃ OH	Sigma Aldrich Germany M _w = 100.00 g/mol, Purity ≥ 99 %
Ether (Diethyl ether)	(C ₂ H ₅) ₂ O	Merck, GmbH, Germany M _w = 74.00 g/mol, Purity ≥ 99 %
Phosphate buffer saline (PBS)	Cl ₂ H ₃ K ₂ Na ₃ O ₈ P ₂	Merck, GmbH, Germany, pH = 7.3 M _w = 411.04 g/mol, Purity ≥ 99 %
Tococalciferol (Vitamin D3) VD3, 5000 IU	C ₂₇ H ₄₄ O	Sigma Aldrich, USA M _w = 374.64 g/mol, Purity = 99 %
Normal saline solution	NaCl	Otsuka Pharmaceutical, India
Galantin (GEL), Type A	C ₁₀₂ H ₁₅₁ N ₃₁ O ₃₉	Nature works, USA, M _w = 300 Bloom
Polycaprolactone (PCL)	(C ₆ H ₁₀ O ₂) _n	Nature works, USA, M _w = 80 kDa
Poly (L- Lactic acid) (PLLA)	(C ₃ H ₄ O ₂) _n	Nature works, USA, M _w = 250 kDa

3.2 Methods

3.2.1 Research Plan

The schematic research plan of the materials and methods used for the synthesis of nano-HAp, its acute toxicity test, and the fabrication of nano-HAp-incorporated polymer composite scaffolds using the electrospinning method for biomedical applications is shown in **Figure 25**.

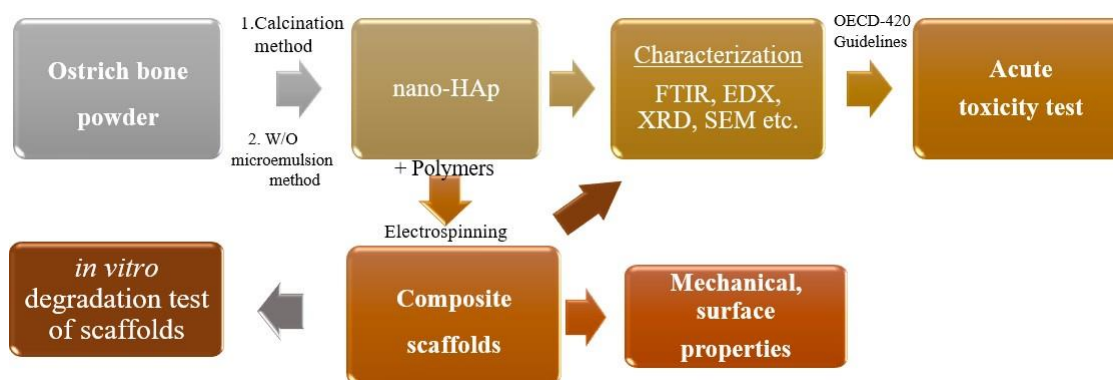


Figure 25: Schematic diagram of the research plan

3.2.1 HAp Preparation

For the extraction of HAp, the raw ostrich bone samples were cleaned to remove visible impurities using a sharp knife. It was cut to a size of 2 cm using a hacksaw and then converted into small pieces in an iron mortar (commonly called *Khal* in Nepali). These pieces were boiled for 4 h in a closed container for deproteinization. After that it was washed with acetone and dried in a hot air oven for 12 h at 120 °C to avoid shoot formation at the time of grinding. Finally, the dried pieces were powdered in a disc mill. The bone powder was then filtered through a mesh of 450 µm. The raw bone samples, their pieces and powder after grinding are shown in **Figure 25**.



Figure 26: Photographs of (a) raw bones, (b) its pieces and (c) bone powder after grinding

To remove the residual organic impurities, the bone powder was further subjected to alkaline hydrothermal hydrolysis using a 4M sodium hydroxide solution for 6 h at

250 °C. After pH neutralization through multiple washings with distilled water, it was dried for 3 h in a hot air oven at 80 °C. **Figure 27** shows the alkaline hydrothermal hydrolysis process for removing residual organic impurities from the bone powder.



Figure 27: Photograph of alkaline hydrothermal hydrolysis to remove impurities from bone powder

Finally, the clean and dried bone powder was calcined at 650 °C in an electric furnace with a heating rate of 5 °C/min for 6 h and cooled to obtain grayish-white bone ash. It was further calcined at 950 °C for another 6 h in similar conditions of electric furnace to obtain the HAp powder by following the procedure of Barakat *et al.* (2009) and Sobczak *et al.* (2009). Different step involved in the preparation of HAp from ostrich bone powder is shown in **Figure 28**.

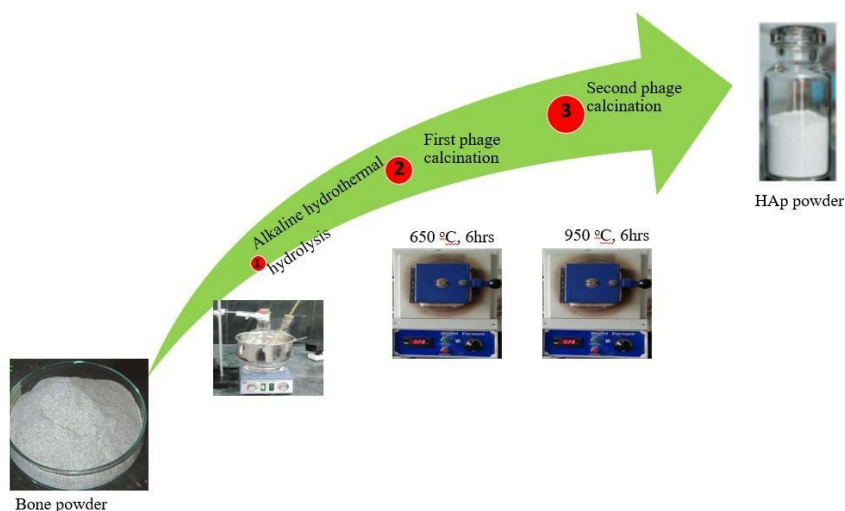


Figure 28: Photographs showing steps in the extraction of HAp from ostrich bone powder

3.2.2 Microemulsion Technique

The size of the HAp particles that are extracted from bone powder by calcination method is not fixed. It is varying in between a few μm to a few tenths of nm range. Therefore, to segregate the nano-sized HAp from the bulk of the particles, W/O

microemulsion technique was used. For this, 1:2 v/v ratios of double distilled water were used for the water phase and cyclohexane (C₆H₁₂) was used for the oil phase and then were mixed in a glass flask that contained 10 g of recalcined ash of bone powder which contains HAp (**Figure 29**) according to the protocol of Nga *et al.* (2014) and Collilla *et al.* (2018).

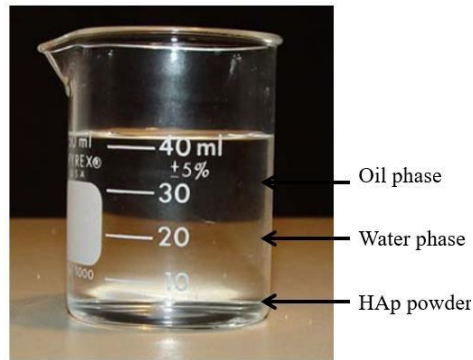


Figure 29: Photograph of the preparation of W/O microemulsion for segregation of nano-HAp from recalcined bone ash powder

The schematic flow chart of the W/O microemulsion technique used to segregate the nano-HAp from the aggregate bulk of the HAp particles in recalcined bone ash powder is shown in **Figure 29**.

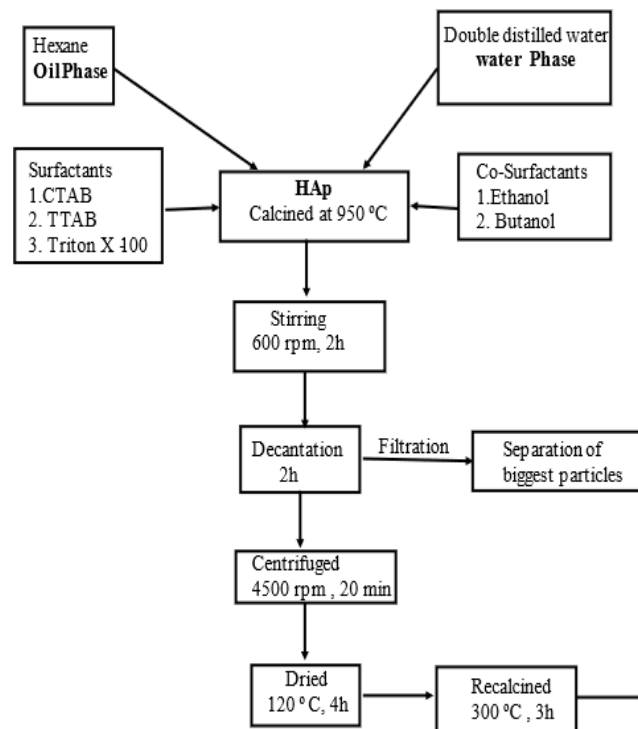


Figure 30: Flow chart of W/O microemulsion technique used to segregate the nano-HAp form the recalcined bone ash powder

According to the guidelines provided by Uson *et al.* (2004) and Bose *et al.* (2015) the ratios of mixing each of the individual components of the W/O microemulsion are shown in **Table 10** and the mixing volumes of water, oil, surfactants and cosurfactants for the preparation of the W/O microemulsion are shown in **Table 11**.

Table 10: Mixing by volume ratios of water, oil, surfactants and co-surfactants for the preparation of W/O microemulsion

Water	Oil	CTAB	TTAB	Triton X-100	Ethanol	1-butanol
1	2	1	1	2	1	1

To separate the nano-HAp from bulk of the particles the solution was agitated using a magnetic stirrer for 2 h at 600 rpm before being centrifuged for 20 min at 4500 rpm. After centrifugation the final yields of segregated nano-HAp were then oven-dried at 120 °C for 4 h and again recalcined by heating at 300 °C for another 3 h.

Table 11: Mixing volumes of water, oil surfactants and co-surfactants for the preparation of W/O microemulsion

Water phase	Oil phase	Surfactants			Co-surfactants	
		<i>Ionic</i>		<i>Nonionic</i>		
Double distilled water 50 mL	Cyclohexane 100 mL	CTAB (2%) 2 mL	TTAB (10 %) 2 mL	Triton X-100 (2 %) 4 mL	Ethanol 2 mL	1-butanol 2 mL

The coding of samples of bone powder and HAp for the study is listed in **Table 12**.

Table 12: List of samples used in the study

S. No.	Sample Code	Remarks
1.	RBP	Raw bone powder
2.	OB HAp	Ostrich bone-based hydroxyapatite obtained by heating the bone powder at 650 °C and 950 °C for 6h
3.	OB nano-HAp	Nano hydroxyapatite segregated using water in oil (W/O) microemulsion technique
4.	OB nano-HAp-GEL	Ostrich bone nano-hydroxyapatite blended in 5wt.-% gelatin solution

3.2.3 Preparation of Biomedical Scaffolds

a. Solution Preparation

For fabrication of scaffolds using electrospinning technique all polymer (10 wt.-% PCL, PLLA and GEL) and 10 wt.-% VD3 solutions were prepared separately in aTFE solvent at lab temperature (25 ± 1 °C). These solutions were mixed into 30:30:40 by volume ratios of PCL, PLLA and GEL in a magnetic stirrer by stirring at 500 rpm for 6 h to make the mixture uniform (**Figure 31**) and then rearing it for 24 h. Again, the same ratios of each polymer, as well as 50 μ L of VD3 solution, were blended separately at 500 rpm for 6 h before letting them settle again for 24 h.

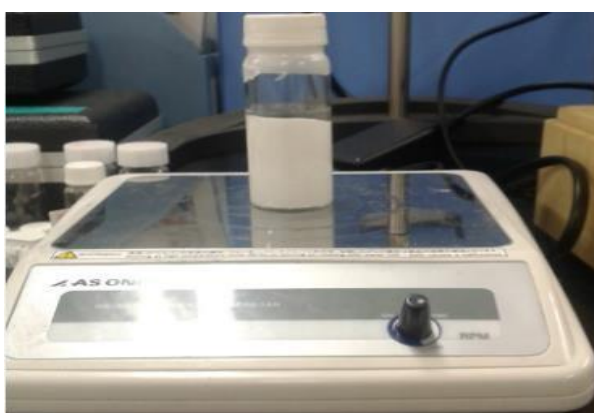


Figure 31: Blending of nano-HAp in VD3 and polymer composite solutions for the fabrication of scaffolds

The sample coding and all the required solutions for electrospinning were prepared according to **Table 14**. For better dispersion of the nano-HAp and VD3 in the polymer composite blends, the mixture solutions were again sonicated for 25 min before electrospinning.

Table 13: The volume of nano-HAp and VD3 blended in PCL, PLLA and GEL composite blends

Sample code	Blending by volume ratio of PCL, PLLA and GEL	Volume of VD3 (μ L)	Volume of nano-HAp (5 wt. %) in polymer blends
CB-1	30:30:40	0	0
CB-2	30:30:40	50	0
CB-3	30:30:40	50	2
CB-4	30:30:40	50	3
CB-5	30:30:40	50	6
CB-6	30:30:40	50	12

b. Electrospinning Setup

The scaffolds were fabricated using a horizontal electrospinning setup (**Figure 32**). The sample solutions CB-1 to CB-6 were loaded separately into a 5 mL capacity plastic syringe and that was connected to a 21G blunt needle (0.80 mm in diameter and 22mm in length) with a tip inner diameter of 0.21mm. The syringe was placed on a syringe pump (B. Braun Melsungen AG, Model 871801/6, Germany).

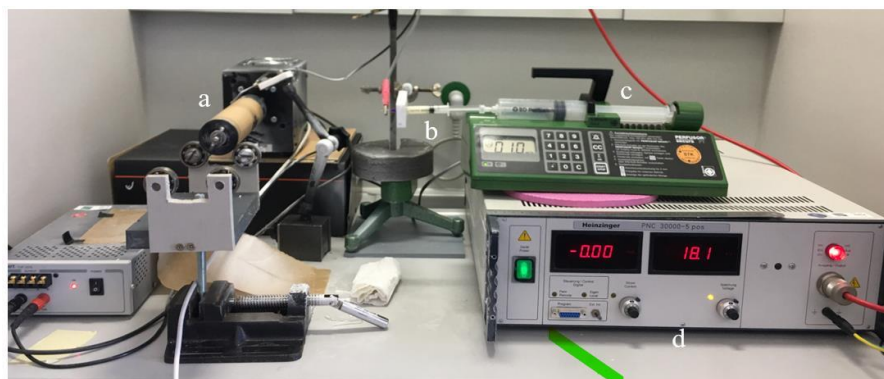


Figure 32: Instrumental setup for electrospinning of fibrous scaffold: (a) Rotating drum, (b) polymers solution in a syringe, (c) Pumping set, (d) DC power supply

The flow rate of the delivered solution was controlled at 1 mL/h through the syringe pump. A high-voltage (17–25 kV) DC power supply (Heinzinger Electronic GmbH, 83026 Rosenheim, Germany) was applied at the tip of the needle. The scaffolding fibers were collected in a rotating drum covered with aluminium foil. The distance between the tip of the needle tip and the collector was fixed at 17–20 cm according to the procedure of Sattary *et al.* (2019). All experiments were carried out at lab temperature (25 ± 1 °C) with a relative humidity of 30–50 % maintained within a closed experimental cupboard and the scaffolds were dried overnight at 37 °C and stored in a desiccator for complete dryness. The experimental conditions were kept constant for all sets of experiments.

3.3 Characterization Techniques

3.3.1 Fourier Transform Infrared (FTIR) Spectroscopy

FTIR is an instrumental analytical technique for the characterization of chemical compounds. It provides information about the chemical modification, new bond formation and chemical components of HAp. For analysis, a Shimadzu IRT racer-100 A217064 00746, Japan, FTIR spectrophotometer was used in an ATR transmission

mode in the mid-infrared range with a resolution of 4 cm⁻¹ and wavenumbers from 400 to 4000 cm⁻¹. It was also used with a resolution of 2 cm⁻¹ in the wavenumber range of 500-4500cm⁻¹ in the same transmission mode of the mid-infrared range for the analysis of different functional groups of used polymers such as; PCL, PLLA and GEL their modification, the effect of blending and their interaction with nano-HAp and VD3 in the scaffold fibers.

3.3.2 X-ray Diffraction (XRD)

The particle size and the degree of crystallinity of HAp powder before and after segregation was investigated by using the powder X-ray diffraction (XRD) method. The spectra were taken with a Bruker D2 Phaser (Germany) advanced X-ray diffractometer equipped with a monochromatic Cu-K α radiation source (=1.5406Å) and a running acceleration voltage of 40 kV and an emission current of 30 mA. The diffraction profiles were accumulated over a 2 θ range from 20° to 80° with an increment step measurement of 0.02° using the flat plane geometry. The acquisition time was set at 2.5° per minute for each scan. The crystallite size (D) of the particles in the powder was calculated by using the Debye-Scherrer **equation 4**:

$$D = \frac{k\lambda}{\beta \cos\theta} \quad (4)$$

Where k is the shape factor, λ is an X-ray wavelength, β is full width at half maxima (FWHM) and, θ is a Bragg's angle.

3.3.3 Scanning Electron Microscopy (SEM)

SEM (JEOL JSM 6490LA analytical scanning electron microscope, Japan) was used to examine the morphology of HAp powder before and after segregation using the W/O microemulsion technique. All of the samples were sputtered with gold before being analyzed by SEM at a 10 kV accelerating voltage. However, the morphology and allocation of the scaffolds' randomly oriented nanofibers (CB-1 to CB-6) before and after the tensile test were examined using an FEI Quanta 650 ESEM-FEG instrument operating at a 15 kV accelerating voltage. For this, the scaffold samples were cut into 10 mm by 10 mm pieces, attached to SEM stubs with double-sided conductive adhesive tabs and coated with a thin layer of carbon for conductivity using a sputter coater (Scan Coat 6 sputter from Edwards) in an inert atmosphere before imaging. Imaging was carried out at 15 kV and 1 mA current for 3 minutes to increase the conductivity. To investigate the fiber morphology of each scaffold, at

least five different positions were tested. The average fiber diameter of the scaffold was measured using the digital image processing method and the Fiji-Win 64 image J software.

3.3.4 Transmission Electron Microscopy (TEM)

The morphology of the electrospun polymeric composite fibers was also investigated by conventional transmission electron microscopy (TEM) (JEOL 200CX, Germany) operated with an acceleration voltage of 200 kV. For this, the scaffold samples (CB-1 to CB-6, **Table 15**) were collected by directly depositing electrospun fibers onto Cu-grids of 3 mm in diameter. To know more about the phases of each polymer and their affinity to nano-HAp and VD3, the Cu-grid was coated with ruthenium tetra oxide (RuO₄) vapour in a sealed chamber for a short period of time (3 min) to improve contrast during the TEM imaging.

3.3.5 Energy Dispersive X-ray (EDX) Spectroscopy

The estimation of calcium to phosphorous (Ca/P) molar ratio and elemental composition of HAp powder was analyzed by using an energy-dispersive X-ray (Shimadzu, EDX-800, Japan).

3.3.6 Zeta Potential Measurement

The zeta potential of nano-HAp was investigated to know the surface charge (+ve/-ve). For this, a Malvern Zetasizer (nano series, Nano -ZS, UK) was used. A 633 nm red laser beam at room temperature and the neutral pH of the dispersion medium was also used. Moreover, for the measurement, the HAp suspensions were made in a 5 wt.-% gelatine solution in a distilled water and then injected into the capillary cell (DTS1060) of the zeta-sizer.

3.3.7 Optical Microscopy (OM)

The morphology of scaffold fibers CB-1 to CB-6 after *in vitro* degradation test was observed by laser optical microscopy (VE 7800 from Keyence, Japan) at room temperature.

3.3.8 Thermogravimetric Analysis (TGA)

A thermogravimetric analysis (TGA) was done to determine the mass loss pattern of HAp during heating. For this, a TGA analyzer, model Q600, USA, was used. This

analyzer gives the exact mass loss pattern of the sample with increasing temperature in an inert atmosphere. The analysis was carried out between 30 °C to 1000 °C with a continuous flow of nitrogen gas and a heating rate of 10 °C/min.

3.3.9 Tensile Testing

The tensile test was performed to examine the stress-strain behaviour of nano-HAp incorporated scaffolds. This behaviour was measured using a uniaxial tensile testing machine Z2.5 (ZwickRoell GmbH & Co KG, Ulm, Germany) (load cell: 500 N, traverse speed: 2 mm/min up to 20 % strain and 10 mm/min elsewhere) according to the standard International Organization for Standardization (ISO) 527-3.

For this, the scaffold samples were cut into 20 mm by 10 mm pieces to provide a 10 mm test gauge length and mounted on rectangular graph paper frames with the outer dimensions of the external frame being: 40 mm × 40 mm and an inner rectangular cut out at 20 mm × 10 mm as shown in **Figure 33**.

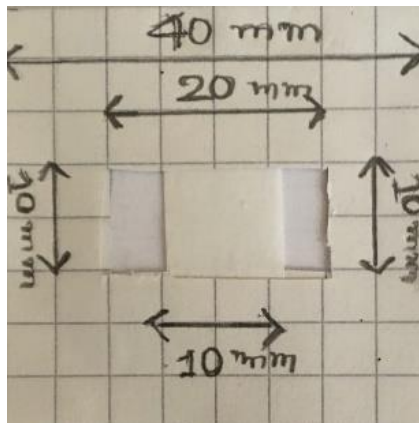


Figure 33: Photograph of the tensile test sample of the electrospun scaffold mounted on the rectangular frame of graph paper

The tested scaffolds have dimensions of $10 \times 10 \times 0.03 \text{ mm}^3$ (length, width and thickness) and are attached to the frame with double-sided adhesive tape. The frames were then set into the instrument and the sidewalls of the frame were cut for testing. At least five samples were tested for each scaffold and the force-displacement data was collected. The stress-strain was calculated from the force-displacement curve. The values of the tensile strength (Ultimate Tensile Stress, UTS) and strain at break were calculated according to ISO 527-3. Unlike ISO 527-3, the elastic modulus is defined as the maximum positive slope of the stress-strain curve.

3.3.10 Wettability/Hydrophilicity Test

The wettability or hydrophilicity test of the nano-HAp and VD3 incorporated scaffold is an important consideration that helps to evaluate the possible effect of a scaffold material on osteoblast cell adhesion, proliferation and differentiation. For this, the scaffolds were cut into 2 cm×4 cm dimensions and held in position by a glass slide. The static value of the water drop contact angle (WDCA) on the surface of the scaffolds was measured in a humidity chamber with the Contact Angle Unit OCA15+, Data Physics Instruments, (Filderstadt, Germany/Contact angle meter, Model: Phoenix series, SEO Co., Ltd., Korea). The test scaffolds sample and water dispensing needle of the device were enclosed in a chamber containing Petri dishes with a wet salt solution of sodium hydrogen sulphate (ROTH, Germany) to control the humidity of the chamber (relative humidity of about 50% ±1). At least three measurements on different sides of scaffold locations were tested and the mean values were recorded.

3.3.11 *in vitro* Degradation Test

For the *in vitro* degradation test, the scaffolds CB-1 to CB-6 (listed in **Table 13**) were cut into squares with dimensions of 1×2 cm, weighted (3-6 mg) and placed in the 16-well tissue culture tubes. In each tube, 4 mL of phosphate-buffered saline (PBS; 2.7 mM KCl, 137 mM NaCl, 1.4 mM KH₂PO₄, 4.3 mM Na₂HPO₄ dihydrate, pH 7.4) was added.

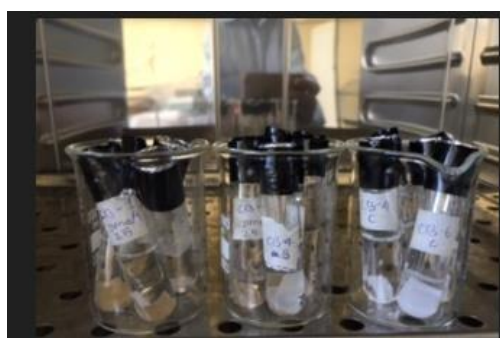


Figure 34: Photograph of incubation of the scaffolds at 37 °C for simulation in a biological environment for 7 weeks

The scaffolds were then incubated at 37 °C to simulate the biological environment for 7 weeks (**Figure 34**). The PBS solution was changed every 7 days and the samples

were taken out every 1, 2, 3, 4, 5, 6 and 7 weeks and thoroughly washed with distilled water, then dried to a steady weight.

The weight loss of these scaffolds was measured using a precise electric balance. The weight loss percentage of scaffolds was calculated by using the **equation 5** as reported by Augustine *et al.* (2014), Naeem *et al.* (2016) and Sattary *et al.* (2018). Where W_o is the initial weight of the scaffold and W_t is the dried weight of the scaffold after incubation.

$$\text{Weight loss \%} = \frac{W_o - W_t}{W_t} \times 100 \quad (5)$$

3.4 Acute Toxicity Test

3.4.1 Preparation of Oral Gavage Solutions

The HAp is a CaP-based ceramic compound that is insoluble in water and alkali solution and its nanoparticles show poor dispersion in water (Dorozhkin, 2016). However, it is soluble only in dilute mineral acids having a pH of less than 3.0.

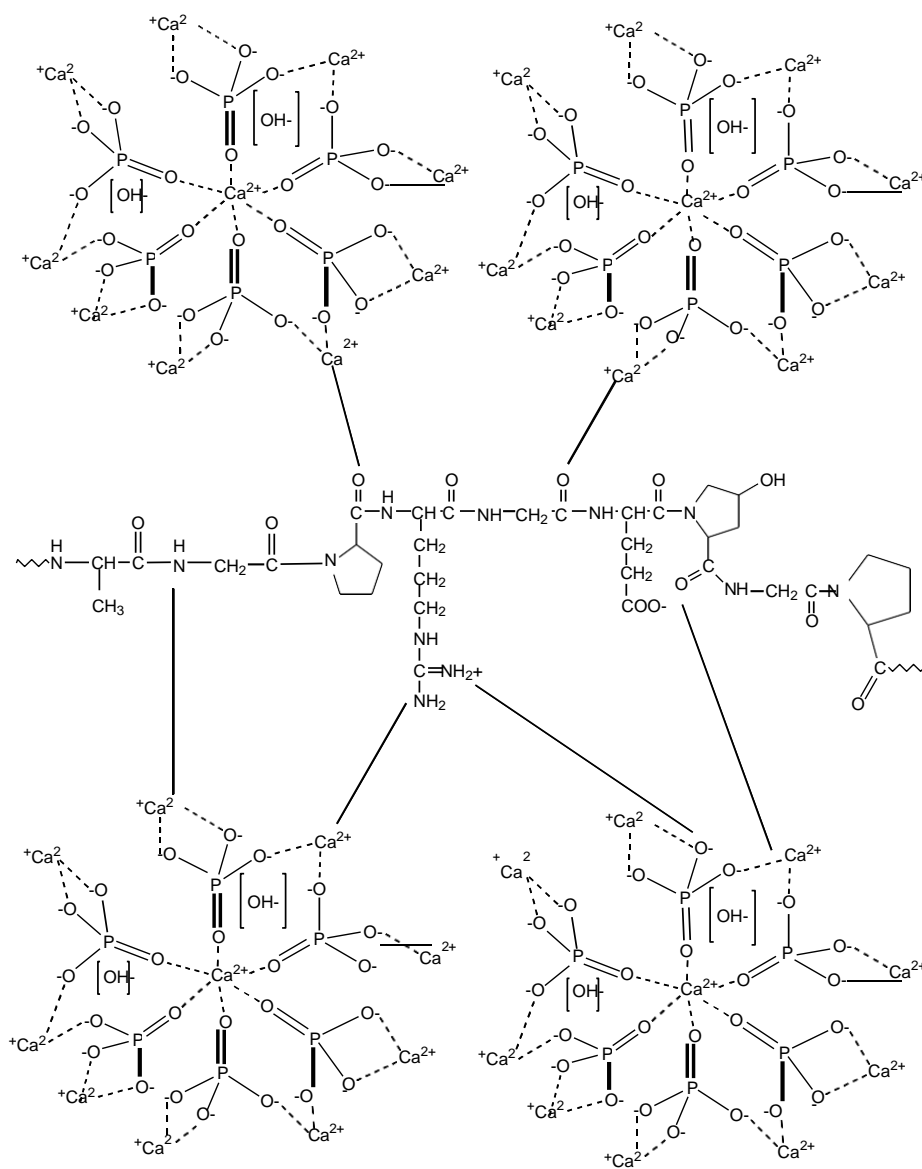


Figure 35: Crosslinking between gelatin and nano-HAP

It can be dispersed in water until the existence of mechanical force which is created by agitation of the solution unless starts to segregate after the discontinuation of this force. The nano-particle of HAp show stable dispersion in gelatin solution due to its hydrophilic nature and crosslinking ability (**Figure 35**). Gelatin can bind the nano-HAP molecules through crosslinking bonds and mitigate the problems associated with segregation in an aqueous medium (Kim *et al.*, 2005). For this 15 wt.-% of gelatin solution and 300 mg of nano-HAP as per the body weight of rats were blended at 500 rpm for 6 h. The suspension was then sonicated for 15 min before oral gavage.

3.4.2 Experimental Animals

According to Organization for Economic Co-operation and Development-420 (OECD-420) guidelines 2005, for the acute toxicity test, 11 healthy Albino Wistar rats (*Ratus norvegicus*), each approximately 10 weeks old and weighing 100-133 g were purchased from the animal breeding center, Department of Plant Resources (DPR), Ministry of Forest and Environment (MoFE), Thapathali, Kathmandu.

Research models are dosed in a stepwise procedure using fixed dose method. The initial dose level was selected based on a sighting study, as the dose is expected to produce some signs of toxicity without causing severe toxic effects or mortality. All rats were treated in compliance with Nepal's ethical guidelines for animal care and utilization in health research (Pahari *et al.*, 2005). The moral approval for the toxicity test was taken from the Nepal Veterinary Council (NVC) (Ref. No. Ethical.17/2077/78).

The random selection method was used for the selection and grouping of rats and they were then kept in clean polypropylene cages for 7 days before being gavaged the nano-HAp gelatin suspension to allow them to acclimate to the laboratory environment. The temperature and the relative humidity of the room where the rats were kept were maintained at 23-25 °C and 50-65%, respectively, throughout the experiment. Artificial lighting was provided with 12 h light and 12 h dark cycles according to animal handling guidelines. Each rat was handled with proper attention and care, without causing any physical stress. The rats were kept on a clean paddy husk bed that was replaced twice a week and fed with a commercially available standard diet and distilled water. Each animal was marked with a color for identification.

3.4.3 Toxicity Test

The toxicity tests were conducted using a fixed-dose method as prescribed by the OECD-420 guideline that provides information about the substance under investigation according to the principles of the Globally Harmonized System (GHS). The guideline recommends the tests on single-sex animals whereby female rats have been considered more sensitive than males. For the tests, rats were divided into 3 groups (**Table 12**) and orally gavaged with 10 mL of the nano-HAp-GEL suspension per kg body weight of each rat.

Table 14: Grouping of rats and their numbers for acute toxicity test of nano-HAp-GEL suspension

Group I	Group II	Group III
Vehicle	Medium dose (300 mg/kg)	High dose (2000 mg/kg)
3	3	5

According to guidelines, the vehicle group was gavaged with a 15 wt. % plain gelatin solution only. Group II, was given 300 mg/kg of the nano-HAp gelatin suspension and group III was gavaged with a dose of 2000 mg/kg (high dose) of body weight. The starting dosage was selected at 300 mg/kg body weight due to the lack of preclinical toxicity evidence of the nano-HAp in gelatin suspension. Before oral gavage, the rats were made to fast overnight, but distilled water was given sufficiently.

Summary of the Experimental Works

The materials, tools, and techniques used in the experimental works along with the information obtained are summarized in **Figure 35** as well as in **Tables 15** and **16**.

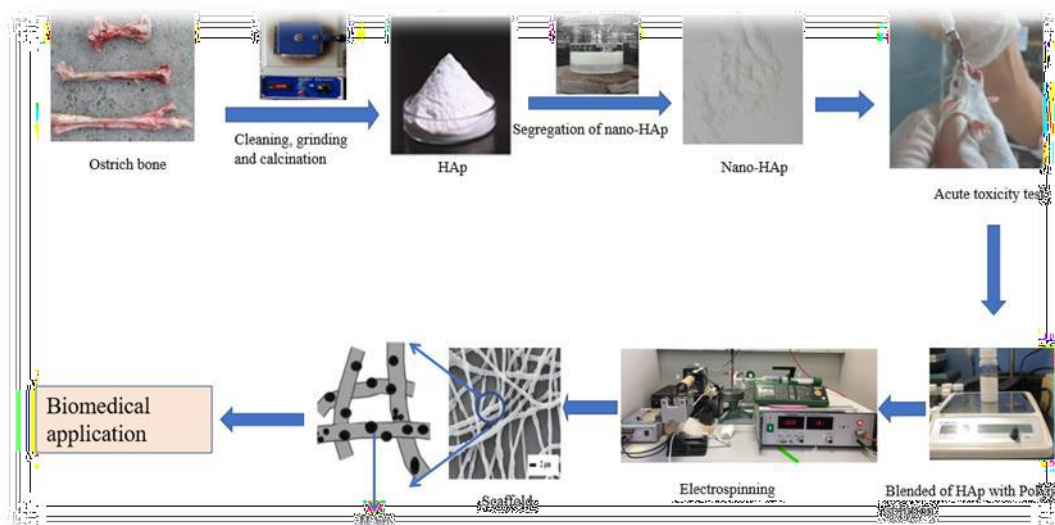











Figure 36: Diagrammatic representation of the summary of the experimental works


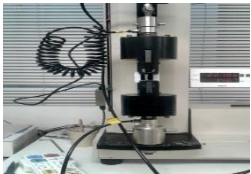

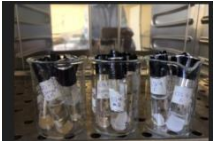
Table 15: Summary of tools and techniques used for the sample preparation for various purposes

S. No.	Tools and techniques used	Information gained/ <i>Work station</i>
1.	 <p>Alkaline hydrothermal hydrolysis for 6 h at 250 °C</p>	<p>Removal of bone related organic impurities from bone powder. <i>Research Center for Applied Science and Technology (RECAST), TU, Nepal</i></p>
2.	 <p>Two steps (6 h 650 °C and 950 °C) thermal decomposition of bone powder in a Muffle furnace</p>	<p>Preparation of HAp from bone powder. <i>Research Center for Applied Science and Technology (RECAST), TU, Nepal</i></p>
3.	 <p>W/O microemulsion technique</p>	<p>Segregated nano-HAp from aggregate particles. <i>Research Center for Applied Science and Technology (RECAST), TU, Nepal</i></p>
4.	<p>Organization for Economic Co-operation and Development- 420 (OECD-420) guidelines</p> 	<p>Acute toxicity test of nano-HAp in Albino Wister rats. <i>GandakiMedicalCollage (GMC), Pokhara, Nepal</i></p>
5.		<p>Fabrication of nano-HAp loaded polymer composite scaffolds for biomedical applications. <i>Polymer Synthesis and Modification (PSM), Merseburg, Germany</i></p>

	Electrospinning technique for fabrication of nano-HAp blended polymer composite scaffolds	
--	-------------------------------------------------------------------------------------------	--

Table 16: Summary of analytical tools/techniques used for the characterization of HAp and scaffolds

Tools and techniques	Studied properties	Samplepreparation/Work station
 Thermogravimetric analysis (TGA)	Mass loss pattern of HAp and thermostability	~0.5 g second phase thermally decomposed HAp powder in a TGA experimental weighting pan. <i>Kyoto Institute of Technology (KIT), Japan</i>
 Fourier Transform Infrared (FTIR) Spectroscopy	Types of bonding interaction of different inorganic and organic group in HAp, on electrospun scaffold molecular structure of polymers and their physical and chemical interaction with HAp and VD3	A pinch of second phase thermally decomposed HAp used. For scaffold a 10 mm ×10 mm sample of CB-1to CB-6 directly used for analysis. <i>Polymer Synthesis and Modification (PSM), Merseburg, Germany</i>
 X-ray Diffraction (XRD)	The particle size and crystalline nature of HAp powder before and after segregation	A pinch of second phase thermally decomposed HAp powder and segregated sample. <i>Nepal Academy of Science and Technoligy (NAST), Nepal</i>
 Electron Microscopy (SEM/TEM/OM)	Structure, morphology and agglomeration of HAp. Morphology and fiber diameter of scaffolds before and after tensile testing	Gold sputtering for SEM analysis of HAp before and after segregation. <i>Fraunhofer institute, Germany</i> For TEM analysis the scaffold samples directly deposited onto Cu-grid. <i>Fraunhofer institute, Germany</i>
 Estimation of calcium and phosphorous ratio and elemental composition of HAp	Estimation of calcium and phosphorous ratio and elemental composition of HAp	A pinch of thermally decomposed HAp powder. <i>Polymer Synthesis and Modification (PSM), Merseburg, Germany</i>

Energy Dispersive X-ray (EDX)		
 <p>Malvern Zetasizer (nano series, Nano-ZS, UK)</p>	Surface charge on HAp	<p>Nano-HAp suspension in 5 wt.-% gelatins.</p> <p><i>University of Siegen, Germany</i></p>
 <p>Tensile testing machine</p>	The stress-strain behaviour of the OB nano-HAp incorporated polymer composite scaffolds	<p>The scaffolds prepared for testing have dimensions of $10 \times 10 \times 0.03$ mm attached to the frame with double-sided adhesive tape.</p> <p><i>Polymer Synthesis and Modification (PSM), Merseburg, Germany</i></p>
 <p>Contact angle measurement</p>	Hydrophilicity test of scaffolds	<p>The smooth surface the of scaffold glued onto the glass slide and air dried.</p> <p><i>Fraunhofer institute, Germany</i></p>
 <p>Incubator for <i>in vitro</i> degradation test of scaffolds</p>	<i>in vitro</i> biodegradation of scaffolds in PBS solution	<p>The scaffold samples cut into squares with dimensions of $1\text{cm} \times 2\text{cm}$, weighted (3-6 mg) and placed in 16-well tissue culture plates.</p> <p><i>Polymer Synthesis and Modification (PSM), Merseburg, Germany</i></p>

CHAPTER 4

4. RESULTS AND DISCUSSION

This chapter discusses the results of the experimental works which are divided into four sections: (1) nano-HAp preparation and characterization, (2) acute toxicity test in Albino Wistar rats by following the OECD guidelines-420, (3) fabrication and characterization of polymers and VD3 composite scaffolds that integrate nano-HAp as a filler using electrospinning technique and (4) analyzing the *in vitro* degradation test of the scaffolds in PBS solution.

4.1 Nano-HAp Preparation and Characterization

This work emphasizes the extraction of HAp from waste ostrich bone using alkaline hydrothermal hydrolysis and the two-step thermal decomposition method. The nano-HAp is segregated from the bulk particles by applying the W/O microemulsion technique and then subjected to characterization using various analytical tools and techniques. In addition, this section first introduces the basic physicochemical parameters of HAp and then discusses the chemical, structural and morphological results obtained by using spectroscopic, microscopic and thermally characterized devices.

4.1.1 Physicochemical Parameters of HAp

HAp is a calcium phosphate-related ceramic compound with the formula $\text{Ca}_5(\text{PO}_4)_3(\text{OH})_1$. However, it is generally written as $\text{Ca}_{10}(\text{PO}_4)_6(\text{OH})_2$ to indicate the crystal unit cell of two entities. It is also a hydroxyl-end member of the complex apatite group in which the hydroxy (OH^-) group can be replaced by fluoride (F^-), chloride (Cl^-), or carbonate (CO_3^{2-}) groups. It crystallizes in the hexagonal crystal system. It has a specific gravity of 3.08 g/cc and a Mohs hardness scale of 5. The chemically synthesized HAp is generally white. However, the colour might be different depending on the fluoride, chloride, or carbonate substitution instead of the hydroxy group. The biosource-based HAp has a generally brown, yellow, or green coloration due to its nonstoichiometric nature.

4.1.2 Structural Characterization

This section of the study discussed the characterized results of FTIR, XRD, EDX and SEM analysis of HAp.

The FTIR spectrum of the raw bone powder and after two-steps of thermal decomposition/calcination is shown in **Figures 37 and 38** respectively. The spectra of bone powder show a series of bands in the mid-infrared ($4000\text{--}500\text{ cm}^{-1}$) region. Due to the change in the molecular environment of the bone powder, there is a shift in the intensities and positions of their corresponding absorption bands (Khoo *et al.*, 2015). In spectra, the broad mixed band in the range of $3853.77\text{ cm}^{-1}\text{--}3564.45\text{ cm}^{-1}$ was attributed to the volatile impurities and trace amounts of water molecules incorporated into the bone powder. The 6 h thermal decomposition at low ($650\text{ }^{\circ}\text{C}$) and high ($950\text{ }^{\circ}\text{C}$) temperature helps to eliminate most of these impurities from the bone powder. The hydroxyl (OH^-) band of HAp at 3568 cm^{-1} is not visible due to the overlapping of some bands of impurities or by their masking effect over the bands of HAp as reported by Rana *et al.* (2017). The spectral bands associated with the amide groups of proteins and collagens of bone powder in the range of 1315.45 cm^{-1} , 1338.59 cm^{-1} , 1504 cm^{-1} and 1651 cm^{-1} are evidently visible in the spectrum of the raw bone powder (**Figure 37**). However, these bands are not visible in the spectrum of bone powder calcined at $950\text{ }^{\circ}\text{C}$ for 6 h due to the elimination of organic moieties at the time of cleaning and alkaline hydrothermal hydrolysis (Kim *et al.*, 2014). The band at 2360.87 cm^{-1} with a shoulder at 2337.72 cm^{-1} might be credited by free carbon dioxide as reported by Rana *et al.*, (2017). Similarly, a strong band at 999.13 cm^{-1} is associated with the P–O stretching vibration of the phosphate (PO_4^{3-}) group (Shavandi *et al.*, 2015). A small band at 871.82 cm^{-1} is associated with the out-of-plane bending mode of a carbonate group (CO_3^{2-}) (Nga *et al.*, 2014) and a small band at 667.37 cm^{-1} is associated with the bending vibration of a hydroxyl group (OH^-) of HAp. Khoo *et al.* (2015) suggested similar types of findings in the bone powder extracted from the bovine bone using the calcination method.

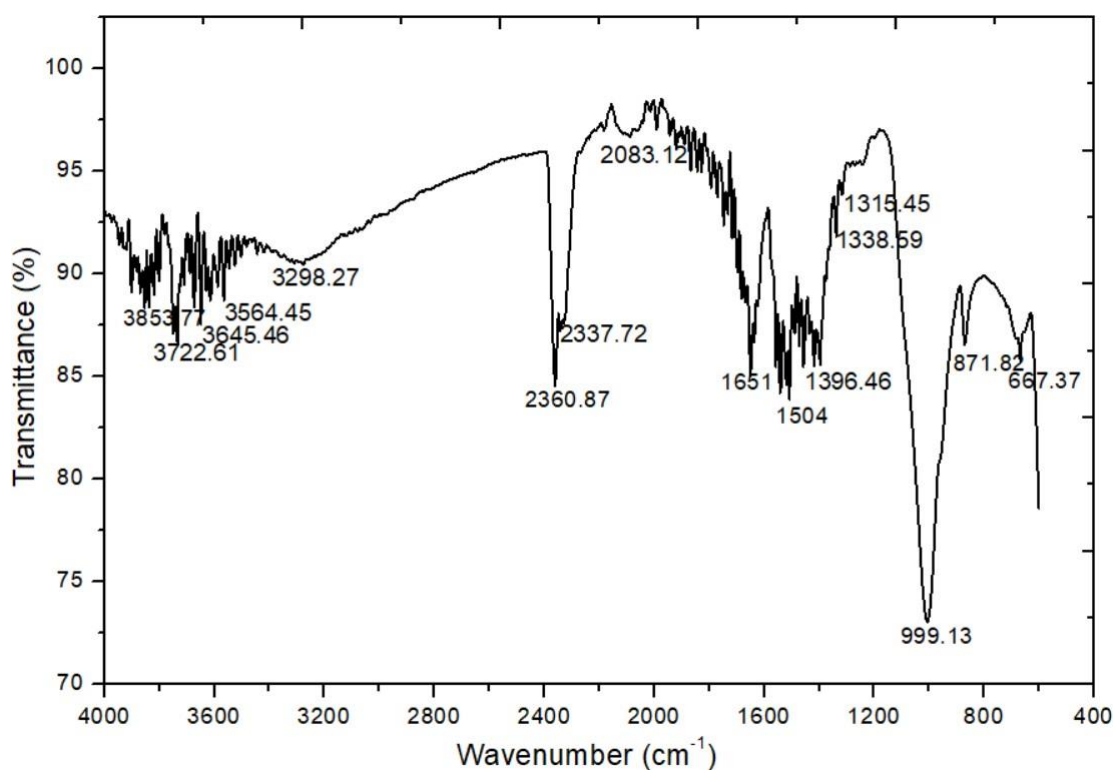


Figure 37: FTIR spectra of raw ostrich bone powder

The spectrum of the bovine bone powder as reported by Barakat *et al.* (2008), Khoo *et al.* (2015) and Sobacsak *et al.* (2009) shows the presence of major inorganic components such as phosphate (PO_4^{3-}), hydroxyl (OH^-) and carbonate (CO_3^{2-}) groups and organic components such as amide-I groups from the protein and collagen constituents of the bone powder in the spectral range of $4000\text{-}500\text{ cm}^{-1}$. In this study, most of the organic moieties were disappeared after first phase thermal decomposition at $650\text{ }^\circ\text{C}$ for 6 h and subsequently $950\text{ }^\circ\text{C}$ for another 6 h heating helped to break the cross-linking of organic moieties with major functional groups of HAp. The spectral bands 1315.45 cm^{-1} , 1338.59 cm^{-1} , 1396.46 cm^{-1} , 1504.0 cm^{-1} and 1651.0 cm^{-1} associated with the amide-I groups of proteins and collagen which are observed in the spectrum of the raw bone powder was totally disappeared after calcination.

The FTIR spectra of HAp obtained after calcinating at $950\text{ }^\circ\text{C}$ for another 6 h (**Figure 38**) expose the presence of major phosphate (PO_4^{3-}), carbonate (CO_3^{2-}) and hydroxyl (OH^-) groups of HAp. The results show that the thermal decomposition applied here was satisfactory for removing organic moieties from the bone powder. There were no absorption bands related to carbon-hydrogen, C-H (1396 cm^{-1}) and nitrogen-

hydrogen, N-H (1580 cm^{-1}), bonds were found in the spectrum of HAp after the second-phase thermal decomposition.

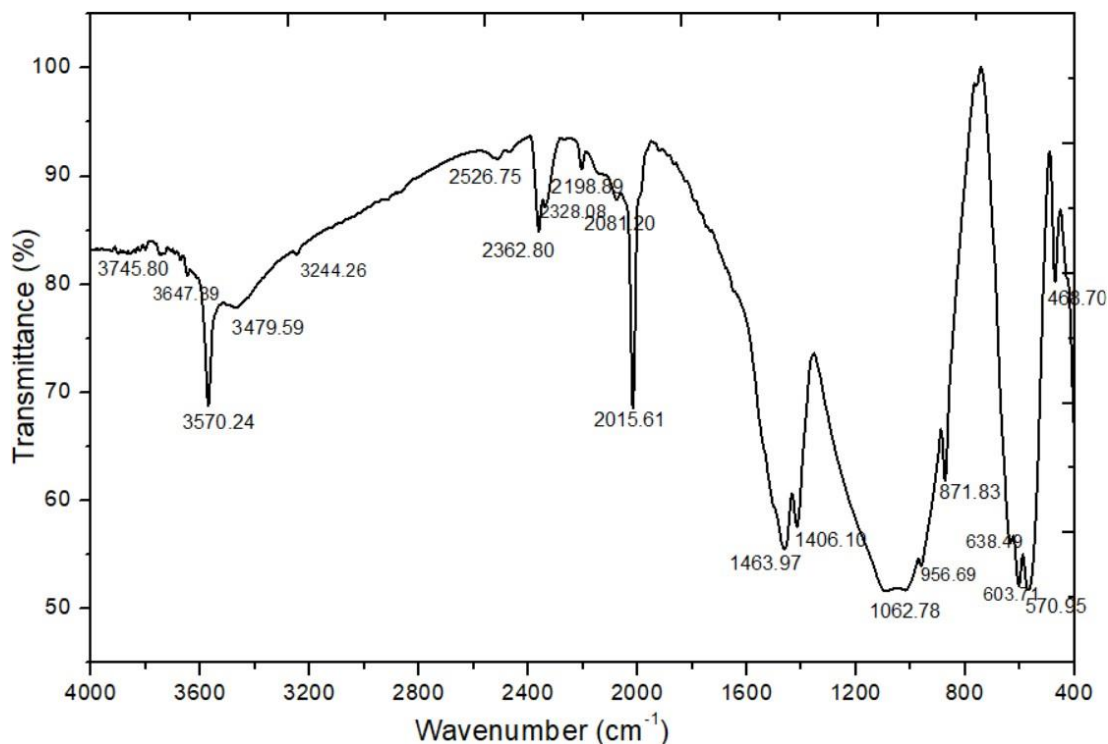


Figure 38: FTIR spectra of HAp calcined at $950\text{ }^{\circ}\text{C}$ for 6 h

Therefore, all these bands observed in the spectra of **Figure 37** are associated with the inorganic components of bone minerals. One strong and relatively broad band at 1062.78 cm^{-1} , two relatively strong and sharp bands at 570.95 cm^{-1} and 603.71 cm^{-1} and another band at 956.69 cm^{-1} appeared due to the presence of the phosphate (PO_4^{3-}) group of HAp. Bahrololoom *et al.* (2009) observed similar types of two bands in the bovine cortical bone ash at 603 cm^{-1} and 1051 cm^{-1} due to the presence of the PO_4^{3-} group. Similarly, the bands at 871.83 cm^{-1} , 1406.10 cm^{-1} and 1463.97 cm^{-1} respectively are associated with the brushite (CaHPO_4) and carbonate (CO_3^{2-}) groups (Khoo *et al.*, 2015). Moreover, in the bone-based HAp, the carbonate group is competitively substitute at two sites: the hydroxyl site and the phosphate site of the HAp crystal lattice, giving A-type and B-type carbonate-substituted HAp, respectively. These two types of substitution can occur simultaneously, resulting in a mixed AB-type substitution that constitutes the mineral part of the bone (Bano *et al.*, 2019). As a result, the peak position of carbonate in the spectra depends on whether the carbonate is substituted by the OH^- or the PO_4^{3-} groups on the HAp lattice. There is also relative broad band at 3570.24 cm^{-1} which is attributed to the

OH group of HAp independently. The spectral bands of amide-I groups of proteins and collagen, as mentioned above, are not visible in this spectrum because of thermal decomposition of bone powder at 950 °C for 6 h heating.

From these results, it can be concluded that the spectrum of raw bone powder before and after calcination shows a series of bands in the mid-infrared region due to changes in the molecular environment. The hydroxyl band of HAp at 3570.24 cm⁻¹ is not visible in the spectrum of HAp due to the masking effect of organic moieties. The spectra of HAp calcinated at 950 °C for 6h revealed the presence of major phosphate (PO₄³⁻), carbonate (CO₃²⁻) and hydroxyl (OH⁻) groups in HAp. The thermal decomposition applied in this study was satisfactory for removing organic moieties from the bone powder, with no absorption bands related to carbon-hydrogen and nitrogen-hydrogen

bonds. The carbonate (CO₃²⁻) group in bone source related HAp can substitute at two sites, resulting in A-type and B-type carbonate-substituted HAp.

The elemental composition of the HAp (obtained from the bone ash calcined at 950 °C for 6 h) was investigated by Energy Dispersive X-ray (EDX) spectroscopy. The spectra are presented in **Figure 39**. This spectrum consists primarily the atoms of calcium (Ca), phosphorus (P) and oxygen (O), apart from other traces of elements. Joscheki *et al.* (2000) reported that animal bone-derived HAp has chiefly trace amounts of aluminium, iron, magnesium, potassium, silica, sodium, vanadium and zinc despite of the fundamental elements. The results of this study also corelated with Joscheki *et al.* The calcium to phosphorous (Ca/P) molar ratio of HAp was calculated from the elemental peak intensities of Ca and P found approximately 1.78. This ratio lies within in a range of 1.50 -1.85 which is the range of nonstoichiometric HAp.

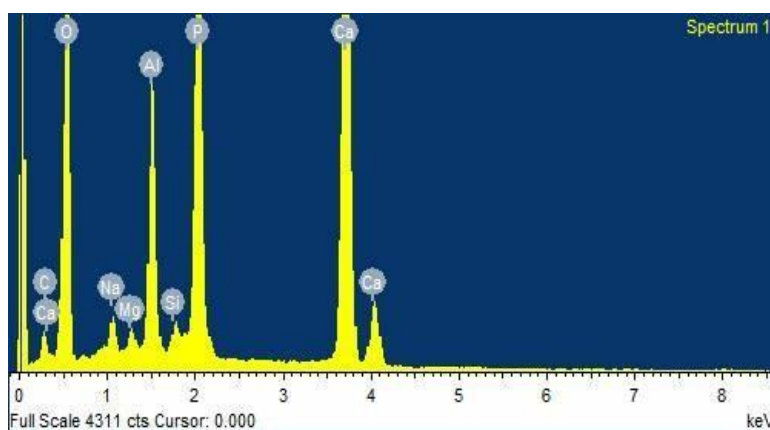


Figure 39: EDX spectra of HAp obtained from the ostrich bone ash calcined at 950 °C for 6 h

This value of Ca/P molar ratio deviates slightly from the standard value (1.67) of the stoichiometric HAp, due to presence of other elements as discussed above. Similar types of finding also reported by Ramesh *et al.* (2018) and Yoganand *et al.* (2011).

Table 17: Major and trace elements found in ostrich bone HAp

Basic elements	Trace elements
Calcium (Ca)	Carbon (C)
Phosphorous (P)	Sodium (Na)
Oxygen (O)	Magnesium (Mg)
	Aluminum (Al)
	Silicon (Si)

Therefore, from the EDX results, it can be concluded that the elemental composition of HAp extracted from ostrich bone consists primarily of calcium, phosphorus and oxygen, with trace amounts of carbon, sodium, magnesium, aluminium and silicon. The average Ca/P molar ratios of HAp were found (1.87) which is found within a range of 1.5–1.88.

4.1.3 Morphological Characterization

The morphological analysis of the bone powder heated at 650 °C for 6h and 950 °C for another 6h was investigated by X-ray diffraction (XRD) and scanning electron microscopy. The results of XRD analysis of samples provided the information about the size and the crystalline state of HAp. The SEM electron micrographs show morphology, particle shape and size as well as overall agglomeration of HAp.

The X-ray diffraction profiles of the HAp before and after segregation using the W/O microemulsion technique are shown in **Figure 40**. The profile shows the poor crystalline nature of HAp point d in **Figure 40** in the bone powder before thermal decomposition. The phase becomes quite clear compared to the profile of raw bone powder on first-phase calcination at 650 °C for 6 h without decomposition into any other phase of the calcium phosphate.

Although the decomposition of HAp was not detected in the second phase of thermal decomposition point b in **Figure 40** (i.e., heating at 950 °C for 6 h) dehydroxylation might take place after reheating the segregated HAp at 300 °C for 3 h. As a result, the peak position of HAp shifted to a higher value of 2 θ compared to the first and second phases of calcinated HAp, as shown in point a in **Figure 40**. The average particle size

of nano-HAp calculated by using Debye Scherer's equation before and after segregation appeared in the range from 36.44 nm to 19.23 nm, which shows that the W/O microemulsion technique used in this study is effective in segregating of nano-HAp from the bulk of the particles.

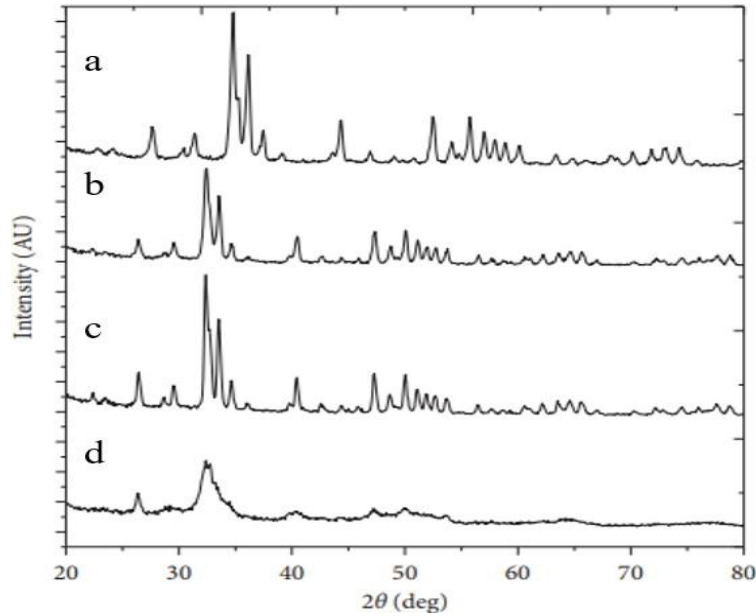


Figure 40: XRD patterns of (a) the segregated HAp using W/O microemulsion technique, (b) HAp recalcination at 950 °C for 6 h, (c) HAp calcined at 650 °C for 6 h and (d) the bone powder

The phase analysis of the segregated nano-HAp has been compared with the International Centre for Diffraction Data (ICDD) standard of HAp, PDF card no. 00-009-0432 which shows that the major diffraction peaks at 2θ values of 32.026° , 33.165° , 32.424° , 49.722° , 46.954° and 34.271° corresponding to the (211), (300), (112), (213), (222) and (202) Miller planes are in good agreement with the ICDD standard. Little deviation of these peaks from standard values may be due to the existence of a small number of foreign elements in an ionic form other than calcium, oxygen and phosphorous (e.g., Na^+ , K^+ , Zn^{2+} , Mg^{2+} , Al^{3+} and Sr^{2+}) (Bano *et al.*, 2019). **Table 18** shows the comparative value of diffraction profiles of prominent XRD peak position, d-spacing and relative intensity that correspond to the planes (211), (300), (112), (213), (222) and (202) of standard and segregated HAp, which confirms the matching of the XRD profiles of HAp with the diffraction peaks obtained with d-spacing of 2.79, 2.76 and 2.61 and so on. This analysis is in good agreement with the results that have been reported by Rana *et al.* (2017).

Table 18: Comparison of phase analysis of segregated ostrich bone HAp with ICDD file no. 00-09-0432

Miller indices (h, k, l)	d-spacing (Å)		2θ value (°)		Relative intensity	
	Standard	Segregated	Standard	Segregated	Standard	Segregated
211	2.79685	2.79467	31.973	34.7850	100.0	100.0
300	2.69969	2.79126	33.157	33.1654	54.3	65.4
112	2.77146	2.76131	32.275	32.4240	43.7	49.6
213	1.83574	1.83373	49.620	49.7223	32.3	35.3
222	1.93385	1.93515	46.947	46.9548	24.8	33.3
202	2.62219	2.61660	34.167	34.2711	24.5	23.0

Hence, from the XRD results, it can be concluded that, the X-ray diffraction profiles of HAp before segregation have a poor crystalline state and a crystalline state after two steps of thermal decomposition. The W/O microemulsion technique is useful for segregating nano-HAp from the bulk of particles, with an average particle size of 36.44 nm to 19.23 nm. The phase analysis of segregated HAp showed that the major diffraction peaks at 2θ values of 32.026°, 33.165°, 32.424°, 49.722°, 46.954° and 34.271° were in good agreement with the ICDD standard.

The SEM images confirm the effect of thermal decomposition on bone powder and some morphological changes of HAp segregated by the W/O microemulsion technique. The micrographs, as shown point a in **Figure 40** are of the bone powder heated at 650 °C for 6 h and show a wide range of particle sizes shapes and morphology. The particles have irregular shapes and sizes with edges and corners rather than spherical. The irregular morphology of the particles might be due to the milling effect of bone powder. The micrograph does not show any amorphous organic material, indicating that the organic moieties of the bone powder have been completely removed during thermal decomposition.

The bone powder recalcined at 950 °C for another 6 h point b in **Figure 40** shows the occurrence of a microstructural change in the HAp, which includes recrystallization of the bone mineral. Bahrololoom *et al.* (2009) attempted SEM observations of the heat-treated bovine bone and reported that the organic moieties of the bone tissue are completely eliminated during heating at 800 °C. The bone mineral, HAp, is then recrystallized at 800 °C, producing a variety of irregular crystal morphologies such as spherical, hexagonal, platelet and rod shapes. Similar types of observations were also seen in this study, as shown point b in **Figure 40**.

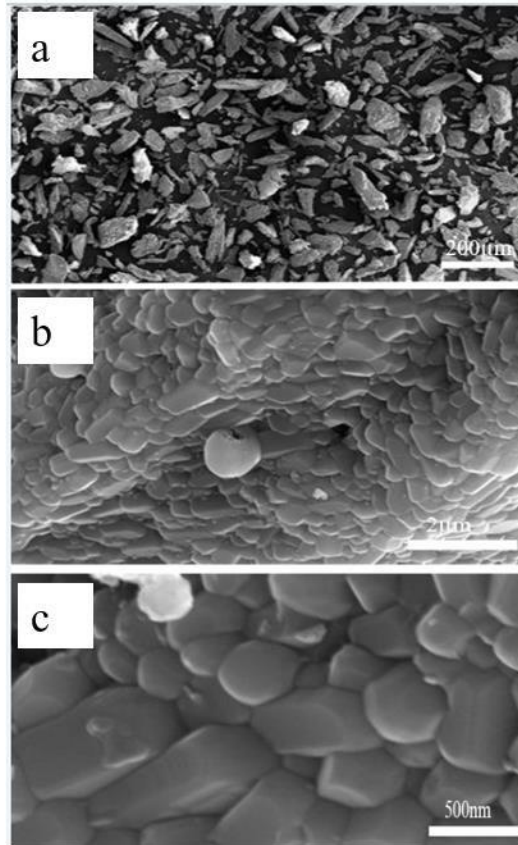


Figure 41: SEM micrographs of (a) the bone powder calcined at 650 °C for 6 h, (b) the bone powder after recalcination at 950 °C for another 6 h and (c) the nano-HAp extracted after segregation

Ooi *et al.* (2007) report that the particle morphology is influenced by the source of the bone, the heating duration and the heating temperature. However, in this study, the morphology of the particles might have been influenced by the gender, age and food habits of the ostrich form which bone sample collected. Hence, further studies are necessary to understand the influence of these biological factors on the exact morphology of the particles. Some changes in colour, morphology and recrystallization of bone minerals due to the calcinations have also been reported by Ain *et al.* (2020). Point c in **Figure 41** shows a clear picture of the SEM micrograph of the nano-HAp after segregation using W/O microemulsion technique. As evident, the particles have irregular shapes, including small spheres, rods and mostly hexagonal shapes and are also partially agglomerated together in some parts. The individual particles ranged in size from micrometres to nanometres. Therefore, from the microscopic results, it can be concluded that the two steps of thermal decomposition brought the morphological changes on the particle shape. The particle size and agglomerate condition of nano-HAp are more distinct compared to two-step

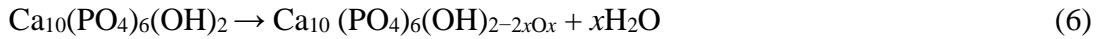
thermally decomposed bone powder. In conclusion, these results clearly show the hexagonal morphology of the nano-HAp with irregular shapes and sizes.

4.1.4 Structural Stability

The mass loss pattern of HAp (obtained from the bone powder calcined at 650 °C for 6 h) was confirmed by TGA analysis (**Figure 42**). The curve shows three inflection points with a minute mass loss on heating in an inert environment. Hu *et al.* (1999) investigated similar types of results for the thermogravimetric analysis of HAp extracted from coral shells. In this study, at the first inflection point a in **Figure 42**, a negligible mass loss (0.19 wt.%) at a temperature of 275 °C to 369 °C corresponds to the removal of physisorbed and chemisorbed moisture, as well as residual volatile organic impurities incorporated in it (Barinov *et al.*, 2006). Similarly, at the second inflection point b in **Figure 42** the mass loss pattern (0.23 wt.%) at a temperature between 535 °C and 646 °C is attributed to the decomposition of carbonate-related impurities (Abdulrahman *et al.*, 2014; Manalu *et al.*, 2015), which is very common in the HAp extracted from biogenic sources.

Olsen *et al.* (2008) suggested that the mass loss at a temperature between 225 °C and 500 °C is caused by the decomposition of organic components and that at a temperature higher than 500 °C is due to the decomposition of the structural carbonate and the release of carbon dioxide. The studies of Miculescu *et al.* (2011) show similar types of decomposition of biosource based HAp at 550 °C to 600 °C. There is no exothermic reaction related to the carbonate decomposition in the curve of the bone powder investigated in this study. However, the presence of carbonate groups has also been detected by FTIR analysis and its elemental constituent from EDX analysis which is a very common constituent of the HAp extracted from bone waste.

Finally, a significant mass loss (0.89 wt.%) was found at temperatures ranging from 770 °C to 1000 °C, indicating the removal of most of the residual organic moieties such as fatty tissues, collagen, chondroitin sulfate, keratin sulfate, etc. if any present in the HAp see the point 'c' (**Figure 42**). Furthermore, according to Eslami *et al.* (2010) and Younesi *et al.* (2011) any other likely reason for continuous mass loss during heating might be due to the partial dehydroxylation (**equation 6**) of HAp within this range of temperature.



Bahrololoom *et al.* (2009) and Younesi *et al.* (2011) reported similar types of weight loss patterns of HAp extracted from the bovine bone. Hence, the TGA studies showed that the mass loss was due to the removal of water, residual organic moieties and might be the partial dehydroxylation of HAp. The studies of Ragab *et al.* (2014) also reported similar types of finding in their analysis.

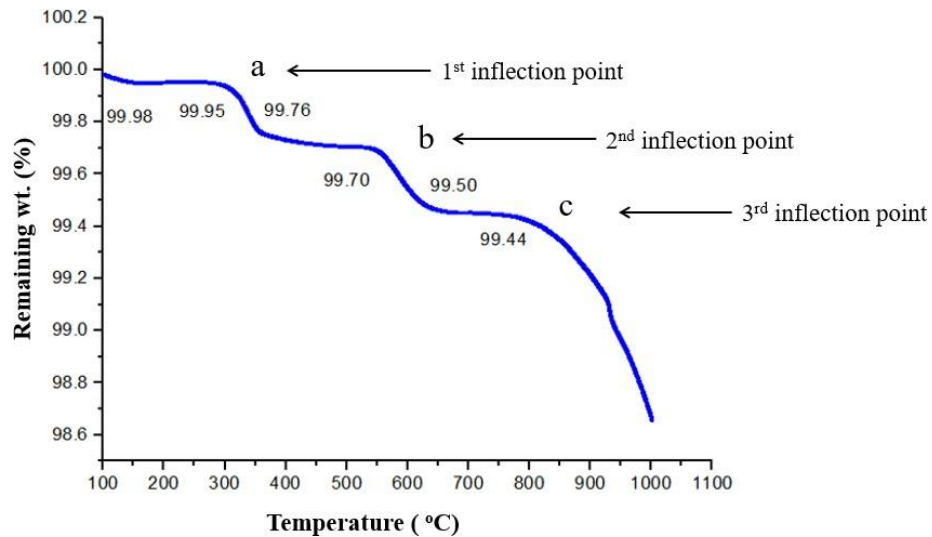


Figure 42: TGA analysis curve of the HAp (obtained from the bone powder calcined at 650 °C for 6 h) heated from 100 °C to 1000 °C under N₂ atmosphere

From these results, it can be concluded, that the mass loss pattern of HAp shows three inflection points with a negligible mass loss on heating from 100 °C to 1000 °C in an inert environment. This minute mass loss pattern exposed the structural and thermal stability of HAp.

The results of zeta potential analysis were used to get information about the surface charge on the HAp. This value shows the stability of HAp in colloidal systems. This finding is noteworthy for the determination of the interaction of nano-HAp with bone tissue in a biological environment (Vogelman *et al.*, 1988). In this study, the average zeta potential value of OB nano-HAp was found to be -3.06 mV. Cooper and Hunt (2006) reported that the HAp that has a negative least value of zeta potential has a vital role for bone tissue engineering, chiefly in the proliferation and differentiation of bone cells in a scaffold prepared by using polymers and nano-HAp. Studies show that biosource based HAp has a negative zeta potential than chemically synthesized one. Such HAp shows better biological activities due to its bioactive nature (Dizaj *et al.*, 2019; Maleki-Dizaj *et al.*, 2009; Smeets *et al.*, 2009). In addition, Teng *et al.* (2001)

reported that osteoblast cells can get attached and grow on the scaffold surfaces incorporating biosource-based nano-HAp having a negative zeta potential more easily compared to the scaffold surfaces having neutral or positive value of zeta potential. From these results, it can be concluded that the average zeta potential value of nano-HAp was found to be -3.06 mV and it will be one of the most potent biomaterials for biomedical applications.

Summary of the Preparation and Characterization of HAp

1. The results of the FTIR spectra of the HAp showed the presence of phosphate (PO_4^{3-}), hydroxyl (OH^-) and carbonate (CO_3^{2-}) as the major groups of the HAp. The two-step thermal decomposition method employed here is found to be effective one for the extraction of the HAp.
2. The EDX results revealed the major (Ca, P, O and trace (C, Na, Mg, Al and Si) elements in the HAp. The average Ca/P molar ratio was found 1.78 which lies in the range of 1.50 to 1.85 suggesting a nonstoichiometric HAp.
3. The XRD results showed the crystalline state of HAp with average particle size 19.23 nm after segregation by W/O microemulsion technique. The major diffraction peaks were found at 2θ values of 34.7850° , 33.1654° , 32.4240° , 49.7223° , 46.9548° and 34.2711° with Miller indices (211), (300), (112), (213), (222) and (202) respectively. It signifies that the Miller planes are in good agreement with the ICDD standard of HAp file no. 00-09-0432.
4. SEM micrographs suggested the hexagonal shape of the HAp particles and their partial agglomerated texture.
5. The mass loss curves obtained from TGA showed that HAp is thermally stable in the temperature range of 100°C to 1000°C .
6. Measurement of the zeta potential confirmed the minimum value with negative surface charge in HAp.

4.2 Acute Toxicity Analysis of nano-HAp

The acute toxicity test is suggested for drugs that are chemically synthesized or crude drugs extracted from natural products (Reymal *et al.*, 2017). For this the test compound is orally administered to the test animals (mostly Albino Wistar rats) and their symptoms afterward are monitored carefully following a standard OECD-420 guideline. In this study, this analysis was performed using nano-HAp in gelatin (GEL) suspension and following the same guidelines. The analysed results are presented below.

4.2.1 Observation of Physical Signs, Behavioural Effects and Sensory Parameters

The physical signs and symptoms of all the experimental rats were recorded after oral gavage of the test nano-HAp-GEL suspension according to guidelines. The observation showed that the physical symptoms of eating and drinking habits of rats in Group III declined until 4 h after gavage. The behavioral properties, such as alertness and reaction toward the changes in the surrounding environment, were also found to decrease slightly in the first 30 min in comparison to the rats of the vehicle group might be the stress of gavage. All rats showed normal behavior after 30 min throughout the study period (**Table 19**). On the other hand, grooming, which is an important common behavior of rats, was found to be completely absent in the first critical hour after that found normal.

The central nervous system (CNS)-related excitation was also found to be totally absent during the study period. However, a slight increase in sedative sleep and pain response was observed after 30 min. The effect lasted for 2 h, which could have been caused by the physical stress of the gavage. **Table 19** shows results of all the observed physical signs, behavioral effects, autonomic effects, sensory responses, respiratory effects and somatomotor effects of test suspension in rats of group III.

In the experiment, the rats in group III gavage a higher dose (2000 mg/Kg) of test suspension compared to the low-dose (300 mg/Kg) group according to test guidelines. The viscosity of the prepared test solution is comparatively higher for the high dose group than for the low dose group. For these reasons, slightly higher pressure had to be applied to the syringe piston of the gavage needle, which might be the cause of pain. However, all the other notated physical, behavioural, sensory and respiratory signs and symptoms were found to be normal after 2 h and throughout the study

periods. Furthermore, no autonomic, respiratory, or somatomotor effects were noted in any of the groups. Therefore, significant alterations were not observed in the parameters used to evaluate the acute toxicity test. Hanh *et al.* (2019) and Venkatasubbu *et al.* (2015) reported similar types of findings in their studies. The results of all observed physical signs, behavioural effects, autonomic effects, sensory responses, respiratory effects and somatomotor effects are indexed in **Table 19**.

Table 19: Observation variables of group III rats administered OB nano-HAp-GEL suspension at a dosage of 2000 mg/kg body mass (n=5)

A. Physical observations	Times								
	0 min	30 min	1 h	2 h	4 h	8 h	24 h	7 D	14 D
1. Fur colour	N	N	N	N	N	N	N	N	N
2. Skin colour	N	N	N	N	N	N	N	N	N
3. Eyes colour	N	N	N	N	N	N	N	N	N
4. Urine colour	N	N	N	N	N	N	N	N	N
5. Mucous secretion	N	N	N	N	N	N	N	N	N
6. Eating and drinking habits	N	D	D	D	D	N	N	N	N
7. Itching	A	A	A	A	A	A	A	A	A
8. Mortality	A	A	A	A	A	A	A	A	A
B. Behavioural effects									
(I) Mood									
9. Alertness exploratory activities	N	D	N	N	N	N	N	N	N
10. Eye opened/closed	N	C	C	N	N	N	N	N	N
11. Grooming	N	A	A	N	N	N	N	N	N
12. Restlessness	A	A	A	A	A	A	A	A	A
13. Reactivity toward the environment	N	D	N	N	N	N	N	N	N
(II) CNS excitation									
14. Tremors	A	A	A	A	A	A	A	A	A
15. Twitches	A	A	A	A	A	A	A	A	A
16. Convulsions	A	A	A	A	A	A	A	A	A
(III) CNS depression									
17. Sedation sleep	A	P	P	P	A	A	A	A	A
18. Catatonia	A	A	A	A	A	A	A	A	A
19. Ataxia	A	A	A	A	A	A	A	A	A
20. Coma	A	A	A	A	A	A	A	A	A
C. Autonomic effects									

21. Faces consistency	N	N	N	N	N	N	N	N	N
22. Lacrimation/Tearing	A	A	A	A	A	A	A	A	A
23. Urination	N	N	N	N	N	N	N	N	N
24. Salivation	N	N	N	N	N	N	N	N	N
25. Piloerection	A	A	A	A	A	A	A	A	A
26. Emesis	A	A	A	A	A	A	A	A	A
27. Diarrhoea	A	A	A	A	A	A	A	A	A
D. Sensory responses									
28. Touch response	N	N	N	N	N	N	N	N	N
29. Pain response	N	P	P	P	A	A	A	A	A
E. Respiratory effects									
30. Apnea	A	A	A	A	A	A	A	A	A
31. Dyspnea	A	A	A	A	A	A	A	A	A
F. Somatomotor effects									
32. Abnormal gait	A	A	A	A	A	A	A	A	A
33. Righting reflex	N	N	N	N	N	N	N	N	N
34. Body position	N	N	N	N	N	N	N	N	N
35. Limb position	N	N	N	N	N	N	N	N	N

Index: A = Absent, N = Normal, P = Present, D = Decrease, C = Close

This table shows all the observed physical signs, behavioural effects, autonomic effects, sensory responses, respiratory effects and somatomotor effects of test suspension in the high dose group (group III) only. All these signs and symptoms were found to be normal after 2 h and throughout the study periods. Furthermore, no autonomic, respiratory, or somatomotor effects were observed in any of the experimental rats. Therefore, no significant alterations were observed in the parameters used to evaluate the acute toxicity test of test suspension.

From these results, it can be concluded that the physical symptoms of eating and drinking habits declined until 4 h after gavage, while behavioural properties such as alertness and reaction to changes in the surrounding environment and grooming decreased slightly only in the first 30 min after that normal throughout the study period. A slight increase in sedative sleep and pain response was observed after 30 min, which could have been caused by the physical stress of the gavage. Similarly, all the signs and symptoms of autonomic, respiratory and somatomotor effects were found to be normal after 2 h. Hence, no significant alterations were observed in the studied parameters used to evaluate the acute toxicity of tested sample.

4.2.2 Observation of Body Weight Loss

The body weight of all group rats was recorded before and after study. It was slightly decreased in all rats after the second day of gavage, which might be due to the pain caused by the gavage needle afterward, there was a trend of increment. The effect of gavage of sample on average body weight percentage gain is shown in **Figure 42**. Results show that the body weight of all the groups of rats was found to increase remarkably on the 7th and 14th days. However, better improvement was found in Group II rather than in Group I and III which might be due to the lack of rivalry for food and water.

Furthermore, a T-test shows that the body weight gain of group II rats is slightly higher compared to the rats in group I, but the result is not significant. Studies show that the body weight gain in 7 days is significantly higher than in 14 days. It happens sometimes due to handling stress. However, the average body weight gained over 14 days by all groups of rats means that the tested sample is not toxic. The discussion in Section 4.2.1 also correlates with these results. It comprised be noted that Group II kept only 3 rats, while Group III accommodated 5 rats. The number of rats and their competition for intake of food and water might be one of the causes of improvement in body weight gain.

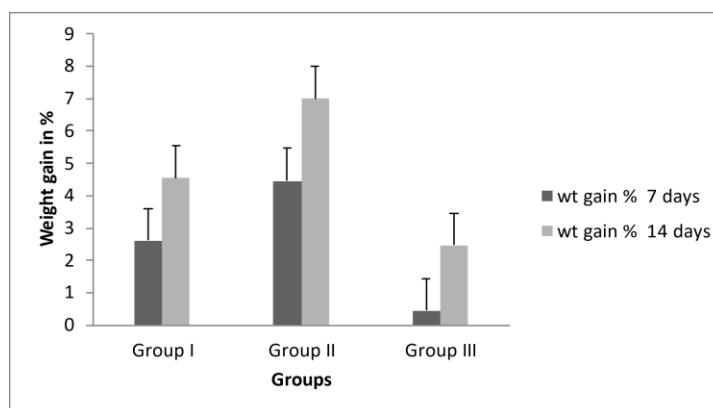


Figure 43: The effect of nano-HAp-GEL suspension on percentage body weight gain. The data are expressed as an average (Vehicle n=3, 300 mg/kg n=3, 2000 mg/kg n=5, p > 0.05)

However, the study of Mosa *et al.* (2021) revealed that a high dose of oral gavage of HAp nanoparticles synthesized from the chemical route was disseminated throughout the body via blood circulation, but mostly accumulated in the kidney and caused apoptosis. It serves crucial functions in physiology and can be triggered by a variety of stimuli, including ischemia and hypoxia. However, in our study no such symptoms

of apoptosis have been seen during the study period and as a consequence, no statistically significant difference in average body weight was noticed among the experimental rats throughout the investigations.

Regardless of the cage setting and accommodations, the percentage of body weight gain depends on physical activity, food intake frequency, dietary preferences and the overall health of the animals. However, the health issue is directly related to the toxic nature of the substance being orally injected into the test animals. Presumably due to the nontoxic nature of biosource-based HAp, the rats in both the high and low-dose groups showed weight gain on the 7th and 14th days of oral gavage.

From these results, it can be concluded that the body weight of all group rats slightly decreased after the second day of gavage, which might be due to the pain caused by the gavage needle. Afterward, there was a slow increment in all group rats. No any symptoms of apoptosis have been seen in the study period and as a consequence, no statistically significant difference in average body weight was noticed among the experimental rats throughout the investigations. The body weight of all the groups of rats was found to increase remarkably on the 7th and 14th days, but better improvement was found in Group II than in Group III. Regardless of the cage setting and accommodations, the percentage of body weight gain depends on physical activity and food intake frequency.

4.2.3 Analysis of Absolute and Relative Mass of Body Organs

The absolute and relative organ weights of both the treated and vehicle group rats were recorded during the necropsy, as shown in **Tables 20 and 21**. The results show that the relative delicate internal organ weight of all the treated rats is comparable to that of the control groups ($p > 0.05$). The internal organs such as the brain, lungs, heart, liver, spleen, kidneys and ovaries are sensitive and might be affected by the metabolic activities of the orally administrated toxic substances that cause changes in their body weights within study periods.

Table 20: The total organ weight of rats which received nano-HAp-GEL suspension at a dose of 300 mg/kg of gr. II (n=3), 2000 mg/kg of gr. III (n=5), & and gr. I, vehicle (n=3)

Absolute Organ Weight (AOW) in g										
Gr	Rats	Brain	Lungs	Heart	Liver	Spleen	Right Kidney	Left Kindny	Right Overy	Left Overy
I	1	1.44	0.81	0.45	5.25	0.40	0.42	0.42	0.03	0.03
	2	1.29	0.94	0.44	3.74	0.35	0.40	0.40	0.04	0.03
	3	1.53	1.16	0.46	4.11	0.46	0.37	0.37	0.04	0.04
	Mean	1.42	0.97	0.45	4.36	0.40	0.40	0.40	0.04	0.03
	SD	0.12	0.18	0.01	0.79	0.05	0.03	0.02	0.00	0.00
	SEM	0.07	0.10	0.00	0.45	0.03	0.01	0.01	0.00	0.00
	II	1	1.34	0.82	0.42	3.85	0.31	0.37	0.38	0.03
	2	1.37	0.81	0.44	3.85	0.30	0.39	0.39	0.04	0.04
	3	1.35	0.81	0.43	3.86	0.30	0.38	0.39	0.03	0.04
	Mean	1.35	0.81	0.43	3.85	0.30	0.38	0.39	0.03	0.04
	SD	0.02	0.01	0.01	0.01	0.01	0.01	0.01	0.00	0.00
	SEM	0.01	0.00	0.01	0.00	0.00	0.01	0.00	0.00	0.00
III	1	1.33	1.05	0.42	3.40	0.49	0.41	0.40	0.04	0.04
	2	1.52	0.82	0.50	4.30	0.40	0.46	0.46	0.05	0.05
	3	1.49	0.83	0.50	3.48	0.37	0.45	0.47	0.02	0.03
	4	1.35	0.94	0.40	2.99	0.33	0.35	0.39	0.03	0.03
	5	1.41	0.87	0.50	4.85	0.36	0.54	0.51	0.04	0.04
	Mean	1.42	0.90	0.46	3.80	0.39	0.44	0.45	0.04	0.04
	SD	0.09	0.10	0.05	0.75	0.06	0.07	0.05	0.01	0.01
	SEM	0.04	0.04	0.02	0.33	0.03	0.03	0.02	0.00	0.00
	T-test	0.96	0.49	0.70	0.35	0.73	0.32	0.17	0.73	0.47

Furthermore, this organ weight might be correlated with the physiological and pathological status of rats, as reported by Venkatusubbu *et al.* (2015). During the necropsy, towards the concluding phase of this study, the overall macroscopic

inspection of the organs of all test groups revealed no abnormalities, even when compared to those of the control groups in terms of colour and texture. However, the change in hypertrophy of these organs might be an initial indication of organ toxicity reported by Mirza & Panchal (2020) in their studies.

Table 21: The relative organ weight of rats which received plain gelatin, gr. I, (n=3), nano-HAp-GEL suspension at a dose of 300 mg/kg, gr. II (n=3) and 2000 mg/kg, gr. III (n=5)

Relative Organ Weight (ROW) in g										
Gr.	Rats	Brain	Lungs	Heart	Liver	Spleen	Right Kidney	Left Kidney	Right Ovary	Left Ovary
I	1	1.25	0.71	0.39	4.56	0.35	0.37	0.36	0.03	0.03
	2	1.14	0.83	0.39	3.30	0.31	0.36	0.36	0.03	0.02
	3	1.14	0.87	0.34	3.07	0.34	0.28	0.28	0.03	0.03
	Mean	1.18	0.80	0.38	3.64	0.33	0.33	0.33	0.03	0.03
	SEM	0.04	0.05	0.02	0.46	0.01	0.03	0.03	0.00	0.00
II	1	1.23	0.75	0.38	3.53	0.28	0.34	0.35	0.03	0.04
	2	1.25	0.74	0.40	3.52	0.27	0.36	0.36	0.03	0.03
	3	1.24	0.74	0.40	3.55	0.28	0.35	0.36	0.03	0.03
	Mean	1.24	0.75	0.39	3.53	0.28	0.35	0.35	0.03	0.03
	SD	0.01	0.01	0.01	0.01	0.01	0.01	0.01	0.01	0.00
	SEM	0.00	0.00	0.00	0.00	0.00	0.00	0.00	0.00	0.00
		72	317	51	7535	3063	5096	31167	184314	109
III	1	1.14	0.91	0.36	2.92	0.42	0.35	0.34	0.04	0.04
	2	1.16	0.62	0.38	3.27	0.30	0.35	0.35	0.04	0.04
	3	1.23	0.69	0.41	2.87	0.30	0.37	0.39	0.02	0.02
	4	1.29	0.91	0.38	2.88	0.32	0.34	0.37	0.03	0.03
	5	1.09	0.67	0.39	3.74	0.28	0.42	0.39	0.03	0.03
	Mean	1.18	0.76	0.38	3.14	0.32	0.37	0.37	0.03	0.03
	SEM	0.04	0.06	0.01	0.17	0.02	0.01	0.01	0.00	0.00
	T- test	0.90	0.63	0.64	0.26	0.77	0.26	0.16	0.71	0.40

The relative organ weight of all rats was found to be normal throughout the study period ($p > 0.05$). Similar types of results were also reported by Remya *et al.* (2017) on the histopathological and organ body weight evaluation of chronic exposure to nano-HAp.

Summary of Acute Toxicity Analysis of nano-HAp

It could be concluded that the oral gavage of test suspension did not show any acute toxic effects up to a lethal dose of 2000 mg/kg body weight of the rats. Hanh *et al.* (2019) reported similar types of findings for the short-term effects of HAp-alginate suspension on Swiss Albino rats.

1. The general behaviour, CNS excitation and depression related activities, autonomic effects, sensory response, respiratory and somatomotor effects of nano-HAp were observed normal in the rats of the tested groups.
2. No differences in absolute and relative organ weight, average body weight and the macroscopic examination of internal organs were observed. These results revealed the non-toxicity of tested materials.
3. The tested suspension has a lethal 50% dose (LD₅₀) exceeding 2000 mg/kg of body weight, which is consistent with globally harmonized system (GHS) of classification and labelling of chemicals.

4.3 Characterization of Electrospun Biomedical Scaffolds

Electrospinning is the bottom-up technique to fabricate nonwoven porous scaffold for biomedical application (Shuai *et.al*, 2020). This technique is widely used to fabricate polymers and nanofiller incorporated hybrid polymer composite scaffold for biomedical applications. The hybrid composite scaffold is generally fabricated by adjusting various parameters such as applying voltage electric field strength, needle-collector distance and solution flow rate (Sattary *et al.*, 2018). To fabricate scaffolds used for biomedical applications especially for BTE, different processing parameters as mention above could also be easily manipulated. In this study nano-HAp and VD3 blended different volume percentage ratio of ternary polymers, such as PCL, PLLA and GEL composite blends was electrospun to prepared the non woven scaffold. The structural, morphological, electrical and mechanical properties of such scaffolds can be confirmed by using various characterization tools and techniques. In this section, the study focuses on the different characterized results of the fabricated scaffolds.

4.3.1 Structural Characterization of the Scaffold

The FTIR spectra of the polymers; PCL, PLLA and GEL, vitamin D3(VD3) and the composite scaffolds CB-1 and CB-6) are shown in **Figure 43**.

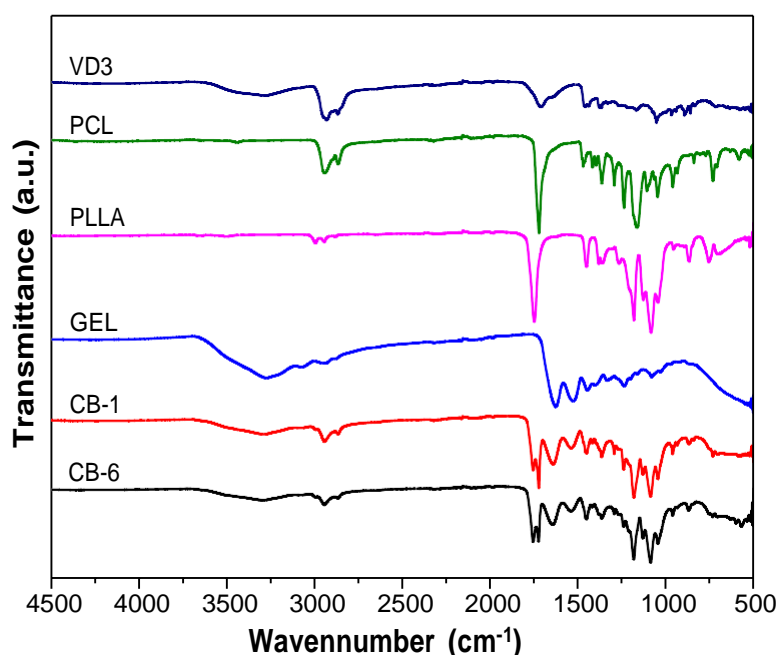


Figure 44: FTIR spectra of VD3, PCL, PLLA, GEL, CB-1 and CB-6

The spectrum of the characteristic vibrational peaks of C–O–C stretching (symmetric and asymmetric), C–O and C–C stretching at 1166 cm^{-1} , 1237 cm^{-1} and 1295 cm^{-1} which are visible in the PCL spectrum is not visible in the analyzed composite scaffolds of CB-1 and CB-6. This might be due to the inter connecting these groups to other groups of polymers. Different researchers, such as Shuai *et al.* (2020) Milovanovic *et al.*, (2019) and Sattary *et al.* (2019) reported similar types of observations in their studies.

The symmetrical vibrational stretching of the peaks C=O, C–O=C, CH₃ and CH₂ at 1723 cm^{-1} , 1103 cm^{-1} , 1363 cm^{-1} and 1462 cm^{-1} of PLLA were also observed in the composite scaffolds of CB-1 and CB-6. These peaks show the evidence of PLLA in scaffolds. Lee *et al.* (2013) reported a similar type of findings in their studies. In addition, according to Fang *et al.* (2010), the peak shifts from 1723 cm^{-1} to 1760 cm^{-1} correspond to the C=O bending vibrations of either PLLA or PCL, which might be attributed to the formation of new bonding between the OH group of nano HAp and the C=O group of polymers. According to Bhattarai *et al.* (2018) due to the masking effect of the C–C stretching band of PLLA at 930 cm^{-1} the small peak of the carbonate (CO₃²⁻) group of HAp at 875 cm^{-1} is not visible in the scaffolds of CB-6. Furthermore, some characteristic peaks for gelatin related to C=O group stretching (amide-I) at 1642 cm^{-1} , N–H bending at 1542 cm^{-1} (amide-II) and N–H bending at 563 cm^{-1} are clearly visible in the spectrum of CB-6.

Fayyazbakhsh *et al.* (2017) Sattary *et al.* (2019) and Shokrgozar *et al.* (2012) also reported similar findings in their studies. Additionally, there might be a attractive force developed between the calcium (Ca²⁺) ion of HAp and the acetate (R-COO⁻) group of gelatins, which exposes that HAp has an affinity towards gelatin but not other polymers. Similar types of agreement with the results reported by Hossan *et al.* (2015).

Furthermore, the spectrum of CB-6 contains some significant bands at 605 cm^{-1} , 1025 cm^{-1} and 1045 cm^{-1} , all of which are assigned to the PO₄³⁻ group of HAp. The bands at 631 cm^{-1} belong to the OH⁻ group of bonded hydrogen. Similarly, the peaks at 2355 cm^{-1} and 2330 cm^{-1} are related to the CO₃²⁻ group, as well as 3570 cm^{-1} related to the OH⁻ group of nano HAp visible also in composite blends of CB-6. Similar types of results were reported by Abdel Sayed (2011) in his studies. On other the hand, the peaks of stretching vibration of CH₂, alkyl C–H, symmetric stretching of

CH₃ and hydrogen bonded O–H stretching at 737 cm⁻¹, 2864 cm⁻¹, 2936 cm⁻¹ and 3289 cm⁻¹ have confirmed the existence of VD3 in the scaffolds of CB-6, which is in agreement with the results found by Kiani *et al.* (2017) and Sattary *et al.* (2019). As conclusion, these results show that the polymers and fillers are well-blended in the scaffolds. The shifting of peaks and the emergence of a new peak indicate a molecular interaction between the polymers and filler.

4.3.2 Microscopic Analysis of Scaffold Fibers

The morphological changes of randomly oriented scaffold fibers (CB-1 to CB-6) as a function of the addition of volume fractions percentage of filler (0-12 %) in the polymer blends are shown in **Figures 44 a-f**. It is considered that any change in fiber diameter and morphology is related to the proportion of filler added to the polymer blends. Because the scaffolds were fabricated under fixed experimental conditions.

The fibers without filler are smooth and have a bead-free morphology, as shown in point a and b **Figure 44**. However, the addition of filler augmented due to agglomerations inside the scaffold fibers. The agglomerate of fillers is clearly visible in point e and f **Figure 44**. Results show that the average fiber diameter increased from 0.17 μm to 4.34 μm with the addition of 0–3 % of filler. However, it decreases significantly (from 4.34 μm to 0.48 μm) on further increasing 3 % to 12 % of the filler. The average fiber diameter of 100 fibers per each scaffold is presented in **Table 22**.

Table 22: Average fiber diameter of scaffolds with respect to volume fraction percentage of filler

Sample code	Content of filler (Vol.%)	Fiber diameter (μm)
CB-1	0	0.17
CB-3	2	1.84
CB-4	3	4.34
CB-5	6	0.58
CB-6	12	0.48

The cause of decreasing fiber diameter with the addition of filler might be the increase in solution conductivity of the electrospinning solution because the filler is a comparatively more conducting material than polymer used. The higher percentage

(6-12%) of filler addition might show this condition in the fiber as reported by Januariyasa *et al.* (2020).

Additionally, the augmentation of solution conductivity might be a cause of the faster elongation of the polymer solution jet from the needle tip under the electrical field generated by using high voltage (17-25KV) between the needle tip and collector drum during electrospinning process (Januariyasa *et al.*, 2020). The decrease in fiber diameter may result in a larger surface area of fibers and it enhanced micromechanical properties of the fibers as reported by Wong *et al.* (2008). Despite this, the fiber diameters depend on how the fillers are encapsulated inside the fibres and its affinity to polymers (Sánchez-Arévalo *et al.*, 2017).

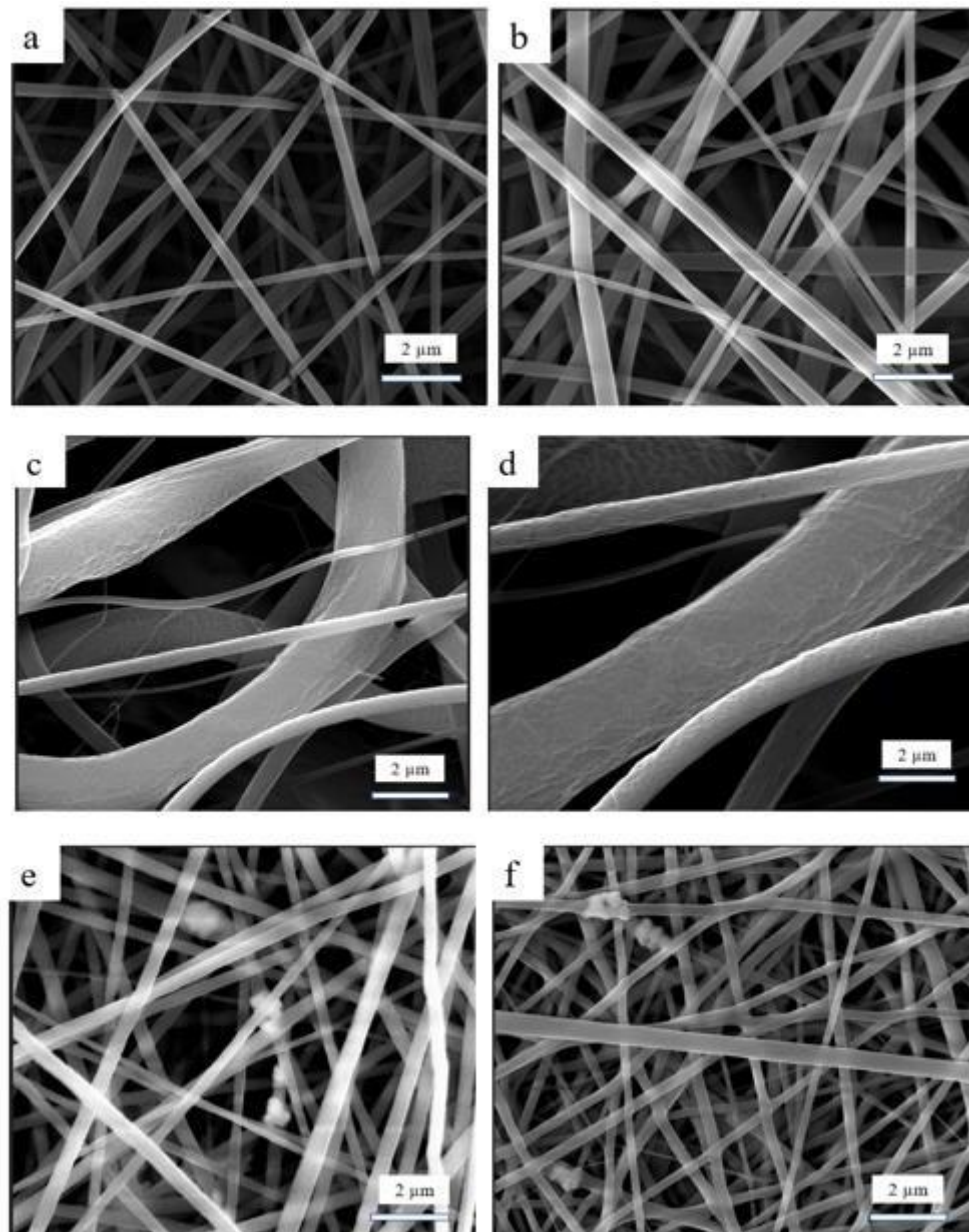


Figure 45: Photographs of SEM images of scaffolds: (a) CB-1, (b) CB-2, (c) CB-3, (d) CB-4, (e) CB-5 and (f) CB-6

Regardless of the normal modification of shapes, any hump texture in the fibers is not visible in addition of a lower volume fraction percentage (2–3 %) to the fillers in the polymer blends shown in point c and d **Figure 45**.

Overall, from the results of the microscopic analysis of the scaffold, it can be concluded that the filler could change the morphology and texture of the scaffold surface. It directly affects the fiber diameter. The fiber diameter is increased to a certain threshold limit (3%) of filler addition and then decreased significantly with an addition of filler beyond this limit (6 % –12 %).

Hence, we can assume that the fiber diameter is a function of filler addition in polymer blends. The cause of a gradual decrease in fiber diameter might be due to the agglomeration of nano-HAp inside the fiber, its affinity to polymers and random distribution during ES process. Furthermore, this distribution might affect the physical properties, such as the conductivity of the solution used for electrospinning as well.

4.3.3 Microscopic Analysis of Single Fibers

The polymers used in this study are not only biodegradable but also thermodynamically immiscible, as reported by Ba Linh *et al.* (2013), Fang *et al.* (2010), Heidari *et al.* (2019) and Scaffaro *et al.* (2017). For this reason, the phases of each polymer (PCL, PLLA and GEL) in the scaffold fiber might also be separated. The lower and higher magnification of the TEM image of a single fiber of scaffold (CB-3) stained with ruthenium tetra oxide vapours (RuO_4) are shown in **Figure 46 a and b**.

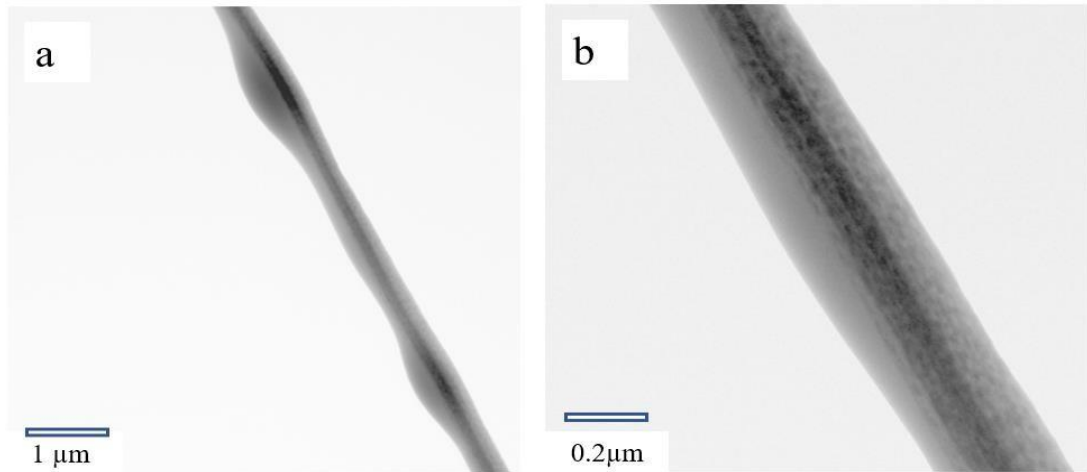


Figure 46: TEM micrograph of single scaffold fiber (CB-3) stained with RuO₄ (a) Low magnification, (b) High magnification

The contrast phase of the RuO₄ layer with gelatin was found in a dark part at the centre of the fiber, whereas the peripheral light part might be either PCL (the clear part from the bottom of the contrast) or PLLA (slightly rough part above the contrast). In addition, HAp has an affinity towards GEL rather than PLC and PLLA due to its hydrophilic nature. Among the used polymers GEL has an ability to crosslink with HAp as discussed in section 3.4.1 and stabilized them at the central part. Owing to this concept GEL with HAp located at the center whereas PCL and PLLA are located at the peripheral parts of the fiber.

From this study it can be concluded that the phase of each polymer is thermodynamically immiscible in the fiber. The hydrophobic polymers, PLC and PLLA, are located at the peripheral part, while the hydrophilic polymer together with filler located at the central part of the scaffold fiber.

4.3.4 Deformation Behavior of Scaffolds

An overview of the stress-strain curves of the scaffolds as a function of the volume fraction percentage of filler used is shown in point a–e of **Figures 47**. The neat polymer scaffolds presented in **Figure 47a** exhibits a brittle behavior with a noticeable crack growth (Junuariyasa *et al.*, 2020). Similarly, other scaffolds (CB-3 to CB-6) with 3% to 12% fillers respectively, show a ductile behaviour with no unstable crack growth represented in point b–e in **Figure 47**. In this connection, the strain at break of the composite scaffolds is in the range of 18%-37% which is dependant on the fillers concentration. Increasing the fillers concentration from 2% to 3% does not possess a change in ductility of the composite scaffolds whereas

increasing to 6% concentration of fillers from 3% significantly increases the strain at break (~146%). However, this value remained almost unchanged up on increasing the HAp concentration to 12%. Hence, it is concluded that incorporation of nano-HAp as a fillers into the polymers provides them with the ductility of the composite scaffolds. This result is correlated to the transition in the micromechanical deformation mechanisms as discussed in section 4.3.2. As found in this section crazing behaviour of the fibers is related only to a small amount of local deformation and has therefore low ductility. However, the thin-layer process that was seen to increase not only the amount of local deformation but also the ductility of the material as a whole.

The results show that the brittle-to-ductile transition is triggered by the incorporation of fillers. This behaviour is confirmed by the strain at break as a function of filler percentage, as shown in point c **Figure 48**. The strain at the break of neat polymer scaffolds is very low, at only 2%; however, the strain at break of other tested scaffolds (CB-3–CB-6) is comparatively higher (18 –37%) than that of CB-1.

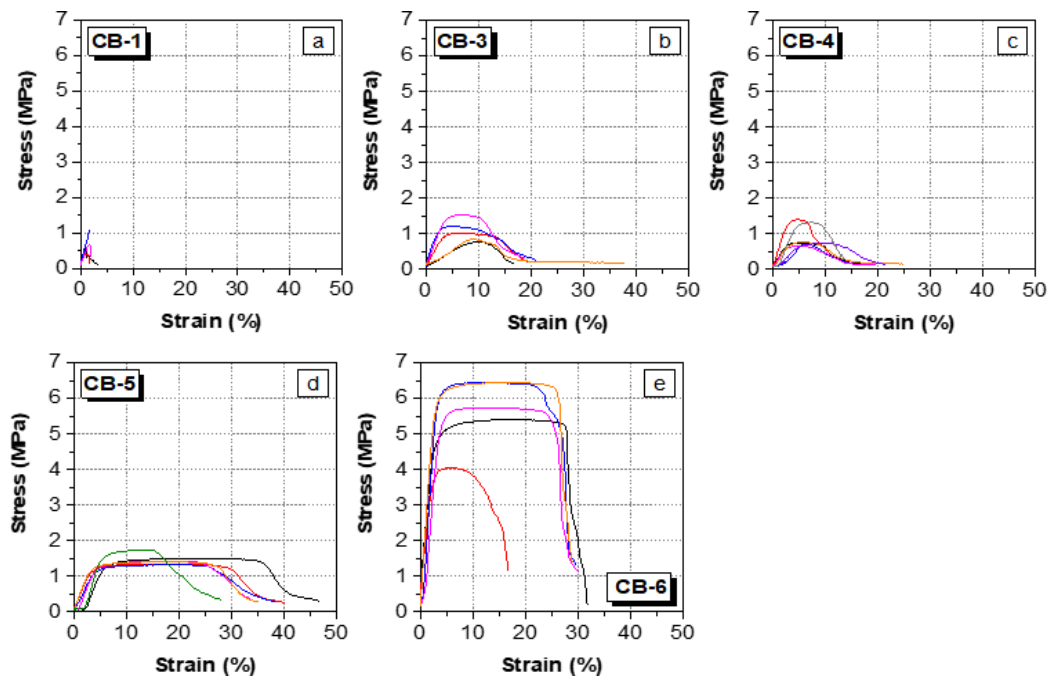


Figure 47: Stress-strain curves of fibrous scaffolds: (a) CB-1, (b) CB-3, (c) CB-4, (d) CB-5 & (e) CB-6

This finding can be supported by the hydrophilic nature of gelatine as well. Due to this nature, it might bind the filler at the centre of the fiber via the electrostatic force between the filler’s hydroxyl (OH^-) and phosphate (PO_4^{3-}) groups and the amino

(-NH₂) cationic groups of gelatins. This is one of the causes of the increasing ductile properties of fiber.

The point 'a' in the figure 48 shows the curve of elastic modulus versus filler percentage in composite scaffolds. The elastic modulus of scaffolds (CB-1–CB-5) that contain 0–6% fillers have a nearly constant value (about 44 MPa). However, the modulus jumps in CB-6 interestingly from 44 to 199 MPa at 12% filler addition. This might be the high-volume fraction of filler in the scaffold. This result shows the effect of filler addition on the micromechanical behaviours of scaffolds (i.e., brittle to ductile transition) of scaffolds. Junuariyasa *et al.* (2020) showed similar types of finding and reported that such a scaffold is prefer to *in vitro* or *in vivo* bone tissue regeneration study. The point 'b' of figure 48 also shows the micromechanical properties of scaffold fiber.

The tensile strength of scaffold fiber without filler (CB-1) is minimum only 0.7 MPa shown in point b of figure 48. This value is increased from 0.7–1.6MPa on increasing 0–6% of filler in polymer blends. However, the value was found suddenly higher i.e., 1.6–5.6MPa on increasing 12% of filler due to the high-volume fraction of filler in the scaffold. This increasing trend in tensile strength also shows the brittle-to-ductile transition of the scaffold fibers. Similar types of findings are reported by Junuariyasa *et al.* (2020) and Lach *et al.* (2023).

The point 'c' of figure 48 also shows the brittle to ductile transition of scaffolds with addition of filler in the polymer blends. The strain at break of the scaffolds without filler (CB-1) is very low at only 2%. However, the value of other scaffolds (CB-3–CB-6) is much higher (18–37%) due to decreasing fiber diameter on increasing filler percentage. Results shows that the increasing trends of filler percentage not only makes the scaffolds more biocompatible but also makes them more flexible, which is necessarily important for biodegradation and biomedical applications of scaffolds. Literature shows that such scaffolds are used for the proliferation and differentiation of osteoblast cell.

So, from the results of the above discussion, it can be concluded that the scaffolds without filler exhibit very brittle behaviour with unstable crack growth, while all of the PCL, PLLA, GEL, VD3 and filler composite scaffolds (CB-3 to CB-6) studied (filler fraction: 2-12%) changed to be ductile with no unstable crack growth. This

observation can be related to the transition in the micromechanical deformation mechanisms as discussed in section 4.3.2. The crazing behaviour of the fibers is only related to a small amount of local deformation and has low ductility, but the thin-layer process increased not only the amount of local deformation but also the ductility of the material as a whole. The brittle-to-ductile transition is triggered by the incorporation of fillers, which can be confirmed by the strain at break as a function of filler percentage, as shown in point c in **Figure 48**. Additionally, the tensile strength increases from 0.7 MPa for the scaffold without filler to 5.6 MPa for the composite containing 12 % filler.

This finding can also be supported by the hydrophilic nature of gelatin, which might bind the filler at the centre of the fiber via the electrostatic force between the filler's hydroxy and phosphate groups and the amino cationic groups of gelatins. The elastic modulus is first nearly constant at 0 – 6 % filler (about 44 MPa), but then jumps to 199 MPa at 12% of filler. The same jump can be observed for the tensile strength as well.

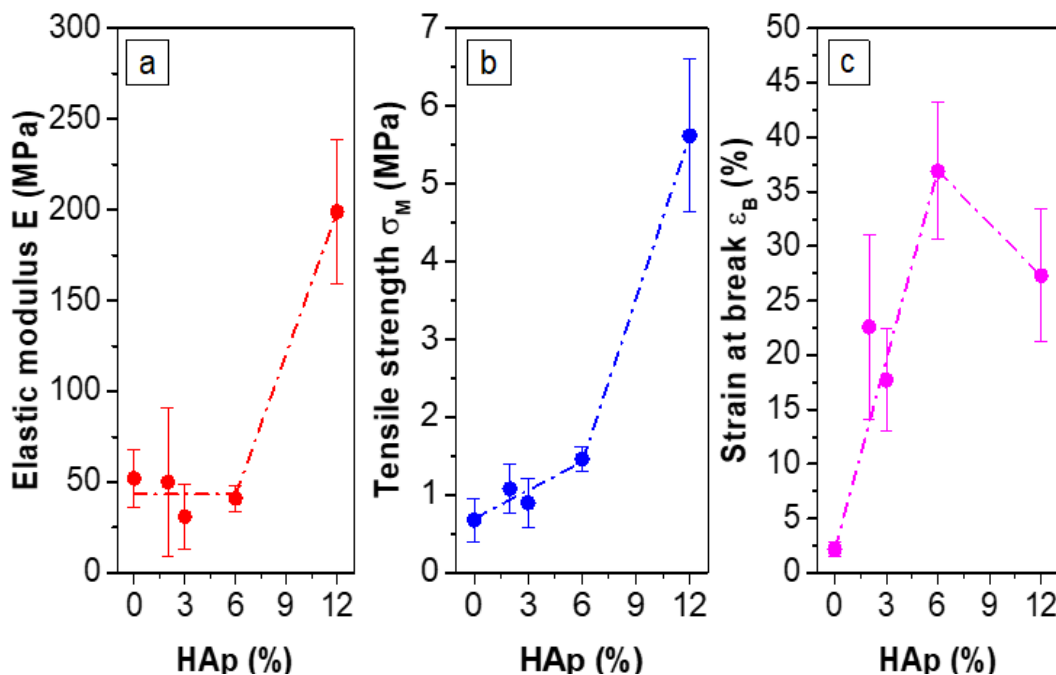


Figure 48: Tensile properties of the nanofibrous scaffolds as a function of the filler (nano-HAp) fraction percentage (a) elastic modulus, (b) tensile strength and (c) strain at break; the lines are visualizing the trend only

Therefore, from the results of the deformation behaviour of scaffolds, it can be concluded that the brittle to ductile transition of scaffold fiber with the addition of

filler percentage and the strain at the break without filler are very low (2%). However, this value increased (18-37%) with the addition of certain filler percentages to the polymer blends. The increasing trend of tensile strength (0.7 MPa-5.6 MPa) was found by increasing the filler percentage (3-12%) in polymer blends. The elastic modulus of scaffolds containing 0-6% filler addition was found to be 44 MPa; this value increased to 199 MPa with the addition of 12% filler and a similar trend was also observed in the investigation of the tensile strength of the scaffold

4.3.5 Microscopic Analysis of Fracture Surface after Tensile Test

The SEM micrograph of fracture surface of fiber after tensile test show the micromechanical behaviour of fiber. The scaffold fiber which contains a limited percentage of filler (CB-4) exhibits brittle behaviour; such fiber shows several modulated crazing marks after fracture shown in point a **Figure 49**. This might be the effect of filler, local deformation and the phase separation of each polymer in the fiber.

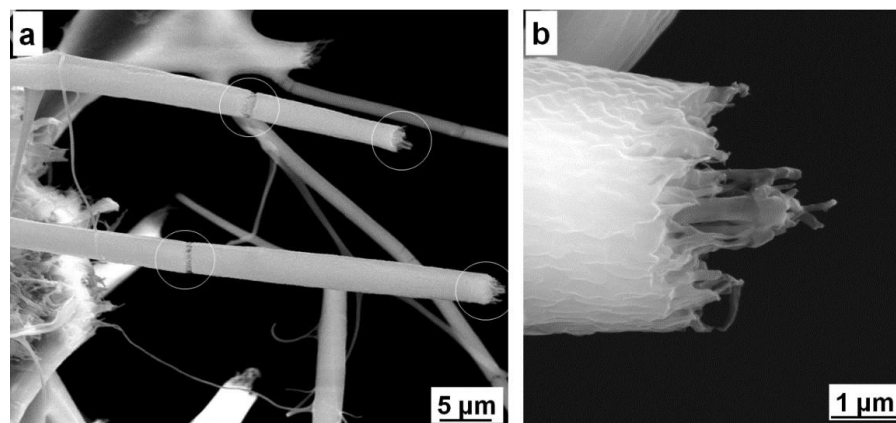


Figure 49: Photographs of representative SEM images of CB-4 after tensile test: modulated crazing in fibers; a) overview image, b) detail

The results show that the ductile property of fiber improves with an increase in the filler percentage in polymer blends. Januariyasa *et al.* (2020) reported similar types of findings in their studies.

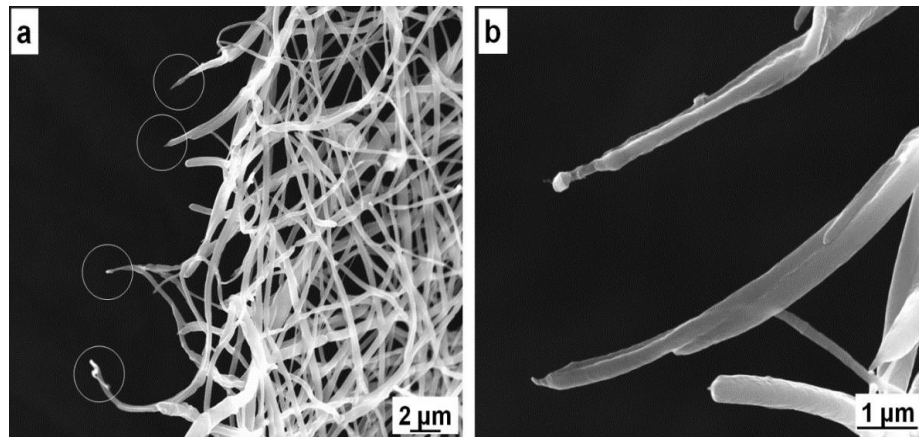






Figure 50: Representative SEM images of sample CB-6 after tensile test: thin layer yielding behaviour; a) overview image, b) detail

By increasing the filler percentage ($>3\%$), it remarkably increases the surface area of the fiber and decreases the fiber diameter, which in turn decreases the brittle property and increases its ductile behaviour. **Figure 50** shows various types of yielding marks on fibers of CB-6, which contains 12% filler. Hence, from this study, it can be concluded that fiber without filler has high brittle properties. The addition of a certain percentage (3-12%) of nano-HAp as a filler in polymer blends shows an improvement in the brittle-to-ductile transition in the fibers. The crazing to yielding transition of fiber improved by decreasing fiber diameter which is facilitated by increasing filler content.

4.3.6. Wettability Analysis of the Scaffolds

Sattary *et al.* (2018) reported that, hydrophilic scaffolds are highly recommended for various biomedical applications including drug delivery, BTR study and BTE.

Table 23: WDCA values of each scaffold with drop shapes

Sample Code	Vol. % of Nano-HAp in polymer blends	Contact angle	Photograph of contact angle
CB-1	0	79.0 °	(a) 
CB-4	3	64.12 °	(b) 
CB-5	6	50.21 °	(c) 
CB-6	12	44.78 °	(d) 

The analysis of water drop contact angle (WDCA) measurement is considered as a simple approach for analysing the surface property and hydrophilicity test on the scaffold surface (Jaiswal *et al.*, 2013; Sattary *et al.*, 2018). The hydrophilic behaviour measured by WDCA measurements can be correlated with the *in vivo/in vitro* degradation susceptibility of the scaffolds. The outcomes of this study on the scaffold surface (CB-1, CB-4, CB-5 and CB-6) are presented in **Table 23**.

The results show that the scaffold without filler (CB-1) has a comparatively higher value (79 °) of contact angle. This result signifies that water molecules do not wet or absorb sufficiently on the scaffold surface which might be the hydrophobic nature of scaffold despite the higher volume ratio (30:30:40) of gelatin being blended into the polymer blends of PCL and PLLA. Moreover, among the used polymers, PCL and PLLA have a hydrophobic nature, while GEL has a hydrophilic nature due to its amino and carboxylic groups in its monomer unit that help to reduce the interfacial tension of the aqueous medium (Fang *et al.*, 2010; Meng *et al.*, 2010). However, on increasing filler percentage in the polymer blends (3-12%), the contact angle decreased significantly due to the surface roughness and an increment of hydrophilic behaviour on the scaffold surface.

Studies shows that nano-HAp enhances the surface roughness on the scaffolds, which in turn decreases the WDCA values and enhances the hydrophilic nature of the scaffolds. The studies of Ba Linh *et al.* (2013) and Hassan *et al.* (2014) show that the

enhanced biodegradability of the scaffolds can be feasible by lowering the WDCA value and increasing their hydrophilicity. The scaffold having minimum WDCA value has hydrophilic nature and absorbs more water, which makes it biodegradable through hydrolytic actions (Ba Linh *et al.*, 2013; Sattary *et al.*, 2018; Shitole *et al.*, 2019).

From this study, it can be concluded that the nano-HAp incorporated scaffold has better hydrophilic behaviour and water absorption ability compared to the scaffold without filler. So, the hydrophilic behaviour of scaffold measured by WDCA measurements can be correlated with the *in vitro/in vivo* degradation susceptibility of the scaffolds. Such scaffolds have been found to be more susceptible to water absorption and thereby provide higher rate of degradation under *in vivo/in vitro* study in biological environment. The scaffold without filler has a comparatively higher WDCA value (79 °) and this value is in decreasing order on addition of filler percentage in the polymer blends. This type of scaffold is highly preferable for various biomedical applications chiefly in bone tissue engineering (BTE) and bone tissue regeneration (BTR) studies.

Summary of Biomedical Scaffolds Characterization

1. The FTIR spectra showed that the polymers and fillers are well mixed. The shifting of peaks and the appearance of a new peak in these spectra signify the molecular interaction between PCL, PLLA, GEL with VD3 and HAp.
2. SEM micrographs showed that the fillers changed the morphology, shape, fiber diameter and the texture of the scaffold fibers.
3. TEM micrographs of a single fiber showed that the used polymers were in thermodynamically separable phases and the fillers possessed affinity only towards hydrophilic polymer.
4. Deformation behaviour of the scaffolds showed that a brittle-to-ductile transition of fibers was triggered by the incorporation of 3 to 12% fillers, which is confirmed by the elastic modulus, tensile strength and strain at break as a function of filler concentration.

5. SEM micrographs of the fracture surface of scaffold fibers CB-4 and CB-6 show that increase in filler concentration in polymer blends facilitates the crazing-to-yielding transition of the fibers decreasing the fiber diameter.
6. The decreasing trends of water drop contact angles (WDCA) values from 79° to 44.78° on the tested scaffold showed that the hydrophilic behaviour of the scaffold improved with the addition of filler percentage in the polymer blends. Filler enhances the surface roughness and decreases the contact angle value, which in turn increases the water absorption ability of the scaffold. Lowering the contact angle value signify the hydrophilic nature of the scaffold.

4.4 *in vitro* Biomedical Test of the Scaffolds

For the biomedical application, it is important to determine the *in vitro* degradation rate of the scaffolds in a biological environment. In this study, this test was measured by placing the scaffold in phosphate buffered saline (PBS) solution (pH = 7.4) for 7 weeks. The experimental results of the remaining weight percentage of each scaffold after 7 weeks are presented in **Figure 51**.

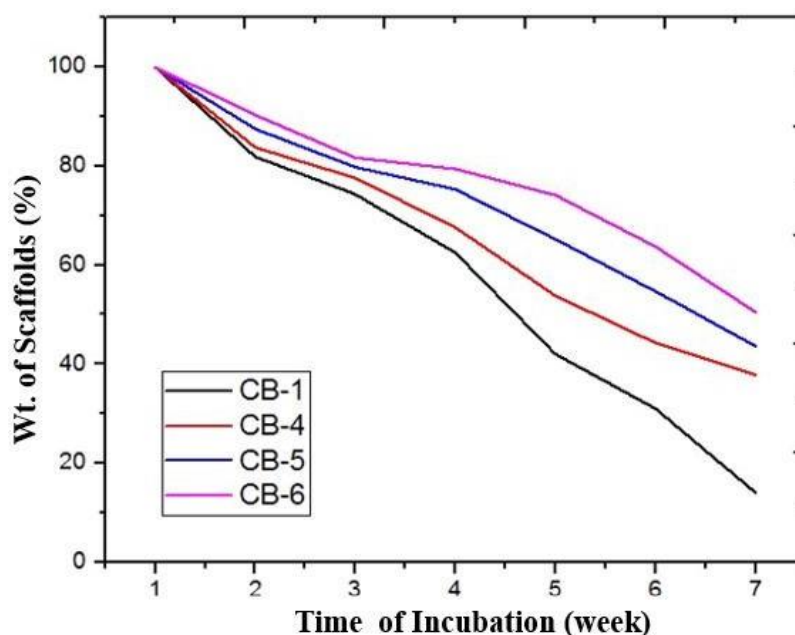


Figure 51: The graphs of *in vitro* degradation test of the scaffolds of CB-1, CB-4, CB-5 and CB-6

The results showed that the scaffolds without fillers (CB-1) have a higher degradation rate in compared to other scaffolds incorporated with fillers (CB-4 to CB-6). Due to the crystalline nature of filler as discussed in section 4.1.3 the rate of hydrolytic degradation was found in the declining order on increasing volume fraction percentage of filler (Nahavandizadeh & Rezaei, 2020; Oprea, 2005; Sattary *et al.*, 2018). The scaffold, which contains 3% v/v (CB-4), 6% v/v (CB-5) and 12% v/v (CB-6) filler, exhibits a comparatively slower degradation rate than the scaffold without filler (CB-1). On the basis of the percentage of filler in each scaffold, the order of degradation was found $CB-6 < CB-5 < CB-4 < CB-1$ within the 7-weeks of study period.

After 2nd week of the incubation period, CB-1 showed comparatively faster degradation rate compared to CB-4, CB-5 and CB-6 and this trend remained

consistent until the next 7 weeks. The sample code CB-2 and CB-3 are not included in the **Figure 50** because of the low volume fraction percentage of filler in this sample. The final remaining weight percent of scaffolds is shown in the **Table 24**. According to Mi *et al.* (2014) the rate of hydrolytic degradation is noticeable in the region of amorphous distribution of filler comparison to the region of crystalline distribution. Similar types of observations reported by Sattary *et al.* (2018) and Tetteh *et al.* (2014) in their studies.

Table 24: Hydrolytic degradation of scaffolds in PBS solution for 7 weeks

Time (in Week)	Weigth of Scaffolds (%)			
	CB-1	CB-4	CB-5	CB-6
1	100	100	100	100
2	81.9	83.8	87.5	90.3
3	74.3	77.6	79.8	81.7
4	62.5	67.6	75.3	79.4
5	42.0	53.8	65.2	74.1
6	31.0	44.3	54.7	63.7
7	14.0	37.8	43.6	50.5

Among the polymers used in this study, both PCL and PLLA have a hydrophobic nature as discussed in section 4.3.6, whereas GEL is a hydrophilic polymer (Fang *et al.*, 2010; Song *et al.*, 2013). It has a carbonyl (>C=O) and amino (-NH₂) groups in its monomer unit that showed affinity to PBS solutions and were simply hydrolyzed compared to PCL and PLLA. In addition, compared to PCL and PLLA, it has a better affinity to filler due to its crosslinking behaviour (Beachley & Wen, 2010; Fu *et al.*, 2013), as discussed in Section 4.3.3. This behaviour also helps to improve the *in vitro* degradation of filler incorporated scaffolds in PBS solution (Bölgen *et al.*, 2005; Haponiuk & Karlsson, 2002).

The TEM image also proved the phage separation of PCL and PLLA in scaffold fibers and the affinity of filler towards the GEL surface, as discussed in Section 4.3.3. Augustine *et al.* (2014) reported that among the three polymers used in this study, The PCL undergoes hydrolytic degradation due to the presence of hydrolytically breakable aliphatic ester linkages in its monomer backbone. However, it has a passive

mode of degradation in comparison to GEL due to the conversion of long polymer chains into shorter water-soluble fragments (Augustine *et al.*, 2014; Haponiuk & Karlsson, 2002; Lien *et al.*, 2013). However, the rate of hydrolytic degradation of both PCL and PLLA is affected by the degree of crystalline and semi-crystalline nature of both polymers, as well as their crosslinking tendency towards fillers (de Souza *et al.*, 2019; Rajzer *et al.*, 2018; Shuai *et al.*, 2020). Despite this, PCL and PLLA provide a strong and inflexible shape for the scaffold, which is beneficial for them for biomedical application (Zhang *et al.*, 2005). Because of the very low concentration (50 μL) of VD3 in the polymer blends, it has no specific role in the scaffold degradation. It shows its specific role only in the biomedical application of scaffolds, mainly calcium absorption and osteoblast cell differentiation (Kato *et al.*, 2015; Sattary *et al.*, 2019). The morphological observations of changes taking place in the fiber of the scaffold during degradation in PBS solution are shown point a and b in **Figure 51**. From the laser micrographs, it is clear that there was a noticeable change in fiber morphology that occurred during degradation. There was a considerable increase in fiber breakage and scratch formation on the scaffold surface after the 7 weeks of the degradation study. The morphology of individual fibers of the scaffolds becomes rough due to the surface erosion of used polymers. These scratches might be formed due to the breakdown of the main chain of ester bonds in PCL and PLLA during hydrolytic degradation. When the PBS molecules attack the ester bonds, the polymer chains become shorter and finally, this process leads to the formation of short fragments of chains having hydroxyl (-OH) and carboxyl end groups (-COOH), which become soluble in the degraded solution (Augustine *et al.*, 2014). This process might be continuous for the bulk degradation of monomer units of all polymers.

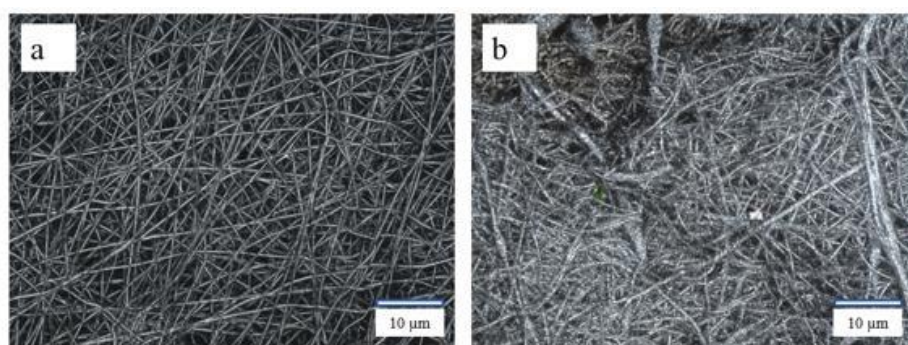


Figure 52: Representative laser microscopy images of degrading electrospun CB-1 scaffolds (a) before degradation and (b) after 7 weeks incubation in PBS solution

There are two main approaches by which used polymers can be hydrolyzed in this study: inactively by chemical hydrolysis or actively by enzymatic reaction. However, PCL and PLLA are such polymers that degrade by simple hydrolysis of the ester bond and do not require the presence of any enzymes to catalyze hydrolysis. Furthermore, the micrograph confirms that the degradation starts at the surface of the fibers and finally proceeds to the inner regions. The scratches formed in certain regions of the fiber indicate the amorphous parts, which are more susceptible to hydrolytic degradation. However, the narrow, unseparated regions represent the crystalline parts of the polymer.

The TEM image also proved the phase separation of PCL and PLLA in scaffold fibers and the affinity of nano-HAp towards the GEL surface as discussed in section 4.3.3. Therefore, the rate of hydrolytic degradation of both PCL and PLLA is affected by the degree of crystallinity and semi-crystalline nature of both polymers and has a poor affinity for degradation medium (Nithya R. & Sundaram NM., 2015). Despite this, PCL and PLLA have a slower degradation rate than GEL, but they provide a strong and inflexible shape for the scaffold, which is beneficial for biomedical applications of this scaffold. On the other hand, GEL shows greater affinity towards filler (Fu *et al.*, 2013; Beachley V. & Wen X., 2010) which is beneficial for binding the filler on the scaffold fiber. Such scaffold is highly preferable for biomedical applications especially for bone tissue engineering (Bolagen *et al.*, 2005; Haponiuk J. & Karlsson S., 2002).

Summary of *in vitro* Biomedical Analysis of Scaffolds

1. The declining order of hydrolytic degradation rate of scaffolds CB-6 to CB-1 within the 7-week study period was found by increasing the volume fraction percentage of filler in polymer blends.
2. The weight loss trends of each scaffold CB-1 to CB-6 were found to decline with increasing duration of *in vitro* degradation test and continued for 7 weeks.
3. After 2nd week of degradation test, the laser micrographs of scaffolds CB-6 to CB-1 showed that the surface of the scaffold fibers was broken and scratched which continued for 7 weeks.

CHAPTER 5

5. CONCLUSIONS AND RECOMMENDATIONS

5.1 Conclusions

1. FTIR spectra showed phosphate (PO_4^{3-}), hydroxyl (OH^-) and carbonate (CO_3^{2-}) ions as major functional groups of HAp. Thermal decomposition is an effective method for the removal of organic moieties and extraction of HAp from bone powder.
2. The EDX spectra showed average Ca/P molar ratio=1.87 (i.e. the ratio of nonstoichiometric HAp) and the presence of major elements; Ca, P and O with some trace elements (C, Na, Mg, Al and Si) in HAp.
3. The XRD pattern showed crystalline HAp with average particle size of 19.23 nm. The main diffraction peaks were found at 2θ values of 34.7850° , 33.1654° , 32.4240° , 49.7223° , 46.9548° and 34.2711° , with Miller indices of (211), (300), (112), (213), (222) and (202) close to the ICDD standard of HAp.
4. SEM micrographs showed the hexagonal shape of particles with agglomerated morphology.
5. TGA showed thermal stability of HAp at the temperature range of 100 – 1000 °C.
6. Zeta potential showed the negative surface charge (- 0.30EV) in HAp.
7. Physical, behavioural, autonomic effects, sensory response, respiratory and somatomotor effects of nano-HAp were observed normal and absent in the rats upto starting to 14 days.
8. No significant statistical difference in mean body weight between treated and vehicle groups from onset up to end of the study period ($p>0.05$).
9. No differences in absolute organ weight and the macroscopic examination of internal organs of the rats of experimental and vehicle groups.
10. The tested nano-HAp has a lethal 50% dose (LD_{50}) value exceeding 2000 mg/Kg of body weight which is consistent with globally harmonized system (GHS) of classification and labelling of chemicals.

11. FTIR spectra of composite scaffolds showed that polymers and fillers are well mixed. The shifting of peaks and the appearance of a new peak signify the molecular interaction between PCL, PLLA, GEL with VD3 and nano-HAp.
12. SEM micrographs showed that the fillers changed the morphology, shape, fiber diameter and the texture of the scaffold.
13. TEM micrographs of a single fiber showed that polymers are thermodynamically separable phases and the fillers possessed affinity only towards hydrophilic polymer (i.e., GEL).
14. Deformation behaviour of the scaffolds showed a brittle-to-ductile transition triggered by the incorporation of 3% to 12% fillers which is confirmed by the elastic modulus, tensile strength and strain at break as a function of filler concentration.
15. The decreasing trend of water drop contact angles (79° to 44.78°) with increasing filler concentration showed a hydrophilic nature of scaffolds and its water absorption ability.
16. The declining order of hydrolytic degradation rate of scaffolds CB-1, CB-4, CB-5 and CB-6 within 7 weeks was found by increasing the volume fraction percentage of nano-HAp in polymer blends.
17. The weight loss trend of each scaffolds CB-1 to CB-6 were declined with increasing duration of degradation and continued till 7 weeks of *in vitro* degradation in PBS solution.
18. *In vitro* degradation test showed the surface erosion and scratched in the scaffolds during study period.

5.2 Recommendations for Future Works

1. The concept and mechanism behind phase separation of each polymer in scaffolds using different microscopic techniques can be studied in detail for *in vivo* application of the scaffolds in bone tissue engineering.
2. The acute and sub-acute toxicity tests of nano-HAp by daily dosing of Albino Wistar rats of both sexes for a maximum period can be investigated in order to get wide-range toxic information about nano-HAp.

3. The histopathological analysis of internal organs (hearts, lungs, spleens, kidneys and livers) after dosing nano-HAp could be investigated to get cytotoxic information on nano-HAp.
4. Investigation of the mechanism of *in vitro* degradation can be further studied to understand its *in vivo* biomedical applications.

CHAPTER 6

6. SUMMARY

This study focuses on the conversion of biowastes to nano-HAp, a very important calcium phosphate-based biomaterial. This study's first goal is to use the thermal decomposition method to synthesize HAp from waste ostrich bone, then use the W/O microemulsion technique to segregate nano-HAp from the bulk of the particles. After that, the acute toxicity test was performed in Albino Wister rats according to OECD-420 guidelines and it was used as a filler with VD3 to prepare a polymer composite scaffold using electrospinning techniques. Then, investigations of the structure, morphology, micromechanical behaviour, wettability and *in vitro* degradation tests of the scaffolds were carried out. The structural properties of scaffolds were linked with their morphological, micromechanical and wettability properties, targeting their biomedical applications.

Chapter 1 introduces, in this context, the prime essence of the rationale behind the proposed research work and focuses on the needs for developing valuable biomaterials by utilizing locally available resources and then justification of the study. The objective of the research has been identified and is categorized into general and specific forms. The overall work performed to achieve the objectives of the research study is included in the specific objectives. Finally, this chapter includes the scope of the study, its limitations and its delimitations.

Chapter 2 deals with the extensive survey of literature around the thesis objective, provides an overview of related works and identifies a research gap from the literature survey of relevant works. The main summary of the literature works focuses on the explanation of the anatomy of human bone, its chemical composition, types, mineral composition, mechanical properties and healing mechanisms of fractured bones. In another part of the literature survey, it explains rigorously the different biogenic sources of HAp chiefly animal bones, as well as other unexplored sources and methods of extracting HAp from these sources. Finally, it focuses on the biomedical application chiefly in the fields of tissue engineering scaffold, drug delivery transporter, 3D printing composite and implant coating.

Chapter 3 summarizes the materials and methods used for the preparation of nano-HAp from ostrich bone powder, tools and techniques used for their characterization,

guidelines used for the acute toxicity test of nano-HAp and instruments used for fabrication, characterization and *in vitro* degradation study of the scaffolds.

Chapter 4 presents the results and discussion of experimental works.

Section 4.1: Nano-HAp Preparation and Characterization

The **FTIR spectroscopy** shows the presence of major groups such as phosphate (PO_4^{3-}), carbonate (CO_3^{2-}) and hydroxyl (OH^-) in HAp. The two-step thermal decomposition was satisfactory for removing organic moieties from the bone powder, with no absorption bands related to carbon-hydrogen or nitrogen-hydrogen bonds.

The **EDX analysis** suggested the elemental composition of HAp, which was primarily calcium, phosphorus and oxygen with trace amounts of carbon, sodium, magnesium, aluminium and silicon. The average Ca/P molar ratios of HAp were found in a range of 1.50 to 1.85, which is the range of nonstoichiometric HAp.

The crystalline nature of HAp after segregation using W/O microemulsion technique was confirmed by **XRD results**. The average particle size was found in the range of 36.44 nm to 19.23 nm before and after segregation respectively.

The phase analysis of segregated HAp showed that the major diffraction peaks at 2θ values of 34.7850° , 33.1654° , 32.4240° , 49.7223° , 46.9548° and 34.2711° with Miller indices (211), (300), (112), (213), (222) and (202) were in good agreement with the ICCD standard card no 00-09-0432 of HAp.

The **SEM** showed that two steps of thermal decomposition confirmed morphology and agglomerate condition of HAp. The hexagonal morphology of the particle with irregular shapes and sizes becomes more distinct after segregation.

The **TGA results** presented the mass loss pattern of HAp. It shows three inflection points with a negligible mass loss on heating from 100°C to 1000°C . This loss pattern is due to the exclusion of water and residual organic moieties and the partial dehydroxylation of HAp.

The average surface charge value of HAp (-3.06 mV) was confirmed by the **zeta potential analysis**.

Section 4.2: Acute Toxicity Analysis

The physical and behavioral effects of nano-HAp, including excitement and depression of the central nervous system (CNS), autonomic effects, sense reactions, effects on breathing and somatomotor effects, were all normal in the groups of rats that were studied. There were no differences in the exact and relative weights of the organs, the normal body weight, or a macroscopical look at the organs. These studies show that nano-HAp is not toxic.

The tested HAp had a 50% deadly dose (LD₅₀) that was higher than 2000 mg/Kg of body weight. This is in line with how GHS classifies and labels chemicals. It proved that nano-HAp can be used as a filler in making polymer composite scaffolds for biomedical uses.

Section 4.3: Characterization of Electrospun Biomedical Scaffolds

The **FTIR results** of scaffolds show that the polymers and fillers are well-blended and the shifting of peaks and the emergence of a new peak indicate a molecular interaction between the polymers VD3 and nano-HAp.

The **SEM results** showed that the fibers without filler have smooth morphology, but the addition of filler augmented the agglomerations of filler on the scaffold fibers.

The average fiber diameter increased from 0.17 μm to 4.34 μm with the addition of 0-3% of filler but decreased significantly (from 4.34 μm to 0.48 μm) on further increasing the 3% to 12% of the filler.

The decrease in fiber diameter may result in a larger surface area of fibers and enhanced micromechanical properties of the fibers.

The **TEM** micrographs of a single fiber proved that the polymers were in different phases and that the filler was attracted to the gelatin (GEL) which has hydrophilic nature compared to PCL and PLLA.

The **elastic modulus, tensile strength** and **strain at break** as a function of filler concentration provide evidence that the addition of 3 to 12% fillers caused a brittle-to-ductile transition of the fibers in the scaffolds. The increase in filler concentration helps the transition of the fibers from crazing to yielding by lowering the fiber diameter on increasing the filler % in the polymer blend, according to SEM micrographs of the fracture surface of scaffold fibers CB-4 and CB-6.

The results of water drop contact angle (WDCA) gives an idea of how rough the scaffold surface and its hydrophilic nature are. The decreasing trend of the WDCA contact angle (79° to 44.78°) on increasing filler percentage (3 to 12%) in turn intensifications the water absorption ability of the scaffolds. Lowering the contact angle value enhances the hydrophilic property of the scaffold surface and enhances the biodegradability of the scaffolds in aqueous medium.

Section 4.4: *In vitro* Biomedical Test of the Scaffolds

Owing to the crystalline state of fillers, the *in vitro* biomedical test of the scaffold showed that the scaffolds without fillers (CB-1) have a higher degradation rate in compared to scaffolds with fillers. On the basis of the percentage of filler the order of degradation was found CB-6<CB-5< CB-4< CB-1. The noticeable signs of breakage and scratch formation on the surface of scaffold were seen in optical laser micrographs after 2 weeks of *in vitro* degradation and the trends was continued until 7 weeks.

Chapters 5 and 6 present the conclusion and recommendations of the research works and the summary of the entire thesis, respectively.

REFERENCES

- Abdulrahman, I., Tijani, H. I., Mohammed, B. A., Saidu, H., Yusuf, H., Jibrin, M. N., & Mohammed, S. (2014). From Garbage to Biomaterials: An Overview on Eggshell- based Hydroxyapatite. *Journal of Materials*, **2014**: 1-6.
- Agbabiaka, O. G., Oladele, I. O., Akinwekomi, A. D., Adediran, A. A., Balogun, A. O., Olasunkanm, O. G., & Olayanju, T. M. A. (2020). Effect of Calcination Temperature on Hydroxyapatite Developed from Waste Poultry Eggshell. *Scientific African*, **8**:1-12.
- Agbeboh, N. I., Oladele, I. O., Daramola, O. O., Adediran, A. A., Olasukanmi, O. O., & Tanimola, M. O. (2020). Environmentally Sustainable Processes for the Synthesis of Hydroxyapatite. *Heliyon*, **6**(4): 1-13.
- Ain, Q., Munir, H., Jelani, F., Anjum, F., & Bilal, M. (2020). Antibacterial Potential of Biomaterial Derived Nanoparticles for Drug Delivery Application. *Materials Research Express*, **6**(12): 1-12. Doi: 10.1088/2053-1591/ab715d.
- Akhavan, K. (2012). Synthesis of Hydroxyapatite Nanoparticles trough Polyelectrolyte-modified Microemulsions. *International Journal of Nano Dimension (IJND)*, **3**(2): 121-125.
- Akram, M., Ahmed, R., Shakir, I., Ibrahim, W. A. W., & Hussain, R. (2014). Extracting Hydroxyapatite and its Precursors from Natural Resources. *Journal of Materials Science*, **49**(4): 1461–1475.
- Albanese, C. V., & Faletti, C. (2016). *Imaging of Prosthetic Joints*. Springer Verlag.
- Alshemary, A. Z., Akram, M., Goh, Y.-F., Tariq, U., Butt, F. K., Abdolahi, A., & Hussain, R. (2015). Synthesis, Characterization, *In-vitro* Bioactivity and Antimicrobial Activity of Magnesium and Nickel Doped Silicate Hydroxyapatite. *Ceramics International*, **41**(9): 11886–11898.
- Anderson, P. H. (2017). Vitamin D Activity and Metabolism in Bone. *Current Osteoporosis Reports*, **15**(5): 443–449.
- Anjaneyulu, U., Priyadarshini, B., Grace, A. N., & Vijayalakshmi, U. (2017). Fabrication and Characterization of Ag Doped Hydroxyapatite-polyvinyl Alcohol Composite Nanofibers and its In vitro Biological Evaluations for

- Bone Tissue Engineering Applications. *Journal of Sol-Gel Science and Technology*, **81**(3): 750–761.
- Arcos, D., & Vallet-Regí, M. (2020). Substituted Hydroxyapatite Coatings of Bone Implants. *Journal of Materials Chemistry B*, **8**(9): 1781–1800.
- Arsad, M. S., Lee, P. M., & Hung, L. K. (2011). Synthesis and Characterization of Hydroxyapatite Nanoparticles and β -TCP Particles. *2nd International Conference on Biotechnology and Food Science, IPCBEE*, 7, 184–188.
- Augustine, R., Kalarikkal, N., & Thomas, S. (2016). Effect of Zinc Oxide Nanoparticles on the In vitro Degradation of Electrospun Polycaprolactone Membranes in Simulated Body Fluid. *International Journal of Polymeric Materials and Polymeric Biomaterials*, **65**(1): 28–37.
- Ba Linh, N. T., Min, Y. K., & Lee, B.-T. (2013). Hybrid Hydroxyapatite Nanoparticles-loaded PCL/GE Blend Fibers for Bone Tissue Engineering. *Journal of Biomaterials Science, Polymer Edition*, **24**(5): 520–538.
- Bahrololoom, M. E., Javidi, M., Javadpour, S., & Ma, J. (2009). Characterization of Natural Hydroxyapatite Extracted from Bovine Cortical Bone Ash. *Journal of Ceramic Processing Research*, **10**(2): 129–138.
- Bakan, F. (2018). Gene Delivery by Hydroxyapatite and Calcium Phosphate Nanoparticles: A Review of Novel and Recent Applications. *Hydroxyapatite-Advances in Composite Nanomaterials, Biomedical Applications and Its Technological Facets*, 157–176.
- Bakhsheshi-Rad, H. R., Hamzah, E., Ismail, A. F., Aziz, M., Daroonparvar, M., Saebnoori, E., & Chami, A. (2018). In vitro Degradation Behaviour, Antibacterial Activity and Cytotoxicity of TiO₂-MAO/ZnHA Composite Coating on Mg Alloy for Orthopaedic Implants. *Surface and Coatings Technology*, **334**, 450–460.
- Balu, S., Sundaradoss, M. V. andra, S., & Jeevanandam, J. (2020). Facile Biogenic Fabrication of Hydroxyapatite Nanorods Using Cuttlefish Bone and Their Bactericidal and Biocompatibility Study. *Beilstein Journal of Nanotechnology*, **11**(1): 285–295.

- Bang, L. T., Ramesh, S., Purbolaksono, J., Ching, Y. C., Long, B. D., Chandran, H., & Othman, R. (2015). Effects of Silicate and Carbonate Substitution on the Properties of Hydroxyapatite Prepared by Aqueous Co-precipitation Method. *Materials & Design*, **87**: 788–796.
- Bano, N., Jikan, S. S., Basri, H., Adzila, S., & Zago, D. M. (2019). XRD and FTIR Study of A&B type Carbonated Hydroxyapatite Extracted from Bovine Bone. *AIP Conference Proceedings*, **2068**(1): 020100.
- Barakat, N. A., Khalil, K. A., Sheikh, F. A., Omran, A. M., Gaihre, B., Khil, S. M., & Kim, H. Y. (2008). Physiochemical Characterizations of Hydroxyapatite Extracted from Bovine Bones by Three Different Methods: Extraction of Biologically Desirable HAp. *Materials Science and Engineering: C*, **28**(8): 1381–1387.
- Barakat, N. A., Khil, M. S., Omran, A. M., Sheikh, F. A., & Kim, H. Y. (2009). Extraction of Pure Natural Hydroxyapatite from the Bovine Bone Biowaste by Three Different Methods. *Journal of Materials Processing Technology*, **209** (7): 3408–3415.
- Barhate, R. S., & Ramakrishna, S. (2007). Nanofibrous Filtering Media: Filtration Problems and Solutions from Tiny Materials. *Journal of Membrane Science*, **296**(1–2): 1–8.
- Barinov, S. M., Rau, J. V., Cesaro, S. N., Ďurišin, J., Fadeeva, I. V., Ferro, D., Medvecký, L., & Trionfetti, G. (2006). Carbonate Release from Carbonated Hydroxyapatite in the Wide Temperature Range. *Journal of Materials Science: Materials in Medicine*, **17**(7): 597–604.
- Beachley, V., & Wen, X. (2010). Polymer Nanofibrous Structures: Fabrication, Biofunctionalization and Cell Interactions. *Progress in Polymer Science*, **35**(7): 868–892.
- Macha, I. J., Ozyegin, L. S., Oktar, F. N., & Ben-Nissan, B. (2015). Conversion of Ostrich Eggshells (*Struthio camelus*) to Calcium Phosphates. *Journal of The Australian Ceramic Society*, **5**(1): 125-133.
- Ben-Nissan., & Pezzotti, G. (2002). Bioceramics Processing Routes and Mechanical Evaluation. *Journal of the Ceramic Society of Japan*, **110**(1283): 601–608.

- Ben-Nissan, B., & Pezzotti, G. (2004). Bioceramics: An Introduction. *In Engineering materials for biomedical applications*, 6–1.
- Bhandari, N. L., Bista, S., Gautam, T. R., Bist, K., Bhandari, G., Subedi, S., & Dhakal, K. N. (2021). An Overview of Synthesis Based Biomedical Applications of Hydroxyapatite Nanomaterials. *Journal of Nepal Chemical Society*, **42**(1): 64-74.
- Bhattarai, D. P., Aguilar, L. E., Park, C. H., & Kim, C. S. (2018). A Review on Properties of Natural and Synthetic Based Electrospun Fibrous Materials for Bone Tissue Engineering. *Membranes*, **8**(3): 62-69.
- Blazutti Marçal, R. L. S., Muniz Ferreira, J. R., Louro, L. H. L., Costa, A. M., Navarro da Rocha, D., de Campos, J. B., & Prado da Silva, M. H. (2017). Apatite Coatings from Ostrich Eggshell and its Bioactivity Assessment. *Key Engineering Materials*, **720**:185–188.
- Bölgen, N., Menceloğlu, Y. Z., Acatay, K., Vargel, İ., & Pişkin, E. (2005). In vitro and In vivo Degradation of Non-woven Materials Made of Poly (ϵ -caprolactone) Nanofibers Prepared by Electrospinning Under Different Conditions. *Journal of Biomaterials Science, Polymer Edition*, **16**(12): 1537-1555.
- Bose, S., Tarafder, S., & Bandyopadhyay, A. (2015). Hydroxyapatite Coatings for Metallic Implants. *In Hydroxyapatite (Hap) for biomedical applications* (pp. 143–157). Woodhead Publishing.
- Boutinguiza, M., Pou, J., Comesaña, R., Lusquiños, F., De Carlos, A., & León, B. (2012). Biological Hydroxyapatite Obtained from Fish Bones. *Materials Science and Engineering: C*, **32**(3): 478–486.
- Buckwalter, J. A., Glimcher, M. J., Cooper, R. R., & Recker, R. (1996). Bone Biology. II: Formation, form, Modeling, Remodeling and Regulation of Cell Function. *Instructional Course Lectures*, **45**: 387–399.
- Allen, M. R., & Burr, D. B. (2019). Bone Growth, Modeling and Remodeling. *In Basic and applied bone biology* Academic Press., 85-100.
- Chattanathank, T. P., Clement, T. P., Kanel, S. R., Barnett, M. O., & Chatakondi, N. G. (2013). Remediation of Uranium-contaminated Groundwater by Sorption

- onto Hydroxyapatite Derived from Catfish Bones. *Journal of Water Air and Soil Pollution*, **224**: 1429–1437.
- Organisation for Economic Co-operation and Development. (2002). *Test No. 420: Acute Oral Toxicity-Fixed Dose Procedure*. OECD Publishing.
- Chen, J., Lu, L., Wu, D., Yuan, L., Zhang, M., Hua, J., & Xu, J. (2014). Green Poly (ϵ -caprolactone) Composites Reinforced with Electrospun Polylactide/Poly (ϵ -caprolactone) Blend Fiber Mats. *ACS Sustainable Chemistry & Engineering*, **2**(9): 2102–2110.
- Chen, J., Wen, Z., Zhong, S., Wang, Z., Wu, J., & Zhang, Q. (2015). Synthesis of Hydroxyapatite Nanorods from Abalone Shells via Hydrothermal Solid-state Conversion. *Materials & Design*, **87**: 445–449.
- Chen, J.-P., & Chang, Y.-S. (2011). Preparation and Characterization of Composite Nanofibers of Polycaprolactone and Nanohydroxyapatite for Osteogenic Differentiation of Mesenchymal Stem Cells. *Colloids and Surfaces B: Biointerfaces*, **86**(1): 169–175.
- Colilla, M., Izquierdo-Barba, I., & Vallet-Regí, M. (2018). The Tole of Zwitterionic Materials in the Fight Against Proteins and Bacteria. *Medicines*, **5**(4): 125.
- Cooper, J. J., & Hunt, J. A. (2006). The Significance of Zeta Potential in Osteogenesis. *In Annual Meeting-Society for Biomaterials in Conjunction with the International Biomaterials Symposium*, **29**(2): 592.
- de Souza, D. C., de Abreu, H. de L. V., de Oliveira, P. V., Capelo, L. P., Passos-Bueno, M. R., & Catalani, L. H. (2019). A Fast-degrading PLLA Composite with a High Content of Functionalized Octacalcium Phosphate Mineral Phase induces stem cells differentiation. *Journal of the Mechanical Behavior of Biomedical Materials*, **93**: 93–104.
- Díaz, E., Sandonis, I., Puerto, I., & Ibáñez, I. (2014). In vitro Degradation of PLLA/nHA Composite Scaffolds. *Polymer Engineering & Science*, **54**(11): 2571–2578.
- Dimitriou, R., Jones, E., McGonagle, D., & Giannoudis, P. V. (2011). Bone Regeneration: Current Concepts and Future Directions. *BMC Medicine*, **9**(1): 1–10.

- Dinda, S., Bhagavatam, A., Alrehaili, H., & Dinda, G. P. (2020). Mechanochemical Synthesis of Nanocrystalline Hydroxyapatite from $\text{Ca}(\text{H}_2\text{PO}_4)_2 \cdot 2\text{H}_2\text{O}$, CaO , $\text{Ca}(\text{OH})_2$ and P_2O_5 Mixtures. *Nanomaterials*, **10**(11): 22-32.
- Dizaj, S. M., Mokhtarpour, M., Shekaari, H., & Sharifi, S. (2019). Hydroxyapatite-Gelatin Nanocomposite Films; Production and Evaluation of the Physicochemical Properties. *Journal of Advanced Chemical and Pharmaceutical Materials (JACPM)*, **2**(2): 111–115.
- Do, A.-V., Khorsand, B., Geary, S. M., & Salem, A. K. (2015). 3D Printing of Scaffolds for Tissue Regeneration Applications. *Advanced Healthcare Materials*, **4**(12): 1742–1762.
- Doostmohammadi, A., Monshi, A., Salehi, R., Fathi, M. H., Karbasi, S., Pieleś, U., & Daniels, A. U. (2012). Preparation, Chemistry and Physical Properties of Bone-Derived Hydroxyapatite Particles having a Negative Zeta Potential. *Materials Chemistry and Physics*, **132**(2–3): 446–452.
- Dorozhkin, S. V. (2010). Calcium Orthophosphates as Bioceramics: State of the Art. *Journal of Functional Biomaterials*, **1**(1): 22–107.
- Dorozhkin, S. V. (2010). Nanosized and Nanocrystalline Calcium Orthophosphates. *Acta Biomaterialia*, **6**(3): 715–734.
- Dorozhkin, S. V. (2016). Multiphasic Calcium Orthophosphate, $\text{Ca}_3(\text{PO}_4)_2$ Bioceramics and their Biomedical Applications. *Ceramics International*, **42**(6): 6529–6554.
- Elliott, J. C., Wilson, R. M., & Dowker, S. E. P. (2002). Apatite Structures. *Advances in X-Ray Analysis*, **45**: 172–181.
- Eslami, H., Tahriri, M., & Bakhshi, F. (2010). Synthesis and Characterization of Nanocrystalline Hydroxyapatite Obtained by the Wet Chemical Technique. *Materials Science-Poland*, **28**(1): 5–13.
- Esmailkhanian, A., Sharifianjazi, F., Abouchenari, A., Rouhani, A., Parvin, N., & Irani, M. (2019). Synthesis and Characterization of Natural Nano-Hydroxyapatite Derived from Turkey Femur-bone Waste. *Applied Biochemistry and Biotechnology*, **189**(3): 919–932.

- Fahmy, M. D., Jazayeri, H. E., Razavi, M., Masri, R., & Tayebi, L. (2016). Three-dimensional Bioprinting Materials with Potential Application in Preprosthetic Surgery. *Journal of Prosthodontics*, **25**(4): 310–318.
- Fang, R., Zhang, E., Xu, L., & Wei, S. (2010). Electrospun PCL/PLA/HA Based Nanofibers as Scaffold for Osteoblast-like Cells. *Journal of Nanoscience and Nanotechnology*, **10**(11): 7747–7751.
- Fathi, M. H., Hanifi, A., & Mortazavi, V. (2008). Preparation and Bioactivity Evaluation of Bone-like Hydroxyapatite Nanopowder. *Journal of Materials Processing Technology*, **202**(1–3): 536–542.
- Fayyazbakhsh, F., Solati-Hashjin, M., Keshtkar, A., Shokrgozar, M. A., Dehghan, M. M., & Larijani, B. (2017). Release Behavior and Signaling Effect of Vitamin D3 in Layered Double Hydroxides-hydroxyapatite/Gelatin Bone Tissue Engineering Scaffold: An In vitro evaluation. *Colloids and Surfaces B: Biointerfaces*, **158**: 697–708.
- Fazzalari, N. L. (2011). Bone Fracture and Bone Fracture Repair. *Osteoporosis International*, **22**(6): 2003–2006.
- Ferreira, A., Oliveira, C., & Rocha, F. (2003). The Different Phases in the Precipitation of Dicalcium Phosphate Dihydrate. *Journal of Crystal Growth*, **252**(4): 599–611.
- Ferreira, J. R. M., Louro, L. H. L., Costa, A. M., de Campos, J. B., & Silva, M. H. (2016). Ostrich Eggshell as Calcium Source for the Synthesis of Hydroxyapatite and Hydroxyapatite Partially Substituted with Zinc. *Cerâmica*, **62**: 386–391.
- Ferreira, J. R. M., Navarro da Rocha, D., Louro, L. H. L., & Prado da Silva, M. H. (2014). Phosphating of Calcium Carbonate for Obtaining Hydroxyapatite from the Ostrich Eggshell. *In Key Engineering Materials*, **587**: 69–73.
- Fu, Q., Saiz, E., Rahaman, M. N., & Tomsia, A. P. (2013). Tissue Engineering: Toward Strong and Tough Glass and Ceramic Scaffolds for Bone Repair. *Advanced Functional Materials*, **23**(44): 5460–5460.

- Ganachari, S. V., Bevinakatti, A. A., Yaradoddi, J. S., Banapurmath, N. R., Hunashyal, A. M., & Shettar, A. S. (2016). Rapid Synthesis, Characterization and Studies of Hydroxyapatite Nanoparticles. *Advance Mater Science Research*, **1**(1): 9-13.
- Gergely, G., Wéber, F., Lukács, I., Tóth, A. L., Horváth, Z. E., Mihály, J., & Balázs, C. (2010). Preparation and Characterization of Hydroxyapatite from Eggshell. *Ceramics International*, **36**(2): 803–806.
- Ghiasi, B., Sefidbakht, Y., & Rezaei, M. (2019). Hydroxyapatite for Biomedicine and Drug Delivery. *Nanomaterials for Advanced Biological Applications*, 85–120.
- Ghosh, S., Ghosh, S., Jana, S. K., & Pramanik, N. (2020). Biomedical Application of Doxorubicin Coated Hydroxyapatite—Poly(lactide-co-glycolide) Nanocomposite for Controlling Osteosarcoma Therapeutics. *Journal of Nanoscience and Nanotechnology*, **20**(7): 3994–4004.
- Gopi, D., Indira, J., Kavitha, L., Sekar, M., & Mudali, U. K. (2012). Synthesis of Hydroxyapatite Nanoparticles by a Novel Ultrasonic Assisted with Mixed Hollow Sphere Template Method. *Spectrochimica Acta Part A: Molecular and Biomolecular Spectroscopy*, **93**: 131–134.
- Goulart, C. O., Lopes, F. R. P., Monte, Z. O., Dantas Jr, S. V., Souto, A., Oliveira, J. T., Almeida, F. M., Tonda-Turo, C., Pereira, C. C., & Borges, C. P. (2016). Evaluation of Biodegradable Polymer Conduits—poly (L-lactic acid)—for Guiding Sciatic Nerve Regeneration in Mice. *Methods*, **99**: 28–36.
- Guimond-Lischer, S., Ren, Q., Braissant, O., Gruner, P., Wampfler, B., & Maniura-Weber, K. (2016). Vacuum Plasma Sprayed Coatings Using Ionic Silver Doped Hydroxyapatite Powder to Prevent Bacterial Infection of Bone Implants. *Biointerphases*, **11**(1): 011012.
- Guo, L., Li, B., & Zhang, C. (2020). Optimization of Process Parameters for Preparation of Hydroxyapatite by the Sol–gel Method. *Journal of Sol-Gel Science and Technology*, **96**(1): 247–255.
- Haberko, K., Bućko, M. M., Brzezińska-Miecznik, J., Haberko, M., Mozgawa, W., Panz, T., Pyda, A., & Zarębski, J. (2006). Natural Hydroxyapatite—Its

- Behaviour During Heat Treatment. *Journal of the European Ceramic Society*, **26**(4–5): 537–542.
- Haider, A., Gupta, K. C., & Kang, I.-K. (2014). PLGA/nHA Hybrid Nanofiber Scaffold as a Nanocargo Carrier of Insulin for Accelerating Bone Tissue Regeneration. *Nanoscale Research Letters*, **9**(1): 1–12.
- Haider, A., Haider, S., Han, S. S., & Kang, I.-K. (2017). Recent Advances in the Synthesis, Functionalization and Biomedical Applications of Hydroxyapatite: A Review. *Rsc Advances*, **7**(13): 7442–7458.
- Haleem, A., Javaid, M., Khan, R. H., & Suman, R. (2020). 3D Printing Applications in Bone Tissue Engineering. *Journal of Clinical Orthopaedics and Trauma*, **11**: S118–S124.
- Hanh, N. T., Bich, P. T. N., & Thao, H. T. T. (2019). Acute and Subchronic Oral Toxicity Assessment of Calcium Hydroxyapatite-alginate in Animals. *Vietnam Journal of Chemistry*, **57**(1): 16–20.
- Hannink, G., & Arts, J. C. (2011). Bioresorbability, Porosity and Mechanical Strength of Bone Substitutes: What is Optimal for Bone Regeneration? *Injury*, **42**: S22–S25.
- Haponiuk, J., & Karlsson, S. (2002). Biodegradation of Modified Poly (ϵ -caprolactone) in Different Environments. *Polish Journal of Environmental Studies*, **11**(4): 413–420.
- Hart, A., Ebiundu, K., Peretomode, E., Onyeaka, H., Nwabor, O. F., & Oibileke, K. (2022). Value-added Materials Recovered from Waste Bone Biomass: Technologies and Applications. *RSC Advances*, **12**(34): 22302–22330.
- Harun, W. S. W., Asri, R. I. M., Alias, J., Zulkifli, F. H., Kadirgama, K., Ghani, S. A. C., & Shariffuddin, J. H. M. (2018). A Comprehensive Review of Hydroxyapatite-based Coatings Adhesion on Metallic Biomaterials. *Ceramics International*, **44**(2): 1250–1268.
- Hassan, M. I., Sultana, N., & Hamdan, S. (2014). Bioactivity Assessment of Poly (ϵ -caprolactone)/Hydroxyapatite Electrospun Fibers for Bone Tissue Engineering Application. *Journal of Nanomaterials*, **2014**: 1-6.

- Hassan, M. N., Mahmoud, M. M., Abd El-Fattah, A., & Kandil, S. (2015). Microwave Rapid Conversion of Sol–gel-derived Hydroxyapatite into β -tricalcium Phosphate. *Journal of Sol-Gel Science and Technology*, **76**(1): 74–81.
- Heidari, M., Bahrami, S. H., Ranjbar-Mohammadi, M., & Milan, P. B. (2019). Smart Electrospun Nanofibers Containing PCL/Gelatin/Graphene Oxide for Application in Nerve Tissue Engineering. *Materials Science and Engineering: C*, **103**: 109768.
- Hong, Z., Qiu, X., Sun, J., Deng, M., Chen, X., & Jing, X. (2004). Grafting Polymerization of L-lactide on the Surface of Hydroxyapatite Nano-crystals. *Polymer*, **45**(19): 6699–6706.
- Hossain, S., Fatema, U. K., Mollah, M. Y. A., & Rahman, M. M. (2012). Microemulsions as Nanoreactors for Preparation of Nanoparticles with Antibacterial Activity. *Journal of the Bangladesh Chemical Society*, **25**(1): 71–79.
- Hossan, M. J., Gafur, M. A., Karim, M. M., & Rana, A. A. (2015). Mechanical Properties of Gelatin Hydroxyapatite Composite for Bone Tissue Engineering. *Bangladesh Journal of Scientific and Industrial Research*, **50**(1): 15–20.
- Hoyer, B., Bernhardt, A., Heinemann, S., Stachel, I., Meyer, M., & Gelinsky, M. (2012). Biomimetically Mineralized Salmon Collagen Scaffolds for Application in Bone Tissue Engineering. *Biomacromolecules*, **13**(4): 1059–1066.
- Huang, F. L., Wang, Q. Q., Wei, Q. F., Gao, W. D., Shou, H. Y., & Jiang, S. D. (2010). Dynamic Wettability and Contact Angles of Poly (vinylidene fluoride) Nanofiber Membranes Grafted with Acrylic Acid. *Express Polymer Letters*, **4**(9): 551-558.
- Huang, Y., Zhang, X., Qiao, H., Hao, M., Zhang, H., Xu, Z., Zhang, X., Pang, X., & Lin, H. (2016). Corrosion Resistance and Cytocompatibility Studies of Zinc-Doped Fluorohydroxyapatite Nanocomposite Coatings on Titanium Implant. *Ceramics International*, **42**(1): 1903–1915.

- Huang, Y.-C., Hsiao, P.-C., & Chai, H.-J. (2011). Hydroxyapatite Extracted from Fish Scale: Effects on MG63 Osteoblast-like Cells. *Ceramics International*, **37**(6): 1825–1831.
- Indira, J., & Malathi, K. S. (2021). Comparison of Template Mediated Ultrasonic and Microwave Irradiation Method on the Synthesis of Hydroxyapatite Nanoparticles for Biomedical Applications. *Materials Today: Proceedings*, **51**: 765-1769.
- Irfan, M., Suprajaa, P. S., Baraneedharan, P., & Reddy, B. M. (2020). A Comparative Study of Nanohydroxyapatite Obtained from Natural Shells and Wet Chemical Process. *Journal of Materials Science & Surface Engineering*, **7**(1): 938–943.
- Irfan, M., Suprajaa, P. S., Praveen, R., & Reddy, B. M. (2021). Microwave-assisted One-step Synthesis of Nanohydroxyapatite from Fish Bones and Mussel Shells. *Materials Letters*, **282**: 1–4.
- Ishack, S., Mediero, A., Wilder, T., Ricci, J. L., & Cronstein, B. N. (2017). Bone Regeneration in Critical Bone Defects Using Three-dimensionally Printed β -tricalcium Phosphate/Hydroxyapatite Scaffolds is Enhanced by Coating Scaffolds with Either Dipyrindamole or BMP-2. *Journal of Biomedical Materials Research Part B: Applied Biomaterials*, **105**(2): 366–375.
- Ismail, S. A., & Abdullah, H. Z. (2020). Extraction and Characterization of Natural Hydroxyapatite from Goat Bone for Biomedical Applications. *Materials Science Forum*, **1010**: 573–578.
- Ivankovic, H., Tkalcec, E., Orlic, S., Ferrer, G. G., & Schauerl, Z. (2010). Hydroxyapatite Formation from Cuttlefish Bones: Kinetics. *Journal of Materials Science: Materials in Medicine*, **21**(10): 2711–2722.
- Iyer, K. M. (2019). Anatomy of Bone, Fracture and Fracture Healing. In *General Principles of Orthopedics and Trauma* (pp. 1-17). Springer, Cham.
- Jaber, H. L., Hammood, A. S., & Parvin, N. (2018). Synthesis and Characterization of Hydroxyapatite Powder from Natural Camelus Bone. *Journal of the Australian Ceramic Society*, **54**(1): 1–10.

- Jaiswal, A. K., Chhabra, H., Soni, V. P., & Bellare, J. R. (2013). Enhanced Mechanical Strength and Biocompatibility of Electrospun Polycaprolactone-gelatin Scaffold with Surface Deposited Nano-hydroxyapatite. *Materials Science and Engineering: C*, **33**(4): 2376–2385.
- Janković, A., Eraković, S., Mitrić, M., Matić, I. Z., Juranić, Z. D., Tsui, G. C., Tang, C., Mišković-Stanković, V., Rhee, K. Y., & Park, S. J. (2015). Bioactive Hydroxyapatite/Graphene Composite Coating and its Corrosion Stability in Simulated Body Fluid. *Journal of Alloys and Compounds*, **624**: 148–157.
- Januariyasa, I. K., Ana, I. D., & Yusuf, Y. (2020). Nanofibrous Poly (vinyl alcohol)/Chitosan Contained Carbonated Hydroxyapatite Nanoparticles Scaffold for Bone Tissue Engineering. *Materials Science and Engineering: C*, **107**: 1–13. <https://doi.org/10.1016/j.msec.2019.110347>.
- Janus, A. M., Faryna, M., Haberko, K., Rakowska, A., & Panz, T. (2008). Chemical and Microstructural Characterization of Natural Hydroxyapatite Derived from Pig Bones. *Microchimica Acta*, **161**(3): 349–353.
- Jena, P. (2007). *Synthesis and Characterization of Hydroxyapatite*. Engineering and Technology, Department of Ceramic Engineering, National Institute of Technology, Rourkela, Odisha-769008, India.
- Kareem, M. M. (2018). *Composite Bone Tissue Engineering Scaffolds Produced by Coaxial Electrospinning*. Biomedical Engineering Division School of Engineering College of Science and Engineering, University of Glasgow, Scotland, UK.
- Kato, H., Ochiai-Shino, H., Onodera, S., Saito, A., Shibahara, T., & Azuma, T. (2015). Promoting Effect of 1, 25 (OH) 2 Vitamin D3 in Osteogenic Differentiation from Induced Pluripotent Stem Cells to Osteocyte-like Cells. *Open Biology*, **5**(2): 140201.
- Katsogiannis, K. A. G., Vladislavljević, G. T., & Georgiadou, S. (2015). Porous Electrospun Polycaprolactone (PCL) Fibres by Phase Separation. *European Polymer Journal*, **69**: 284–295.
- Kehoe, S. (2008). Optimisation of Hydroxyapatite (HAp) for Orthopaedic Application Via the Chemical Precipitation Technique. Department of

Chemistry, Dublin City University, Collins Ave Ext, Whitehall, Doubling, Ireland.

- Khiri, M. Z. A., Matori, K. A., Zainuddin, N., Abdullah, C. A. C., Alassan, Z. N., Baharuddin, N. F., & Zaid, M. H. M. (2016). The Usability of Ark Clam Shell (*Anadara granosa*) as Calcium Precursor to Produce Hydroxyapatite Nanoparticle via Wet Chemical Precipitate Method in Various Sintering Temperature. *SpringerPlus*, **5**(1): 1-15.
- Khoo, W., Nor, F. M., Ardhyanta, H., & Kurniawan, D. (2015). Preparation of Natural Hydroxyapatite from Bovine Femur Bones Using Calcination at Various Temperatures. *Procedia Manufacturing*, **2**: 196–201.
- Kiani, A., Fathi, M., & Ghasemi, S. M. (2017). Production of Novel Vitamin D3 Loaded Lipid Nanocapsules for Milk Fortification. *International Journal of Food Properties*, **20**(11): 2466–2476.
- Kim, B.-S., Kang, H. J., Yang, S.-S., & Lee, J. (2014). Comparison of *In vitro* and *In vivo* Bioactivity: Cuttlefish-bone-derived Hydroxyapatite and Synthetic Hydroxyapatite Granules as a Bone Graft Substitute. *Biomedical Materials*, **9**(2): 025004. doi:10.1088/1748-6041/9/2/025004.
- Kim, C. H., Khil, M. S., Kim, H. Y., Lee, H. U., & Jahng, K. Y. (2006). An improved Hydrophilicity via Electrospinning for Enhanced Cell Attachment and Proliferation. *Journal of Biomedical Materials Research Part B: Applied Biomaterials: An Official Journal of The Society for Biomaterials, The Japanese Society for Biomaterials and The Australian Society for Biomaterials and the Korean Society for Biomaterials*, **78**(2): 283–290.
- Kim, H.-W., Song, J.-H., & Kim, H.-E. (2005). Nanofiber Generation of Gelatin–hydroxyapatite Biomimetics for Guided Tissue Regeneration. *Advanced Functional Materials*, **15**(12): 1988–1994.
- Kim, M. H., Yun, C., Chalisserry, E. P., Lee, Y. W., Kang, H. W., Park, S.-H., Jung, W.-K., Oh, J., & Nam, S. Y. (2018). Quantitative Analysis of the Role of Nanohydroxyapatite (nHA) on 3D-printed PCL/nHA Composite Scaffolds. *Materials Letters*, **220**: 112–115.

- Klinkaewnarong, J., & Utara, S. (2018). Ultrasonic-assisted Conversion of Limestone into Needle-like Hydroxyapatite Nanoparticles. *Ultrasonics Sonochemistry*, **46**: 18–25.
- Kodali, D., Hembrick-Holloman, V., Gunturu, D. R., Samuel, T., Jeelani, S., & Rangari, V. K. (2022). Influence of Fish Scale-Based Hydroxyapatite on Forcespun Polycaprolactone Fiber Scaffolds. *ACS Publications*, **7**(10): 8323–8335.doi: 10.1021/acsomega,1c05593.
- Kongsri, S., Janpradit, K., Buapa, K., Techawongstien, S., & Chanthai, S. (2013). Nanocrystalline Hydroxyapatite from Fish Scale Waste: Preparation, Characterization and Application for Selenium Adsorption in Aqueous Solution. *Chemical Engineering Journal*, **215**: 522–532.
- Kulanthaivel, S., Mishra, U., Agarwal, T., Giri, S., Pal, K., Pramanik, K., & Banerjee, I. (2015). Improving the Osteogenic and Angiogenic Properties of Synthetic Hydroxyapatite by Dual Doping of Bivalent Cobalt and Magnesium Ion. *Ceramics International*, **41**(9): 11323–11333.
- Kumar, G. S., Karunakaran, G., Girija, E. K., Kolesnikov, E., Van Minh, N., Gorshenkov, M. V., & Kuznetsov, D. (2018). Size and Morphology-controlled Synthesis of Mesoporous Hydroxyapatite Nanocrystals by Microwave-assisted Hydrothermal Method. *Ceramics International*, **44**(10): 11257–11264.
- Kumar, P. A., Irudhayam, J. S., & Naviin, D. (2012). A Aeviuw on importance and Recent Applications of Polymer Composites in Orthopaedics. *International Journal of Engineering Research and Development*, **5**(2): 40–43.
- Kwak, S., Haider, A., Gupta, K. C., Kim, S., & Kang, I.-K. (2016). Micro/Nano Multilayered Scaffolds of PLGA and Collagen by Alternately Electrospinning for Bone Tissue Engineering. *Nanoscale Research Letters*, **11**(1): 1–16.
- Lach R., Adhikari R., Giri J., Malla Komal P., Henning S., & Grellmann W. (2023). Morphology and Performance of Natural Fibre-Renforced and Biobased-Filled Polymer Materials. *Polymer Composites*, 2023 Tabor, Czech republic.

- Le Ray, A.-M., Gautier, H., Laty, M.-K., Daculsi, G., Merle, C., Jacqueline, C., Hamel, A., & Caillon, J. (2005). In vitro and In vivo Bactericidal Activities of Vancomycin Dispersed in Porous Biodegradable Poly (ϵ -caprolactone) Microparticles. *Antimicrobial Agents and Chemotherapy*, **49**(7): 3025–3027.
- Lee, J. B., Park, H. N., Ko, W.-K., Bae, M. S., Heo, D. N., Yang, D. H., & Kwon, I. K. (2013). Poly (L-lactic acid)/Hydroxyapatite Nanocylinders as Nanofibrous Structure for Bone Tissue Engineering Scaffolds. *Journal of Biomedical Nanotechnology*, **9**(3): 424–429.
- Lei, B., Guo, B., Rambhia, K. J., & Ma, P. X. (2019). Hybrid Polymer Biomaterials for Bone Tissue Regeneration. *Frontiers of Medicine*, **13**(2): 189–201.
- Lett, J. A., Sundareswari, M., & Ravichandran, K. (2016). Porous Hydroxyapatite Scaffolds for Orthopedic and Dental Applications-the Role of Binders. *Materials Today: Proceedings*, **3**(6): 1672–1677.
- Lieberman, J. R., & Friedlaender, G. E. (2005). *Bone regeneration and repair: Biology and clinical applications*. Humana Press.
- Lien, Y.-H., Wu, J.-H., Liao, J.-W., & Wu, T.-M. (2013). In vitro Evaluation of the Thermosensitive and Magnetic Nanoparticles for the Controlled Drug Delivery of Vitamin D 3. *Macromolecular Research*, **21**(5): 511–518.
- Linh, N. T. B., & Lee, B.-T. (2012). Electrospinning of Polyvinyl Alcohol/gelatin Nanofiber Composites and Cross-linking for Bone Tissue Engineering Application. *Journal of Biomaterials Applications*, **27**(3): 255–266.
- Linh, N. T. B., Min, Y. K., & Lee, B.-T. (2013). Fabrication and in Vitro Evaluations with Osteoblast-like MG-63 Cells of Porous Hyaluronic Acid-gelatin Blend Scaffold for Bone Tissue Engineering Applications. *Journal of Materials Science*, **48** (12): 4233–4242.
- Liu, A., Xue, G., Sun, M., Shao, H., Ma, C., Gao, Q., Gou, Z., Yan, S., Liu, Y., & He, Y. (2016). 3D Printing Surgical Implants at the Clinic: An Experimental Study on Anterior Cruciate Ligament Reconstruction. *Scientific Reports*, **6** (1): 1–13.
- Londoño-Restrepo, S. M., Jeronimo-Cruz, R., Millán-Malo, B. M., Rivera-Muñoz, E. M., & Rodríguez-García, M. E. (2019). Effect of the Nano Crystal size on the

- X-ray Diffraction Patterns of Biogenic Hydroxyapatite from Human, Bovine and Porcine Bones. *Scientific Reports*, **9** (1): 1–12.
- Londoño-Restrepo, S. M., Ramirez-Gutierrez, C. F., del Real, A., Rubio-Rosas, E., & Rodriguez-García, M. E. (2016). Study of Bovine Hydroxyapatite Obtained by Calcination at Low Heating Rates and Cooled in Furnace air. *Journal of Materials Science*, **51**(9): 4431–4441.
- López-Noriega, A., Quinlan, E., Celikkin, N., & O'Brien, F. J. (2015). Incorporation of Polymeric Microparticles into Collagen-hydroxyapatite Scaffolds for the Delivery of a Pro-osteogenic Peptide for Bone Tissue Engineering. *APL Materials*, **3**(1): 014910.
- Lü, X. Y., Fan, Y. B., Gu, D., & Cui, W. (2007). Preparation and Characterization of Natural Hydroxyapatite from Animal Hard Tissues. *Key Engineering Materials*, **342**: 213–216.
- Lu, Y., Dong, W., Ding, J., Wang, W., & Wang, A. (2019). Hydroxyapatite Nanomaterials: Synthesis, Properties and Functional Applications. *Nanomaterials from Clay Minerals Elsevier*, 485–536.
- Ma, X., Chen, Y., Qian, J., Yuan, Y., & Liu, C. (2016). Controllable Synthesis of Spherical Hydroxyapatite Nanoparticles Using Inverse Microemulsion Method. *Materials Chemistry and Physics*, **183**: 220–229.
- Macha, I. J., Ozyegin, L. S., Oktar, F. N., & Ben-Nissan, B. (2015). Conversion of Ostrich Eggshells (*Struthio camelus*) to Calcium Phosphates. *Journal of The Australian Ceramic Society*, **5**(1):125-133.
- Madhumathi, K., Kumar, P. S., Kavya, K. C., Furuike, T., Tamura, H., Nair, S. V., & Jayakumar, R. (2009). Novel Chitin/Nanosilica Composite Scaffolds for Bone Tissue Engineering Applications. *International Journal of Biological Macromolecules*, **45**(3): 289–292.
- Maleki-Dizaj, S., Mokhtarpour, M., Shekaari, H., & Sharifi, S. (2019). Hydroxyapatite-Gelatin Nanocomposite Films; Production and Evaluation of the Physicochemical Properties. *Journal of Advanced Chemical and Pharmaceutical Materials*, **2**(2): 111-115.

- Malla, K. P., Regmi, S., Nepal, A., Bhattarai, S., Yadav, R. J., Sakurai, S., & Adhikari, R. (2020). Extraction and Characterization of Novel Natural Hydroxyapatite Bioceramic by Thermal Decomposition of Waste Ostrich Bone. *International Journal of Biomaterials*, 2020, 1-10, Article ID 1690178. doi:10.1155/2020/1690178.
- Manalu, J., Soegijono, B., & Indrani, D. J. (2015). Characterization of Hydroxyapatite Derived from Bovine Bone. *Asian Journal of Applied Sciences*, 3(4): 758-765.
- Marins, N. H., Lee, B. E., e Silva, R. M., Raghavan, A., Carreño, N. L. V., & Grandfield, K. (2019). Niobium Pentoxide and Hydroxyapatite Particle Loaded Electrospun Polycaprolactone/Gelatin Membranes for Bone Tissue Engineering. *Colloids and Surfaces B: Biointerfaces*, 182, 110386.
- Martínez-Vázquez, F. J., Cabañas, M. V., Paris, J. L., Lozano, D., & Vallet-Regí, M. (2015). Fabrication of Novel Si-doped Hydroxyapatite/Gelatine Scaffolds by Rapid Prototyping for Drug Delivery and Bone Regeneration. *Acta Biomaterialia*, 15: 200–209.
- McKinley, T. (2003). Principles of Fracture Healing. *Surgery (Oxford)*, 21(9): 209–212.
- Mellon, S. J., & Tanner, K. E. (2012). Bone and its Adaptation to Mechanical Loading: A review. *International Materials Reviews*, 57(5): 235–255.
- Meng, Z. X., Wang, Y. S., Ma, C., Zheng, W., Li, L., & Zheng, Y. F. (2010). Electrospinning of PLGA/Gelatin Randomly-oriented and Aligned Nanofibers as Potential Scaffold in Tissue Engineering. *Materials Science and Engineering: C*, 30 (8): 1204 –1210.
- Meski, S., Tazibt, N., Khireddine, H., Ziani, S., Biba, W., Yala, S., Sidane, D., Boudjouan, F., & Moussaoui, N. (2019). Synthesis of Hydroxyapatite from Mussel Shells for Effective Adsorption of Aqueous Cd (II). *Water Science and Technology*, 80 (7): 1226–1237.

- Mi, H.-Y., Jing, X., Salick, M. R., Cordie, T. M., Peng, X.-F., & Turng, L.-S. (2014). Morphology, Mechanical Properties and Mineralization of Rigid Thermoplastic Polyurethane/Hydroxyapatite Scaffolds for Bone Tissue Applications: Effects of Fabrication Approaches and Hydroxyapatite Size. *Journal of Materials Science*, **49** (5): 2324–2337.
- Mi, H.-Y., Palumbo, S., Jing, X., Turng, L.-S., Li, W.-J., & Peng, X.-F. (2014). Thermoplastic Polyurethane/Hydroxyapatite Electrospun Scaffolds for Bone Tissue Engineering: Effects of Polymer Properties and Particle Size. *Journal of Biomedical Materials Research Part B: Applied Biomaterials*, **102** (7): 1434–1444.
- Michler, G. H. (2008). Transmission electron microscopy: Conventional and Special Investigations of Polymers. In: *Electron Microscopy of Polymers. Springer Laboratory. Springer, Berlin, Heidelberg*. https://doi.org/10.1007/978-3-540-36352-1_4
- Michler, G. H., & Lebek, W. (2016). Electron Microscopy of Polymers. Polymer Morphology: Principles, Characterization and Processing. *Hoboken, New Jersey: Wiley*, 37–54.
- Miculescu, F., Ciocan, L., Miculescu, M., & Ernuteanu, A. (2011). Effect of Heating Process on Micro Structure Level of Cortical Bone Prepared for Compositional Analysis. *Dig. J. Nanomater. Biostruct*, **6**: 225–233.
- Mihailescu, N., Stan, G. E., Duta, L., Chifiriuc, M. C., Bleotu, C., Sopronyi, M., Luculescu, C., Oktar, F. N., & Mihailescu, I. N. (2016). Structural, Compositional, Mechanical Characterization and Biological Assessment of Bovine-derived Hydroxyapatite Coatings Reinforced with MgF₂ or MgO for Implants Functionalization. *Materials Science and Engineering: C*, **59**: 863–874.
- Milovanovic, S., Markovic, D., Mrakovic, A., Kuska, R., Zizovic, I., Frerich, S., & Ivanovic, J. (2019). Supercritical CO₂-Assisted Production of PLA and PLGA Foams for Controlled Thymol Release. *Materials Science and Engineering: C*, **99**: 394–404.

- Mirza, A. C., & Panchal, S. S. (2020). Safety Assessment of Vanillic Acid: Subacute Oral Toxicity Studies in Wistar Rats. *Turkish Journal of Pharmaceutical Sciences*, **17** (4): 432.
- Mondal, B., Mondal, S., Mondal, A., & Mandal, N. (2016). Fish Scale Derived Hydroxyapatite Scaffold for Bone Tissue Engineering. *Materials Characterization*, **121**, 112–124.
- Mondal, S., Dorozhkin, S. V., & Pal, U. (2018). Recent Progress on Fabrication and Drug Delivery Applications of Nanostructured Hydroxyapatite. *Wiley Interdisciplinary Reviews: Nanomedicine and Nanobiotechnology*, **10**(4), e1504.
- Mondal, S., & Pal, U. (2019). 3D Hydroxyapatite Scaffold for Bone Regeneration and Local Drug Delivery Applications. *Journal of Drug Delivery Science and Technology*, **53**, 101131.
- Mosa, I. F., Abd, H. H., Abuzreda, A., Yousif, A. B., & Assaf, N. (2021). Chitosan and Curcumin Nanoformulations against Potential Cardiac Risks Associated with Hydroxyapatite Nanoparticles in Wistar Male Rats. *International Journal of Biomaterials*, **2021**:1-19. <https://doi.org/10.1155/2021/3394348>.
- Mota, C., Puppi, D., Dinucci, D., Gazzarri, M., & Chiellini, F. (2013). Additive Manufacturing of Star poly (ϵ -caprolactone) Wet-spun Scaffolds for Bone Tissue Engineering Applications. *Journal of Bioactive and Compatible Polymers*, **28** (4): 320–340.
- MubarakAli, D. (2019). Microwave Irradiation Mediated Synthesis of Needle-shaped Hydroxyapatite Nanoparticles as a Flocculant for *Chlorella Vulgaris*. *Biocatalysis and Agricultural Biotechnology*, **17**: 203–206.
- Mustafa, N., Ibrahim, M. H. I., Asmawi, R., & Amin, A. M. (2015). Hydroxyapatite Extracted from Waste Fish Bones and Scales via Calcination Method. *Applied Mechanics and Materials*, **773**: 287–290.

- Naeimi, M., Rafienia, M., Fathi, M., Janmaleki, M., Bonakdar, S., & Ebrahimian-Hosseiniabadi, M. (2016). Incorporation of Chitosan Nanoparticles into Silk Fibroin-based Porous Scaffolds: Chondrogenic Differentiation of Stem cells. *International Journal of Polymeric Materials and Polymeric Biomaterials*, **65** (4): 202–209.
- Nahavandizadeh, N., & Rezaei, M. (2020). Preparation of Shape Memory Polyurethane/Hydroxyapatite Nanocomposite Scaffolds by Electrospinning Method and Investigation of Their Microstructure and Physical-Mechanical Properties. *Polymer-Plastics Technology and Materials*, **59** (14): 1562–1573.
- Nakamura, H. (2007). Morphology, Function and Differentiation of Bone Cells. *Journal of Hard Tissue Biology*, **16** (1): 15–22.
- Narayanan, G., Gupta, B. S., & Tonelli, A. E. (2015). Enhanced Mechanical Properties of Poly (ϵ -caprolactone) Nanofibers Produced by the Addition of Non-stoichiometric Inclusion Complexes of Poly (ϵ -caprolactone) and α -cyclodextrin. *Polymer*, **76**: 321–330.
- Neira, I. S., Kolen'ko, Y. V., Lebedev, O. I., Van Tendeloo, G., Gupta, H. S., Guitián, F., & Yoshimura, M. (2009). An Effective Morphology Control of Hydroxyapatite Crystals via Hydrothermal Synthesis. *Crystal Growth and Design*, **9** (1): 466–474.
- Nga, N. K., Giang, L. T., Huy, T. Q., Viet, P. H., & Migliaresi, C. (2014). Surfactant-Assisted Size Control of Hydroxyapatite Nanorods for Bone Tissue Engineering. *Colloids and Surfaces B: Biointerfaces*, **116**: 666–673.
- Nirmala, R., Sheikh, F. A., Kanjwal, M. A., Lee, J. H., Park, S.-J., Navamathavan, R., & Kim, H. Y. (2011). Synthesis and Characterization of Bovine Femur Bone Hydroxyapatite Containing Silver Nanoparticles for the Biomedical Applications. *Journal of Nanoparticle Research*, **13** (5): 1917S–1927.
- Nithya, R., & Sundaram, N. M. (2015). Biodegradation and Cytotoxicity of Ciprofloxacin-loaded Hydroxyapatite-polycaprolactone Nanocomposite Film for Sustainable Bone Implants. *International Journal of Nanomedicine*, **10** (Suppl 1): 119-127. doi: 10.2147/IJN.S79995.

- Nudelman, F., & Sommerdijk, N. A. (2012). Biomineralization as an Inspiration for Materials Chemistry. *Angewandte Chemie International Edition*, **51**(27): 6582–6596.
- Obada, D. O., Aliyu, A., Kuta, U. M., Lisiyas, A., Ogenyi, V. F., Aquatar, M. O., Joseph, S., Adewole, I. A., Musa, S. M., & Jaafar, M. (2022). Trends in the Development of Hydroxyapatite from Natural Sources for Biomedical Applications. *Transactions on Ecology and the Environment*, **257**, 199–210.
- Oduosote, J. K., Danyuo, Y., Baruwa, A. D., & Azeez, A. A. (2019). Synthesis and Characterization of Hydroxyapatite from Bovine Bone for Production of Dental Implants. *Journal of Applied Biomaterials & Functional Materials*, **17** (2),
doi: 10.1177/2280800019836829.
- Ofudje, E. A., Rajendran, A., Adeogun, A. I., Idowu, M. A., Kareem, S. O., & Pattanayak, D. K. (2018). Synthesis of Organic Derived Hydroxyapatite Scaffold from Pig Bone Waste for Tissue Engineering Applications. *Advanced Powder Technology*, **29** (1): 1–8.
- O'Hare, P., Meenan, B. J., Burke, G. A., Byrne, G., Dowling, D., & Hunt, J. A. (2010). Biological Responses to Hydroxyapatite Surfaces Deposited via a Coincident Microblasting Technique. *Biomaterials*, **31**(3): 515–522.
- Okada, M., & Matsumoto, T. (2015). Synthesis and Modification of Apatite Nanoparticles for Use in Dental and Medical Applications. *Japanese Dental Science Review*, **51**(4): 85–95.
- Oladapo, B. I., Zahedi, S. A., Ismail, S. O., Omigbodun, F. T., Bowoto, O. K., Olawumi, M. A., & Muhammad, M. A. (2021). 3D Printing of PEEK–cHAp Scaffold for Medical Bone Implant. *Bio-Design and Manufacturing*, **4** (1): 44–59.
- Oladele, I. O., Agbabiaka, O. G., Olasunkanmi, O. G., Balogun, A. O., & Popoola, M. O. (2018). Non-synthetic Sources for the Development of Hydroxyapatite. *Journal of Applied Biotechnology and Bioengineering*, **5** (2): 88–95.

- Olsen, J., Heinemeier, J., Bennike, P., Krause, C., Hornstrup, K. M., & Thrane, H. (2008). Characterisation and Blind Testing of Radiocarbon Dating of Cremated Bone. *Journal of Archaeological Science*, **35** (3): 791–800.
- Ooi, C. Y., Hamdi, M., & Ramesh, S. (2007). Properties of Hydroxyapatite Produced by Annealing of Bovine Bone. *Ceramics International*, **33** (7): 1171–1177.
- Oprea, S. (2005). Effect of Solvent Interactions on the Properties of Polyurethane Films. *High Performance Polymers*, **17** (2): 163–173.
- Oranger, A., Colaianni, G., & Grano, M. (2014). Bone cClls. In *Imaging of Prosthetic Joints* (3–13). Springer, Milano.
- Orlovskii, V. P., Komlev, V. S., & Barinov, S. M. (2002). Hydroxyapatite and Hydroxyapatite-based Ceramics. *Inorganic Materials*, **38**(10): 973–984.
- Pahari, S. K., Singh, S. P., Banmali, M. P., Thaler, F. J. L., & Rathour, M. S. S. (2005). Ethical Guidelines for the Care and Use of Animals in Health Research in Nepal. Kathmandu, Nepal: Nepal Health Research Council.
- Pal, A., Maity, S., Chabri, S., Bera, S., Chowdhury, A. R., Das, M., & Sinha, A. (2017). Mechanochemical Synthesis of Nanocrystalline Hydroxyapatite from Mercenaria Clam Shells and Phosphoric Acid. *Biomedical Physics & Engineering Express*, **3**(1): 015010. doi: 10.1088/2057-1976/aa54f5.
- Palazzo, B., Iafisco, M., Laforgia, M., Margiotta, N., Natile, G., Bianchi, C. L., Walsh, D., Mann, S., & Roveri, N. (2007). Biomimetic Hydroxyapatite–drug Nanocrystals as Potential Bone Substitutes with Antitumor Drug Delivery Properties. *Advanced Functional Materials*, **17**(13): 2180–2188.
- Palmer, L. C., Newcomb, C. J., Kaltz, S. R., Spoerke, E. D., & Stupp, S. I. (2008). Biomimetic Systems for Hydroxyapatite Mineralization Inspired by Bone and Enamel. *Chemical Reviews*, **108**(11): 4754–4783.
- Panda, N. N., Pramanik, K., & Sukla, L. B. (2014). Extraction and Characterization of Biocompatible Hydroxyapatite from Fresh Water Fish Scales for Tissue Engineering Scaffold. *Bioprocess and Biosystems Engineering*, **37**(3): 433–440.

- Pati, F., Adhikari, B., & Dhara, S. (2010). Isolation and Characterization of Fish Scale Collagen of Higher Thermal Stability. *Bioresource Technology*, **101**(10): 3737–3742.
- Pati, F., Song, T.-H., Rijal, G., Jang, J., Kim, S. W., & Cho, D.-W. (2015). Ornamenting 3D Printed Scaffolds with Cell-laid Extracellular Matrix for Bone Tissue Regeneration. *Biomaterials*, **37**: 230–241.
- Paul, S., Pal, A., Choudhury, A. R., Bodhak, S., Balla, V. K., Sinha, A., & Das, M. (2017). Effect of Trace Elements on the Sintering Effect of Fish Scale Derived Hydroxyapatite and its Bioactivity. *Ceramics International*, **43**(17): 15678–15684.
- Pawarangan, I., & Yusuf, Y. (2018). Characteristics of Hydroxyapatite from Buffalo Bone Waste Synthesized by Precipitation Method. *IOP Conference Series: Materials Science and Engineering*, **432**(1), 012044.
- Paz, A., Guadarrama, D., López, M., E González, J., Brizuela, N., & Aragón, J. (2012). A Comparative Study of Hydroxyapatite Nanoparticles Synthesized by Different Routes. *Química Nova*, **35**(9): 1724–1727.
- Petricca, S. E., Marra, K. G., & Kumta, P. N. (2006). Chemical Synthesis of Poly (lactic-co-glycolic acid)/Hydroxyapatite Composites for Orthopaedic Applications. *Acta Biomaterialia*, **2**(3): 277–286.
- Piccirillo, C., Silva, M. F., Pullar, R. C., Da Cruz, I. B., Jorge, R., Pintado, M. M. E., & Castro, P. M. (2013). Extraction and Characterisation of Apatite-and Tricalcium Phosphate-based Materials from Cod Fish Bones. *Materials Science and Engineering: C*, **33**(1): 103–110.
- Pon-On, W., Suntornsaratoon, P., Charoenphandhu, N., Thongbunchoo, J., Krishnamra, N., & Tang, I. M. (2016). Hydroxyapatite from Fish Scale for Potential Use as Bone Scaffold or Regenerative Material. *Materials Science and Engineering: C*, **62**: 183–189.
- Posa, F., Di Benedetto, A., Colaianni, G., Cavalcanti-Adam, E. A., Brunetti, G., Porro, C., Trotta, T., Grano, M., & Mori, G. (2016). Vitamin D effects on Osteoblastic Differentiation of Mesenchymal Stem Cells from Dental Tissues. *Stem Cells International*, **2016**: 1-9. <https://doi.org/10.1155/2016/9150819>

- Prabhakaran, M. P., Venugopal, J., & Ramakrishna, S. (2009). Electrospun Nanostructured Scaffolds for Bone Tissue Engineering. *Acta Biomaterialia*, **5**(8): 2884–2893.
- Puppi, D., Chiellini, F., Piras, A. M., & Chiellini, E. (2010). Polymeric Materials for Bone and Cartilage Repair. *Progress in Polymer Science*, **35**(4): 403–440.
- Puppi, D., Piras, A. M., Detta, N., Ylikauppila, H., Nikkola, L., Ashammakhi, N., Chiellini, F., & Chiellini, E. (2011). Poly (vinyl alcohol)-based Electrospun Meshes as Potential Candidate Scaffolds in Regenerative Medicine. *Journal of Bioactive and Compatible Polymers*, **26**(1): 20–34.
- Ragab, H. S., Ibrahim, F. A., Abdallah, F., Al-Ghamdi, A. A., El-Tantawy, F., Radwan, N., & Yakuphanoglu, F. (2014). Synthesis and In vitro Antibacterial Properties of Hydroxyapatite Nanoparticles. *IOSR Journal of Pharmacy and Biological Sciences (IOSR-JPBS)*, **9** (1): 77–85.
- Rahavi, S. S., Ghaderi, O., Monshi, A., & Fathi, M. H. (2017). A Comparative Study on Physicochemical Properties of Hydroxyapatite Powders Derived from Natural and Synthetic Sources. *Russian Journal of Non-Ferrous Metals*, **58**(3): 276–286.
- Rajzer, I., Kurowska, A., Jabłoński, A., Jatteau, S., Śliwka, M., Ziabka, M., & Menaszek, E. (2018). Layered Gelatin/PLLA Scaffolds Fabricated by Electrospinning and 3D Printing-for Nasal Cartilages and Subchondral Bone Reconstruction. *Materials & Design*, **155**: 297–306.
- Ramesh, S., Loo, Z. Z., Tan, C. Y., Chew, W. K., Ching, Y. C., Tarlochan, F., Chandran, H., Krishnasamy, S., Bang, L. T., & Sarhan, A. A. (2018). Characterization of Biogenic Hydroxyapatite Derived from Animal Bones for Biomedical Applications. *Ceramics International*, **44**(9): 10525–10530.
- Ramírez-Agudelo, R., Scheuermann, K., Gala-García, A., Monteiro, A. P. F., Pinzón-García, A. D., Cortés, M. E., & Sinisterra, R. D. (2018). Hybrid Nanofibers Based on Poly-caprolactone/Gelatin/Hydroxyapatite Nanoparticles-loaded Doxycycline: Effective Anti-tumoral and Antibacterial Activity. *Materials Science and Engineering: C*, **83**: 25–34.

- Rana, M., Akhtar, N., Rahman, S., Jamil, H. M., & Asaduzzaman, S. M. (2017). Extraction of Hydroxyapatite from Bovine and Human Cortical Bone by Thermal Decomposition and Effect of Gamma Radiation: A comparative Study. *International Journal of Complement and Alternavive Medicine*, **8**(00263), 10–15406.
- Rattan, P. V., Sidhu, T. S., & Mittal, M. (2012). An Overview of Hydroxyapatite Coated Titanium Implants. *Asian Journal of Engineering and Applied Technology*, **1**(2): 40–43.
- Rauci, M. G., Guarino, V., & Ambrosio, L. (2012). Biomimetic Strategies for Bone Repair and Regeneration. *Journal of Functional Biomaterials*, **3**(3): 688–705.
- Remya, K. R., Joseph, J., Mani, S., John, A., Varma, H. K., & Ramesh, P. (2013). Nanohydroxyapatite Incorporated Electrospun Polycaprolactone/ Pycaprolactone–polyethyleneglycol–polycaprolactone Blend scaffold for Bone Tissue Engineering Applications. *Journal of Biomedical Nanotechnology*, **9**(9):1483–1494.
- Remya, N. S., Syama, S., Sabareeswaran, A., & Mohanan, P. V. (2017). Investigation of Chronic Toxicity of Hydroxyapatite Nanoparticles Administered Orally for One Year in Wistar Rats. *Materials Science and Engineering: C*, **76**: 518–527.
- Rho, J.-Y., Kuhn-Spearing, L., & Zioupos, P. (1998). Mechanical Properties and the Hierarchical Structure of Bone. *Medical Engineering & Physics*, **20**(2): 92–102.
- Rimola, A., Corno, M., Zicovich-Wilson, C. M., & Ugliengo, P. (2008). Abinitio Modeling of Protein/Biomaterial Interactions: Glycine Adsorption at Hydroxyapatite Surfaces. *Journal of the American Chemical Society*, **130**(48): 16181–16183.
- Roseti, L., Parisi, V., Petretta, M., Cavallo, C., Desando, G., Bartolotti, I., & Grigolo, B. (2017). Scaffolds for Bone Tissue Engineering: State of the Art and New Perspectives. *Materials Science and Engineering: C*, **78**:1246–1262.
- Rujitanapanich, S., Kumpapan, P., & Wanjanoi, P. (2014). Synthesis of Hydroxyapatite from Oyster Shell via Precipitation. *Energy Procedia*, **56**: 112–117.

- Ruksudjarit, A., Pengpat, K., Rujjanagul, G., & Tunkasiri, T. (2008a). Synthesis and Characterization of Nanocrystalline Hydroxyapatite from Natural Bovine Bone. *Current Applied Physics*, **8**(3–4): 270–272.
- Sadat-Shojai, M., Khorasani, M.-T., Dinpanah-Khoshdargi, E., & Jamshidi, A. (2013). Synthesis Methods for Nanosized Hydroxyapatite with Diverse Structures. *Acta Biomaterialia*, **9**(8): 7591–7621.
- Sagadevan, S., & Dakshnamoorthy, A. (2013). Synthesis and Characterization of Nano-hydroxyapatite (n-HAP) Using the Wet Chemical Technique. *International Journal of Physical Sciences*, **8**(32): 1639–1645.
- Sánchez-Arévalo, F. M., Muñoz-Ramírez, L. D., Álvarez-Camacho, M., Rivera-Torres, F., Maciel-Cerda, A., Montiel-Campos, R., & Vera-Graziano, R. (2017). Macro-and Micromechanical Behaviors of Poly (Lactic Acid)–Hydroxyapatite Electrospun Composite Scaffolds. *Journal of Materials Science*, **52**(6): 3353–3367.
- Santhosh, S., & Prabu, S. B. (2013). Thermal Stability of Nano Hydroxyapatite Synthesized from Sea Shells through Wet Chemical Synthesis. *Materials Letters*, **97**: 121–124.
- Sari, T., Jamarun, N., Syukri, S., Azharman, Z., & Asril, A. (2014). Effect of Mixing Temperature on the Synthesis of Hydroxyapatite by Sol-gel Method. *Oriental Journal of Chemistry*, **30**(4): 1799–1804.
- Sattary, M., Khorasani, M. T., Rafienia, M., & Rozve, H. S. (2018). Incorporation of Nanohydroxyapatite and Vitamin D3 into Electrospun PCL/Gelatin Scaffolds: The Influence on the Physical and Chemical Properties and Cell Behavior for Bone Tissue Engineering. *Polymers for Advanced Technologies*, **29**(1): 451–462.
- Sattary, M., Rafienia, M., Kazemi, M., Salehi, H., & Mahmoudzadeh, M. (2019). Promoting Effect of Nano Hydroxyapatite and Vitamin D3 on the Osteogenic Differentiation of Human Adipose-derived Stem Cells in Polycaprolactone/Gelatin Scaffold for Bone Tissue Engineering. *Materials Science and Engineering: C*, **97**: 141–155.

- Satter, S. S., Hoque, M., Rahman, M. M., Mollah, M. Y. A., & Susan, M. A. B. H. (2014). An Approach Towards the Synthesis and Characterization of ZnO@ Ag core@ Shell Nanoparticles in Water-in-oil Microemulsion. *RSC Advances*, **4**(39): 20612–20615.
- Sayed, A., & Asran, A. S. (2011). *Electrospinning of polymeric nanofibers and nanocomposite materials-fabrication, physicochemical characterization and medical applications*. Martin-Luther University, Halle-Wittenberg, Germany. <http://dx.doi.org/10.25673/392>.
- Scaffaro, R., Lopresti, F., & Botta, L. (2017). Preparation, Characterization and Hydrolytic Degradation of PLA/PCL Co-mingled Nanofibrous Mats Prepared via Dual-jet Electrospinning. *European Polymer Journal*, **96**: 266–277.
- Shavandi, A., Bekhit, A. E.-D. A., Ali, A., & Sun, Z. (2015). Synthesis of Nano-Hydroxyapatite (nHA) from Waste Mussel Shells Using a Rapid Microwave Method. *Materials Chemistry and Physics*, **149**: 607–616.
- Shi, Y. Y., Li, M., Liu, Q., Jia, Z. J., Xu, X. C., Cheng, Y., & Zheng, Y. F. (2016). Electrophoretic Deposition of Graphene Oxide Reinforced Chitosan–Hydroxyapatite Nanocomposite Coatings on Ti substrate. *Journal of Materials Science: Materials in Medicine*, **27**(3): 48.
- Shin, H., Jo, S., & Mikos, A. G. (2003). Biomimetic Materials for Tissue Engineering. *Biomaterials*, **24**(24): 4353–4364.
- Shitole, A. A., Raut, P. W., Sharma, N., Giram, P., Khandwekar, A. P., & Garnaik, B. (2019). Electrospun Polycaprolactone/Hydroxyapatite/ZnO Nanofibers as Potential Biomaterials for Bone Tissue Regeneration. *Journal of Materials Science: Materials in Medicine*, **30**(5): 1–17.
- Shokrgozar, M. A., Fattahi, M., Bonakdar, S., Kashani, I. R., Majidi, M., Haghighipour, N., Bayati, V., Sanati, H., & Saeedi, S. N. (2012). Healing Potential of Mesenchymal Stem Cells Cultured on a Collagen-based Scaffold for Skin Regeneration. *Iranian Biomedical Journal*, **16**(2): 68.

- Shuai, C., Yang, W., & Feng, P. (2021). Accelerated Degradation of HAP/PLLA Bone Scaffold by PGA Blending Facilitates Bioactivity and Osteoconductivity. *Bioactive Materials*, **6**(2021): 490–502.
- Singh, A., Tiwari, A., Bajpai, J., & Bajpai, A. K. (2018). 3.Polymer-Based Antimicrobial Coatings as Potential Biomaterials: *Handbook of Antimicrobial Coatings*, 27-61.
- Smeets, R., Kolk, A., Gerressen, M., Driemel, O., Maciejewski, O., Hermanns-Sachweh, B., Riediger, D., & Stein, J. M. (2009). A New Biphasic Osteoinductive Calcium Composite Material with a Negative Zeta Potential for Bone Augmentation. *Head & Face Medicine*, **5**(1): 1–8.
- Sobczak, A., Kowalski, Z., & Wzorek, Z. (2009). Preparation of Hydroxyapatite from Animal Bones. *Acta of Bioengineering and Biomechanics*, **11**(4): 23–28.
- Sofronia, A. M., Baies, R., Anghel, E. M., Marinescu, C. A., & Tanasescu, S. (2014). Thermal and Structural Characterization of Synthetic and Natural Nanocrystalline Hydroxyapatite. *Materials Science and Engineering: C*, **43**:153–163.
- Son, J. S., Appleford, M., Ong, J. L., Wenke, J. C., Kim, J. M., Choi, S. H., & Oh, D. S. (2011). Porous Hydroxyapatite Scaffold with Three-dimensional Localized Drug Delivery System Using Biodegradable Microspheres. *Journal of Controlled Release*, **153**(2): 133–140.
- Song, X., Ling, F., Ma, L., Yang, C., & Chen, X. (2013). Electrospun Hydroxyapatite Grafted Poly (L-lactide)/poly (lactic-co-glycolic acid) Nanofibers for Guided Bone Regeneration Membrane. *Composites Science and Technology*, **79**: 8–14.
- Sözüğeçer, S., & Bayramgil, N. P. (2021). Preparation and Characterization of Polyacrylic Acid-hydroxyapatite Nanocomposite by Microwave-assisted Synthesis Method. *Heliyon*, **7**(6): e07226.
- Su, W.-Y., Chen, Y.-C., & Lin, F.-H. (2013). A New Type of Biphasic Calcium Phosphate Cement as a Gentamicin Carrier for Osteomyelitis. *Evidence-*

Based Complementary and Alternative Medicine, 2013. Article ID 801374.
doi.org/10.1155/2013/801374.

- Sun, R.-X., Lv, Y., Niu, Y.-R., Zhao, X.-H., Cao, D.-S., Tang, J., Sun, X.-C., & Chen, K.-Z. (2017). Physicochemical and Biological Properties of Bovine-derived Porous Hydroxyapatite/Collagen Composite and its Hydroxyapatite Powders. *Ceramics International*, **43**(18): 16792–16798.
- Surya, P., Nithin, A., Sundaramanickam, A., & Sathish, M. (2021). Synthesis and Characterization of Nano-hydroxyapatite from Sardinella Longiceps Fish Bone and its Effects on Human Osteoblast Bone Cells. *Journal of the Mechanical Behavior of Biomedical Materials*, **119**:104501.
- Szczęś, A., Holysz, L., & Chibowski, E. (2017). Synthesis of Hydroxyapatite for Biomedical Applications. *Advances in Colloid and Interface Science*, **249**: 321–330.
- Tanner, K. E. (2010). Bioactive Composites for Bone Tissue Engineering. Proceedings of the Institution of Mechanical Engineers, Part H: *Journal of Engineering in Medicine*, **224**(12): 1359–1372.
- Tanner, K. E., Downes, R. N., & Bonfield, W. (1994). Clinical Applications of Hydroxyapatite Reinforced Materials. *British Ceramic Transactions*, **93**(3): 104–107.
- Teng, N. C., Nakamura, S., Takagi, Y., Yamashita, Y., Ohgaki, M., & Yamashita, K. (2001). A New Approach to Enhancement of Bone Formation by Electrically Polarized Hydroxyapatite. *Journal of Dental Research*, **80**(10): 1925–1929.
- Tetteh, G., Khan, A. S., Delaine-Smith, R. M., Reilly, G. C., & Rehman, I. U. (2014). Electrospun Polyurethane/Hydroxyapatite Bioactive Scaffolds for Bone Tissue Engineering: The Role of Solvent and Hydroxyapatite Particles. *Journal of the Mechanical Behavior of Biomedical Materials*, **39**: 95–110.
- Thorvaldsson, A., Stenhamre, H., Gatenholm, P., & Walkenström, P. (2008). Electrospinning of Highly Porous Scaffolds for Cartilage Regeneration. *Biomacromolecules*, **9**(3): 1044–1049.

- Uson, N., Garcia, M. J., & Solans, C. (2004). Formation of Water-in-oil (W/O) Nano-emulsions in a Water/mixed Non-ionic Surfactant/Oil Systems Prepared by a Low-energy Emulsification Method. *Colloids and Surfaces A: Physicochemical and Engineering Aspects*, **250**(1–3): 415–421.
- Varadarajan, N., Balu, R., Rana, D., Ramalingam, M., & Kumar, T. S. (2014). Accelerated Sonochemical Synthesis of Calcium Deficient Hydroxyapatite Nanoparticles: Structural and Morphological Evolution. *Journal of Biomaterials and Tissue Engineering*, **4**(4): 295–299.
- Vaz, C. M., Van Tuijl, S., Bouten, C. V. C., & Baaijens, F. P. T. (2005). Design of Scaffolds for Blood Vessel Tissue Engineering Using a Multi-layering Electrospinning Technique. *Acta Biomaterialia*, **1**(5): 575–582.
- Venkatasubbu, G. D., Ramasamy, S., Gaddam, P. R., & Kumar, J. (2015). Acute and Subchronic Toxicity Analysis of Surface Modified Paclitaxel Attached Hydroxyapatite and Titanium Dioxide Nanoparticles. *International Journal of Nanomedicine*, **10**(Suppl 1): 137.
- Venkatesan, J., & Kim, S. K. (2010). Effect of Temperature on Isolation and Characterization of Hydroxyapatite from Tuna (*Thunnus obesus*) Bone. *Materials*, **3**(10): 4761–4772.
- Venkatesan, J., Qian, Z. J., Ryu, B., Thomas, N. V., & Kim, S. K. (2011). A Comparative Study of Thermal Calcination and an Alkaline Hydrolysis Method in the Isolation of Hydroxyapatite from *Thunnus Obesus* Bone. *Biomedical Materials*, **6**(3): 035003.
- Venugopal, J. R., Low, S., Choon, A. T., Kumar, A. B., & Ramakrishna, S. (2008). Nanobioengineered Electrospun Composite Nanofibers and Osteoblasts for Bone Regeneration. *Artificial Organs*, **32**(5): 388–397.
- Vogelman, B., Gudmundsson, S., Leggett, J., Turnidge, J., Ebert, S., & Craig, W. A. (1988). Correlation of Antimicrobial Pharmacokinetic Parameters with Therapeutic Efficacy in an Animal Model. *Journal of Infectious Diseases*, **158**(4): 831–847.
- Wan, Y. Z., Hong, L., Jia, S. R., Huang, Y., Zhu, Y., Wang, Y. L., & Jiang, H. J. (2006). Synthesis and Characterization of Hydroxyapatite–Bacterial

- Cellulose nanocomposites. *Composites Science and Technology*, **66**(11–12): 1825–1832.
- Wang, C., Huang, W., Zhou, Y., He, L., He, Z., Chen, Z., He, X., Tian, S., Liao, J., & Lu, B. (2020). 3D Printing of Bone Tissue Engineering Scaffolds. *Bioactive Materials*, **5**(1): 82–91.
- Wang, J., Wang, G., Shan, H., Wang, X., Wang, C., Zhuang, X., Ding, J., & Chen, X. (2019). Gradiently Degraded Electrospun Polyester Scaffolds with Cytostatic for Urothelial Carcinoma Therapy. *Biomaterials Science*, **7**(3): 963–974.
- Wang, L., Chen, D., Jiang, K., & Shen, G. (2017). New Insights and Perspectives into Biological Materials for Flexible Electronics. *Chemical Society Reviews*, **46**(22): 6764–6815.
- Wang, R., & Gupta, H. S. (2011). Deformation and Fracture Mechanisms of Bone and Nacre. *Annual Review of Materials Research*, **41**(1): 41–73.
- Ward, I. M. (2010). Electron Microscopy of Polymers, in the Series Springer Laboratory, by GH Michler: Scope: Textbook. Level: postgraduate. *Taylor & Francis*.
- Weiner, S., & Wagner, H. D. (1998). The Material Bone: Structure-mechanical Function Relations. *Annual Review of Materials Science*, **28**(1): 271–298.
- Wong, S.-C., Baji, A., & Leng, S. (2008). Effect of Fiber Diameter on Tensile Properties of Electrospun Poly (ϵ -caprolactone). *Polymer*, **49**(21): 4713–4722.
- Wraighte, P. J., & Scammell, B. E. (2006). Principles of Fracture Healing. *Surgery (Oxford)*, **24**(6): 198–207.
- Wu, S.-C., Hsu, H.-C., Hsu, S.-K., Chang, Y.-C., & Ho, W.-F. (2016). Synthesis of Hydroxyapatite from Eggshell Powders Through Ball Milling and Heat Treatment. *Journal of Asian Ceramic Societies*, **4**(1): 85–90.
- Yang, H., Hao, L., Zhao, N., Du, C., & Wang, Y. (2013). Hierarchical Porous Hydroxyapatite Microsphere as Drug Delivery Carrier. *Cryst Eng Comm*, **15**(29): 5760–5763.

- Yao, Q., Wei, B., Guo, Y., Jin, C., Du, X., Yan, C., Yan, J., Hu, W., Xu, Y., & Zhou, Z. (2015). Design, Construction and Mechanical Testing of Digital 3D Anatomical Data-based PCL–HA Bone Tissue Engineering Scaffold. *Journal of Materials Science: Materials in Medicine*, **26**(1): 51-58.
- Yelten-Yilmaz, A., & Yilmaz, S. (2018). Wet Chemical Precipitation Synthesis of Hydroxyapatite (HA) Powders. *Ceramics International*, **44**(8): 9703–9710.
- Yeong, K. C. B., Wang, J., & Ng, S. C. (2001). Mechanochemical Synthesis of Nanocrystalline Hydroxyapatite from CaO and CaHPO₄. *Biomaterials*, **22**(20): 2705–2712.
- Yi, Z., Wang, K., Tian, J., Shu, Y., Yang, J., Xiao, W., Li, B., & Liao, X. (2016). Hierarchical Porous Hydroxyapatite Fibers with a Hollow Structure as Drug Delivery Carriers. *Ceramics International*, **42**(16): 19079–19085.
- Yoganand, C. P., Selvarajan, V., Goudouri, O. M., Paraskevopoulos, K. M., Wu, J., & Xue, D. (2011). Preparation of Bovine Hydroxyapatite by Transferred arc Plasma. *Current Applied Physics*, **11**(3): 702–709.
- Yoon, H., & Kim, G. (2011a). A Three-dimensional Polycaprolactone Scaffold Combined with a Drug Delivery System Consisting of Electrospun Nanofibers. *Journal of Pharmaceutical Sciences*, **100**(2): 424–430.
- Yorug, A. H., & Ipek, Y. (2012). Sonochemical Synthesis of Hydroxy Apatite Nanoparticles with Different Precursor Reagents. *Acta Physica Polonica-Series A General Physics*, **121**(1): 230-238.
- Younesi, M., Javadpour, S., & Bahrololoom, M. E. (2011). Effect of Heat Treatment Temperature on Chemical Compositions of Extracted Hydroxyapatite from Bovine Bone Ash. *Journal of Materials Engineering and Performance*, **20**(8): 1484–1490.
- Yuan, X., Zhu, B., Tong, G., Su, Y., & Zhu, X. (2013). Wet-chemical Synthesis of Mg-doped Hydroxyapatite Nanoparticles by Step Reaction and Ion exchange Processes. *Journal of Materials Chemistry B*, **1**(47): 6551–6559.
- Zainon, I., Alwi, N. M., Abidin, M. Z., Haniza, H. M. Z., Ahmad, M. S., & Ramli, A. (2012). Physicochemical Properties of Hydroxyapatite Extracted from Fish Scales. *Advanced Materials Research*, **545**: 235–239.

- Zhang, Y., Liu, X., Zeng, L., Zhang, J., Zuo, J., Zou, J., Ding, J., & Chen, X. (2019). Polymer Fiber Scaffolds for Bone and Cartilage Tissue Engineering. *Advanced Functional Materials*, **29**(36): 1903279.
- Zhang, Y., Ouyang, H., Lim, C. T., Ramakrishna, S., & Huang, Z.-M. (2005). Electrospinning of Gelatin Fibers and Gelatin/PCL Composite Fibrous Scaffolds. *Journal of Biomedical Materials Research Part B: Applied Biomaterials: An Official Journal of The Society for Biomaterials, The Japanese Society for Biomaterials and The Australian Society for Biomaterials and the Korean Society for Biomaterials*, **72**(1): 156–165.
- Zhou, H., & Lee, J. (2011). Nanoscale Hydroxyapatite Particles for Bone Tissue Engineering. *Acta Biomaterialia*, **7**(7): 2769–2781.
- Zhou, W. Y., Wang, M., & Cheung, W. L. (2007). Fabrication and Characterization of Composite Microspheres Containing Carbonated Hydroxyapatite Nanoparticles. *Key Engineering Materials*, **334**: 1221–1224.

APPENDIX

List of Publications

Malla, K.P., Adhikari, R., Yadav, R.J., Nepal, A. & Neupane, B.P. (2018). Removal of Lead (II) Ions from Aqueous Solution by Hydroxyapatite Biosorbent Synthesis from Ostrich bone. *Journal of Health and Allied Sciences*, 1(7):27-33. [Peer reviewed open access journal. SJR 0.14]

Malla, K.P., Regmi, S., Nepal, A., Bhattarai, S., Yadav, R.J., Sakurau, S., & Adhikari, R., (2020). Extraction and Characterization of Novel Natural Hydroxyapatite Bioceramic by Thermal Decomposition of Waste Ostrich Bone. *International Journal of Biomaterials*, Vol 2020 article ID 1690178, [https:// doi.org/10.1155/2020/1690178](https://doi.org/10.1155/2020/1690178) [Journal Rank Q2]

Malla, K.P., Henning, S., Lach, R., Jennissen, H., Michler, G., Beiner, M., Yadav, R.J., & Adhikari, R., (2022). Deformation and Micromechanical Behavior of Electrospun Nano-hydroxyapatite Blended Biohybrid Scaffolds. *Macromol. Symp*, 403, 2200079,1-9, Wiley-VCH GmbH doi.: 10.1002/masy.202200079 [Journal Rank Q3]

List of Presentations

Posters

Synthesis and Characterization of Hydroxyapatite Nano Particles (nano HAp) from Ostrich Biowaste for Biomedical Applications. Nepal Chemical Society (NCS), National Chemical Congress-2017, August 29, 2017, Amrit Science Campus, Lainchaur, Kathmandu, Nepal.

Synthesis, size control and characterization of noble biomaterial hydroxyapatite from ostrich femur bones using calcinations at various temperatures. 4th International Conference, Kathmandu Symposia on Advanced Materials (KaSAM-2018); October 26-29, 2018, Kathmandu, Nepal.

Oral Presentations

Invited Lecture: Removal of Lead (II) Ions from Aqueous Solution by Hydroxyapatite Biosorbent Prepared from Ostrich Bone Waste. Fourth International

Symposium on Advances in Sustainable Polymers (ASP 2017) Guwahati, India. January 8-11, 2018.

Electrospun Composite Fibers Comprising Polycaprolactone, Poly-L-lactic Acid, Gelatin, Vitamin D3 and Natural Hydroxyapatite. 5th International Symposium on Advances in Sustainable Polymers (ASP-19), Kyoto Institute of Technology (KIT) Matsugasaki Sakau ku, Kyoto, Japan. October 14-18, 2019.

An approach for Electrospinning and Characterization of Natural Hydroxyapatite Nanoparticle Loaded PCL/PLLA/GEL/VitD3 Blend Fiber Scaffolds for Bone Tissue Engineering. Poly-Char 2019 Kathmandu. May 19-23, 2019.

Extraction and characterization of natural hydroxyapatite from ostrich bone via calcinations at various temperatures. 8th Asian Conference on Colloid & Interface Science (ACCIS 2019). Punchwork Campus, Institute of Engineering, Tribhuvan University, Lalitpur, Kathmandu, Nepal. September 24-27, 2019.

Fabrication of hydroxyapatite and vitamin D3 reinforced polymers scaffold for bone tissue engineering. International Conference, Poly-Char 2020 Venice, Italy April 12-14, 2021.

Electrospun blends of polycaprolactone/poly-L-lactic acid/gelatin and natural hydroxyapatite incorporated scaffold for bone tissue engineering. International Conference on PolyMerTec digital 2021 Merseburg, Germany, June 9-11, 2021.

Removal of lead (II) ions from aqueous solution by Hydroxyapatite biosorbent extracted from Ostrich bone

^{1,2}Komal Prasad Malla, ²Rameshwar Adhikari, ³Ram Jeewan Yadav, ²Achyut Nepal and ¹Bishnu Prasad Neupane

¹School of Health and Allied Sciences, Pokhara University, Nepal

²Research Center for Applied Science and Technology (RECAST), Kathmandu, Nepal

³Department of Chemistry, Prithvi Narayan Campus, Pokhara, Nepal

ABSTRACT

Hydroxyapatite (HAp) is a broadly studied bioceramic for biomedical implant and bone tissue regeneration. Despite this, it is a good adsorbent of heavy metal ions. Its chemical formula is $\text{Ca}_{10}(\text{PO}_4)_6(\text{OH})_2$. It was extracted by the calcination process from Ostrich bone. The obtained HAp was characterized by X-ray diffraction (XRD) and Fourier transforms infrared (FTIR) spectroscopy and was used for removal of lead (II) ion from aqueous solutions. A series of experiments were conducted in order to determine the effects of pH, contact time and sorbent dosage in a optimize condition for maximum adsorption. The results showed that the removal efficiency of Pb (II) ions reached 99.04% with an initial concentration of 50 mgL^{-1} , pH range; 3 to 7 and 1 hour contact time. The adsorption rate of Pb (II) ions onto the HAp was found incredibly fast and equilibrium was reached within 5 minute. Within this time 72.32% of lead (II) ions were removed. The equilibrium removal process of Pb (II) ions at pH range 4.5-5.5 were well described by the Langmuir isotherm model, with a maximum adsorption capacity of 430.7 mg/g.

Key words: Ostrich bone, hydroxyapatite, calcinations, adsorption, Pb (II) ion, pH.

Corresponding address: Komal Prasad Malla
E-mail: komalmalla1971@gmail.com

INTRODUCTION

Heavy metals are the elements having a specific gravity at least five times than water as well as toxic even intake in a low amount¹. These metal ions found in water especially from transition metal series are of foremost concern due to their toxicity to several life forms. Its effect is cumulative and can cause serious health problems including damage of visceral organs and the nervous system. On prolonged exposure, it can cause cancer in these organs which may go ahead to death².

The toxicity of these metal ions is enhanced due to the accumulation in living tissues through food chain³. Among the different heavy metal ions, the lead (II) ion is important on the viewpoint of environmental toxicology⁴. Lead metal and its ionic compounds are widely applied in different industries such as paint and pigments, ceramics and pottery, storage batteries, alloys, and solder as well as in petrol refining⁵. Owing to these uses, this ion often found in industrial effluent and there is a high risk of intermixing with drinking

water resources. Therefore, the removal of this ion from industrial effluent as well as drinking water resources is necessary for public health concern.

Although the different removal techniques have been proposed by different researchers, chemical precipitation, membrane filtration, ion exchange, and biosorption are the most commonly applied techniques⁶. Among these, the biosorption is more reliable and convenient technique because of its low processing cost, high efficiency of adsorption, minimization of chemical and biological sludge, high possibility of regeneration of adsorbent and metal recovery⁷⁻⁹. Because of these beneficial aspects, in this study, the biosorbent technique was applied for the removal from an aqueous medium. HAp biosorbent can be prepared either from chemical precursors or from biogenic resources. In compare to chemical precursors bio-based resources are economical and HAp extracted from this resources are highly preferable for removal of heavy metal ions due to its low water solubility and greater stability under redox conditions. The

elemental components of HAp are hydrogen, oxygen, phosphorous and calcium along with carbon which is expected to have no toxicity¹⁰. Moreover, HAp isolated from biogenic resources have received considerable attention in the field of dental and bone tissue engineering because of its chemical, structural and morphological resemblance with human hard tissue minerals¹¹⁻¹³.

MATERIALS AND METHOD

Bone sample collection

Minimum 2 kg of cortical bone was collected from Ostrich farmhouse located at Gangolya-1, Rupendehi district, the western region of Nepal. The samples were cleaned to remove visible adhered substances and then cut into small pieces using a hacksaw.

Chemicals and Reagents

All necessary analytical grade chemicals and reagents such as $Pb(NO_3)_2$, KNO_3 , $NaOH$, HCl , HNO_3 , $NaCl$ and Acetone were purchased from Merck Chemicals (India) and used without further purification.

Preparation of Biosorbent

Bone pieces were boiled for about 4 hours in a closed container for deproteination after that wash several times by tap water and dried overnight at 120°C in a hot air oven. The dried bone pieces were crushed in an iron mortar and powdered in a high-speed disc pulverized machine. Furthermore, alkaline hydrothermal hydrolysis process was applied for removal of residual collagens and fatty tissues. Finally, the bone powder was calcinated at 650°C in a muffle furnace using a heating rate of 5°C/min for 6 hours holding time and slow furnace cooling to obtain grayish-white bone ash and recalcinated at 950°C for another 6 hours in the same condition to obtained final product. The flow sheet diagram of preparation process is shown in figure 1.

Preparation of Lead (II) ion Stock Solution

Analytical grade lead nitrate, $Pb(NO_3)_2$ was used for the preparation of stock solution (1000 mg/L). The experimental solutions were then prepared by diluting the stock solution. The concentration of these solutions was determined by using Flame Atomic Absorption Spectrometer (FAAS).

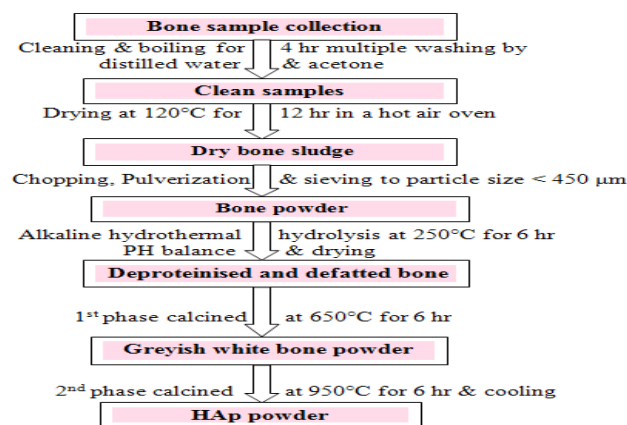


Figure 1. Flow sheet diagram of extraction of HAp biosorbent from Ostrich bone.

Characterization of Biosorbent

To study the crystallinity of the prepared biosorbent, powder X-ray diffraction (Bruker-D2) patterns were recorded using $Cu K\alpha$ radiation target with a second monochromator at 40 kV and 40 mA. Fourier transform infrared (FTIR) spectroscopic (Shimadzu-8300 IRTF) analysis was performed to identify the presence of major functional groups, and the point of zero charge (pH_{PZC}) was measured by a batch equilibrium technique, with 0.1M of KNO_3 as an inert electrolyte¹⁴.

Determination of Acido-basic Properties

The acido-basic properties of biosorbent were determined by using the point of zero charge (pH_{pzc}) method¹⁴. In this method, 500 mL of 0.01M $NaCl$ solution was degassed by using N_2 in order to remove dissolved CO_2 . 10 mL of 0.01M $NaCl$ solution was taken in 10 different conical flasks and 1-10 pH of each solution in flasks were maintained by adding either HCl or by $NaOH$ standard solution. 10 mg of HAp was added in the solution of each flask and kept in a mechanical shaker for 3 hours with 150 rpm. The final pH of each solution was measured after 24 hours.

Batch Sorption Experiments

Biosorption equilibrium assays were carried out by using the batch adsorption process. Each of the batch adsorption studies was carried out by adding HAp powder within experimental lead (II) ions solution at lab temperature ($25^\circ C \pm 0.1$). A series of experiments were conducted in order to determine the effects of pH, contact time, and sorbent dosage on the adsorption. Each experiment was conduct

ed in a mechanical shaker at 150 rpm. After the required time to reach equilibrium, all the samples were filtrate and the final concentration of lead(II) ions in solution were determined by using the flame atomic absorption spectrophotometer (Shimadzu AA 6500, air/acetylene gas mixture).

Calculations

All experiments were carried out in triplicate and the mean of the quantitative results was used for further calculations. The amount of lead (II) ions adsorbed onto the biosorbent surface *qt* (mg/g) was calculated by using a mass balance relationship as;

$$qt = \frac{(C_0 - C_t)V}{m} \dots\dots(I)$$

Where *qt* (mg/g) is the adsorption capacity of biosorbent; *C₀* and *C_t* are the initial and equilibrium concentration (mg/L) of lead (II) ions in solution; *V* (L) is the total volume of solution; and *m* (g) is the weight of the adsorbent taken. Similarly, the percentage of lead (II) ions removal by adsorbent was also determined by using the expression;

$$\text{Removal \%} = \frac{(C_0 - C_t) \times 100}{C_0} \dots\dots (II)$$

RESULTS AND DISCUSSION

X-ray Diffraction (XRD) Phases Analysis

The XRD patterns and exhibiting peaks corresponding to extracted HAp were found to be similar with standard HAp data of Joint Committee on Powder Diffraction Standards (JCPDS) card No 01-074-0565, which indicate that there is no secondary phase and the synthesized HAp was pure¹⁵ as shown in figure 2.

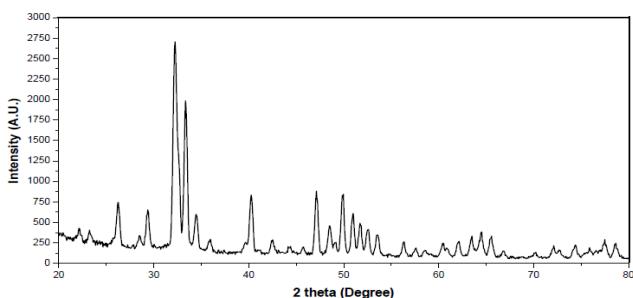


Figure 2. X-ray diffraction (XRD) patterns of HAp biosorbent extracted from Ostrich bone.

FTIR Analysis

The Fourier transform infrared (FTIR) analysis was performed to identify the presence of different functional groups in biosorbent. The FTIR spectrum of the HAP after two phase calcination is shown in figure 3. The spectrum noticeably shows the presence of phosphate bands at 1062.78, 871.83, 607.57 and 570.95 *cm*⁻¹ and hydroxyl bands at 3570.24 and 3479.59 *cm*⁻¹ which indicate the presence of major functional groups¹⁶⁻¹⁹ in addition with carbonate bands at 2015.61 and 2362.80 *cm*⁻¹.

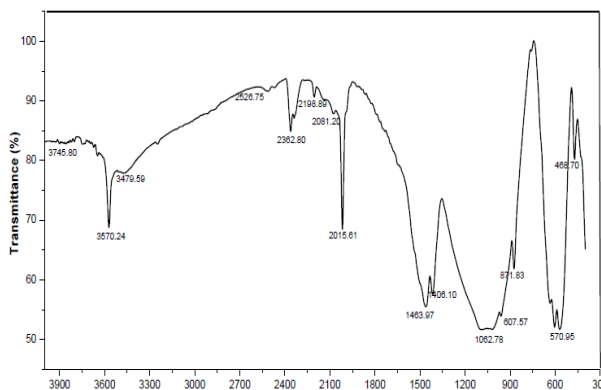


Figure 3. FTIR spectra of HAp biosorbent extracted from Ostrich bone.

Point of Zero Charge (pHpzc)

Point of zero charge method was used to determine the acido-basic properties on HAp surface²⁰. It is defined as the pH at which the total surface charges of biosorbent become zero. The plot of pHpzc is shown in Figure 4. The graph is plotted against the difference data of initial pH (i.e. pH₀) and final pH (i.e. pH_f) values (i.e. ΔpH = pH₀ - pH_f) versus initial data of pH. The point of intersection of the resulting curve at abscissa gave the pH_{PZC} value of HAp. In this study, this value was found exactly 3.0. The value signify that at pH less than 3.0, the positive charge surface of the HAp was predominated, while at pH greater than 3.0, the negative charge surface was predominated. This study shows that pH is the significant domain for determining the charge on HAp surface in aqueous medium which greatly influence the adsorption process²¹.

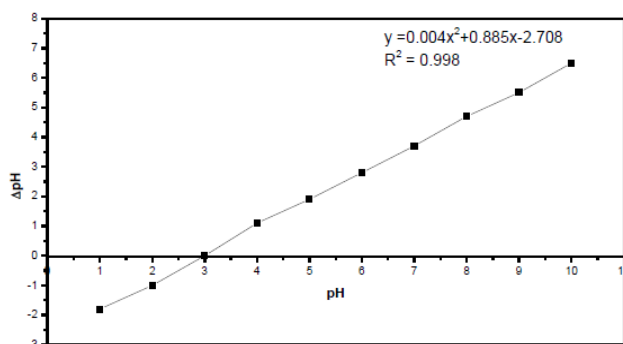


Figure 4. Point of zero charge (pHpzc) of HAp biosorbent extracted from Ostrich bone.

Effect of pH

The effect of solution pH on adsorption of lead (II) ions was investigated by varying the solution pH from 1 to 8. The solution pH was adjusted by using 0.1M HNO₃ and 0.1M NaOH and recorded in a digital pH meter. The initial lead (II) ion concentration was taken 50 mg/L. Figure 5 shows the efficiency of removal was increased significantly as pH increased from 1 to 6 and remains constant beyond 6.

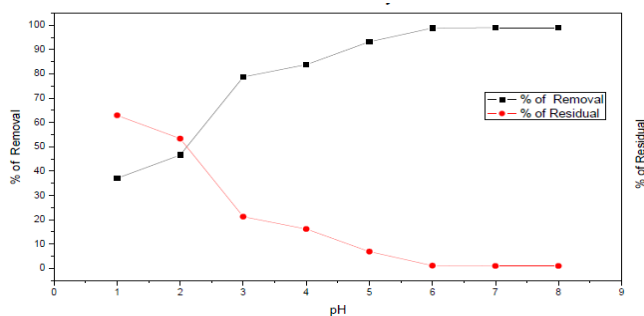


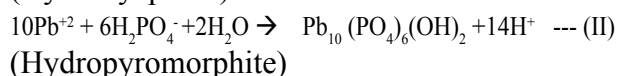
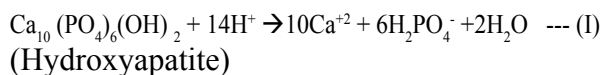
Figure 5. Effect of pH on percentage of removal of pb(II) ion on HAp surface.

A result shows that adsorption process is strongly pH dependent. Previous studies shows 49% of HAp is dissolved at pH 1 and 16 % at pH 2²². In one fold, there is no great effect of dissolution of HAp at pH 3. Therefore, the adsorption of lead (II) ions was suppressed at pH less than 3 due to the damage of crystalline phase of HAp as well as it may also be caused due to the formation of soluble hydroxyl complexes in acidic environments²³⁻²⁵. But in another fold, increasing the pH of solution, the competition between the positive charge bearing lead (II) ions becomes decreases due to the domination of negatively charged surface active

sites of HAp which improve the adsorption of the positively charged lead (II) ions by electrostatic force of attraction^{26,27}. As a result, on conducting the experiments at optimum pH range from 4-6 make sure the presence of the divalent form of lead ions as well as conserve the chemical stability of HAp. Moreover, in one hand, the pHpzc value of HAp was found 3.0 which signify that, HAp surface has +ve charged at solution pH less than 3.0 due to which lead(II) ions were repelled with HAp surface resulting in the reduction of adsorption. In another hand, at pH elevated than pHpzc, the surface of HAp starts to deprotonated (i.e. it bears negative charge) due to which adsorption kinetics increases^{28, 29}. Thus, at optimum pH (4-6) the removal efficiency was reached up to 98.86 %. This result is in good agreement with the results of previous works of Mousa *et al.*

Removal mechanism

Among the different prescribed mechanisms such as; ion exchange, surface complexation, dissolution, precipitation of metal phosphate and substitution of calcium ion of HAp by metal ion during re-crystallization, presented by Meski *et al.* dissolution and precipitation is the most preferable for removal of lead (II) ion from aqueous solution. According, to these mechanism, at optimum pH, HAp ionize to provide free hydrogen phosphate (H₂PO₄⁻) ion and this ion combines with Pb(II) ions in aqueous medium to form insoluble lead complex which is precipitate as a hydroxyromorphite and decrease the concentration of lead (II) ion in solution. The reactions of removal mechanism are shown below;



Effect of contact time

Result shows that the adsorption of lead (II) ions onto the HAp surface was remarkably fast and equilibrium was reached within 5 minutes in which the removal percentage reached up to 72.32% as shown in the figure 6. The adsorption curve was single, smooth and continuous, leading to saturation and indicated the possible monolayer coverage on the surface of the adsorbent by the lead (II) ions.

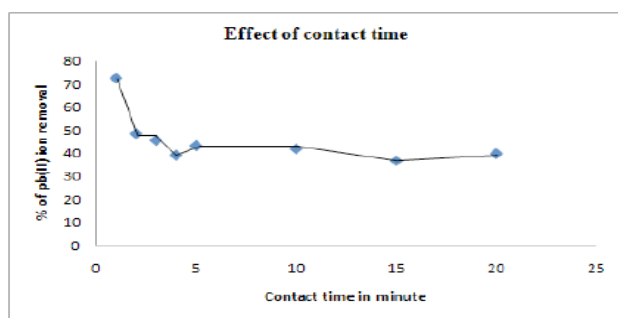


Figure 6. Effect of contact time on percentage of removal of pb(II) ion on HAp surface.

Further increase in contact time has no radical effect on the removal percent. Therefore, 5 minute shaking time was sufficient to reach equilibrium for maximum adsorption. The decrease in the rate of removal with contact time may be due to aggregation of lead (II) ions around HAp surfaces. This aggregation may hamper the migration of lead (II) ions from bulk to HAp surface as the adsorption

sites become saturated, as well as resistance to the diffusion of lead (II) ions in the adsorbents increases³⁰. Moreover, this aggregation of lead (II) ions with increase in contact time makes it almost impossible to diffuse lead (II) ions deeper into the HAp structure at the highest energy sites. These results are in good agreement with the results of earlier studies of Meski *et al.*

Effect of adsorbent dosage

Principally adsorption process is the surface phenomenon, on that basis effectiveness affect by surface area and available active sites of adsorbent which depends on its amount taken³¹. In this study, effect of adsorbent was studied at various experimental dosages: 10mg/L, 20mg/L, 25mg/L, 30mg/L, 40mg/L, 50mg/L and 100mg/L at constant initial concentration of Pb(II) ion (i.e. 50mg/L), constant pH range of 4.5-5.5 and fixed contact time of 90 minutes as shown in table 1.

Table 1. Amount of lead (II) ions removal by HAp biosorbent.

SN	Initial conc. of Pb (II) ion (C_0)	Final conc. of Pb(II) ion (C_f)	Adsorbent dosage	pH range	qt = $(C_0 - C_f)V/m$
1	50mg/L	6.93 mg/L	10 mg/L	4.5-5.5	430.7 mg/g
2	50mg/L	13.31mg/L	20 mg/L	4.5-5.5	183.45 mg/g
3	50mg/L	5.79 mg/L	25 mg/L	4.5-5.5	176.84 mg/g
4	50mg/L	2.71 mg/L	30 mg/L	4.5-5.5	157.63 mg/g
5	50mg/L	1.21mg/L	40 mg/L	4.5 -5.5	121.23 mg/g
6	50mg/L	0.91 mg/L	50 mg/L	4.5-5.5	98.18 mg/g
7	50mg/L	0.52 mg/L	100 mg/L	4.5-5.5	49.48 mg/g

In adsorbent dose 10 g/L, there is a significant removal of lead (II) ions. A previous study shows that adsorption processes are mainly a surface phenomenon; therefore, adsorption efficiency can be considerably affected by surface area and availability of active sites which is ultimately related to the mass of adsorbent³². As the adsorbent dosage increases there are inverse trends of removal due to the aggregation and overlapping of active sites of adsorbent which show the way to the decrease in the effective surface area required for maximum adsorption^{33, 34}.

CONCLUSION

This study shows that the biosorbent extracted from Ostrich bone has a good result for adsorp-

tion of lead (II) ions from aqueous solution. The adsorption was greatly pH dependent, with a high uptake (430.7mg/g) of lead (II) ion at pH range 4 - 6. Results also show the lead (II) ion adsorption is very sensitive to the initial concentration of lead ion in solution. The mechanism of dissolution of HAp and precipitation of hydrophyromorphite was dominant by a low concentration (50mg/L) and in optimum (4-6) pH range. The adsorption of lead (II) ions is very fast and the equilibrium was attended within 5 minutes. 72.32% lead (II) ions were removed within this time. There is an inverse relationship between contact time and percentage of removal. A similar trend was also found in between adsorbent dosage and amount of removal of lead (II) ions from aqueous solution.

SCOPE OF THE STUDY

The application of HAP as a biosorbent has shown the better potential for removing lead ion (II) from aqueous solution. Results obtained in this study are significant to previous research works which proved that it is a well-known biosorbent and provide good background for further investigation of removal of other heavy metal ions like Cd (II), Cr (III), Hg (II), Sb (III) and Ni (II) from aqueous solution. Furthermore, this biosorbent has the potential on removing different color dyes such as; Methylene blue, Congo red, Reactive yellow, Lemon yellow, Cheery red etc from industrial effluents of dye industries. Further characterization of this biosorbent is highly recommended before and after adsorption study.

ACKNOWLEDGMENTS

This research work was funded by the Nepal Academy of Science and Technology (NAST), Khumaltar, Lalitpur. Authors would like to acknowledge with thanks to NAST for technical and financial support as well as Regional office of Department of water supply and sewage management (DWSS), Pardi, Pokhara, Research Center for Applied Science and Technology (RECAST) and Central Department of Chemistry (CDC) Tribhuvan University Kirtipur, Kathmandu, Nepal for equipment and laboratory supports.

REFERENCES

1. Usha kumary, E. R., & Madhu, G. Waste water treatment using low cost natural adsorbents: Doctoral dissertation, Cochin University of Science And Technology. Kerala, India. 2013.
2. Baptista Neto, J. A.; Smith, B. J.; McAllister, J. J. Heavy metal concentrations in surface sediments in a near shore environment, Jurujuba Sound, Southeast Brazil. *Environ. Pollut.* 2000, 109, 1–9.
3. Zhuang, P.; Zou, H.; Shu, W. Biotransfer of heavy metals along a soil-plant-insect-chicken food chain: Field study. *J. Environ. Sci.* 2009, 21, 849–853.
4. Ahamed, M.; Verma, S.; Kumar, A.; Siddiqui, M. K. J. Environmental exposure to lead and its correlation with biochemical indices in children. *Sci. Total Environ.* 2005, 346, 48–55.
5. Mousa et al. Removal of lead ions using hydroxyapatite nano- material prepared from phosphogypsum waste, *J. S.Chem. Soc.* 2016, 20, 357–365.
6. Meski S., Ziani, S. and Khireddine H. Removal of Lead Ions by Hydroxyapatite Prepared from the Egg Shell. *J. Chem.Eng.* 2010, 55, 3923–3928.
7. Martinez-Garcia, G. R.; Bachmann, Th.; Williams, C. J.; Burgoyne, A.; Edyvean, R. G. J. Olive oil waste as a biosorbent for heavy metals. *Int. Biodeterior. Biodegrad.* 2006, 58, 231–238.
8. Saeed, A.; Akhter, M. W.; Iqbal, M. Removal and recovery of heavy metals from aqueous solution using papaya wood as a new biosorbent. *Sep. Purif. Technol.* 2005, 45, 25–31.
9. Reza Sangi, M.; Shahmoradi, A.; Zolgharnein, J.; Azimi, Gh. H.; Ghorbandoost, M. Removal and recovery of heavy metals from aqueous solution using *Ulmuscarpinifolia* and *Fraxinus excelsior* tree leaves. *J. Hazard. Mater.* 2008, 155, 513–522.
10. Murugan R., Ramakrishna S., Development of nanocomposites for bone grafting, *compos. Sci. Technol.* 2005, 65, 2385–2405.
11. Jarcho M., et al., Hydroxyapatite Synthesis and Characterization in dense polycrystalline form, *J. Mater. Sci.* 1976, 2027–2035.
12. Dupoirieux, L.; Plane, L.; Gard, C.; Penneau, M. Anatomical basis and results of the facial artery musculomucosal flap for oral reconstruction. *Br. J. Oral Maxillofacial Surg.* 1999, 37, 25–28.
13. Sevgi Ozyegin, L.; Oktar, F. N.; Gultekin Goller, E.; Kayali, S.; Yazici, T. Plasma-sprayed bovine hydroxyapatite coatings. *Mater. Lett.* 2004, 58, 2605–2609.
14. Al-Asheh, S.; Banat, F.; Mohai, F. Sorption of copper and nickel by spent animal bones. *Chemosphere* 1999, 39, 2087–2096.
15. Hassan, S. S. M.; Awwad, N. S.; Aboterika, A. H. A. Removal of mercury(II) from wastewater using camel bone charcoal. *J. Hazard. Mater.* 2008, 154, 992–997.
16. Wei, Z.; Xiao-ming, Li.; Qi, Y.; Guang-ming, Z.; Xiang-xin, S.; Ying, Z.; Jing-jin, L. Adsorption of Cd(II) and Cu(II) from aqueous solution by carbonate hydroxylapatite derived

- from eggshell waste. *J. Hazard. Mater.* 2007, 147, 534–539.
17. I. Mobasherpour, E. Salahi, M. Pazouki, Potential of nano crystalline hydroxyapatite for lead (II) removal from aqueous solutions: Thermodynamic and Adsorption isotherm study. *A. J. of Pure and App. Che.* 2011 5, 383-392.
 18. R. Palanivelu, A. Rubankumar, Synthesis and Spectroscopic Characterization of Hydroxyapatite by Sol-Gel Method. *International Journal of ChemTech Ressearch.* 2013 5, 2965-2969.
 19. J. Cheng, J. Li, J. Y. Zhang, Curing behavior and thermal properties of trifunctional epoxy resin cured by 4, 4'-diaminodiphenyl sulfone. *eXPRESS Poly.Lett.* 2009 3, 501–509.
 20. J. Venkatean, S. K. Kim, Effect of temperature on isolation and characterization of hydroxyapatite from tuna (*Thunnus obesus*) bone. *Mat.* 2010 3, 4761-4772.
 21. M. Butu, S. Rodino, M. Pentea, A. Negrea, P. Petrache, M. Butnariuir, Spectroscopy of the flour from bones of European hare. *Digest J. of Nanomat. and Biostructures.* 2014, 9, 1317-1322.
 22. Y. Bessekhoud, D. Robert, J-V Weber, N. Chaoui, Effect of alkaline-doped TiO₂ on photocatalytic efficiency, *Journal of Photochemistry and Photobiology A: Che.* 2004 ,167, 49–57.
 23. V.K. Gupta, S. Agarwal, T.A. Saleh, Synthesis and characterization of alumina-coated carbon nanotubes and their application for lead removal, *J Hazard. Mat.* 2011,185, 17–23.
 24. I.Sneddon, H.Garellick, E.Valsami-Jones, An investigation into arsenic (V) removal from aqueous solutions by hydroxylapatite and bone-char, *Mineral. Mag.* 2005, 69, 769- 780.
 25. D.Mohan, C. Pittman, Arsenic removal from water/wastewater using adsorbents-a critical review, *J. Hazard. Mater.* 2007, 142, 1-53.
 26. H. Hasan, P. Srivastava, M. Talatb, Biosorption of lead using immobilized *Aeromonashydrophila* biomass in up flow column system: Factorial design for process optimization, *J. Hazard. Mater.* 2010,177, 312–322.
 27. Corami, A.; Mignardi, S.; Ferrini, V. Cadmium removal from single and multi-metal (Cd²⁺ Pb²⁺ Zn²⁺ Cu²⁺) solutions by sorption on hydroxyapatite. *J. Colloid Interface Sci.* 2008, 317, 402–408.
 28. M. A. M. Khraisheh, Y. S. Al-degs, W. A. M. McMinn, Remediation of wastewater containing heavy metals using raw and modified diatomite, *Chem. Eng. J.* 2004 99, 177–184.
 29. M.A. Al-Ghouti, M.A.M. Khraisheh, S.J. Allen, M.N. Ahmad, and The Removal of Dyes from Textile Wastewater: a Study of the Physical Characteristics and Adsorption Mechanisms of Diatomaceous Earth, *J. Environ. Manage.* 2003, 69, 229-238.
 30. A. Mittal, J. Mittal, A. Malviya, V.K. Gupta, Removal and recovery of Chrysoidine Y from aqueous solutions by waste materials, *J. Colloid. Interf. Sci.* 2010, 344, 497–507.
 31. A.E.Nemr, Potential of pomegranate husk carbon for Cr (VI) removal from waste water: Kinetic and isotherm studies. *J. Hazard Mater.* 2009, 161 132-141.
 32. A.E.Nemr, Potential of pomegranate husk carbon for Cr (VI) removal from wastewater: Kinetic and isotherm studies. *J. Hazard ater.* 2009,161, 132- 141.
 33. T.K. Naiya, A.K. Bhattacharya, S. K. Das, Adsorption of Cd(II) and Pb(II) from aqueous solutions on activated alumina, *J. Colloid Interface Sci.* 2009,333, 14–26.
 34. M.M. Rao, G.P. Rao, K. Sessaiah, N.V. Choudary, M.C. Wang, Activated carbon from Ceibapentandrahulls, an agricultural waste, as an adsorbent in the removal of lead and zinc from aqueous solutions, *Waste Manage.* 2008, 28, 849–858.

Research Article

Extraction and Characterization of Novel Natural Hydroxyapatite Bioceramic by Thermal Decomposition of Waste Ostrich Bone

Komal Prasad Malla,^{1,2,3} Sagar Regmi,^{1,4} Achyut Nepal,¹ Sitaram Bhattarai,⁵
Ram Jeewan Yadav,⁶ Shinichi Sakurai,⁷ and Rameshwar Adhikari^{1,2}

¹Research Centre for Applied Science and Technology (RECAST), Tribhuvan University, Kirtipur, Kathmandu, Nepal

²Central Department of Chemistry, Tribhuvan University, Kirtipur, Kathmandu, Nepal

³School of Health and Allied Sciences, Pokhara University, Pokhara, Nepal

⁴Nepal Academy of Science and Technology (NAST), Khumaltar, Lalitpur, Nepal

⁵Department of Chemistry, Tri-Chandra Multiple Campus, Tribhuvan University, Kathmandu, Nepal

⁶Department of Chemistry, Prithvi Narayan Campus, Tribhuvan University, Pokhara, Nepal

⁷Department of Biobased Materials Science, Kyoto Institute of Technology, Kyoto, Japan

Correspondence should be addressed to Rameshwar Adhikari; nepalpolymer@yahoo.com

Received 6 May 2020; Accepted 16 June 2020; Published 28 August 2020

Academic Editor: Vijaya Kumar Rangari

Copyright © 2020 Komal Prasad Malla et al. This is an open access article distributed under the Creative Commons Attribution License, which permits unrestricted use, distribution, and reproduction in any medium, provided the original work is properly cited.

A novel natural hydroxyapatite (HAp) bioceramic was extracted from the ostrich cortical bone by the thermal decomposition method. HAp was characterized by different analytical tools such as thermogravimetric analysis (TGA), Fourier-transform infrared spectroscopy (FTIR), X-ray diffraction (XRD) analysis, and scanning electron microscopy (SEM). Removal of organic impurities from the bone powder was confirmed by TGA analysis. FTIR spectra of HAp confirmed the presence of the major functional groups such as phosphate (PO_4^{3-}), hydroxyl (OH^-), and carbonate (CO_3^{2-}) in the bioceramic. The XRD data revealed that the HAp was the crystalline phase obtained by calcination of the bone powder at 950°C , and the SEM analyses confirmed the typical plate-like texture of the nanosized HAp crystals.

1. Introduction

At the molecular level, the animal bone is composed of 30–35% organic and 65–70% inorganic components on a dry weight basis [1]. The organic part of the bone contains mainly collagen (95%) and proteins [2]. Besides these, there are other organic substances such as chondroitin sulphate and keratin sulphate along with different lipids such as phospholipids, cholesterol, fatty acids, and triglycerides [3]. The inorganic part of the bone is mainly HAp. It is a calcium/phosphate-based bioceramic which is chemically like the inorganic constituent of the bone matrix (a very complex bone tissue) with the general formula $\text{Ca}_{10}(\text{PO}_4)_6(\text{OH})_2$ [4]. This ceramic is not only biocompatible, osteoconductive, noninflammatory, and nonimmunogenic but also bioactive; i.e., it has an ability to form a direct bond with living tissues

and promote tissue growth [5]. Owing to these properties and chemical likeness to the mineral constituent of the bone matrix, it is a prime filler material to replace damaged bone or is a coating on implants to promote bone ingrowth into prosthetic implants and many more non-load bearing applications [6]. HAp can either be synthesized from inorganic calcium and phosphorous-based precursors or from natural biogenic resources. However, HAp synthesized from both resources is bioactive and are considered equally for *in vitro* and *in vivo* biomedical applications. The most frequently used chemical routes of synthesis are sol-gel [7], precipitation [8], coprecipitation [9], sonochemical [10], hydrothermal [11], mechanochemical [12], and microemulsion [13]. However, the major drawbacks of chemically synthesis routes are it demands a high degree of pure chemicals in addition to the lengthy procedures associated with the

synthetic routes [14]. To produce biologically preferable and to avoid the lengthy procedure, biogenic resources are alternative sources for synthesis. In comparison with chemical precursors, these sources are biologically safe as no foreign chemicals are utilized and are ecofriendly and cost effective.

Although the ostrich farms are available in Nepal since 2008, their numbers are declining throughout the world. As it is not a widely available biowaste, according to Mr. C.P. Sharma, CEO of Ostrich Nepal Pvt. Ltd, this farm is producing 1000 kg meat per day and 15–20% bone waste tentatively based on the body weight (180–300 kg) of the ostrich. For sustainable development, waste should be recycled, reused, and channeled towards the production of value-added products. In this context, the ostrich (*Struthio camelus*) bone, which is the biowaste, is an economical source of HAp for hard tissue replacement in biomedical and dental applications [15].

Furthermore, HAp extracted from biogenic resources such as mammalian, avian, and fish bones, corals, seashells, and eggshells can exhibit better biological properties in comparison with the chemical sources [16]. Moreover, such an extract contains beneficial cations such as Na^+ , K^+ , Mg^{+2} , Sr^{+2} , Zn^{+2} , and Al^{+3} or anions such as F^- , Cl^- , SO_4^{-2} , and CO_3^{-2} or presence of both ions. These resources are beneficial for biomedical applications [17]. Different researchers have used various biogenic resources for the extraction of HAp. Barakat et al. [18] and Sofronia et al. [19] used bovine bones, Lu et al. [20] used pig bone and teeth, and Abdulrahman et al. [21], Wu et al. [5], and Khandelwal and Prakash [1] used wastes from eggshells. Similarly, Ferreira et al. [22] extracted from ostrich eggshells. Kongsri et al. [23] and Panda et al. [24] extracted from fish scales, and Venkatesan et al. [25] extracted from the fish bone. Furthermore, Zainon et al. [26] and Kim et al. [27] extracted from the cuttle fish bone. Chattanathan et al. [28] used the catfish bone. Piccirillo et al. [29] used the codfish bone, and Wan et al. [30] extracted from plant resources.

Alkaline hydrothermal hydrolysis process was used to decompose and dissolve organic impurities as well as fatty tissues. Two-step thermal decomposition was done in a muffle furnace (Model no: STM-8-12, Henan Sante Furnace Technology Co. Ltd, Henan, China) to eliminate the collagen and other residual organic moieties. Water-in-oil (W/O) microemulsion technique was used to control the particle size of the extracted HAp. This technique is effective to control the particle size from the micron to the nanometer range [31]. Moreover, in this method, reverse micelles are formed when an aqueous phase containing HAp nanoparticles has been dispersed as a microdroplet in an oil phase and surrounded by a surfactant molecule. Generally, the size of microdroplets is smaller and uniform which acts as a nanoreactor to control the particle size in the emulsion intermediate [13]. In addition, the literature shows that the size of the HAp controlled by using ionic and nonionic surfactants has been reported to have a nanoscale surface area [32].

Hence, the goal of this study is to synthesize natural HAp from the waste ostrich bone by applying alkaline hydrothermal hydrolysis and two-step thermal decomposition

methods, followed by particle size control by applying the water-in-oil (W/O) microemulsion technique and to find how their unique properties allow for their potential use in various biomedical applications.

2. Materials and Methods

2.1. Materials. The required amount of the femur bone of a male ostrich (2–3 years old) was collected from the commercial ostrich slaughtering house. It is located in Ostrich Nepal Pvt. Ltd, Gangolya-1, Rupendehi district, the western region of Nepal. The femur bone is categorized as cortical bones which contain the highest amount of minerals per unit weight.

2.2. Preparation of Bone Powder. The method adopted for the extraction of HAp was the modified procedures of Barakat et al. [18] and Sobczak et al. [33]. The bone samples were cleaned to get rid of visible impurities employing a sharp knife. Then, they were cut into small pieces using a hacksaw. These pieces were boiled for about 4 h in a closed container to remove macroscopic adhering impurities. Subsequently, the samples were washed multiple times with distilled water and later immersed in acetone for 3 h to remove the invisible fat. They were then dried in a hot air oven for 12 h at 120°C to avoid shoot formation during grinding. The dried bone samples were crushed into small pieces using an iron mortar and pestle (commonly called khaal and lora which is made by a local ironsmith in Birgunj, Nepal) and then pulverized using a grinding machine. Finally, the bone powders were sieved to separate off the particle size of less than 450 μm [34]. Furthermore, the alkaline hydrothermal process was applied for the removal of residual phospholipids and fatty tissues from the bone powder. The bone powder for this was treated with a highly concentrated (4N) sodium hydroxide solution with a 1 : 40 solid/liquid weight ratio and then boiled at 250°C for 6 h with continuous stirring according to the modified protocol. Finally, the bone powder was washed multiple times to neutralize the pH and then dried in a hot air oven for 3 h at 80°C to get the final yield.

2.3. Extraction of HAp Using Thermal Decomposition of the Bone Powder. In general, natural HAp can be extracted by calcination of the bone based on natural resources which could be a reliable and chemical-free method [35]. In this study, 100 g of the bone powder of particle sizes ranging from 0 to 450 μm was placed in the calcination boat and then heated in a muffle furnace at a rate of 5°C/min from room temperature to 650°C for 6 h. The calcined samples were taken out, and then the furnace was cooled slowly to room temperature. The samples were further heated to 950°C for 6 h under a similar heating and cooling rate to get the final product, following the modified method of Sobczak et al. [33] and Barakat et al. [36].

2.4. Controlling Particle Size of the Extracted HAp. The sizes of the extracted HAp were not fixed. They can vary from the micrometer to the nanometer range. But in this study, the

water-in-oil (W/O) reverse microemulsion technique was applied to control the size of HAp. The reagents used for the size control and reasons for choices are shown in Table 1.

The particle size of HAp was controlled using cyclohexane as an oil phase and double distilled water as a water phase. The mixtures of Triton X-100, CTAB, and TTAB were used as a nonionic and ionic surfactants in addition to the mixture of ethanol and 1-butanol which were used as a cosurfactant to stabilize the reverse microemulsion. The micelle of the reverse microemulsion formed by these mixtures which acts as a nanoreactor/capping agent only permits the entry of nanosized HAp particles inside the micelle of the reverse microemulsion and helps to isolate nanosized particles from the rest of the dispersed bulk particles in the emulsion base.

The required amount (10 g) of HAp extracted from the second step of thermal decomposition was taken in a 1L flask. The 1 : 2 v/v mixtures of distilled water and cyclohexane were transferred and agitated into the flask to prepare the microemulsion. The 1 : 1.2 v/v surfactant ratios of 2 % w/v CTAB, 10% w/v TTAB, and Triton X-100 were mixed to stabilize the microemulsion. Furthermore, 1 : 2 v/v mixtures of pure ethanol and 1-butanol were also mixed in the same emulsion as cosurfactants to enhance the activity of the surfactants and stabilization of the microemulsion. The solutions were agitated in a magnetic stirrer at 600 rpm for 2 h. At the time of agitation, there is an interparticle attraction between nano-HAp (which has a zwitter ionic behaviour) and surfactant molecules. This attraction helps them to keep it in the emulsion base and isolate the nanoparticle from the rest of the dispersed random particles of the emulsion base [37]. For better results, the emulsion was ultrasonicated at 40°C for 30 minutes. It was then centrifuged at 4500 rpm for 20 minutes to separate the emulsion-based size-controlled HAp from the rest of the solutions and oven-dried at 120°C for 4 h and heated again at 300°C for another 3 h for better results.

2.5. Thermogravimetric Analysis (TGA). The mass loss pattern of the HAp powder during heating was studied via thermogravimetric analysis. A TGA analyzer, model Q600, USA, was used for this study. The TGA analysis of the HAp powder was recorded from 30°C to 1000°C at the heating rate of 10°C/min with a nonstop glide of nitrogen.

2.6. Fourier-Transform Infrared Spectroscopy (FTIR). FTIR is the vital analytical technique for the characterization of biomaterials. To look into the presence of different functional groups, organic impurities, and the degree of probable dehydroxylation of HAp in the course of the calcination process, a Shimadzu IRT racer-100 A217064 00746, Japan, FTIR spectrophotometer was used in a transmission mode of the mid-infrared range with wavenumbers from 500 to 4000 cm^{-1} via the ATR sampling technique.

2.7. X-Ray Diffraction (XRD). The particle size and crystallinity of HAp before and after size control have been investigated using the powder X-ray diffraction (XRD)

technique. The XRD spectra were recorded at room temperature, using a Bruker D2, Germany, advanced X-ray diffractometer ($\text{Cu-K}\alpha = 1.5406 \text{ \AA}$ radiation source) running at 40 kV and 30 mA. The diffraction profiles were accumulated over a 2θ range from 20° to 80° with an incremental step measurement of 0.02° using the flat plane geometry. The acquisition time was set at 2.5/minutes for each scan. The crystallite size of the particles in the powder was calculated by using Scherer's equation.

2.8. Scanning Electron Microscopy (SEM). The morphology of bone powder and the extracted HAp was analyzed using scanning electron microscopy (SEM; JEOL JSM 6490LA Analytical Scanning Electron Microscope, Japan). All the samples were sputtered with gold and then analyzed by SEM at an accelerating voltage of 10 kV.

3. Results and Discussion

3.1. Two-step Thermal Decomposition Method for the Effective Removal of Organic Moieties from Bone Powder. The FTIR spectra of the raw bone powder, before and after the thermal decomposition at 650°C and 950°C, are shown in Figure 1. This spectrum shows a series of bands in the mid-infrared (4000–500 cm^{-1}) region. Different types of bonds present in various components of the bone powder give characteristic infrared absorption bands. Due to the change in the molecular environment of the bone powder, there is a shift in the intensities and position of their corresponding absorption bands [38]. The mixed broad band in the range of 3854–3568 cm^{-1} is attributed to the volatile impurities and trace amount of water molecules incorporated into the bone powder. Thermal decomposition helps to eliminate most of the volatile organic impurities from the bone powder [39]. Before heating, the hydroxyl band of HAp at 3568 cm^{-1} is not visible, and it is probably due to the overlapping of impurity bands or masking effect of other impurity bands over it [40]. The bands associated with the amide groups of proteins and collagens in the range 1315.45 cm^{-1} , 1338.59 cm^{-1} , 1504 cm^{-1} , and 1651 cm^{-1} are clearly visible in the spectrum (Figure 1 A) due to the partial elimination of organic moieties at the time of cleaning and alkaline hydrothermal hydrolysis [27]. The band at 2360.87 cm^{-1} with a shoulder at 2337.72 cm^{-1} is credited by free carbon dioxide [41]. A strong band at 999.13 cm^{-1} is associated with P-O stretching vibration of the phosphate group [42]. A small band at 871.82 cm^{-1} is associated with the out-of-plane bending mode of a carbonate group [43], and a small band at 667.37 cm^{-1} is associated with the bending vibration of a hydroxyl group of HAp [42]. Similar types of findings have been reported by Khoo et al. in HAp extracted from the bovine bone [39].

The FTIR spectrum of the bovine bone powder reported by Barakat [36], Khoo [39], and Sobacsak [33] shows the presence of major inorganic components such as phosphate, hydroxyl, and carbonate groups and organic components such as amide-I groups from the protein constituent of the bone powder in the range 4000–500 cm^{-1} . But, in this

TABLE 1: Reagent source and explanation for choice.

Reagents	Source	Explanation for choice
(1) Cyclohexane	Merck, Germany	Used as an oil phase. It can form reverse micelle easily with water in comparison with other organic solvents.
(2) Cetyltrimethylammonium bromide (CTAB)	Merck, Germany	Used as an ionic surfactant to produce and stabilize microemulsion.
(3) Tetradecyltrimethylammonium bromide (TTAB)	Merck, Germany	Used as an ionic surfactant to produce and stabilize microemulsion.
(4) Triton X-100 (TX-100)	Packard Co. Inc., USA	Used as the nonionic surfactant to produce and stabilize microemulsion.
(5) Ethanol (99.9%)	Merck, Germany	Used as a cosurfactant to enhance the activity of surfactants in emulsion.
(6) 1-Butanol (99.5%)	Merck, Germany	Used as a cosurfactant to enhance the activity of surfactants in emulsion.

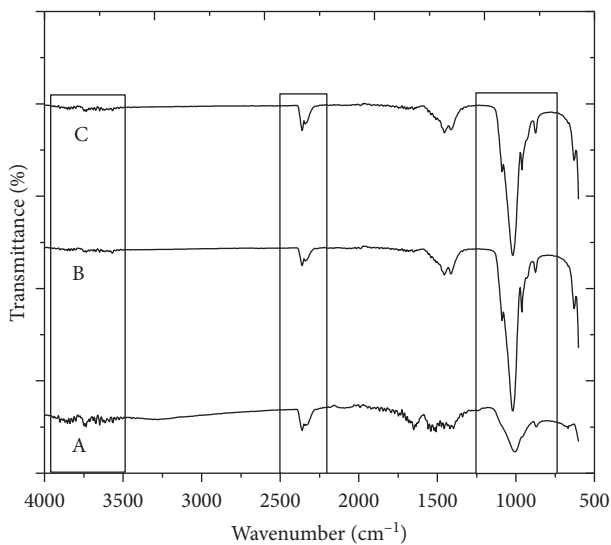


FIGURE 1: FTIR spectra showing the effect of two-step thermal decomposition on the bone powder structure: (A) raw bone powder, (B) bone powder heated at 650°C for 6 h, and (C) bone ash recalcined at 950°C for 6 h.

present study, comparing their results with the spectrum range 4000–500 cm^{-1} obtained for the ostrich bone ash calcined at 650°C (Figure 1 B) clearly shows that most of the organic moieties have disappeared after calcination. The spectral bands 1315.45 cm^{-1} , 1338.59 cm^{-1} , 1396.46 cm^{-1} , 1504.0 cm^{-1} , and 1651.0 cm^{-1} associated with the amide-I groups of proteins and collagen which are observed in the spectrum of the raw bone powder (Figure 1 C) have totally disappeared after thermal decomposition. This significance change in the bone powder is not visible on direct heating till 950°C. Nevertheless, the FTIR spectra (Figure 1 B), reveal the presence of major phosphate (PO_4^{3-}), carbonate (CO_3^{2-}), and hydroxyl (OH^-) groups. These spectra have more clearly appeared in the first-phase calcined products because the cross-linked structure in the raw bone powder is destroyed after calcination. This comparison shows that the thermal decomposition applied here is adequate to remove organic moieties from the bone powder. In addition, there are no absorption bands related to carbon-hydrogen, C-H (1396 cm^{-1}), and nitrogen-hydrogen, N-H (1580 cm^{-1}), bonds in the spectrum after the first-phase calcinations [39]. Therefore, all bands observed in the spectrum of Figure 1 B

are associated with the inorganic components of the bone minerals. One strong and relatively broad band at 1062.78 cm^{-1} , two relatively strong and sharp bands at 570.95 cm^{-1} and 603.71 cm^{-1} , and another band at 956.69 cm^{-1} have appeared due to the presence of the phosphate (PO_4^{3-}) group of HAp. Bahrololoom et al. observed the similar types of two bands in the bovine cortical bone ash at 603 cm^{-1} and 1051 cm^{-1} in their investigation due to the stretching vibration of the phosphate (PO_4^{3-}) group. Similarly, the bands at 871.83 cm^{-1} , 1406.10 cm^{-1} , and 1463.97 cm^{-1} , respectively (Figure 1 B) are associated with the brushite (CaHPO_4) and carbonate (CO_3^{2-}) groups [39]. In the bone-based HAp, the carbonate group can competitively substitute at two sites: in the hydroxyl (OH^-) site and in the phosphate site of the HAp structure, giving A-type and B-type carbonate-substituted HAp, respectively. These two types of substitution can occur simultaneously, resulting in a mixed AB-type substitution which constitutes the mineral part of the bone. As a result, the peak position of carbonate ions in the spectra depends on whether the carbonate ions are substituted by the hydroxyl ion or the phosphate ion on the HAp lattice. There is also a relatively broad band at 3570.24 cm^{-1} (Figure 1 B) which is attributed to the hydroxyl group of HAp independently. The spectral bands of amide-I groups of proteins and collagen as mentioned above are not visible in this spectrum because of thermal decomposition which is the significance change followed by two-step calcination.

The FTIR spectrum of the bone ash calcined again at 950°C for another 6 h is presented in Figure 1 C. This spectrum provides various spectral information indicating some changes which occurred during recalcination. The band at 2362.80 cm^{-1} has disappeared after calcination again which might be due to the elimination of residual impurities. This is in good agreement with the change in gray to clear white color of the bone ash after the second-phase calcination as shown in Figure 2.

The broad band at 3570.24 cm^{-1} observed in the spectrum of Figure 1 (A and B) has almost disappeared and been replaced by a diminutive peak at 3568.46 cm^{-1} as shown in the spectra in Figure 1 C, and this is due to the hydroxyl stretching. This spectrum is in good agreement with the spectra reported by Younesi et al. [44]. It shows the significant difference between curves B and C. In this spectrum, the stretching band at 3568.46 cm^{-1} and the vibration band

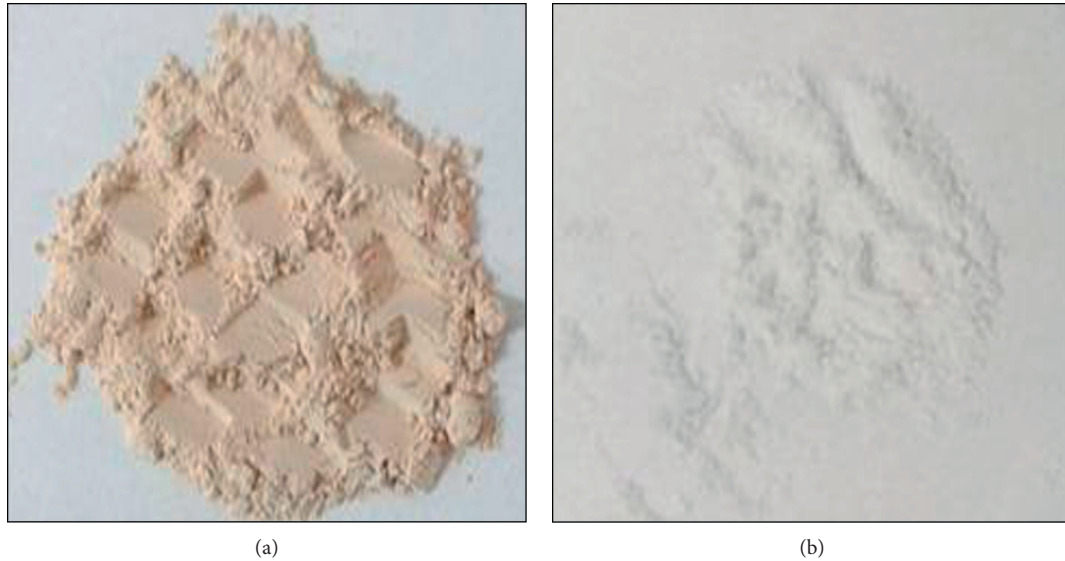


FIGURE 2: Visual observation of bone ash showing the effect of the recalcination structure: (a) bone ash calcined at 650°C for 6 h and (b) bone ash recalined at 950°C for another 6 h.

at 629 cm^{-1} are contributed by OH^- groups and the bands located at 960.55 cm^{-1} , 1018.41 cm^{-1} , and 1087 cm^{-1} are due to phosphate groups [20, 45]. Similarly, the bands at 1412 cm^{-1} and 1454 cm^{-1} are contributed by carbonate groups [46]. Usually, carbonate groups are the common impurity in the natural HAp extracted from animal bones [45]. Moreover, the intensity of the O-H stretching vibration in HAp is comparatively weaker than that of P-O stretching because of the HAp stoichiometry [46]. Therefore, this result shows that 6 h of heating at 950°C is the appropriate method for extraction of HAp from the bone powder after the first-phase calcination in similar conditions. In our finding, 525 g of HAp is extracted from 1 kg of the clean bone powder as a dry weight basis after two-phase calcinations at 650°C and 950°C, respectively.

3.2. Negligible Mass Loss of HAp Found on Heating under Inert Atmosphere. The mass loss pattern of HAp was further confirmed by TGA analysis (Figure 3). This curve indicates the three inflection points with minute mass loss on heating in an inert environment. Hu et al. investigated similar results for thermal analysis of HAp extracted from coral shells [47]. But, in this study, in the first inflection point, a negligible mass loss (0.19 wt.%) at a temperature from 275°C to 369°C corresponds to the evaporation of physisorbed and chemisorbed water molecules, as well as residual volatile organic impurities incorporated in the HAp powder [48]. Similarly, in the second inflection point, the mass loss (0.23 wt.%) at a temperature between 535°C and 646°C is attributed to the probable decomposition of carbonate-based impurities [21, 49]. These types of impurities are very common in bone-based resources [50].

Olsen et al. suggested that the mass loss at a temperature between 225°C and 500°C is caused by the decomposition of organic components and at a temperature higher than 500°C is a result of decomposition of the structural carbonate by

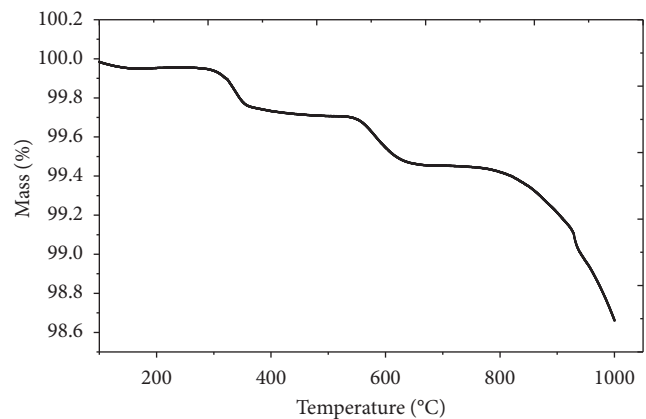


FIGURE 3: TGA curve of the HAp heated from 100°C to 1000°C under N_2 atmosphere.

release of carbon dioxide [51]. Miculescu et al. reported similar types of decomposition at a temperature between 550°C and 600°C [50]. There is no exothermic reaction related to the carbonate decomposition in the TGA curve of the bone powder investigated in this study. However, the presence of carbonate groups was also detected by FTIR analysis.

Finally, the significant mass loss (0.89 wt.%) was once found at a temperature between 770°C and 1000°C, indicating the removal of most of the residual organic moieties such as fatty tissues, collagen, chondroitin sulphate, and keratin sulphate. Furthermore, any other likely reason for continuous mass loss during heating might be due to the partial dehydroxylation of HAp in this temperature range [45, 52]. The reaction is given in the following equation:



Younesi et al. and Bahrololoom et al. investigated similar types of weight loss in their studies of HAp extracted from bovine bone ash [38, 42]. Hence, TGA studies have shown that the mass loss is due to the removal of water, residual organic moieties, and partial dehydroxylation of HAp [46].

3.3. Degree of Crystallinity of HAp Increased Highly after Size Control. The structural analysis of the bone powder and samples heated in different temperatures was done by XRD. The XRD profiles of the extracted HAp before and after size control are shown in Figure 4. The XRD profile of the bone powder before calcination is shown in Figure 4 A. This profile indicates the poor crystalline nature of HAp in the bone powder before calcination. The crystalline nature becomes clear on thermal decomposition at 650°C without decomposition to any other form of the calcium phosphate family. The XRD profile shown in Figure 4 B corresponds to a semicrystalline nature of HAp. This is due to the partial removal of organic impurities and presence of a slight amount of the carbonate group in the bone ash.

The diffraction profile shown in Figure 4 C is sharper in comparison with the curves in Figure 4 (A and B), which points out better crystallinity and declining order of organic impurities on increasing the calcination temperature above 650°C. The thermal decomposition peaks of HAp into alpha tricalcium phosphate (α -TCP) and beta tricalcium phosphate (β -TCP) are not observed at any temperature up to 950°C for 6 h of heating [53]. This signifies the gradual increment in the degree of sharpness of the peak or increase in the crystalline nature of HAp with the increasing calcination temperature.

The sharp and clear peak positions observed in Figure 4 D after size control confirm the phase purity and the high degree of crystallinity [43]. Venkatesan et al. also reported similar types of fully crystallized HAp extracted from the salmon fish bone [2]. Although the decomposition of HAp phases was not detected in the second-phase calcinations, dehydroxylation of HAp could have taken place after size control and reheating it up to 300°C for 3 h. Due to this reason, the peak of size-controlled HAp shifted as shown in Figure 4 D when compared to the first- and second-phase calcinated bone ash as shown in Figure 4 (B and C).

The average particle size of HAp nanoparticles calculated by Scherer's equation before and after size control is shown in Table 2.

Table 2 shows a remarkable decrement in the average particle size from 36.44 nm to 19.23 nm which points out that the reverse microemulsion is an effectual technique for controlling the particle size. The phase analysis of size-controlled HAp nanoparticles is compared with the ICDD (International Centre for Diffraction Data standard HAp) PDF card no. 00-009-0432 which shows that the major diffraction peaks at 2θ values of 32.026°, 33.165°, 32.424°, 49.722°, 46.954°, and 34.271° corresponding to the (211), (300), (112), (213), (222), and (202) Miller planes are in good agreement with the standard HAp. Small deviation of these peaks from standard values may be due to the existence of a

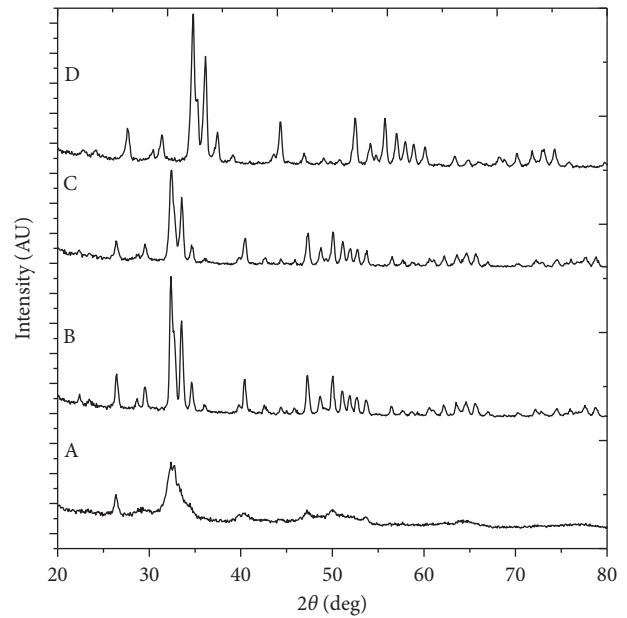


FIGURE 4: XRD patterns of (A) the raw ostrich bone powder, (B) the powder calcined at 650°C for 6 h, (C) the ash obtained after recalcination at 950°C for another 6 h, and (D) the HAp size control after the microemulsion technique.

slight amount of foreign ions (e.g., Na^+ , K^+ , Zn^{2+} , Mg^{2+} , and Sr^{2+}) found in this case [3]. The comparative data of diffraction profiles of prominent XRD peak position, d -spacing, and relative intensity which correspond to the planes (211), (300), (112), (213), (222), and (202) of standard and size-controlled HAp are shown in Table 3. It shows that the XRD profiles of HAp with the diffraction peaks obtained with d -spacing values of 2.79 Å, 2.76 Å, and 2.61 Å and the other d -spacing values match exactly with the hexagonal system with the primitive lattice. This result of XRD analysis obtained in the present investigation is in good agreement with the reported results [54].

3.4. Hexagonal Shape of HAp Is Clearer after Refining and Size Control. To confirm the effect of calcination and size control on the particle size and morphology, the calcined bone powder before and after size control was investigated by SEM. The SEM micrographs are shown in Figure 5. The SEM image (Figure 5(a)) for the bone powder heated at 650°C for 6 h shows a wide range of particle size and shapes. The particles have irregular shapes and size with edges and corners rather than being spherical. This irregular shape and size of the particles might be due to the grinding effect at the time of preparation. It does not show any presence of amorphous organic material, indicating that the organic moieties of the bone powder have been completely removed during calcinations. Similarly, the bone powder recalcined at 950°C for another 6 h (Figure 5(b)) shows the occurrence of a microstructural change which includes recrystallisation of the bone mineral. Bahrololoom et al. [38] attempted SEM observations of the heat-treated bovine bone and reported that the organic moieties of the bone tissue are completely

TABLE 2: The average particle size of HAp calcined at 950°C and after size control by the reverse microemulsion technique.

HAp samples	Crystallite size in the $\langle h k l \rangle$ direction
Sample-C (calcined at 950°C)	36.44 nm
Sample-D (size control after calcination)	19.23 nm

TABLE 3: Comparison of phase analysis of size-controlled HAp with ICDD file no. 00-09-0432.

Miller indices ($h k l$)	d -spacing (Å)		2θ value		Relative intensity	
	Standard	Size control	Standard	Size control	Standard	Size control
211	2.79685	2.79467	31.973	34.785	100.0	100.00
300	2.69969	2.79126	33.157	33.1654	54.3	65.39
112	2.77146	2.76131	32.275	32.4240	43.7	49.61
213	1.83574	1.83373	49.620	49.7223	32.3	35.33
222	1.93385	1.93515	46.947	46.9548	24.8	33.30
202	2.62219	2.61660	34.167	34.2711	24.5	23.01

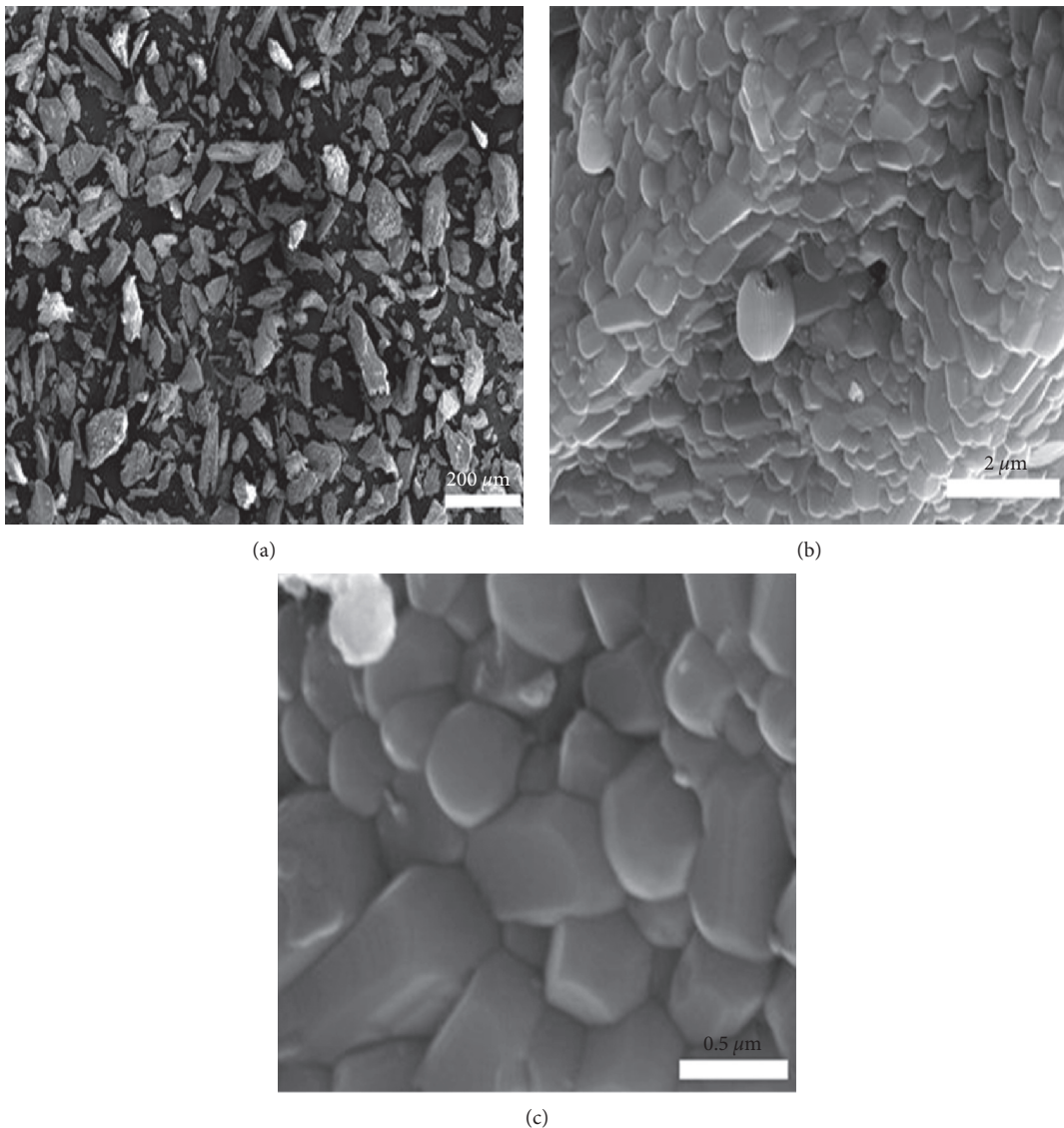


FIGURE 5: SEM micrographs of (a) the bone powder calcined at 650°C for 6 h, (b) the bone powder after recalcination at 950°C for another 6 h, and (c) the HAp obtained after the W/O microemulsion technique.

eliminated during heating at 800°C. This is followed by recrystallisation of the bone mineral, i.e., HAp at 800°C, which produces a certain range of irregular shapes of crystal morphologies including spherical, hexagonal, platelet, and rod shapes. Similar types of observations were seen in this study as shown in Figure 5(b).

Moreover, the morphology of HAp particles also depends on the source of the bone, time period of calcinations, and calcination temperature [55]. However, in this study, the morphology of the particle might be influenced by the gender, age, and food habit of the ostrich from which the bone was collected. Hence, more studies are required to understand the influence of these biological factors on the morphology. Some changes in color, morphology, and recrystallisation of bone minerals due to calcinations have also been reported by Ooi et al. [55] and Sagadevan and Dakshnamoorthy [56]. Figure 5(c) shows the clear picture of the SEM micrograph of the HAp after size control. As evident, the particles have irregular shapes, including small spheres, rods, and hexagonal shape, and are also in agglomerated condition together in some parts. The size of the individual particle is in the micrometer range but has not been investigated in detail.

4. Conclusion

This study shows that natural HAp can easily be extracted from the raw ostrich bone powder by the two-step thermal decomposition method at temperatures 650°C and 950°C, respectively. The results showed that calcination at 650°C for 6 h produces the semidecomposed powder, while heating at 950°C for another 6 h synthesizes HAp from the raw bone powder. It can be incidental that treatment temperature and time are the key parameters in determining the composition of the extracted product. Water-in-oil (W/O) micro-emulsion is an efficient technique for controlling the particle size of HAp from 36.44 nm to 19.23 nm. The results of TGA, FTIR, and XRD show that the major chemical components of the prepared materials are HAp, in addition to a small amount of carbonate (CO_3^{2-}) ions which is preferable for biomedical application in bone tissue engineering. The SEM result confirms the condition of agglomeration shape, size, and nature of particles before and after size control. HAp produced from this source has a great potential to be used as a viable and economical bone graft material for non-load bearing orthopaedic application.

Data Availability

The data used to support the findings of this study are available from the corresponding author upon request.

Conflicts of Interest

The authors declare that they have no conflicts of interest.

Authors' Contributions

The study and the first draft of writing were done by Komal Prasad Malla, and the supervision and edition were done by

Prof. Dr. Rameshwar Adhikari and Dr. Sagar Regmi. Co-authors Prof. Dr. Shinichi Sakurai, Assist. Prof. Dr. Ram Jeewan Yadav, Sitaram Bhattarai, and Mr. Achyut Nepal participated in analysing the results and editing the manuscript.

Acknowledgments

The authors acknowledge the University Grants Commission (UGC) Sanothimi, Bhaktapur, Nepal, for providing the Collaborative Research Grant (CRG 73/74-ST-02; From Waste to Biomaterials: Preparing Hydroxyapatite Nanomaterial from Ostrich Bone and Biomedical Application) and PhD research grant (PhD 74-75/S&T-3) to Komal Prasad Malla. The authors would also like to thank the University Grants Commission (UGC) Sanothimi, Bhaktapur, Nepal (UGC Award no. PF-76/77-S&T-01) for providing a postdoctoral fellowship to Dr. Sagar Regmi. The authors sincerely acknowledge the supports of the Nepal Academy of Science and Technology (NAST) for characterization of the samples by XRD.

References

- [1] H. Khandelwal and S. Prakash, "Synthesis and characterization of hydroxyapatite powder by eggshell," *Journal of Minerals and Materials Characterization and Engineering*, vol. 4, no. 2, pp. 119–126, 2016.
- [2] J. Venkatesan, B. Lowe, P. Manivasagan et al., "Isolation and characterization of nano-hydroxyapatite from salmon fish bone," *Materials*, vol. 8, no. 8, pp. 5426–5439, 2015.
- [3] N. Bano, S. S. Jikan, H. Basri, S. Adzila, and D. M. Zago, "XRD and FTIR study of A&B type carbonated hydroxyapatite extracted from bovine bone," in *Proceedings of the AIP Conference*, AIP Publishing, Article ID 020100, November 2019.
- [4] Y. Zhu, S. Murali, M. D. Stoller et al., "Carbon-based supercapacitors produced by activation of graphene," *Science*, vol. 332, no. 6037, pp. 1537–1541, 2011.
- [5] Y. Wu, L. Xia, Y. Zhou et al., "Evaluation of osteogenesis and angiogenesis of icariin loaded on micro/nano hybrid structured hydroxyapatite granules as a local drug delivery system for femoral defect repair," *Journal of Materials Chemistry B*, vol. 3, no. 24, pp. 4871–4883, 2015.
- [6] M. D. Fahmy, H. E. Jazayeri, M. Razavi, R. Masri, and L. Tayebi, "Three-dimensional bioprinting materials with potential application in preprosthetic surgery," *Journal of Prosthodontics*, vol. 25, no. 4, pp. 310–318, 2016.
- [7] T. Sari, N. Jamarun, S. Syukri, Z. Azharman, and A. Asril, "Effect of mixing temperature on the synthesis of hydroxyapatite by sol-gel method," *Oriental Journal of Chemistry*, vol. 30, no. 4, pp. 1799–1804, 2014.
- [8] G. Gergely, F. Wéber, I. Lukács et al., "Preparation and characterization of hydroxyapatite from eggshell," *Ceramics International*, vol. 36, no. 2, pp. 803–806, 2010.
- [9] M. S. Arsad, P. M. Lee, and L. K. Hung, "Synthesis and characterization of hydroxyapatite nanoparticles and β -TCP particles," in *Proceedings of the 2nd International Conference on Biotechnology and Food Science*, IPCBEE, Bali Island, Indonesia, pp. 184–188, April 2011.
- [10] A. H. Yorug and Y. Ipek, "Sonochemical synthesis of hydroxyapatite nanoparticles with different precursor reagents," *Acta*

- Physica Polonica A: General Physics, Solid State Physics*, vol. 121, no. 1, p. 230, 2012.
- [11] I. S. Neira, Y. V. Kolen'ko, O. I. Lebedev et al., "An effective morphology control of hydroxyapatite crystals via hydrothermal synthesis," *Crystal Growth & Design*, vol. 9, no. 1, pp. 466–474, 2008.
 - [12] K. C. B. Yeong, J. Wang, and S. C. Ng, "Mechanochemical synthesis of nanocrystalline hydroxyapatite from CaO and CaHPO₄," *Biomaterials*, vol. 22, no. 20, pp. 2705–2712, 2001.
 - [13] S. A. Jahan, M. Y. A. Mollah, S. Ahmed, and M. A. B. H. Susan, "Nano-hydroxyapatite prepared from eggshell-derived calcium-precursor using reverse microemulsions as nano-reactor," *Materials Today*, vol. 4, no. 4, pp. 5497–5506, 2017.
 - [14] M. Akram, R. Ahmed, I. Shakir, W. A. W. Ibrahim, and R. Hussain, "Extracting hydroxyapatite and its precursors from natural resources," *Journal of Materials Science*, vol. 49, no. 4, pp. 1461–1475, 2014.
 - [15] J. K. Odusote, Y. Danyuo, A. D. Baruwa, and A. A. Azeez, "Synthesis and characterization of hydroxyapatite from bovine bone for production of dental implants," *Journal of Applied Biomaterials & Functional Materials*, vol. 17, no. 2, 2019.
 - [16] S. M. Londoño-Restrepo, C. F. Ramirez-Gutierrez, A. del Real, E. Rubio-Rosas, and M. E. Rodriguez-García, "Study of bovine hydroxyapatite obtained by calcination at low heating rates and cooled in furnace air," *Journal of Materials Science*, vol. 51, no. 9, pp. 4431–4441, 2016.
 - [17] P. Palmero, "Ceramic-polymer nanocomposites for bone-tissue regeneration," in *Nanocomposites for Musculoskeletal Tissue Regeneration*, pp. 331–367, Elsevier, Amsterdam, Netherlands, 2016.
 - [18] N. A. M. Barakat, M. S. Khil, A. M. Omran, F. A. Sheikh, and H. Y. Kim, "Extraction of pure natural hydroxyapatite from the bovine bones bio waste by three different methods," *Journal of Materials Processing Technology*, vol. 209, no. 7, pp. 3408–3415, 2009.
 - [19] A. M. Sofronia, R. Baies, E. M. Anghel, C. A. Marinescu, and S. Tanasescu, "Thermal and structural characterization of synthetic and natural nanocrystalline hydroxyapatite," *Materials Science and Engineering: C*, vol. 43, pp. 153–163, 2014.
 - [20] X. Y. Lü, Y. B. Fan, D. Gu, and W. Cui, "Preparation and characterization of natural hydroxyapatite from animal hard tissues," *Key Engineering Materials*, vol. 342, pp. 213–216, 2007.
 - [21] I. Abdulrahman, H. I. Tijani, B. A. Mohammed et al., "From garbage to biomaterials: an overview on egg shell based hydroxyapatite," *Journal of Materials Chemistry*, vol. 2014, Article ID 802467, 6 pages, 2014.
 - [22] J. R. M. Ferreira, D. Navarro da Rocha, L. H. L. Louro, and M. H. Prado da Silva, "Phosphating of calcium carbonate for obtaining hydroxyapatite from the ostrich egg shell," *Key Engineering Materials*, vol. 587, pp. 69–73, 2014.
 - [23] S. Kongsri, K. Janpradit, K. Buapa, S. Techawongstien, and S. Chanthai, "Nanocrystalline hydroxyapatite from fish scale waste: preparation, characterization and application for selenium adsorption in aqueous solution," *Chemical Engineering Journal*, vol. 215–216, pp. 522–532, 2013.
 - [24] N. N. Panda, K. Pramanik, and L. B. Sukla, "Extraction and characterization of biocompatible hydroxyapatite from fresh water fish scales for tissue engineering scaffold," *Bioprocess and Biosystems Engineering*, vol. 37, no. 3, pp. 433–440, 2014.
 - [25] J. Venkatesan and S. K. Kim, "Effect of temperature on isolation and characterization of hydroxyapatite from tuna (*Thunnus obesus*) bone," *Materials*, vol. 3, no. 10, pp. 4761–4772, 2010.
 - [26] I. Zainon, N. M. Alwi, M. Z. Abidin, H. M. Z. Haniza, M. S. Ahmad, and A. Ramli, "Physicochemical properties of hydroxyapatite extracted from fish scales," *Advanced Materials Research*, vol. 545, pp. 235–239, 2012.
 - [27] B.-S. Kim, H. J. Kang, S.-S. Yang, and J. Lee, "Comparison of in vitro and in vivo bioactivity: cuttlefish-bone-derived hydroxyapatite and synthetic hydroxyapatite granules as a bone graft substitute," *Biomed Materials*, vol. 9, no. 2, 2014.
 - [28] S. A. Chattanathan, T. P. Clement, S. R. Kanel, M. O. Barnett, and N. Chatakondi, "Remediation of uranium-contaminated groundwater by sorption onto hydroxyapatite derived from catfish bones," *Water Air Soil Pollution*, vol. 224, no. 2, p. 1429, 2013.
 - [29] C. Piccirillo, M. F. Silva, R. C. Pullar et al., "Extraction and characterisation of apatite- and tricalcium phosphate-based materials from cod fish bones," *Materials Science and Engineering: C*, vol. 33, no. 1, pp. 103–110, 2013.
 - [30] Y. Wan, L. Hong, S. Jia et al., "Synthesis and characterization of hydroxyapatite-bacterial cellulose nanocomposites," *Composites Science and Technology*, vol. 66, no. 11–12, pp. 1825–1832, 2006.
 - [31] S. Hossain, U. K. Fatema, M. Y. A. Mollah, M. M. Rahman, and M. A. B. Hasan Susan, "Microemulsions as nanoreactors for preparation of Nanoparticles with antibacterial activity," *Journal of the Bangladesh Chemical Society*, vol. 25, no. 1, pp. 71–79, 2012.
 - [32] M. A. Malik, M. Y. Wani, and M. A. Hashim, "Microemulsion method: a novel route to synthesize organic and inorganic nanomaterials," *Arabian Journal of Chemistry*, vol. 5, no. 4, pp. 397–417, 2012.
 - [33] A. Sobczak, Z. Kowalski, and Z. Wzorek, "Preparation of hydroxyapatite from animal bones," *Acta Bioeng Biomech*, vol. 11, no. 4, pp. 23–28, 2009.
 - [34] J. K. Odusote, Y. Danyuo, A. D. Baruwa, and A. A. Azeez, "Synthesis and characterization of hydroxyapatite from bovine bone for production of dental implants," *Journal of Applied Biomaterials and Functional Materials*, vol. 17, no. 2, p. 2280800019836829, 2019.
 - [35] N. M. Pu'ad, P. Koshy, H. Z. Abdullah, M. I. Idris, and T. C. Lee, "Syntheses of hydroxyapatite from natural sources," *Heliyon*, vol. 5, no. 5, Article ID e01588, 2019.
 - [36] N. A. M. Barakat, K. A. Khalil, F. A. Sheikh et al., "Physicochemical characterizations of hydroxyapatite extracted from bovine bones by three different methods: extraction of biologically desirable HAp," *Materials Science and Engineering: C*, vol. 28, no. 8, pp. 1381–1387, 2008.
 - [37] M. Colilla, I. Izquierdo-Barba, and M. Vallet-Regí, "The role of zwitterionic materials in the fight against proteins and bacteria," *Medicines*, vol. 5, no. 4, p. 125, 2018.
 - [38] M. E. Bahrololoom, M. Javidi, S. Javadpour, and J. Ma, "Characterisation of natural hydroxyapatite extracted from bovine cortical bone ash," *Journal of Ceramic Processing Research*, vol. 10, no. 2, pp. 129–138, 2009.
 - [39] W. Khoo, F. M. Nor, H. Ardhyana, and D. Kurniawan, "Preparation of natural hydroxyapatite from bovine femur bones using calcination at various temperatures," *Procedia Manufacturing*, vol. 2, pp. 196–201, 2015.
 - [40] M. Rana, N. Akhtar, S. Rahman, H. M. Jamil, and S. M. Asaduzzaman, "Extraction of hydroxyapatite from bovine and human cortical bone by thermal decomposition and effect of gamma radiation: a comparative study," *International Journal of Complementary and Alternative Medicine*, vol. 8, Article ID 00263, 2017.

- [41] A. Doostmohammadi, A. Monshi, R. Salehi et al., "Preparation, chemistry and physical properties of bone-derived hydroxyapatite particles having a negative zeta potential," *Materials Chemistry and Physics*, vol. 132, no. 2-3, pp. 446–452, 2012.
- [42] A. Shavandi, A. E. Bekhit, A. Ali, and Z. Sun, "Synthesis of nano-hydroxyapatite (nHA) from waste mussel shells using a rapid microwave method," *Materials Chemistry and Physics*, vol. 149-150, pp. 607–616, 2015.
- [43] N. K. Nga, L. T. Giang, T. Q. Huy, P. H. Viet, and C. Migliaresi, "Surfactant-assisted size control of hydroxyapatite nanorods for bone tissue engineering," *Colloids and Surfaces B: Biointerfaces*, vol. 116, pp. 666–673, 2014.
- [44] S. Joschek, B. Nies, R. Krotz, and A. Göpferich, "Chemical and physicochemical characterization of porous hydroxyapatite ceramics made of natural bone," *Biomaterials*, vol. 21, no. 16, pp. 1645–1658, 2000.
- [45] M. Younesi, S. Javadpour, and M. E. Bahrololoom, "Effect of heat treatment temperature on chemical compositions of extracted hydroxyapatite from bovine bone ash," *Journal of Materials Engineering and Performance*, vol. 20, no. 8, pp. 1484–1490, 2011.
- [46] H. S. Ragab, F. A. Ibrahim, F. A. Ibrahim et al., "Synthesis and in vitro antibacterial properties of hydroxyapatite nanoparticles," *IOSR Journal of Pharmacy and Biological Sciences*, vol. 9, no. 1, pp. 77–85, 2014.
- [47] J. Hu, J. J. Russell, B. Ben-Nissan, and R. Vago, "Production and analysis of hydroxyapatite from Australian corals via hydrothermal process," *Journal of Materials Science Letters*, vol. 20, no. 1, pp. 85–87, 2001.
- [48] S. M. Barinov, J. V. Rau, S. N. Cesaro et al., "Carbonate release from carbonated hydroxyapatite in the wide temperature range," *Journal of Materials Science: Materials in Medicine*, vol. 17, no. 7, pp. 597–604, 2006.
- [49] J. L. Manalu, B. Soegijono, and D. J. Indrani, "Characterization of hydroxyapatite derived from bovine bone," *Asian Journal of Applied Sciences ISSN 2321-0893*, vol. 3, no. 04, 2015.
- [50] J. Olsen, J. Heinemeier, P. Bennike, C. Krause, K. Margrethe, and H. Thrane, "Characterisation and blind testing of radiocarbon dating of cremated bone," *Journal of Archaeological Science*, vol. 35, no. 3, pp. 791–800, 2008.
- [51] F. Miculescu, L. T. Ciocan, M. Miculescu, and A. Ernuteanu, "Effect of heating process on micro structure level of cortical bone prepared for compositional analysis," *Digest Journal of Nanomaterials and Biostructures*, vol. 6, pp. 225–233, 2011.
- [52] H. Eslami, M. Tahriri, and F. Bakhshi, "Synthesis and characterization of nanocrystalline hydroxyapatite obtained by the wet chemical technique," *Materials Science*, vol. 28, no. 1, pp. 5–13, 2010.
- [53] E. Bouyer, F. Gitzhofer, and M. I. Boulos, "Morphological study of hydroxyapatite nanocrystal suspension," *Journal of Materials Science: Materials in Medicine*, vol. 11, no. 8, pp. 523–531, 2000.
- [54] M. M. Rana, N. Akhtar, M. S. Rahman, M. Z. Hasan, and S. M. Asaduzzaman, "Extraction and characterization of hydroxyapatite from bovine cortical bone and effect of radiation," *International Journal of Biosciences*, vol. 11, no. 3, pp. 20–30, 2017.
- [55] C. Y. Ooi, M. Hamdi, and S. Ramesh, "Properties of hydroxyapatite produced by annealing of bovine bone," *Ceramics International*, vol. 33, no. 7, pp. 1171–1177, 2007.
- [56] S. Sagadevan and A. Dakshnamoorthy, "Synthesis and characterization of nano-hydroxyapatite (n-HAP) using the wet chemical technique," *International Journal of Physical Sciences*, vol. 8, no. 32, pp. 1639–1645, 2013.



Morphology, Deformation, and Micromechanical Behavior of Electrospun Nano-hydroxyapatite Blended Biohybrid Scaffolds

Komal P. Malla, Sven Henning, Ralf Lach, Herbert Jennissen, Goerg Michler, Mario Beiner, Ram Jeewan Yadav, and Rameshwar Adhikari*

For bone tissue engineering, nano-hydroxyapatite (nano-HAp) is a widely used bioceramic filler in polymer fibrous scaffolds that changes the morphology and micromechanical behavior of fibers. In this study, different volume fraction percentages of nano-HAp and vitamin D3 (VD3) are incorporated into electrospun polymer blend fibrous scaffolds comprising polycaprolactone (PCL), poly-L-lactic acid (PLLA), and gelatin (GEL). Fourier transform infrared spectroscopy (FTIR), scanning electron microscopy (SEM), transmission electron microscopy (TEM), and uniaxial tensile testing are used to characterize the chemical, morphological, and micromechanical properties of the scaffolds. The FTIR analysis showed the presence of functional groups of fillers and polymers and their molecular interactions in the fibers. In the microscopic analysis, the fillers are found to affect the fiber morphology (including diameter, phase separation, and texture) and the response of the fibers under tensile deformation. The addition of 3% by volume of filler suspension results in maximum diameter of 4.34 μm , and the addition of 6%–12% filler leads to an increase in tensile strength from 0.7 to 5.6 MPa and strain at break from 2% to 37% for the composite fibers compared to neat fibers. The crazing behavior of the fiber is more noticeable at a low filler content (0%), whereas thin-layer yielding becomes predominant at a higher filler content (12%). Thus, the study shows that scaffold fibers undergo brittle-to-ductile transitions as the filler percentage in the polymer blend increases from 0% to 12%. It has been further found that morphogens used as growth factors can be easily released from hydroxyapatite after adsorption.

1. Introduction


Recently, composites of biopolymers and bioceramics have attracted increasing attention in the scientific community for their use as scaffolds in bone tissue engineering (BTE). Among others, polycaprolactone (PCL), poly L-lactic acid (PLLA), and gelatin (GEL) are the most studied biopolymers because of their nontoxicity, excellent biocompatibility, and biodegradable nature.^[1,2] Furthermore, the US Food and Drug Administration (FDA) has approved PCL and PLLA for clinical use in humans.^[3–5] For decades, the scaffolds of these biopolymers have been used in various biomedical applications despite their weak mechanical properties.^[6–8] Nevertheless, it has been shown by two independent groups of authors that bulk samples of PLA/PCL blends with optimized morphology may exhibit both high stiffness and toughness.^[9,10] Therefore, there have been numerous studies to enhance the mechanical properties of these scaffolds by incorporating different filler materials.^[11] Some of the commonly used fillers are graphene (G), graphene oxides (GO), carbon nanotubes (CNTs), niobium pentoxide (Nb_2O_5), bioglass,

K. P. Malla, R. Adhikari
Central Department of Chemistry
Tribhuvan University
Kathmandu 56613 Nepal
E-mail: nepalpolymer@yahoo.com

K. P. Malla
Faculty of Health Sciences
Pokhara University
Pokhara 33700, Nepal
K. P. Malla, M. Beiner
Institute of Physics
Martin Luther University Halle-Wittenberg
Von-Danckelmann-Platz 3, 06120 Halle (Saale), Germany

S. Henning, M. Beiner
Fraunhofer Institute for Microstructure of Materials and Systems (IMWS)
Walter-Hülse-Straße 1, 06120 Halle (Saale), Germany

S. Henning, R. Lach, G. Michler
Institute for Polymer
Materials e.V.
Eberhard-Leibnitz-Straße 2
06217 Merseburg, Germany
R. Lach, G. Michler
Polymer Service GmbH Merseburg (PSM)
Geusaer Straße 81f, 06217 Merseburg, Germany
H. Jennissen
Department of Biochemical Endocrinology
Institute for Physiological Chemistry
University of Duisburg-Essen
Hufelandstrasse 55, 45122 Essen, Germany

 The ORCID identification number(s) for the author(s) of this article can be found under <https://doi.org/10.1002/masy.202200079>

DOI: 10.1002/masy.202200079

chitosan (CS), titanium dioxide (TiO₂), cuprous oxide (Cu₂O), zinc oxide (ZnO), and calcium phosphates (CaPs) bioceramics.^[12] However, the selection of filler materials depends on the final application of the scaffolds.^[12] Among the various CaPs bioceramics, due to the bioactive and biocompatible nature nano-hydroxyapatite (nano-HAp) is extensively used as a filler material to enhance the mechanical properties and osteoconductivity of scaffolds for BTE applications.^[1] Furthermore, this ceramic has a chemical composition similar to the inorganic component of natural bone minerals.^[1,13,14] In this context, biopolymer-based scaffolds filled with nano-HAp have received a keen interest in BTE.^[1,15–18] To fabricate such a scaffold, several techniques have been developed, such as solvent casting, emulsion freeze-drying, gas foaming, rapid prototyping, 3D printing, electrospinning (ES), and, in some cases, a combination of two or more of these techniques.^[19–23] But, in this study, we have chosen the ES method to fabricate the nonwoven fibrous scaffolds for BTE. A wide variety of nanomaterials can be produced by this method, including polymer and ceramic composite nanofibers because of their cost-effective and versatile nature.^[23]

A major new medical application of the binary composite scaffold would be to preadsorb growth factors such as rhBMP-2 and VEGF₁₆₅ to nano-HAp before incorporation into a poly-DL-lactic acid (PDLLA) nanofiber. It has been shown that recombinant growth factors (i.e., morphogens) bone morphogenetic protein 2 (rhBMP-2) and vascular endothelial growth factor (rhVEGF₁₆₅)^[24,25] can diffuse through the PDLLA capsule wall out of a nanofiber into the surrounding medium, producing pores of ca. 10 nm diameter in the nanofiber. The advantage of preadsorbing rhBMP-2 or rhVEGF to nano-HAp might be much higher growth factor loads within the fiber by the high capacity of the nano-HAp particles for these proteins. During the fiber lifetime, a restricted release, for example, rhBMP-2 through the nanopores would occur with a high concentration burst at hydrolytic fiber dissolution due to liberation of the nano-HAp particles. In the latter case, the requirements for calcium phosphates during bone induction and bone growth could be simultaneously met. In another manifestation, the two growth factors could be adsorbed simultaneously, for example, with rhBMP-2 adsorbed to the nano-HAp on the inside and VEGF on the outside surface of the nanofiber leading to a bimodal release regimen or with a third factor a multimodal release regimen.^[26]

In the past decades, several studies have attempted to explain the mechanical behavior of HAp-blended electrospun binary composite scaffolds of PCL/PLLA, PCL/GEL, and PLLA/GEL.^[27–29] However, the micromechanical behavior of nano-HAp- and vitamin D3 (VD3)-incorporated ternary blends of PCL/PLLA/GEL scaffold has not been studied yet. Hence, in this work, we aim to fabricate nonwoven fibrous scaffolds with different volume fraction percentages of nano-HAp/TFE suspension blended into ternary composite mixtures of PCL/PLLA/GEL by

Table 1. Addition of volume fraction percentage of nano-HAp in polymer blends.

Sample code	Blending ratio of PCL/PLLA/GEL (% v/v)	Volume of nano-HAp suspension in polymer blend (% v/v)
CB-1	30:30:40	0
CB-2	30:30:40	0
CB-3	30:30:40	2
CB-4	30:30:40	3
CB-5	30:30:40	6
CB-6	30:30:40	12

Except for CB-2 all samples contained VD3. GEL, gelatin; nano-HAp, nano-hydroxyapatite; PCL, polycaprolactone; PLLA, poly-L-lactic acid; VD3, vitamin D3.

ES technique and to study the effect of filler addition on the micromechanical behavior after tensile test of the scaffold fibers.

2. Experimental Section

2.1. Preparation of Fibers by Electrospinning

The scaffolds of ternary biopolymers PCL/PLLA/GEL, VD3, and different volume fraction percentages of nano-HAp were fabricated according to **Table 1** by the ES method.^[30,31] The role of VD3 was only prominent at the time of biomedical application of scaffold (at cell-line work), so its volume (0.50 μL) was ignored in **Table 1**.

PCL ($M_w = 80$ kDa, NatureWorks, USA), PLLA ($M_w > 250$ kDa, NatureWorks), and GEL (type A approximately 300 blooms from Sigma–Aldrich, USA) were used as received. The nano-HAp used in this study was extracted from ostrich bone by thermal decomposition in our earlier studies.^[32] All the polymers were dissolved in 2,2,2-trifluoroethanol (TFE, Sigma–Aldrich) under magnetic stirring to obtain 10% w/v solution of each polymer separately. The 5% w/v nano-HAp/TFE suspension was prepared separately and blended into the above polymer mixture, then magnetically stirred to obtain the nano-HAp blended polymer solution. All the solutions were separately electrospun to obtain randomly oriented fibrous scaffolds collected in a rotatory drum at 700 rpm. The ES was performed at a flow rate of 1 mL h⁻¹ (using a digitally controlled syringe pump, Model 871801/6 from B. Braun Melsungen SE, Germany) with an applied voltage of 18 kV (power supply from Heinzinger electronic GmbH, Rosenheim, Germany). The needle collector distance was fixed at 17 cm. **Figure 1** shows the ES setup.

2.2. Chemical, Morphological, and Mechanical Characterization

2.2.1. Fourier Transforms Infrared (FTIR) Spectroscopy

The scaffolds were investigated using an attenuated total reflectance (ATR) FTIR spectrometer (Frontier from PerkinElmer, USA) to study the chemical groups of polymers and their interactions with HAp and VD3. The spectra were collected in the spectral range of 4500–500 cm⁻¹ and the functional groups were

R. J. Yadav
Department of Chemistry
Tribhuvan University
Prithvi Narayan Campus
Pokhara, Nepal

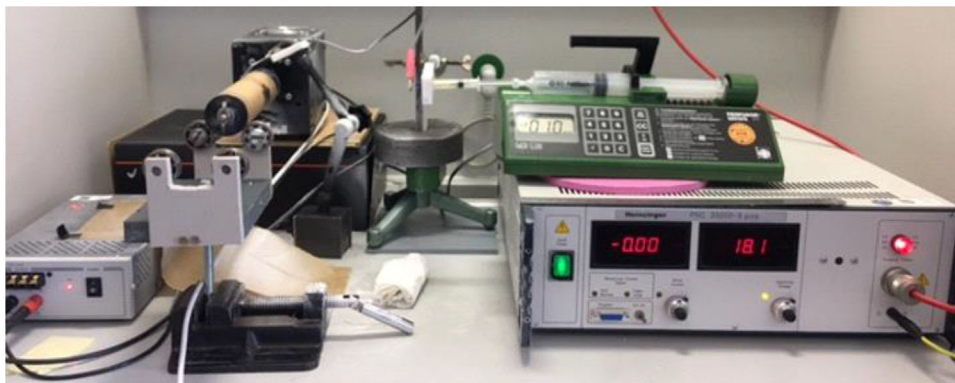


Figure 1. Electrospinning setup for the fabrication of scaffolds.

characterized in the transmission mode in the mid-infrared range with a resolution of 2 cm^{-1} .

2.2.2. Scanning Electron Microscopy (SEM)

The morphology and allocation of the randomly oriented nanofibers of the scaffolds before and after the tensile test were examined using an FEI Quanta 650 ESEM-FEG instrument operated at an accelerating voltage of 15 kV. Scaffold samples were cut into $10\text{ mm} \times 10\text{ mm}$ dimensions, attached to SEM stubs using double-sided conductive adhesive tabs, and coated with platinum. At least five different positions were tested to study the fiber morphology of each of the scaffolds. The Fiji-win 64 image J software was used to measure the average fiber diameter by digital image processing.

2.2.3. Transmission Electron Microscopy (TEM)

To study the morphology of single nanofibers of the scaffolds, samples were prepared by direct deposition of nanofibers onto TEM grids during the ES process (standard Cu grids, 3 mm). Subsequently, the nanofibers were stained with ruthenium tetroxide (RuO_4) vapor. TEM investigation was performed using an FEI Tecnai G2 TEM operated in the bright field mode at an accelerating voltage of 200 kV.

2.2.4. Micromechanical Characterization – Tensile Test

The micromechanical properties of the scaffolds were measured using a uniaxial tensile testing machine Z2.5 from ZwickRoell GmbH & Co KG, Ulm, Germany (load cell: 500 N, traverse speed: 2 mm min^{-1} up to 20% strain and 10 mm min^{-1} elsewhere) according to the standard ISO 527-3. For this, the scaffold samples were cut into 20 mm by 10 mm pieces to provide a 10 mm test gauge length and mounted on rectangular graph paper frames, with the outer dimensions of the external frame being $40 \times 40\text{ mm}^2$, and an inner rectangular cut out at $20 \times 10\text{ mm}^2$. The actual dimension of the tested scaffolds was $10 \times 10 \times 0.03\text{ mm}^3$ (length, width, and thickness) and they were fixed by adhesive double-sided tape to the frame. The frames were

then set into the instrument, and the sidewalls of the frames were cut by scissors. At least five samples were tested for each scaffold, and the force–displacement data was collected for all the samples. The stress–strain curves were calculated from the force–displacement curve. The values of the tensile strength (ultimate tensile stress) and strain at break were calculated according to ISO 527-3. Unlike ISO 527-3, the elastic (tensile) modulus was defined as the maximum positive slope of the stress–strain curve.

2.3. Chemicals and Materials for Desorption Experiments

2.3.1. Morphogens

RhBMP-2 and rhVEGF₁₆₅ prepared in *Escherichia coli*, according to refs. [33] and [34] respectively, were from Morphoplant GmbH, Bochum) and radioactively labeled by the iodine monochloride method, that is, ^{125}I -BMP-2, ^{125}I -VEGF (specific radioactivity: $8000\text{--}10\,000\text{ cpm } \mu\text{g}^{-1}$), according to refs. [35, 36] The biological activity equivalents were determined for rhBMP-2 to $K_{0.5} \sim 5\text{--}20\text{ nM}$) and for rhVEGF₁₆₅ to $K_{0.5} \sim 5\text{--}20\text{ pM}$.^[36]

2.3.2. Hydroxyapatite Particles

Algipore (98% HAp; grain size $0.3\text{--}1\text{ mm}$; $1.3 \times 10^4\text{ particles g}^{-1}$) was obtained from AlgOss Biotechnologies GmbH (A-1180 Vienna, Austria).^[37] The incubation mixture contained: 2.0 g Algipore in 5 mL NaAc-buffer A (20 mM sodium acetate pH 4.5) with ^{125}I -rhBMP-2 (initial concentration: 0.1 mg mL^{-1}) or ^{125}I -rhVEGF₁₆₅ solution (initial concentration: $10\text{ } \mu\text{g mL}^{-1}$) for 15 h at room temperature, leading to 0.81 ± 0.01 ($n = 3$) mg g^{-1} for rhBMP-2 and to 86.5 ± 4.7 ($n = 3$) $\mu\text{g g}^{-1}$ for rhVEGF₁₆₅. For desorption at room temperature the protein-loaded particles (1.0–2.0 g) were washed three times with 2 mL of Tris-buffer B 50 mM Tris/HCl, 150 mM NaCl, pH 7.4 and transferred to fresh 2 mL PBS-buffer C (137 mM NaCl, 8.1 mM Na_2HPO_4 , 2.7 mM KCl, 1.5 mM KH_2PO_4 , pH 7.4) for the next time-period up to 24 days. The desorption measurements were made daily (=cluster) interspersed with a spacing of 2–3 days between clusters. The daily measurements in the clusters did not lie exactly on the fitted line of all clusters indicating that during the time-spans of 2–3 days there may be some readsorption. Readsorption could

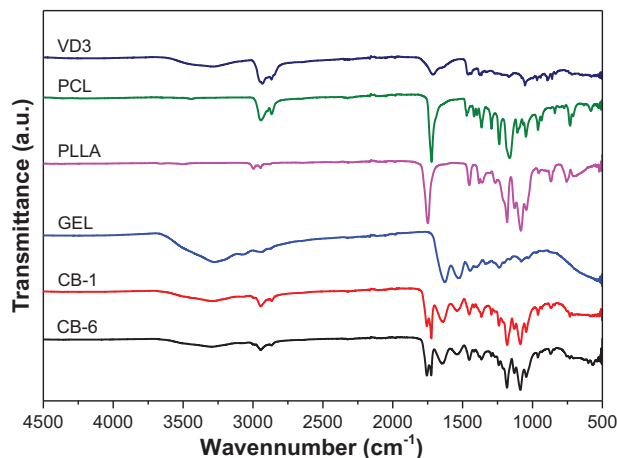


Figure 2. FTIR spectra of VD3, PCL, PLLA, GEL as well as CB-1 and CB-6 (0% v/v and 12% v/v filler [nano-Hap] blended PCL/PLLA/GEL/VD3) scaffold. FTIR, Fourier transform infrared spectroscopy; GEL, gelatin; nano-Hap, nano-hydroxyapatite; PCL, polycaprolactone; PLLA, poly-L-lactic acid; VD3, vitamin D3.

lead to somewhat shorter half-lives, which however would not significantly change the magnitude of rate differences between BMP-2 and VEGF.

2.3.3. Isotope Analysis

The immobilized amounts of ^{125}I -rhBMP and ^{125}I -rhVEGF on the particles were determined in a gamma counter ($n = 3$). In all cases, the calculated half-lives of desorption were corrected for the spontaneous decay of ^{125}I ($t_{1/2} = 60$ days).^[38]

3. Results and Discussion

3.1. FTIR Analysis

Figure 2 shows the FTIR spectra of polymers (PCL, PLLA, GEL), nano-HAp, VD3, and their subsequent blends with nano-HAp and VD3 (CB-1 and CB-6). The characteristic vibrational peaks of C–O–C stretching (symmetric and asymmetric), C–O, and C–C stretching at 1166, 1237, and 1295 cm^{-1} are visible in the native polymer (PCL) spectrum, are not seen in the blend spectra of CB-1 and CB-6. This might be due to the decreasing crystallinity of PCL in the composite blends. Different researchers, such as Shuai et al.,^[1] Milovanovic et al.,^[39] and Sattary et al.,^[40] have reported similar types of observations in their studies.

Similarly, the symmetrical vibrational stretching of the peaks C=O, C–O=C, CH_3 , and CH_2 at 172, 1103, 1363, and 1462 cm^{-1} of PLLA were also observed in the polymer blends. Lee et al.^[41] reported a similar type of findings in their studies. In addition, the peak shifts from 1723 to 1760 cm^{-1} correspond to the C=O bending vibrations of either PLLA or PCL which might be attributed to the formation of hydrogen bonding between the OH^- group of nano-HAp and the C=O group of polymers.^[42] The difference in the intensity of those peaks in CB-1 and CB-6 might be correlated to the amount of the HAp in those composites. Due to the masking effect of the C–C stretching band of PLLA at 930 cm^{-1} the

small peak of the carbonate group (CO_3^{2-}) of HAp at 875 cm^{-1} is not visible in the scaffolds of CB-6.^[43] Furthermore, some characteristic peaks for GEL related to C=O group stretching (amide-I) at 1642 cm^{-1} , N–H bending at 1542 cm^{-1} (amide-II), and N–H bending at 563 cm^{-1} are clearly visible in the spectrum of CB-6. Fayyazbakhsh et al.,^[44] Sattary et al.,^[40] and Shokrgozar et al.^[45] also reported similar findings in their studies. Additionally, there might be a bond formed between the calcium ion (Ca^{2+}) of nano-HAp and the acetate (R-COO^-) group of GEL, which reveals that nano-HAp has an affinity toward GEL, in agreement with the results found by Hossan et al.^[11]

Furthermore, the spectrum of CB-6 contains seven significant bands at 605, 1025, and 1045 cm^{-1} , all of which are assigned to the PO_4^{3-} a group of nano-HAp. The bands at 631 cm^{-1} belong to the OH^- group bonded hydrogen. Similarly, the peaks at 2355 and 2330 cm^{-1} are related to the CO_3^{2-} group, as well as 3570 cm^{-1} related to the OH^- group of nano-HAp visible also in composite blends of CB-6. A similar type of result was reported by Abdel Sayed.^[31] On the other hand, the peaks of stretching vibration of CH_2 , alkyl C–H, symmetric stretching of CH_3 , and hydrogen-bonded O–H stretching at 737, 2864, 2936, and 3289 cm^{-1} have confirmed the existence of VD3 in composite blends of CB-6, which is in agreement with the results found by Kiani et al.^[46] and Sattary et al.^[40] In conclusion, these results show that the polymers and fillers are well blended in the scaffolds. The shifting of peaks and the emergence of a new peak indicate a molecular interaction between the polymers and nano-HAp particles.

3.2. SEM Analysis of the Microstructure of the Scaffold

Figure 3 depicts the morphological changes of randomly oriented scaffold fibers (CB-1 to CB-6) as a function of the addition of volume fraction of nano-HAp percentage (0%–12%) in the polymer blends. As the scaffolds were electrospun under fixed experimental conditions, it is reasonable to attribute changes in fiber diameter and morphology to the proportion of nano-HAp added to the polymer blends.

Figure 3 shows the morphology of scaffold fibers with the nano-HAp contents ranging from 0% to 12% of volume fraction. The fibers of polymer blends without nano-HAp are smooth and bead free as shown in Figure 3a, b. Meanwhile, further addition of nano-HAp enhanced the agglomerations on the scaffold fibers. The agglomerations are clearly visible in 6% and 12% addition as shown in Figure 3e, f. Besides agglomerations, the filler particles were successfully incorporated into the scaffold fibers. Results show that the average fiber diameter increased from 0.17 to 4.34 μm on addition of 0% to 3% of nano-HAp. However, it decreases significantly (from 4.34 to 0.48 μm) on increasing the filler percentage (from 3% to 12%). Table 2 shows the mean fiber diameter (100 fibers per scaffold were measured) of each polymer scaffolds.

The cause of decreasing fiber diameter on the addition of filler might be the increase in solution conductivity because nano-HAp is considered to be a more conducting material than polymers. The higher percentage (6%–12%) of filler addition might show this property in polymer blends.^[47] Furthermore, the augmentation of solution conductivity might be a cause of faster elongation

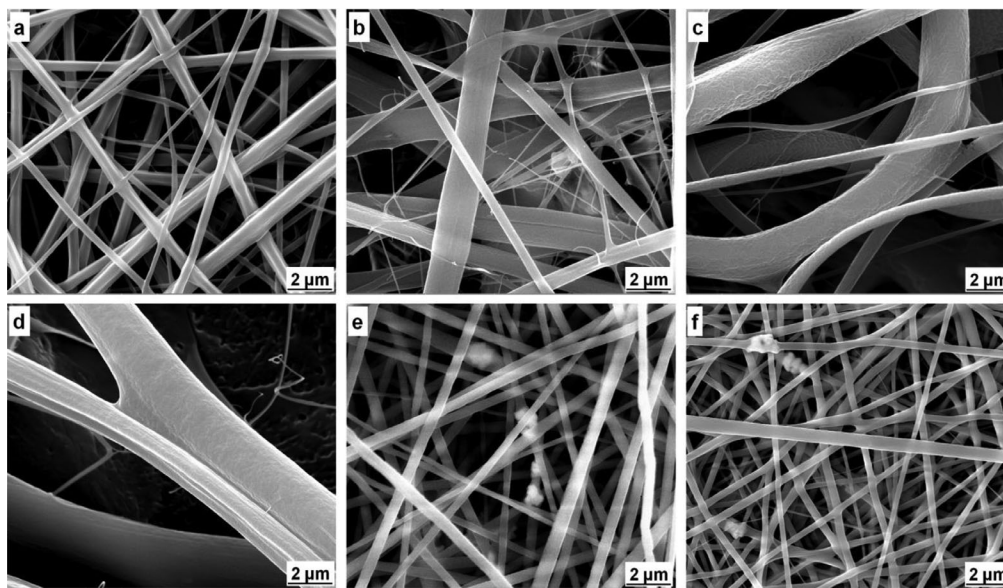


Figure 3. SEM images of fibrous scaffolds: a) CB-1 (PCL/PLLA/GEL), b) CB-2 (PCL/PLLA/GEL/VD3), c) CB-3 (PCL/PLLA/GEL/VD3+2%v/v nano-HAp), d) CB-4 (PCL/PLLA/GEL/VD3+3%v/v nano-HAp), e) CB-5 (PCL/PLLA/GEL/VD3+6%v/v nano-HAp), and f) CB-6 (PCL/PLLA/GEL/VD3+12%v/v nano-HAp). GEL, gelatin; nano-Hap, nano-hydroxyapatite; PCL, polycaprolactone; PLLA, poly-L-lactic acid; SEM, scanning electron microscopy; VD3, vitamin D3.

Table 2. The average fiber diameter of scaffolds as a function of nano-hydroxyapatite (nano-Hap) content in polymer blends.

Sample code	Volume of nano-HAp suspension in polymer blends [% v/v]	Average fiber diameter [μm]
CB-1	0	0.17
CB-3	2	1.84
CB-4	3	4.34
CB-5	6	0.58
CB-6	12	0.48

of polymer solution jet from the needle tip under the electrical field between the needle tip and collector during ES.^[47] The decrease in the fiber diameter may result in a larger surface area of fibers and enhanced micromechanical properties of the fibers.^[48] Despite this, the fiber diameter also depends on how the fillers are encapsulated inside the fibers.^[29] Regardless of the normal modification of shapes, any bulb parts in the fibers are not visible on adding a smaller amount (2%–3% v/v) of fillers in the polymer blends (Figure 3c, d).

3.3. TEM Observation of the Fiber Microstructures

Figure 4 shows a TEM image of a single fiber of scaffold (CB-2) stained with ruthenium tetroxide vapors (RuO_4). The polymers used in this study are not only biodegradable but also thermodynamically immiscible, as reported by Ba Linh et al., Fang et al., Heidari et al., and Scaffaro et al.^[2,42,6,49] For this reason, the phases of each polymer in composite fiber might be separated. So, the dark part at the center of fiber might be the contrast phase

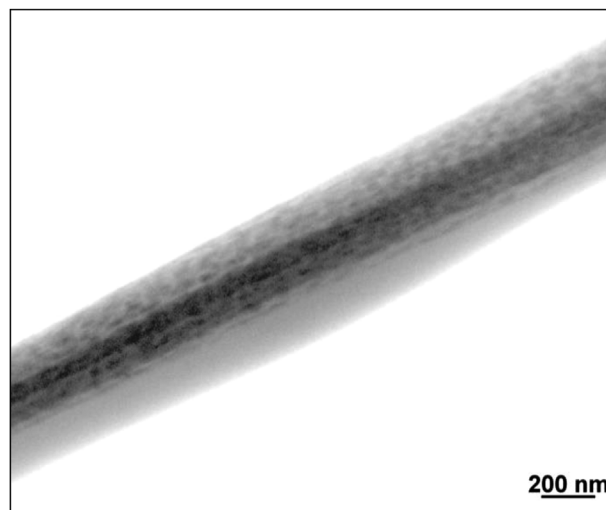


Figure 4. TEM micrograph of single scaffold fiber (CB-2) without filler stained with RuO_4 shows phase separation of each polymer. RuO_4 , ruthenium tetroxide; TEM, transmission electron microscopy.

of RuO_4 layer in GEL, whereas the peripheral light part might be either PCL (clear part from the bottom of contrast) or PLLA (the slightly rough part above the contrast). In addition, due to the hydrophilic nature of GEL (as discussed in Subsection 3.1), it has an affinity toward nano-HAp rather than PCL, PLLA, and VD3 as a result, in the TEM image of nano-HAp-incorporated polymer composite fiber, the PCL and PLLA (hydrophobic polymers) might be located at the periphery and nano-HAp together with GEL located at the center part of the fiber.

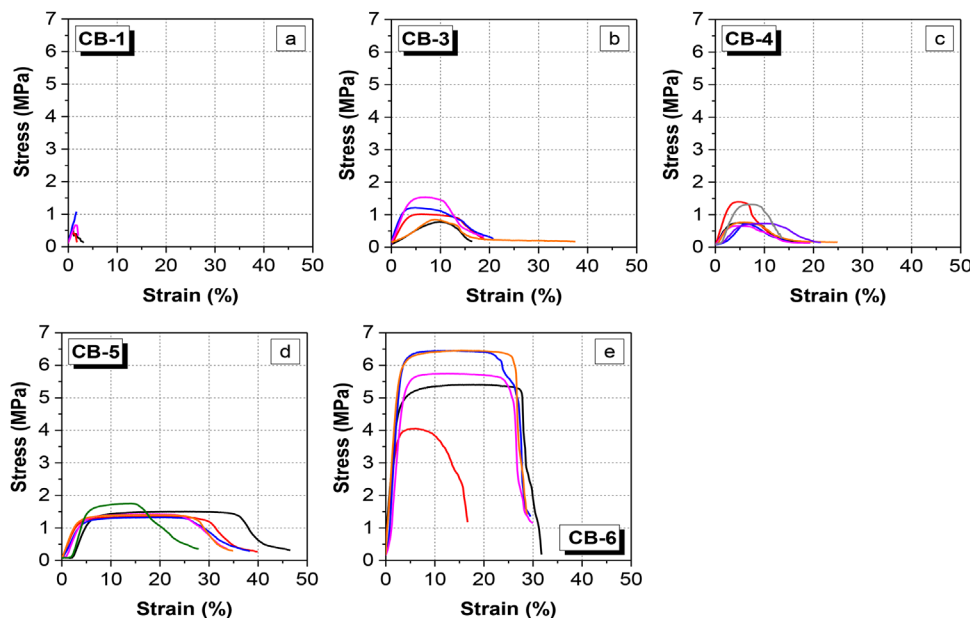


Figure 5. Stress–strain curves of fibrous scaffolds: a) CB-1 (PCL/PLLA/GEL), b) CB-3 (PCL/PLLA/GEL/VD3+2%v/v nano-HAp), c) CB-4 (PCL/PLLA/GEL/VD3+3%v/v nano-HAp), d) CB-5 (PCL/PLLA/GEL/VD3+6%v/v nano-HAp), and e) CB-6 (PCL/PLLA/GEL/VD3+12%v/v nano-HAp). The scaffold CB-2 was not investigated. GEL, gelatin; nano-HAp, nano-hydroxyapatite; PCL, polycaprolactone; PLLA, poly-L-lactic acid; VD3, vitamin D3.

3.4. Tensile Test

Figure 5 shows an overview of the stress–strain curves of polymer scaffolds as a function of the volume fraction percentage of filler used. The scaffolds of pure PCL/PLLA/GEL without any filler (**Figure 5a**) exhibit very brittle performance with unstable crack growth. While all PCL/PLLA/GEL/VD3 and filler composite scaffolds (CB-3 to CB-6) investigated (filler fraction: 2–12 volumes %) changed to be ductile with no unstable crack growth (**Figure 5b–e** and SEM picture after tensile test). This observation can be clearly related to the transition in the micromechanical deformation mechanisms as discussed in Subsection 3.5. As found in this section, crazing of the fibers is only related to a small amount of local deformation and therefore low ductility. However, the observed thin-layer process increased not only the local amount of deformation but also the overall macroscopic ductility.

It seems to be that the brittle-to-ductile transition is triggered by the incorporation of filler (nano-HAp) particles. This assumption can be confirmed by the strain at break as a function of filler percentage as shown in **Figure 6c**. The strain at break of the pure polymer blend without filler is very low at only 2%; however, the strain at break of all composites is much higher (18%–37%). Additionally, the tensile strength increases from 0.7 MPa for the pure polymer blend via 1.5 MPa of the composite containing 6% filler to 5.6 MPa of the composite containing 12% filler (**Figure 6b**). This finding can be supported by the hydrophilic nature of GEL. Due to this nature, it binds the filler at the center of the fiber (as discussed in Subsections 3.1 and 3.3) via the electrostatic force of attraction between the filler's OH^- and PO_4^{3-} groups and the amino cationic groups of GELs. It might be one of the reasons for increasing ductility.

Interestingly, the elastic modulus is first nearly constant at 0%–6% filler (about 44 MPa); afterward, the modulus jumps to

199 MPa at 12% filler (**Figure 5a**). The same jump can be observed for the tensile strength (see **Figure 6b**), probably due to the high-volume fraction of filler percentage in the scaffold fibers. The incorporation of the filler into the fibers improves not only the biocompatibility of the scaffolds but also their ductility, which is essential for easy handling during practical applications (at the time of cell-line work).

3.5. Micromechanical Observation of the Tensile-Tested Scaffolds

The representative SEM images of the scaffold (CB-4, **Figure 7a, b**) show the brittle behavior of fibers after the tensile test. As discussed in Subsection 3.4, the fiber without filler exhibits highly brittle behavior. **Figure 7a** shows several modulated crazing marks in the fibers, which might be the effect of filler addition as well as local deformation, and phase separation of each polymer. Furthermore, up to a certain limit, the average diameter of fiber (calculated from SEM micrographs obtained on samples fractured in the tensile test) increases as the filler percentage is increased in polymer blends. **Table 2** shows the increasing trends of average fiber diameter with the increasing filler percentage in the polymer blends from 0 to 3%. However, when the filler percentage is again increased beyond 3%, the diameter is remarkably decreased due to some reasons as discussed in Subsection 3.2. Hence, we can assume that fiber diameter is a function of filler addition in polymer blends. The cause of a gradual decrease of fiber diameter might be due to the agglomeration of filler inside the fiber and its random distribution during ES. In addition, it might affect the physical properties, that is, the conductivity of the solution, as discussed in Subsection 3.2. The tensile test results reveal that fiber without filler has high brittle properties, as

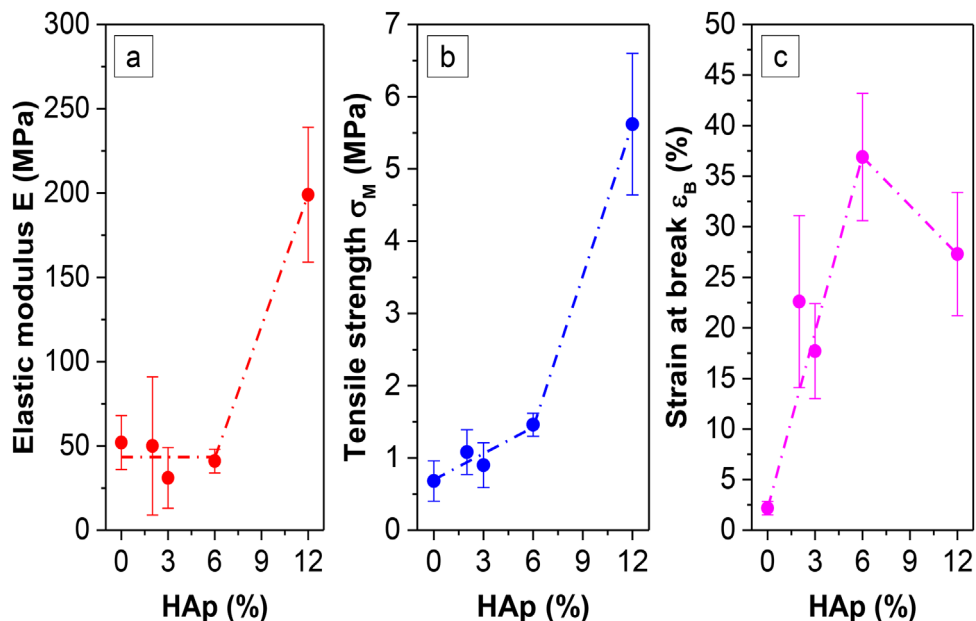


Figure 6. Tensile properties of the nanofibrous scaffolds as a function of the filler (nano-hydroxyapatite [nano-Hap]) fraction: elastic modulus a), tensile strength b) and strain at break c); the lines are visualizing the trend only.

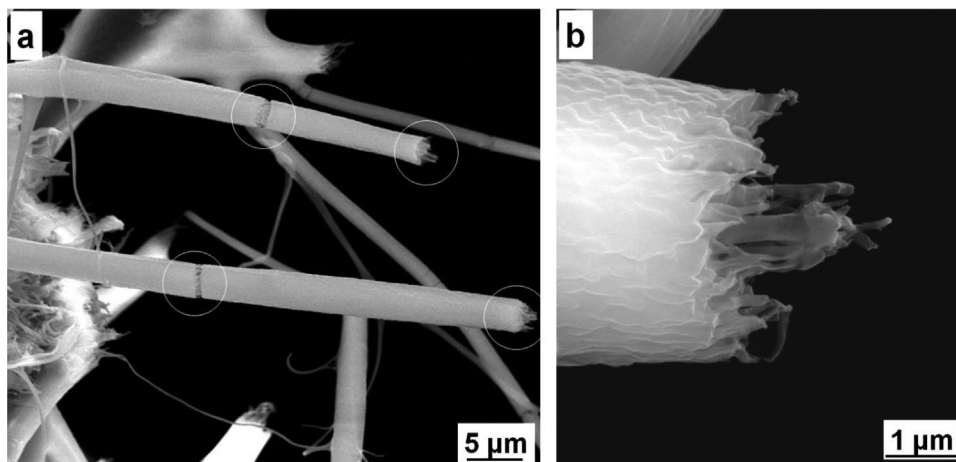


Figure 7. Representative scanning electron microscopy (SEM) images of sample CB-4 after the tensile test: modulated crazing in fibers; a) overview image, b) details of fracture surface morphology.

discussed in Subsection 3.4. However, this property places a certain limit on the increase in the filler percentage. Therefore, the addition of filler increases fiber diameter to a certain limit only, within which it shows crazing points in the fiber (Figure 7a).

Furthermore, the SEM micrographs after tensile test (Figure 8a, b) show that the ductile property of fiber improves with an increase in the filler percentage in polymer blends. Januariyasa et al.^[47] reported similar types of findings in their studies. The increasing filler percentage (>3%) increases the surface area of the fiber remarkably and decreases the fiber diameter, which in turn decreases the brittle nature of the fiber and increases the ductile behavior. Figure 8a, b illustrates many yielding marks of fibers of CB-6, which contains 12% of filler. Hence, the addition of a certain percentage (6%–12%) of

nano-HAp as a filler in polymer blends shows an improvement in the brittle-to-ductile behavior of fiber.

3.6. Desorption of the Morphogens from the Hydroxyapatite Particles

Desorption experiments of ¹²⁵I-rhBMP-2 were first described for metal surfaces in 2002,^[38] illustrating a sustained first-order decay with very long half-lives of 100–138 days.^[38] On hydroxyapatite wafers it was found that release is not always monophasic but may be biphasic, consisting of a first-order burst phase and a first order sustained-release phase.^[50] These observations also apply to the experiments in Figure 9, which were performed with

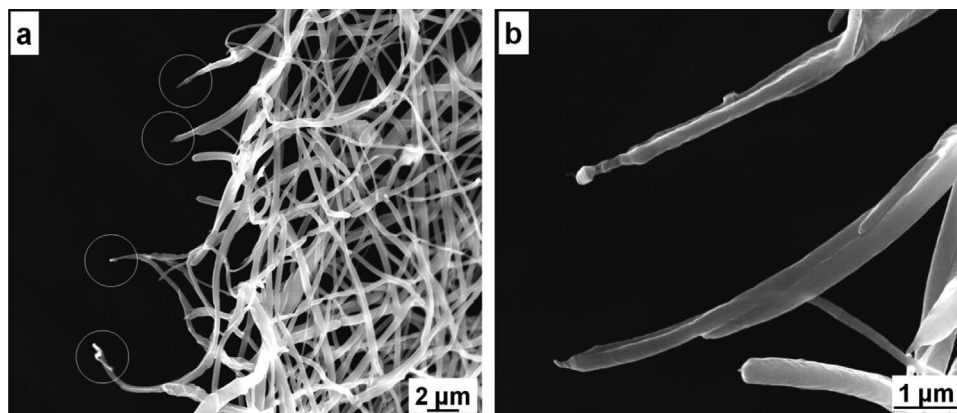


Figure 8. Representative scanning electron microscopy (SEM) images of sample CB-6 after the tensile test: thin layer yielding behavior; a) overview image, b) detail.

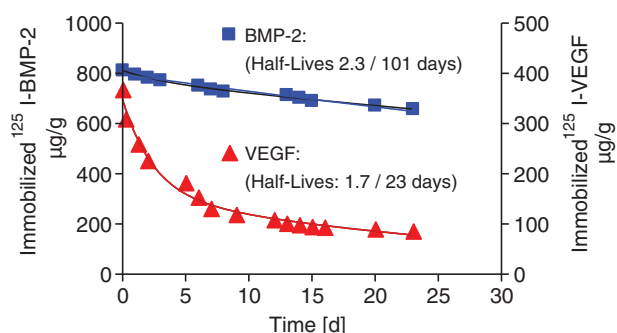


Figure 9. Release of ^{125}I -rhBMP-2 and ^{125}I -rhVEGF₁₆₅ from Algipore particles (24 days). Two separate experiments of ^{125}I -rh-BMP-2 (■) and ^{125}I -rhVEGF₁₆₅ (▲) release from Algipore, respectively, are superimposed. The data has been fitted to two-phase exponential release kinetics yielding half-lives for the burst and sustained release phases. For further details see Subsection 2.3 and ref. [36].

isotope-labeled rhBMP-2 and rhVEGF₁₆₅ in solution on hydroxyapatite bone-replacement particles called Algipore (see Subsection 2.3 and ref. [36]).

After adsorption of ^{125}I -rhBMP-2 (load: $810\ \mu\text{g g}^{-1}$) the morphogen is released with a burst-phase half-life of 2.3 days and a sustained release half-life of 101 days. In contrast ^{125}I -rhVEGF₁₆₅, adsorbed in an ~ 100 -fold lower amount (load: $368\ \mu\text{g g}^{-1}$) is released with a burst-phase half-life of 1.7 days and a five-fold lower sustained-release half-life of 23 days (i.e., at a five-fold higher rate). This shows that on hydroxyapatite rhBMP-2 and rhVEGF₁₆₅ are released at two distinct different off-rates indicating a good basis for a bimodal release.^[26] Further experiments are warranted with simultaneous adsorption and loading of the morphogens on the HAp particles to exclude “protein–protein interference.”^[26] It is then planned to incorporate such morphogens separately or together for the synthesis of bioactive PDLLA–HAp–morphogen biohybrids.

4. Conclusion

In this study, nano-HAp as a filler was successfully incorporated into the PCL/PLLA/GEL and VD3 composite scaffolds fabricated

by the ES method. The diameter of the fiber increased as the nano-HAp % increased to a certain threshold limit (3%) and then decreased significantly as further additions (6%–12%) of filler were made. The fiber has a brittle nature without filler and has a hump-free morphology. However, as the filler percentage was increased (2%–12%), the brittleness decreased, and the ductility increased. The results showed that, at a certain volume fraction of filler (3% v/v), the diameter of the fiber increased, resulting in many crazing points after the tensile test. However, the fiber diameter decreased on further addition of filler due to the agglomeration of filler and its impact on the conductivity of the ES solution. This affects the micromechanical behavior of the fiber. For this reason, the ductile property of the fiber increased, which in turn meant the yielding property became distinct. As a consequence, we concluded that the transition of fibers from crazing to yielding was conveniently enhanced by decreasing the fiber diameter by adding filler percentages to the polymer blends. Furthermore, the successful release of morphogens from HAp can be a promising way to create bioactive polymer–HAp–morphogen biohybrids to be tested in future cell line experiments.

Acknowledgements

K. P. Malla thanks the German Academic Exchange Service (DAAD) for financial support during his stay in Germany (Research Grants – Bi-nationally Supervised Doctoral Degrees/Cotutelle, 2020/21 (57507869)), project: “Electrospun blends of polycaprolactone/poly-L-lactic acid/gelatin and natural hydroxyapatite for bone tissue engineering”. H. Jennissen and G. H. Michler acknowledge the German Research Foundation (DFG) for funding the research project “Resorbable multimodal hybrid materials for regenerative medicine, especially for reconstructive jaw and facial surgery” (JE 84/15-3 and MI 358/37-3). R. Adhikari thanks the University Grants Commission (UGC) for the grant “From waste to biomaterials: preparing hydroxyapatite nanomaterial from ostrich bone and biomedical application, CRG73/74-ST-02”. Furthermore, the authors wish to thank Dr. Andre Wutzler (Polymer Service GmbH Merseburg) for conducting the FTIR investigations.

Conflict of Interest

The authors declare no conflict of interest.

Data Availability Statement

The data that support the findings of this study are available from the corresponding author upon reasonable request.

Keywords

electrospinning, fibrous scaffolds, micromechanical properties, nano-hydroxyapatite, polymer blends

Received: February 19, 2022

Revised: March 30, 2022

- [1] C. Shuai, W. Yang, P. Feng, *Bioact. Mater.* **2020**, *6*, 490.
- [2] R. Scaffaro, F. Lopresti, L. Botta, *Eur. Polym. J.* **2017**, *96*, 266.
- [3] K. R. Remya, J. Joseph, S. Mani, A. John, H. K. Varma, P. Ramesh, *J. Biomed. Nanotechnol.* **2013**, *9*, 1483.
- [4] Z. Su, J. Li, Z. Ouyang, M. M. Arras, G. Wei, K. D. Jandt, *RSC Adv.* **2014**, *4*, 14833.
- [5] Y. Zhang, X. Liu, L. Zeng, J. Zhang, J. Zuo, J. Zou, J. Ding, X. Chen, *Adv. Funct. Mater.* **2019**, *29*, 1903279.
- [6] N. T. Ba Linh, Y. K. Min, B. T. Lee, *J. Biomater. Sci.: Polym. Ed.* **2013**, *24*, 520.
- [7] R. Nithya, N. M. Sundaram, *Int. J. Nanomed.* **2015**, *10*(Suppl 1), 119.
- [8] A. A. Shitole, P. W. Raut, N. Sharma, P. Giram, A. P. Khandwekar, B. Garnaik, *J. Mater. Sci.: Mater. Med.* **2019**, *30*, 1.
- [9] H. W. Bai, C. M. Huang, H. Xiu, Y. Gao, Q. Zhang, Q. Fu, *Polymer* **2013**, *54*, 5257.
- [10] I. Fortelny, A. Ujcic, L. Fambri, M. Slouf, *Front. Mater.* **2019**, *6*, 206.
- [11] M. J. Hossan, M. A. Gafur, M. M. Karim, A. A. Rana, *Bangladesh J. Sci. Ind. Res.* **2015**, *50*, 15.
- [12] F. Lopresti, F. C. Pavia, I. Vitrano, M. Kersaudy-Kerhoas, V. Brucato, V. L. a Carrubba, *J. Mech. Behav. Biomed. Mater.* **2020**, *101*, 103449.
- [13] S. A. Catledge, W. C. Clem, N. Shrikishen, S. Chowdhury, A. V. Stanishvsky, M. Koopman, Y. K. Vohra, *Biomed. Mater.* **2007**, *2*, 142.
- [14] H. Yoon, G. Kim, *J. Pharm. Sci.* **2011**, *100*, 424.
- [15] A. Abdal-hay, N. Abbasi, M. Gwiazda, S. Hamlet, S. Ivanovski, *Eur. Polym. J.* **2018**, *105*, 257.
- [16] C. H. Kim, M. S. Khil, H. Y. Kim, H. U. Lee, K. Y. Jahng, *J. Biomed. Mater. Res. Part B: Appl. Biomater.* **2006**, *78*, 283.
- [17] P. Ni, H. Bi, G. Zhao, Y. Han, M. N. Wickramaratne, H. Dai, X. Wang, *Colloids Surf. B: Biointerfaces* **2019**, *173*, 171.
- [18] X. Yang, Y. Li, W. He, Q. Huang, R. Zhang, Q. Feng, *J. Biomed. Mater. Res.: Part A* **2018**, *106*, 2863.
- [19] C. Mota, D. Puppi, D. Dinucci, M. Gazzarri, F. Chiellini, *J. Bioact. Compat. Polym.* **2013**, *28*, 320.
- [20] L. Roseti, V. Parisi, M. Petretta, C. Cavallo, G. Desando, I. Bartolotti, B. Grigolo, *Mater. Sci. Eng. C* **2017**, *78*, 1246.
- [21] M. Sattary, M. T. Khorasani, M. Rafienia, H. S. Rozve, *Polym. Adv. Technol.* **2018**, *29*, 451.
- [22] J. Wang, G. Wang, H. Shan, X. Wang, C. Wang, X. Zhuang, J. Ding, X. Chen, *Biomater. Sci.* **2019**, *7*, 963.
- [23] L. Wang, D. Chen, K. Jiang, G. Shen, *Chem. Soc. Rev.* **2017**, *46*, 6764.
- [24] T. Sanger, M. Laub, H. P. Jennissen, *Biomed. Tech. (Berl.)* **2013**, *58*(Suppl 1), 989.
- [25] T. Sanger, A. S. Asran, M. Laub, G. H. Michler, H. P. Jennissen, *Biomed. Tech. (Berl.)* **2014**, *59*(Suppl 1), 69.
- [26] H. P. Jennissen, *Curr. Dir. Biomed. Eng.* **2019**, *5*, 303.
- [27] R. L. Andersson, V. Strom, U. W. Gedde, P. E. Mallon, M. S. Hedenqvist, R. T. Olsson, *Sci. Rep.* **2014**, *4*, 6335.
- [28] F. M. Sanchez-Arevalo, L. D. Munoz-Ramerez, M. lvarez-Camacho, F. Rivera-Torres, A. Maciel-Cerda, R. Montiel-Campos, R. Vera-Graziano, *J. Mater. Sci.* **2017**, *52*, 3353.
- [29] M. Selezneva, Y. Swolfs, A. Katalagianakis, T. Ichikawa, N. Hirano, I. Taketa, T. Karak, I. Verpoest, L. Gorbatikh, *Compos. Part A: Appl. Sci. Manuf.* **2018**, *109*, 20.
- [30] Y. Zhang, H. Ouyang, C. T. Lim, S. Ramakrishna, Z.-M. Huang, *J. Biomed. Mater. Res. Part B: Appl. Biomater.* **2005**, *72*, 156.
- [31] S. A. A. Abdel Sayed, Electrospinning of polymeric nanofibers and nanocomposite materials-fabrication, physicochemical characterization and medical applications, *PhD Thesis*, Martin-Luther-Universitat Halle-Wittenberg (Halle) **2011**.
- [32] K. P. Malla, S. Regmi, A. Nepal, S. Bhattarai, R. J. Yadav, S. S. R. Adhikari, *Int. J. Biomater.* **2020**, *2020*, 1690178.
- [33] H. M. Rumpf, E. Dopp, A. W. Rettenmeyer, M. Chatzinikolaidou, H. P. Jennissen, *Materialwiss. Werkstofftech. (Mater. Sci. Eng. Technol.)* **2003**, *34*, 1101.
- [34] X. Zhang, A. S. Potty, G. W. Jackson, V. Stepanov, A. Tang, Y. Liu, K. Kourentzi, U. Strych, G. E. Fox, C. R. J. *Mol. Recognit.* **2009**, *22*, 154.
- [35] M. Laub, M. Chatzinikolaidou, H. P. Jennissen, *Materialwiss. Werkstofftech. (Mater. Sci. Eng. Technol.)* **2007**, *38*, 1020.
- [36] K. Zurlinden, M. Laub, D. S. Dohle, H. P. Jennissen, *Biomed. Tech. (Berl.)* **2012**, *57*(Suppl 1), 989.
- [37] G. Russmueller, L. Winkler, R. Lieber, R. Seemann, K. Pirkbauer, C. Perisanidis, B. Kapeller, E. Spassova, E. Halwax, W. P. Poeschl, K. Macfelda, D. Moser, *Eur. Cell Mater.* **2017**, *34*, 291.
- [38] M. Chatzinikolaidou, M. Laub, H. M. Rumpf, H. P. Jennissen, *Materialwiss. Werkstofftech. (Mater. Sci. Eng. Technol.)* **2002**, *33*, 720.
- [39] S. Milovanovic, D. Markovic, A. Mrakovic, R. Kuska, I. Zizovic, S. Frerich, J. Ivanovic, *Mater. Sci. Eng. C* **2019**, *99*, 394.
- [40] M. Sattary, M. Rafienia, M. Kazemi, H. Salehi, M. Mahmoudzadeh, *Mater. Sci. Eng. C* **2019**, *97*, 141.
- [41] J. B. Lee, H. N. Park, W.-K. Ko, M. S. Bae, D. N. Heo, D. H. Yang, I. K. Kwon, *J. Biomed. Nanotechnol.* **2013**, *9*, 424.
- [42] R. Fang, E. Zhang, L. Xu, S. Wei, *J. Nanosci. Nanotechnol.* **2010**, *10*, 7747.
- [43] D. P. Bhattarai, L. E. Aguilar, C. H. Park, C. S. Kim, *Membranes* **2018**, *8*, 62.
- [44] F. Fayyazbakhsh, M. Solati-Hashjin, A. Keshtkar, M. A. Shokrgozar, M. M. Dehghan, B. Larijani, *Colloids Surf. B Biointerfaces* **2017**, *158*, 697.
- [45] M. A. Shokrgozar, M. Fattahi, S. Bonakdar, I. R. Kashani, M. Majidi, N. Haghighipour, V. Bayati, H. Sanati, S. N. Saeedi, *Iran. Biomed. J.* **2012**, *16*, 68.
- [46] A. Kiani, M. Fathi, S. M. Ghasemi, *Int. J. Food Prop.* **2017**, *20*, 2466.
- [47] I. K. Januariyasa, I. D. Ana, Y. Yusuf, *Mater. Sci. Eng. C* **2020**, *107*, 110347.
- [48] S. C. Wong, A. Baji, S. Leng, *Polymer* **2008**, *49*, 4713.
- [49] M. Heidari, S. H. Bahrami, M. Ranjbar-Mohammadi, P. B. Milan, *Mater. Sci. Eng. C* **2019**, *103*, 109768.
- [50] K. Zurlinden, M. Laub, H. P. Jennissen, *Materialwiss. Werkstofftech. (Mater. Sci. Eng. Technol.)* **2005**, *36*, 820.



It is herewith certified that

Komal P. Malla

presented the oral lecture entitled

**Fabrication of hydroxyapatite and vitaminD3 reinforced polymers
scaffold for bone tissue engineering**

at the

POLY-CHAR 2020 – International Polymer Characterization Forum

Venice, Italy

12 – 14 April 2021

Valerio Causin
Poly-Char[Venice] Chair



Institut für Polymerwerkstoffe e.V. | Eberhard-Leibnitz-Str. 2 | 06217
Merseburg

Mr. Komal Prasad Malla (PhD student)
Department of Chemistry
Tribhuvan University
Kathmandu
NEPAL

Certificate of Presentation

Merseburg; September 22, 2021

**International conference "PolyMerTec 2021" (June 9 – 11, 2021; Merseburg / Germany)
Mr. Komal Prasad Malla (PhD student)**

CERTIFICATE

of Presentation of an Oral Lecture

**Electrospun blends of polycaprolactone/poly-L-lactic acid/gelatin and natural
hydroxyapatite for bone tissue engineering**

Prof. Dr. Beate Langer